

Quantitative Estimation of Surface Soil Moisture in Agricultural Landscapes using Spaceborne Synthetic Aperture Radar Imaging at Different Frequencies and Polarizations

Inaugural-Dissertation

zur

Erlangung des Doktorgrades

der Mathematisch-Naturwissenschaftlichen Fakultät

der Universität zu Köln

vorgelegt von

Christian Naohide Koyama

aus Bergisch-Gladbach

2012

Berichterstatter: Prof. Dr. Karl Schneider

Prof. Dr. Georg Bareth

Tag der mündlichen Prüfung: 27.01.2012

Abstract

Soil moisture and its distribution in space and time plays an important role in the surface energy balance at the soil-atmosphere interface. It is a key variable influencing the partitioning of solar energy into latent and sensible heat flux as well as the partitioning of precipitation into runoff and percolation. Due to their large spatial variability, estimation of spatial patterns of soil moisture from field measurements is difficult and not feasible for large scale analyses. In the past decades, Synthetic Aperture Radar (SAR) remote sensing has proven its potential to quantitatively estimate near surface soil moisture at high spatial resolutions. Since the knowledge of the basic SAR concepts is important to understand the impact of different natural terrain features on the quantitative estimation of soil moisture and other surface parameters, the fundamental principles of synthetic aperture radar imaging are discussed. Also the two spaceborne SAR missions whose data was used in this study, the ENVISAT of the European Space Agency (ESA) and the ALOS of the Japanese Aerospace Exploration Agency (JAXA), are introduced. Subsequently, the two essential surface properties in the field of radar remote sensing, surface soil moisture and surface roughness are defined, and the established methods of their measurement are described. The in situ data used in this study, as well as the research area, the River Rur catchment, with the individual test sites where the data was collected between 2007 and 2010, are specified. On this basis, the important scattering theories in radar polarimetry are discussed and their application is demonstrated using novel polarimetric ALOS/PALSAR data. A critical review of different classical approaches to invert soil moisture from SAR imaging is provided. Five prevalent models have been chosen with the aim to provide an overview of the evolution of ideas and techniques in the field of soil moisture estimation from active microwave data. As the core of this work, a new semi-empirical model for the inversion of surface soil moisture from dual polarimetric L-band SAR data is introduced. This novel approach utilizes advanced polarimetric decomposition techniques to correct for the disturbing effects from surface roughness and vegetation on the soil moisture retrieval without the use of a priori knowledge. The land use specific algorithms for bare soil, grassland, sugar beet, and winter wheat allow quantitative estimations with accuracies in the order of 4 Vol.-%. Application of remotely sensed soil moisture patterns is demonstrated on the basis of mesoscale SAR data by

investigating the variability of soil moisture patterns at different spatial scales ranging from field scale to catchment scale. The results show that the variability of surface soil moisture decreases with increasing wetness states at all scales. Finally, the conclusions from this dissertational research are summarized and future perspectives on how to extend the proposed model by means of improved ground based measurements and upcoming advances in sensor technology are discussed. The results obtained in this thesis lead to the conclusion that state-of-the-art spaceborne dual polarimetric L-band SAR systems are not only suitable to accurately retrieve surface soil moisture contents of bare as well as of vegetated agricultural fields and grassland, but for the first time also allow investigating within-field spatial heterogeneities from space.

Kurzzusammenfassung

Bodenfeuchte und deren Verteilung in Raum und Zeit spielt eine wichtige Rolle in der Energiebilanz an der Erdoberfläche. Sie beeinflusst die Partitionierung von Sonnenenergie in latenten und fühlbaren Wärmefluss sowie die Aufteilung des Niederschlags in Abfluss und Versickerung. Aufgrund ihrer hohen räumlichen Variabilität, ist die Bestimmung von räumlichen Bodenfeuchtemustern anhand von Feldmessungen schwierig und für großräumige Untersuchungen nicht praktikabel. In den vergangenen Jahrzehnten hat die Fernerkundung mittels Radar mit Synthetischer Apertur (SAR) ihr Potenzial zur quantitativen Bestimmung der oberflächennahen Bodenfeuchte mit hoher räumlicher Auflösung erwiesen. Da Kenntnisse über die grundlegenden Eigenschaften der SAR-Fernerkundung wichtig sind, um die Auswirkungen der verschiedenen natürlichen Oberflächen- und Geländeeigenschaften auf die Berechnung der Bodenfeuchte und anderer Oberflächen-Parameter zu verstehen, werden die grundlegenden Prinzipien der SAR Bildgebung diskutiert. In diesem Zusammenhang werden auch die beiden SAR-Satelliten, deren Daten in dieser Studie Verwendung finden, der ENVISAT der europäischen Weltraumorganisation (ESA) und der ALOS der japanischen Weltraumorganisation (JAXA), vorgestellt. Anschließend werden die beiden zentralen Oberflächeneigenschaften im Bereich der Radar-Fernerkundung, die Bodenfeuchte und die Bodenrauigkeit, detailliert erklärt, und die etablierten Messmethoden beschrieben. Die in dieser Studie verwendeten *in situ* Daten, sowie das Untersuchungsgebiet, das Rur Einzugsgebiet mit den einzelnen Test-Standorten, an denen die Daten in den Jahren 2007 - 2010 erhoben wurden, werden beschrieben. Auf dieser Grundlage werden die wichtigen Rückstreuungstheorien in der Radar Polarimetrie diskutiert und ihre Anwendung anhand neuartiger polarimetrischen ALOS/PALSAR Daten gezeigt. Eine kritische Betrachtung verschiedener klassischer Ansätze zur Berechnung der Bodenfeuchte aus SAR Daten erfolgt am Beispiel unterschiedlicher Modelle, welche mit dem Ziel ausgewählt wurden, einen Überblick über die Entwicklung von Ideen und Techniken auf dem Gebiet der Bodenfeuchtebestimmung mit aktiven Mikrowellen-Sensoren zu geben. Als Kernstück dieser Arbeit wird ein neues semi-empirisches Modell für die Inversion der Oberflächenbodenfeuchte mit dual polarimetrischen L-Band SAR Daten vorgestellt. Dieser neuartige Ansatz nutzt polarimetrische Dekompositionstechniken um die störenden Einflüsse

von Bodenrauigkeit und Vegetation auf die Bodenfeuchtebestimmung ohne Zuhilfenahme von a-priori Informationen zu korrigieren. Die landnutzungsspezifischen Algorithmen für Grasland, unbedeckten Boden, Winterweizen und Zuckerrüben ermöglichen eine Abschätzungsgenauigkeit im Bereich von ± 4 Vol.-%. Als Anwendungsbeispiel für fernerkundlich bestimmte Bodenfeuchtemuster, wird auf der Grundlage mesoskaliger SAR Daten die Variabilität der Oberflächenbodenfeuchte auf unterschiedlichen räumlichen Skalen untersucht. Es wird gezeigt, dass die Variabilität der räumlichen Bodenfeuchteverteilung auf allen Skalen mit zunehmendem Feuchtezustand der Bodenoberfläche kleiner wird. Schließlich werden die Schlussfolgerungen aus dieser Doktorarbeit zusammengefasst und es werden Zukunftsperspektiven, wie das vorgestellte Modell durch verbesserte bodengestützte Messungen und kommende Entwicklungen in der Sensor-Technologie erweitert werden kann, diskutiert. Die Ergebnisse dieser Arbeit zeigen, dass moderne, weltraumgestützte dual polarimetrische L-band SAR Systeme nicht nur eine genaue Bestimmung der Bodenfeuchte auf nackten und vegetationsbedeckten landwirtschaftlich genutzten Flächen ermöglichen, sondern zum ersten Mal auch eine kleinräumige Untersuchung von Heterogenitäten innerhalb einzelner Ackerschläge erlauben.

Acknowledgements

The present thesis was prepared during the first phase of the Transregional Collaborative Research Center 32 (SFB/TR32) "Patterns in Soil-Vegetation-Atmosphere Systems: Monitoring, Modeling, and Data Assimilation", funded by the German Research Foundation (DFG). This financial support is gratefully acknowledged. Besides, the European Space Agency (ESA) and the Japanese Aerospace Exploration Agency (JAXA) are greatly thanked for the provision of ENVISAT ASAR and ALOS PALSAR data through their PI program (AOALO.3570).

The thesis was supervised by Prof. Dr. Karl Schneider, to whom I owe my sincere gratitude not only for giving me the chance to participate in the research project and for introducing me to the truly fascinating and challenging field of radar remote sensing, but also for his guidance and invaluable suggestions for improving my work.

I thank Prof. Dr. Bareth for his consent to act as second examiner, as well as for his motivating words whenever we talked. Special gratitude is also expressed to Prof. Dr. Susanne Crewell for chairing the examination committee and more.

I am grateful to all colleagues within the project for their friendly and fruitful collaboration. A very special thank you is due to Dr. Stefan Kollet who not only strongly supported me in his role as scientific coordinator, but who also became a good friend. Moreover, I would also like to thank Prof. Dr. Clemens Simmer and Dr. Karin Boessenkool, for their support.

I thank Dr. Carsten Montzka and Guido Waldhoff for the provision of the land use classifications. Dirk Hoffmeister is greatly thanked for the help with the 3D surface roughness measurements. Gratitude is also owed to Dr. Lutz Damerow from the Technology of Crop Farming Institute of the University of Bonn for making the prototype laser scanner available to this study.

My very special gratitude goes to Dr. Masanobu Shimada, ALOS Science Project Manager at JAXA/EORC, for the quick and cordial responses to my questions concerning the “Daichi” and for providing me with lots of insider information during the friendly conversations at various conferences.

I thank the numerous student assistants who spent so much time with me in the field during the measurement campaigns and without whose help this work could not have been accomplished. Many thanks also go to all the farmers who made their fields available to us.

Finally yet importantly, my most heartfelt thanks go to my parents, Brigitta and Shoji, for everything.

Contents

Abstract.....	III
Kurzzusammenfassung	V
Acknowledgements.....	VII
Contents.....	IX
List of Figures	XII
List of Tables	XVI
List of Abbreviations	XVII
1. Introduction.....	1
1.1 Spaceborne Active Microwave Remote Sensing of Soil Moisture	3
1.2 Scope and Outline of the Thesis	5
2. Remote Sensing with Synthetic Aperture Radar Imaging.....	8
2.1 Development of Imaging Radar	9
2.2 Principles of Synthetic Aperture Radar	10
2.2.1 Radar Penetration Depth	12
2.3 SAR Imaging Geometry	13
2.4 SAR Spatial Resolution	15
2.5 SAR Complex Images.....	18
2.6 Radar Backscattering Coefficient	22
2.7 Speckle	24
2.8 ENVISAT-1 ASAR.....	26
2.8.1 Basic Processing of ASAR Data	29
2.9 ALOS PALSAR.....	31
3. Soil Surface Physical Properties.....	36
3.1 Soil Moisture Content	36
3.1.1 Unique Properties of Water.....	39
3.1.2 Complex Dielectric Constant.....	41
3.1.3 Measurement of Soil Moisture	44
3.1.4 Gravimetric Soil Moisture Determination.....	44
3.1.5 Frequency Domain Reflectometry	46

3.2 Surface Roughness.....	49
3.2.1 Statistical Description of Rough Surfaces	52
3.2.2 Methods of Surface Roughness Measurement	56
3.2.3 Electromagnetic Scattering from Rough Surfaces	58
4. Study Area and Field Measurements	63
4.1 The River Rur Catchment	63
4.1.1 Precipitation Characteristics of the Rur Catchment	64
4.1.2 Geological Overview	66
4.2 Test Sites and Sampling Fields	66
4.2.1 Test Site Selhausen	67
4.2.2 Test Site Rollesbroich.....	68
4.2.3 Test Site Duerwiss	70
4.3 Ground Truth Data Set.....	71
4.3.1 In Situ Surface Soil Moisture	71
4.3.2 In Situ Surface Roughness.....	74
4.3.3 In Situ Vegetation Parameters	77
5. Polarimetric Radar Imaging and the $H/A/\alpha$ Decomposition Theorem	79
5.1 Diagonalization of the Coherency $[T_3]$ Matrix.....	80
5.2 Polarimetric Scattering Alpha Angle	81
5.3 Polarimetric Scattering Entropy.....	83
5.4 Polarimetric Scattering Anisotropy.....	84
5.5 Scattering Mechanism Interpretation.....	85
5.6 ALOS PALSAR Experimental PolSAR Data Analysis.....	91
5.7 ALOS PALSAR Dual Polarimetric Decomposition	96
5.9.1 The Dual Polarized Entropy/Alpha Decomposition	97
5.9.3 Experimental Observations.....	99
6. Classical Models for Quantitative Soil Moisture Estimation	102
6.1 Theoretical Scattering Models	103
6.1.1 The Small Perturbation Model.....	104
6.1.2 The Integral Equation Model	106
6.2 Semi-empirical Inversion Models.....	109
6.2.1 The Oh Model	110
6.2.2 The Dubois Model.....	113

6.3 Empirical Retrieval Models	115
6.3.1 Empirical Soil Moisture Retrieval Model for Single Channel ASAR Data	116
6.3.2 Radar-Vegetation Interactions.....	118
6.4 The Need for a New L-band Model.....	122
7. A New Semi-Empirical Soil Moisture Model for Dual Polarimetric L-band SAR Data.....	124
7.1 Dual Polarimetric ALOS PALSAR Data	125
7.2 Preprocessing of Polarimetric PALSAR Data	126
7.2 Bare Soil Model.....	130
7.2.1 Surface Roughness Estimation.....	131
7.2.2 Soil Moisture Estimation on Bare Soil using Roughness Corrections	133
7.3 Grassland Model.....	134
7.3.1 Soil Moisture Estimation under Grassland Vegetation.....	136
7.4 Sugar Beet Model.....	138
7.4.1 Sugar Beet Biomass Estimation.....	139
7.4.2 Soil Moisture Estimation using Sugar Beet Biomass Corrections	141
7.5 Winter Wheat Model.....	143
7.5.1 Winter Wheat Biomass Estimation	143
7.5.2 Soil Moisture Estimation using Winter Wheat Biomass Corrections.....	145
7.6 PALSAR Soil Moisture Maps.....	147
8. Variability of Surface Soil Moisture	151
8.1 Soil Moisture Patterns	151
8.2 Statistical Description of Soil Moisture Variability.....	153
8.3 ASAR Derived Soil Moisture Patterns	154
8.4 Analysis of Soil Moisture Variability.....	155
9. Conclusions and Perspectives	162
References	168
Appendix	191

List of Figures

Figure 2.1: Microwave section of the electromagnetic spectrum.....	9
Figure 2.2: Schematic representation of radar penetration into vegetation and soil at L- and C-band (redrawn after Ulaby et al., 1981b).	13
Figure 2.3: SAR imaging geometry in strip-map mode.	14
Figure 2.4: Broadside view of the SAR geometry in altitude ground-range domain.	15
Figure 2.5: Broadside view of the SAR geometry in slant-range azimuth domain.	15
Figure 2.6: Geometric effects of terrain slope variations.	18
Figure 2.7: Schematic representation of the ground range to slant range projection.	20
Figure 2.8: Foreshortening effect.	21
Figure 2.9: Layover effect.	21
Figure 2.10: Radar shadow effect.	22
Figure 2.11: Schematic illustration of distributed targets and imaging geometry.	25
Figure 2.12: Coherent sum of discrete scatterers within one image pixel.	26
Figure 2.13: ENVISAT-1 in orbit (left) and the ASAR aperture in the laboratory (right);	27
Figure 2.14: Basis processing chain for ENVISAT-1 ASAR data.	29
Figure 2.15: ALOS PALSAR in orbit (left) and in the laboratory (right);	32
Figure 2.16: The Selhausen test site in ASAR Image Mode VV polarization (left) and PALSAR Fine Beam Mode HV polarization (right).	34
Figure 3.1: Generic relationship between water content and suction for a sand, a silt, and a clay texture (redrawn after Scheffer & Schachtschabel, 2002)	39
Figure 3.2: Top view of the vadose zone with predominant forces restraining water in the soil.	40
Figure 3.3: Schematic representation of the stick cylinder technique.	45
Figure 3.4: Frequency domain reflectometry scheme.	47
Figure 3.5: Concept of electromagnetic wave scattering on rough surfaces (Cloude, 1999).....	54
Figure 3.6: Devices for the measurement of the soil surface roughness: a) classical pin meter, b) field laser scanner, and c) terrestrial 3D laser scanner.	58
Figure 3.7: Schematic representation of Fresnel reflection.	59
Figure 3.8: Characterization of roughness components on a) smooth, b) rough, and c) very rough surfaces.	60

Figure 3.9: Scheme for the determination of the phase difference between two parallel EM waves scattered from different points on a rough surface.	61
Figure 4.1: River Rur catchment with the two major landscape units (grey shaded) and locations of the three test sites for in situ soil moisture measurements.....	64
Figure 4.2: Distribution of annual precipitation in the Rur catchment;	65
Figure 4.3: Aerial view of the Selhausen test site.....	68
Figure 4.4: Aerial view of the Rollesbroich test site.	69
Figure 4.5: Aerial view of the Duerwiss test site.....	70
Figure 4.6: Continuous surface soil moisture measurements with TDR (Rollesbroich, G03) and FDR (Selhausen, A10) probes in 10 cm depth.	74
Figure 4.7: Terrestrial laser scanner 3D composite image of field A01 on May 4, 2008.....	76
Figure 4.8: Tower view of the test field A11 with seedbed (left) and ploughed surface (right).	77
Figure 5.1: Schematic representation of the $\bar{\alpha}$ angle interpretation.....	88
Figure 5.2: ALOS PALSAR Pauli-RGB of the River Rur catchment. The Pauli vectors are color coded as red = $ HH-VV $, green = $ HV-VH $, and blue = $ HH+VV $	93
Figure 5.3: Polarimetric entropy (left), anisotropy (middle), and alpha angle maps (right) of the River Rur catchment.....	94
Figure 5.4: The Poincaré sphere interpretation of the dual polarized alpha angle.....	97
Figure 5.5: Land use specific PALSAR dual-pol $H2\alpha$ planes for different imaging dates; m_v is the mean surface soil moisture in Vol.-%, k_s is the surface roughness, and SD is the corresponding standard deviation.	100
Figure 5.6: HSV image of the Selhausen test site from 21st July 2009.....	101
Figure 6.1: Pixel-wise comparison between estimated and measured m_v using the IEM.....	109
Figure 6.2: Soil moisture distribution on field D01 in the Duerwiss test site on May 14.	109
Figure 6.3: Pixel-wise comparison between estimated and measured m_v using the Oh model.	112
Figure 6.4: Surface soil moisture distribution on field D01 in the Duerwiss test site.	112
Figure 6.5: Pixel-wise comparison between estimated and measured m_v using the Dubois model.	115
Figure 6.6: Soil moisture distribution on field D01 in the Duerwiss test site on May 14, 2009	115
Figure 6.8: Comparison between measured and a) ASAR WS derived and b) ASAR IM derived surface soil moisture.....	120
Figure 6.7: Soil moisture distribution map of the Rur catchment on 25 March 2008 as derived from ASAR WS image.....	120
Figure 7.1: Simplified processing chain for dual polarized ALSO PALSAR data.	127

Figure 7.2: Dual polarization image set of the Selhausen area as obtained from PALSAR FBD data with a) HH, b) HV, c) span, d) entropy, e) anisotropy, and f) alpha angle. 130

Figure 7.3: Comparison between HV/HH ratio and measured k_s 131

Figure 7.4: Comparison between anisotropy A and measured k_s 132

Figure 7.5: Comparison between estimated and measured k_s . The bars indicate the corresponding standard deviations. 133

Figure 7.6: Comparison between measured and estimated m_v before (left) and after surface roughness correction (right). 134

Figure 7.7: Schematic representation of the different scattering contributions occurring in a grassland pixel. 136

Figure 7.8: Grassland parameter model vs. measured dielectric constant. 137

Figure 7.9: Comparison between measured and estimated m_v for grassland pixels on various dates. 138

Figure 7.10: Schematic representation of the different scattering contributions occurring in a sugar beet pixel. 139

Figure 7.11: Comparison between effective biomass parameter M_{BETA} and measured total fresh weight of sugar beet biomass. 140

Figure 7.12: Estimated vs. measured total fresh weight of sugar beet biomass. 141

Figure 7.13: Estimated versus measured soil moisture for sugar beet pixels on various dates. 142

Figure 7.14: Winter wheat biomass parameter model vs. above ground fresh weight. 144

Figure 7.15: Estimated vs. measured above ground fresh weight winter wheat biomass. 145

Figure 7.16: Comparison between estimated and measured m_v for winter wheat pixels. 146

Figure 7.17: PALSAR derived surface soil moisture patterns for the Selhausen sampling fields on June 22 (left) and September 5, 2009 (right). 148

Figure 7.18: PALSAR derived surface soil moisture patterns for the grassland test site Rollesbroich on July 18, 2008 (left) and July 21, 2009 (right). 149

Figure 7.19: PALSAR derived surface soil moisture distribution in the Rur catchment on June 22, 2009. 150

Figure 8.1: Envisat ASAR derived soil moisture pattern of the River Rur catchment from March 25, 2008. 155

Figure 8.2: Relationship between ASAR derived mean soil moisture and the CV for the entire River Rur catchment. 156

Figure 8.3: Relationship between ASAR derived soil moisture and coefficient of variation for the fertile loess plain (left), and the low mountain range region (right). 157

Figure 8.4: Relationship between ASAR derived soil moisture and coefficient of variation for (a) the fertile loess plain pixels taking into account all dates and land cover classes.....	158
Figure 8.5: Relationship between field mean soil moisture and coefficient of variation from in situ measurements at the Selhausen test site.....	159
Figure 8.6: Overview of the scale dependent relationships between coefficient of variation and surface mean soil moisture.....	160
Figure 9.1: Within-field variability of surface soil moisture distribution as seen by ALOS PALSAR....	165
Figure A.0.1: Propagation of a plane EM wave in direction \vec{k}	194
Figure A.0.2: Different shapes of the polarization ellipse expressing the polarization states of a plane wave.	195
Figure A.0.3: Full Poincaré sphere with wave amplitude A , absolute phase α ,.....	196
Figure A.0.4: Back-Scattering Alignment (BSA) geometry.	201

List of Tables

Table 2.1: ASAR instrument parameters.....	28
Table 2.2: PALSAR instrument parameters.....	32
Table 4.1: Corner coordinates of the Selhausen test site.....	67
Table 4.2: Corner coordinates of the test site Rollesbroich.	68
Table 4.3: Corner coordinates of the test site Duerwiss.....	70
Table 4.4: Overview of measured average surface soil moisture for the different land cover types and dates of ASAR and PALSAR acquisitions.....	72
Table 4.5: Measured surface roughness for different test fields and dates.....	75
Table 5.1: Angular values of canonical targets (∞ represents non-fixed values).	89
Table 5.2: Land cover type specific ranges of values for polarimetric target parameters.	95
Table 6.1: Land use dependant coefficients for the inversion of σ^0 to ϵ' using (6.20) and biomass correction coefficients for (6.21) at an incidence angle of 23° . (Loew et al., 2006)	117
Table 7.1: PALSAR data and associated field measurements (m_v , s , and v represent measurements of soil moisture, RMS height, and vegetation parameters, respectively).	125
Table A.0.1: Characteristic polarization states with corresponding polarization descriptors.....	195

List of Abbreviations

ALOS	Advanced Land Observing Satellite
AOI	Angle Of Incidence
ASAR	Advanced Synthetic Aperture Radar
CAS	Canadian Space Agency
CAL/VAL	Calibration/Validation
CCRS	Canadian Centre of Remote Sensing
CEOS	Committee on Earth Observing Satellites
dB	decibel
DC	Dielectric Constant
DEM	Digital Elevation Model
DInSAR	Differential Interferometric Synthetic Aperture Radar
DLR	Deutsches Zentrum für Luft- und Raumfahrt
DN	Digital Number
EM	electromagnetic
EO	Earth Observation
EORC	Earth Observation Research Center
ERS	European Remote sensing Satellite
ESA	European Space Agency
FBD	Fine mode Beam Dual-polarimetric
FBS	Fine mode Beam Single-polarimetric
FDR	Frequency Domain Reflectometry
GIS	Geographical Information System
GNSS	Global Navigation Satellite System
GOM	Geometric Optics Model
GPS	Global Positioning System
HSV	Hue/Saturation/Value
IEM	Integral Equation Model
IPU	International Physical Union
JAXA	Japanese Aerospace Exploration Agency
JERS	Japanese Earth Resources Satellite

JPL	Jet Propulsion Laboratory
KA	Kirchhoff Approximation
LAI	Leaf Area Index
LANDSAT	Land Satellite
LIA	Local Incidence Angle
LiDAR	Light Detecting And Ranging
LOS	Line Of Sight
NASA	National Aeronautics and Space Administration
NDVI	Normalized Difference Vegetation Index
PALSAR	Phased Array type L-band Synthetic Aperture Radar
PAR	parallel to the row direction
POM	Physic Optics Model
PolSAR	Polarimetric Synthetic Aperture Radar
PollnSAR	Polarimetric Interferometry Synthetic Aperture Radar
PPR	perpendicular to the row direction
RADAR	Radio Detecting And Ranging
RADARSAT	Radar Satellite
RCS	Radar Cross Section
RGB	Red/Blue/Green
RLA	Radar Look Angle
RLOS	Radar Line Of Sight
RMS	Root Mean Square
SAR	Synthetic Aperture Radar
SNR	Signal-to-Noise Ratio
SLC	Single Look Complex
SPM	Small Perturbation Model
SPOT	Satellite Probatoire d'Observation de la Terre
TDR	Time Domain Reflectometry
T/R	Transmit/Receive
UAV	Unmanned Airborne Vehicle
UTM	Universal Transverse Mercator
WS	Wide Swath

1. Introduction

Without any doubt, soil moisture can be regarded as one of the important life sustaining entities on our planet. Among its various functions, the first is probably to enable the growth of vegetation on the land surface. Apart from this, water stored in soils has several other roles in the global water cycle. For instance, it controls the partitioning of rainfall into runoff and infiltration, where efficient infiltration commonly means replenishment of aquifers, while runoff may mean both exportation of valuable fresh water to other areas and degradation of top soil through leaching and erosion. The saturation state of a soil may also affect the transformation of rainfall into floods. Thus, surface soil moisture is a key variable for improving the forecasting performance of run-off models in terms of flood risk assessment and water resources management.

Moreover, surface soil moisture is a major driver of spatio-temporal patterns of evaporation and transpiration and thus impacts the energy and mass transfer between the Earth's land surfaces and the atmosphere. Consequently, it is a very important input parameter in weather forecast models as well as in global climate models. Soil moisture deficits and/or surplus greatly affect spatio-temporal dynamics of vegetation systems. Hence, information on spatial and temporal fluctuations of soil water content is relevant to a wide range of agricultural applications such as the prediction of plant growth, the determination of proper sowing dates, irrigation practices, and the identification of arable land areas prone to droughts or water logging.

In situ measurements of soil moisture are time and cost intensive. Due to their large spatial variability, estimation of spatial patterns of soil moisture from field measurements is rather difficult and generally not feasible for large-scale analyses. Although hydrological models have shown their capability to derive spatial soil moisture patterns, their application is still a challenging task, requiring a multitude of input parameters (such as soil properties, i.e. hydraulic characteristics and permeability, along with meteorological and climatological data). Neither the full spatial variability of these environmental parameters nor the full details

of the processes are typically known. Consequently, modeled soil moisture distributions tend to reduce the real magnitude of heterogeneity.

Classical methods in environmental monitoring rely on point measurements to estimate the spatial distributions of soil moisture, and one of the most critical factors is the extrapolation of point samples to catchment scale processes. According to Dooge (1986; 1988) the hydrological theory encompasses 15 orders of magnitude ranging from the molecule scale of H₂O clusters (10^{-8} m) to the planetary scale of the global hydrological cycle (10^7 m). Traditionally, studies in applied hydrology have favored the catchment scale which is also referred to as meso-scale or the lower end of the macro-scale. A large source of error occurs at the interfaces between the different scales of hydrological to meteorological or ecosystem models. These scaling problems may limit the suitability of impact studies which are driven by the output of such models. Hence, methods for both monitoring and representation of sub-grid-scale variability, as well as linking parameters and state variables across disparate dimensions are in great need to bridge the scales between different science applications such meteorological and ecological modeling.

Still today, one of the great challenges in the field of hydrological modeling and monitoring remains the linking and integration of geophysical laws across different spatial scales. Up to the 1970's, environmental monitoring was primarily focused on local-scale processes. Principally, these small observation scales were a consequence of the traditions of applied hydrology on the one hand, and of the relative simplicity of in situ data collection and the available technology for data storage and handling, on the other hand. With growing appreciation of the small and large scale dimensions of environmental changes and concomitant improvements in measurement and data handling techniques within the last decades, there have been strong initiatives to improve monitoring networks and to conduct interregional measurement campaigns such as the TERrestrial ENVironmental Observatoria, TERENO (Zacharias et al., 2011).

Remote sensing provides today mature opportunities to scientists from different fields in terms of monitoring extended processes with spatial resolutions ranging from several decimeters up to a global scale of thousands of kilometers. Remotely sensed data can be used for hydrological model parameter estimation, computation of geophysical parameters as well

as for real time forecasting and disaster monitoring. In the field of hydrology, remote sensing is indeed capable of providing some of the key state variables for water balance modeling like precipitation, snow cover, sea ice, and soil moisture. A variety of remote sensing techniques have been developed to measure various parameters on the land and sea surfaces at meso- to macro-scale (Campbell, 2007). In the field of soil moisture estimation these techniques encompass gamma ray, near to far infrared, and thermal infrared spectrometers, passive microwave radiometers, as well as active radar sensors. Among all these technologies, imaging radar is due to its sensitivity towards the dielectric surface properties, its weather independent day and night operation capabilities and its potential to acquire also subsurface information, the most suitable approach for surface soil moisture estimation.

1.1 Spaceborne Active Microwave Remote Sensing of Soil Moisture

The sensitivity of the radar backscattering coefficient (σ^0) to soil moisture at low microwave frequencies is well described in the literature (Ulaby et al., 1978; Ulaby et al., 1981b; Ulaby et al., 1982a; Ulaby et al., 1982b; Hallikainen et al., 1985; Dobson et al., 1985; Dobson & Ulaby, 1986; Oh et al., 1992). Numerous research activities carried out within the last three decades have demonstrated that sensors operating in the low-frequency portion of the microwave electromagnetic spectrum (especially P and L-band) are suitable to measure the surface moisture content. The penetration depth of the radar beam depends on soil characteristics and moisture state. It is typically in the order of some tenths of the wavelength up to half a wavelength. While the combination of different frequencies, polarizations, and incidence angles provide best results (Dubois et al., 1995; Ji et al., 1996; Wang et al., 1997; Romshoo et al., 2000) such data is today only available from airborne sensors. P-band is not available from current satellite sensors and multi-channel spaceborne L-band data is available only from PALSAR aboard the Advanced Land Observing Satellite (ALOS). However, spaceborne systems generally do not offer the repetition rate, spatial resolution, frequency and polarimetric characteristics needed for continuous high resolution soil moisture monitoring. Current and future satellite based SAR systems such as ALOS-2 (JAXA), SENTINAL-1 (ESA), Tandem-L (NASA/DLR), etc. are, and will be in the foreseeable future,

limited to a single frequency-band. Nonetheless, considerable effort has been successfully devoted to research on the retrieval of soil moisture from C-band radar data (Cognard et al., 1995; Altese et al., 1996; Rombach & Mauser, 1997; Schneider & Oppelt, 1998; Quesney et al., 2000; Verhoest et al., 2000; Le Hégarat-Masclé et al., 2002; Leconte et al., 2004; Loew, 2004; Paloscia et al., 2008), which is operational today on Earth Observation platforms such as ERS-2 (ESA), RADARSAT-1 (CSA), ENVISAT (ESA), and RADARSAT-2 (CSA). However, besides being sensitive to soil moisture, the radar backscatter signal at C-band is significantly disturbed by vegetation and surface roughness. Another major drawback of such high frequency SAR systems is the poor penetration capability rendering a consistent comparison with ground based surface measurements problematic (Shi & van Zyl, 1998).

Besides the surface roughness, a major impediment to accurate quantitative retrievals of soil moisture is the presence of a vegetation cover which is characterized by gradual variations over the growing season. Both factors modulate the radar sensitivity to soil dielectric constant rendering accurate soil moisture retrieval intricate to achieve. Because for a single-channel SAR configuration many combinations of surface parameters exist which explain the same SAR backscatter, it is not possible to separate the different scattering contributions of the soil and vegetation components within one resolution cell without additional information. Thus, the estimation of spatial soil moisture patterns with a suitable accuracy needed for many applications requires the use of correction procedures for vegetation and roughness effects (Jackson et al., 1997; Satalino et al., 2001; Loew et al., 2006; Mattia et al., 2006).

For bare soils, the relationship between SAR backscattering coefficient (σ^0), surface roughness and surface soil moisture is well investigated (Autret et al., 1989; Beaudoin et al., 1990; Mattia & Le Toan, 1999; Le Toan et al., 1999; Satalino et al., 2002). It is based upon the large contrast of the dielectric constant (ϵ') of dry soil (~ 3) and water (~ 80). The dielectric constant directly affects the backscatter intensity. Physically based backscatter models are available for bare soil conditions (Beckmann & Spizzichino, 1987; Ishimaru & Chen, 1991; Fung et al., 1992; Chen & Fung, 1995; Ishimaru, 1997). In general, these scattering models calculate σ^0 as a function of sensor configuration and soil surface state allowing the inversion of near surface volumetric water content. However, these theoretical models require either detailed knowledge of the spatial patterns of soil parameters (e.g.

surface roughness) and/or multiple radar channels (i.e. polarizations) to isolate the effects of surface dielectric constant and surface roughness. A suitable parameterization of these models, especially for larger areas, is therefore often not possible (Romshoo et al., 2000; van Zyl & Kim, 2001). Empirical and semi-empirical algorithms have shown their potential to derive soil moisture from single frequency SAR data (Oh et al., 1992; Dubois et al., 1995; Rombach & Mauser, 1997; Quesney et al., 2000). However, their applicability might be limited to the region where they were developed and thus must be validated and/or adopted if transferred to a different area.

Despite all these great achievements and important contributions from the microwave and SAR community, it is important to point out that up to date there is still no operational retrieval model available which allows robust quantitative estimation of soil moisture under vegetation.

1.2 Scope and Outline of the Thesis

The aim of this dissertation thesis is to answer the following key questions: With what accuracy and under what conditions can soil moisture be retrieved from single-channel and multi-channel (partial or full polarimetric) spaceborne SAR data? Does the available state-of-the-art polarimetric radar satellite data allow development of a soil moisture inversion scheme where information on the disturbing effects from vegetation and surface roughness can be derived directly from the SAR images? Can satellite derived soil moisture patterns help to improve our understanding of the scaling problems in hydrology?

Considering the recent advances made in sensor technology, data processing, and data analysis techniques along with the progress in the physical understanding of microwave scattering from natural terrain, an answer to these questions seems to be in reach. As polarimetric SAR data is becoming more and more available to a wide Earth Observation (EO) community (Lee & Pottier, 2009) and with ongoing discussion of whether only full polarimetric or also partial polarimetric operation should be conducted by future spaceborne

state-of-the-art sensors like ALOS-2 (http://www.jaxa.jp/projects/sat/alos2/index_e.html) answering these questions becomes even more important.

The work is composed of nine chapters organized in a hierarchical manner, with each chapter building upon the previous ones. Following this introduction, the fundamental principles of synthetic aperture radar imaging are presented in *Chapter 2*. Knowledge of the basic SAR concepts is important to understand the impact of different natural terrain features on the quantitative estimation of soil moisture and other surface parameters. The two essential surface properties in the field of radar remote sensing, namely the *surface soil moisture* and the *surface roughness* are then discussed in *Chapter 3*. Both parameters are defined and described in detail, and the established methods of their measurement are presented. *Chapter 4* summarizes the description of the study area, the River Rur catchment, and of the individual test sites as well as of the distributed field measurements as conducted in the framework of this dissertation research. These ground based measurements were taken simultaneously with satellite passes of the European ENVISAT/ASAR (ESA) and the Japanese ALOS/PALSAR (JAXA) operating at C- and L-band, respectively. The information provided in this section is necessary for the discussion of the experimental results presented in the following chapters. Since radar polarimetry is crucial for quantitative parameter inversion by means of surface scattering models, in *Chapter 5* the very basic polarimetric wave and scattering concepts are discussed. This chapter also addresses the differences between classical fully polarimetric radars and the innovative dual polarimetry modes of current state-of-the-art sensors. *Chapter 6* provides a critical review of different classical approaches to invert soil moisture from SAR measurements. Two theoretical scattering models, the small perturbation model (SPM) and the integral equation model (IEM), two semi-empirical models proposed by Oh et al. (1992) and Dubois et al. (1995), as well as one empirical retrieval model (Rombach & Mauser, 1997; Loew et al., 2006) are addressed. Their performance to accurately estimate surface soil moisture is validated against in situ measurements. The five models have been chosen with the aim to provide an overview of the evolution of ideas and techniques in the field of quantitative soil moisture estimation from active microwave data. In *Chapter 7* a new alternative semi-empirical retrieval model is developed for dual polarimetric L-band SAR data. Based on correlation analysis between multitemporal polarimetric radar data and extensive ground based measurements, land use specific parameter models are proposed which allow correcting the measured backscattering

coefficient for the disturbing effects of surface roughness and vegetation. It is demonstrated that partial polarimetric systems using only one co- and one cross-polarized channel have the potential to accurately estimate surface soil moisture under vegetation. Four different models for the land cover types bare soil, grassland, sugar beet, and winter wheat are introduced. Application of remotely sensed soil moisture is demonstrated in *Chapter 8* where mesoscale soil moisture patterns derived from multitemporal C-band SAR data are used to investigate the behavior of spatial variability of surface soil moisture at different spatial scales. The relationships between the spatial variance and the mean soil moisture states are analyzed at the scales of the entire catchment ($\sim 2400 \text{ km}^2$), two major landscape units ($\sim 1000 \text{ km}^2$), boxes (2.25 km^2), and individual fields ($\sim 0.1 \text{ km}^2$). Finally, the obtained results are summarized in *Chapter 9*. Conclusions are drawn from a concise and comprehensive comparative analysis of the pertinent methods addressed in this thesis. An outlook is presented which provides perspectives for future investigations employing novel SAR data and improved ground based monitoring of biophysical surface parameters.

2. Remote Sensing with Synthetic Aperture Radar Imaging

Today, Synthetic Aperture Radar (SAR) imaging is considered a well-developed microwave remote sensing technique suitable to provide large-scaled two-dimensional high spatial resolution images of the Earth's surface reflectivity. The imaging SAR system is an active radar system operating in the microwave region of the electromagnetic wave spectrum, generally between P-band and Ka-band, as illustrated in Fig. 2.1. Usually mounted on a moving platform (i.e. airplane, UAV, space-shuttle, or satellite) it operates in a side-looking geometry with an illumination perpendicular to the flight direction. These systems illuminate the Earth's surface with microwave pulses and receive the EM signal backscattered from the illuminated terrain. Synthetic Aperture Radar employs signal processing to synthesize a two-dimensional image of the Earth's surface from all the received signals. Due to this active operation mode, SAR sensors are independent of solar illumination and thus capable of day and night time acquisitions. In addition, operating in the microwave spectral region avoids the effects of clouds, fog, rain, smokes, etc. on the resulting images. However it should be mentioned that this is unconditionally true only in the case of operation below the S-band, while S-/C-/X-band space-borne SAR systems are sometimes also deployed for cloud and precipitation imaging. Nevertheless, generally speaking, imaging SAR systems allow an almost all-weather continuous global scale Earth monitoring. Moreover, SAR is intrinsically the only viable and practical imaging radar technique to achieve high spatial resolution also from space platforms.

The main scope of this chapter is to provide a brief overview of the basic concepts of Synthetic Aperture Radar. More detailed information can be found in the dedicated literature like, for example, in Brown & Porcello (1969), Tomiyasu (1978), Elachi (1987), Curlander & McDonough (1991), Henderson & Lewis (1998), Franceschetti & Lanari (1999), Oliver & Quegan (2004), and Cumming & Wong (2005). The chapter concludes with a description of the specific SAR systems and their products as used in this study.

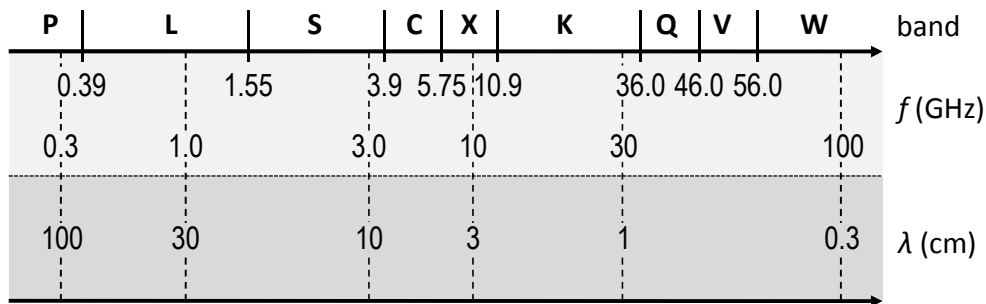


Figure 2.1: Microwave section of the electromagnetic spectrum.

2.1 Development of Imaging Radar

Before discussing the basic principles of Synthetic Aperture Radar in the next sections, firstly some brief information on the development of imaging radar shall be given here. A comprehensive review on the history of radar imaging and microwave sensing can be found in Ulaby et al. (1981b).

The genesis of the synthetic aperture concept appears to have been the work of Carly Wiley of the Goodyear Aircraft Corp. in the early 1950s. As described in a paper by Sherwin et al. (1962), Wiley was the first to observe a one-to-one correspondence between the along-track coordinate of a reflecting object (being linearly traversed by a radar beam) and the *instantaneous Doppler shift* of the signal reflected to the radar from that object. He concluded that a frequency analysis of the reflected signals could enable higher along-track resolutions than that permitted by the along-track width of the physical beam itself.

Imaging radar has then established itself as a capable and indispensable Earth remote sensing instrument since 1978, the year when the SEASAT satellite with SAR aboard was successfully launched. SEASAT was the first earth-orbiting satellite carrying a Synthetic Aperture Radar system designed for remote sensing of oceans and sea ice with wide ground swath. In addition, it also demonstrated its capability in general terrain discrimination and target detection (Birrer et al., 1982). The SEASAT SAR operated at L-band with a center frequency of 23.5 cm in wavelength and a single polarization channel employing horizontal transmit and horizontal receive (HH). Even though the SEASAT SAR observed the Earth for only 105 days due to a massive electric system failure (Jordan, 1980), it demonstrated the capability of imaging radar and opened the door for launching several follow-on space-borne SAR missions in the 1980s and 1990s. Most notable among these were the National

Aeronautics and Space Administration (NASA) Shuttle Imaging Radar missions SIR-A in 1981 and SIR-B in 1984, the European ERS-1 and 2 in 1992 and 1995, the Japanese JERS-1 in 1992, as well as the Canadian RADARSAT-1 in 1995. SEASAT SAR is also considered to have stimulated the development and research in multipolarization and fully polarimetric radar imaging (Lee & Pottier, 2009), which is regarded as a natural extension of single polarization SAR.

Today, many space-borne and airborne SAR systems are available. They are competitive with and complementary to multi- and hyperspectral radiometers as the primary remote sensing instruments. At the time of this writing, the state of the art civil SAR satellites in orbit are namely the Japanese ALOS (JAXA), the Canadian RADARSAT-2 (CSA), and the German TanDEM-X (DLR).

2.2 Principles of Synthetic Aperture Radar

In principle, two main classes of remote sensing imaging sensors can be distinguished: active systems and passive systems. While passive sensors exploit the naturally emitted, reflected, or scattered radiation from the Earth's surface, active sensors are equipped with a transmitting unit and receive the backscattered or reflected echo from the illuminated terrain. An important class of such active imaging systems is radar operating in the microwave region of the electromagnetic spectrum. As mentioned before, this active operation mode renders these systems independent from external illumination sources (e.g. the sun), while additionally, the long wavelengths at the microwave region drastically reduce the impact of weather phenomena like clouds, fog, or rain on the resulting images.

Radar imaging provides a two-dimensional image of the radar reflectivity of a scene by illuminating it with microwave pulses and receiving the backscattered field. For such radar systems two possible operation scenarios exist. The first one is that the same sensor is used for transmitting and receiving. That is, transmitter and receiver are located at the same position. In radar science, this scenario is known as *monostatic configuration*. In case of the second scenario, known as *bi-/or multistatic configuration*, transmitter and receiver are spatially separated using one active transmit-only system to illuminate the terrain and one or

several passive receive-only systems for measuring the scattered field (Skolnik, 1981). Bistatic radar is well established in the field of defence (Ender, 2003) and since the launch of the German TanDEM-X in 2009 it is now also available for the geoscience community (Krieger et al., 2009). However, in this dissertation only the monostatic case is used and thus the bistatic configuration will not be considered in the following.

In SAR imaging, a natural scene is characterized in terms of its three-dimensional reflectivity function describing the density distribution of scattering targets in the scene. In this sense, the SAR imaging process can be regarded as the projection of this three-dimensional scene reflectivity function onto the two-dimensional range-azimuth image space. Consequently, the physical information content of the SAR image is nothing more than the band-limited projection of the scene reflectivity into the SAR image geometry (Elachi, 1987). The reflectivity function of the scene depends mainly on the frequency, the polarization, and the imaging geometry. Thus, the physical information content of SAR images depends also on the choice of these diversified parameters (Henderson & Lewis, 1998). As stated in the beginning of this chapter, radar imaging systems operate within the microwave region at frequencies from 3 MHz up to 300 GHz with corresponding wavelengths from 100 m to 1 mm. Most commonly, civil radars nowadays operate at P-, L-, S-, C-, or X-band (Fig. 2.1). With respect to polarization, conventional SAR systems employ linearly polarized antennas (horizontally and/or vertically) in a single-, dual-, or fully polarimetric mode. In case of the *single polarization* mode the pulse is transmitted in a single polarization defined by the antenna, and the backscattered signal is received in the same polarization (Boerner et al., 1998). The most common mode of *dual-polarization* systems is to transmit in a single polarization and to receive at two orthogonal polarizations. This is for example the case for the dual-polarization mode of ALOS PALSAR (ERSDAC, 2008). Finally, the complete polarimetric information in form of the *scattering matrix* is measured by *fully polarimetric* systems. These systems, also referred to as *quad-polarized*, are capable of simultaneous transmission and reception in two orthogonal polarizations, completely retaining the relative phase information. The information content of such fully polarimetric radar data is discussed in detail in section 5.6, while that of dual-polarized data is discussed in section 5.7.

2.2.1 Radar Penetration Depth

One of the important features of radar remote sensing is the penetration capability of microwaves into material media. The *penetration depth* or *skin depth* is a function of the density and the moisture content of the illuminated medium, as well as frequency and polarization dependent (Ulaby et al., 1981b; Hajnsek et al., 2003b). Hence, the information content depends again on the frequency and polarization. Considering a dry medium, for example, shorter wavelengths (i.e. X- or C-band) interact predominantly with its upper layer and thus the obtained radar image contains information only about this part of the illuminated medium. In contrast, by using radars operating at lower frequencies (L- or P-band), the incident waves penetrate further into the medium, and the obtained images may contain information about deeper layers. Generally speaking, the penetration depth of the radar beam with a given frequency depends on soil characteristics and moisture state. It is typically in the order of some tenths of the wavelength up to half a wavelength. Ulaby et al. (Ulaby et al., 1981a) observed that penetration depth decreases with increasing m_v , at frequencies from 1.3 to 10 GHz. They pointed out that at frequencies higher than 4 GHz the penetration depth decreases rapidly below 1 cm if m_v is high.

The depth of signal penetration was intensively investigated in the context of the SIR- A and B missions (Elachi et al., 1984; Farr et al., 1986; Schaber et al., 1986). One of the key findings was that maximum radar imaging depth can be as large as 3 m when the soil has a favorable distribution of particle sizes and an extremely low moisture content as occurs, for instance, in active sand dunes. In a more recent study by Nolan & Fatland (2003) the authors conclude from DInSAR measurements that a change in soil moisture will cause a change in penetration depth in the order of a millimeter per 1%, above a soil water content of 10 Vol.-%. Moreover, they found that for C-band in soils with typical moisture contents > 10 Vol.-%, the penetration depths remains less than 10 mm.

In case of vegetation-covered soils, the penetration capabilities of a radar beam at a given frequencies is additionally governed by the geometry of the canopy parts, the dielectric properties (i.e. the water content) of the canopy parts, as well as the vegetation volume fraction in the canopy (volume of plant material per unit volume of canopy, which is mostly air). If the water content of the vegetation is low, as is the case for many types of crops during the fruit-filling stage prior to harvest (e.g. cereals), the penetration depth can be

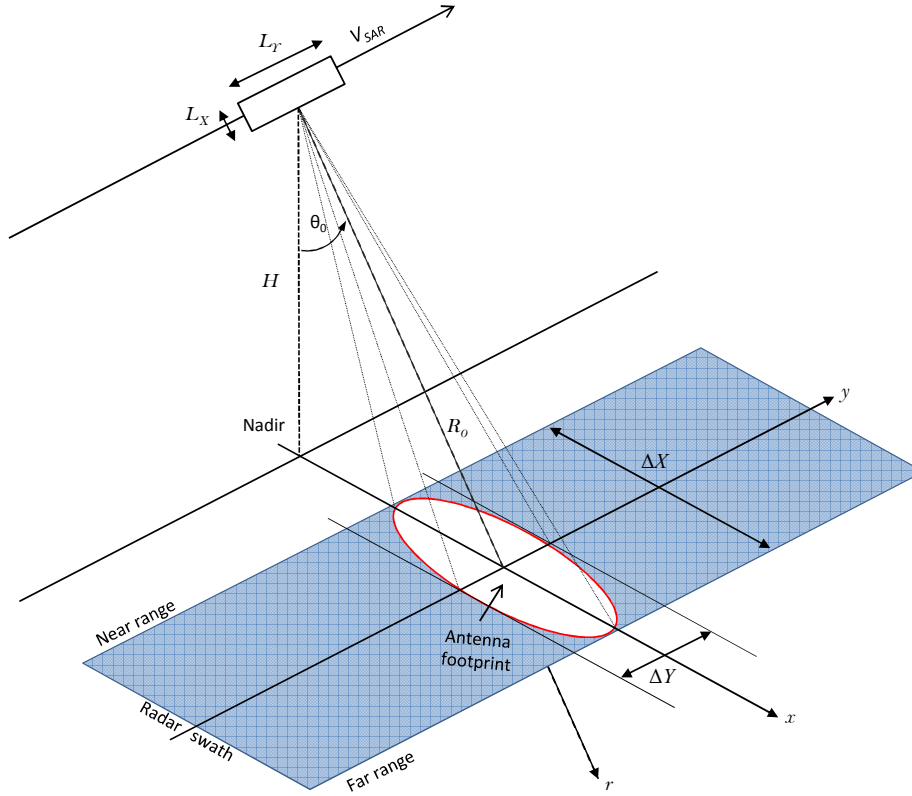


Figure 2.3: SAR imaging geometry in strip-map mode.

The SAR imaging system is situated at a height H and moves with a velocity V_{SAR} . The aperture is aimed perpendicular to the flight direction, referred to as *azimuth* (y). The antenna beam is then directed slant-wise toward the ground with an angle of incidence θ_0 . The radial axis or radar-line-of-sight (RLOS) is referred to as *slant-range* (r). The area covered by the antenna beam in the *ground range* (x) and *azimuth* (y) directions is the so-called *antenna footprint*. The scanning is provided by the movement of the platform along the flight direction. The area scanned by the antenna beam is known as the *radar swath*. The antenna footprint is defined by the antenna apertures dimensions (θ_X, θ_L) given by

$$\theta_X \approx \frac{\lambda}{L_X} \quad \text{and} \quad \theta_Y \approx \frac{\lambda}{L_Y} \quad (2.1)$$

where L_X and L_Y correspond to the physical dimensions of the antenna, while λ denotes the wavelength corresponding to the carrier frequency of the transmitted signal.

From the Fig. 2.4 and 2.5, the approximated expression of the range swath (ΔX) and the azimuth swath (ΔY) can be derived as

$$\Delta X \approx \frac{R_0 \theta_X}{\cos \theta_0} \quad \text{and} \quad \Delta Y \approx R_0 \theta_Y \quad (2.2)$$

where R_0 is the distance between the radar and the center of the antenna footprint. R_{MIN} and R_{MAX} represent the *near range* (nearest to the nadir point) and *far-range* distances, respectively.

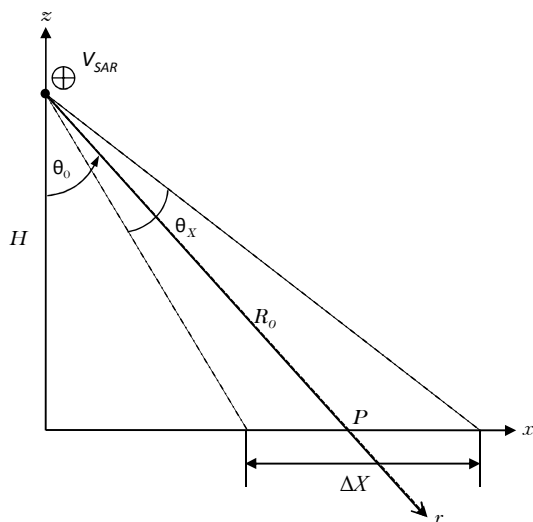


Figure 2.4: Broadside view of the SAR geometry in altitude ground-range domain.

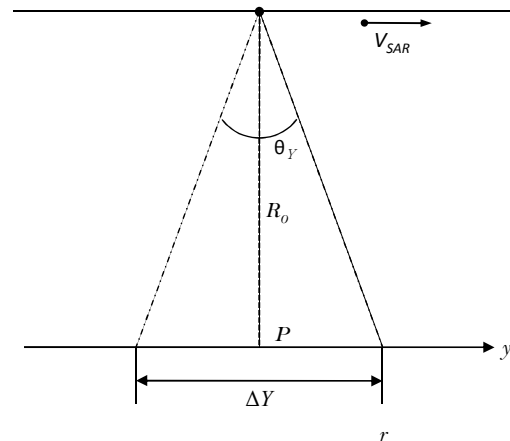


Figure 2.5: Broadside view of the SAR geometry in slant-range azimuth domain.

2.4 SAR Spatial Resolution

Among the most important quality criteria of a SAR imaging system is its spatial resolution. This property describes the ability of the imaging radar to separate two closely spaced targets. For a high resolution in range direction, very short pulse durations are necessary. Besides, in order to obtain a sufficient *signal-to-noise ratio* (SNR) it is important to generate short pulses with high energy to enable the detection of the reflected signals. A major limitation in the design of a SAR, however, is the fact that the equipment required to transmit such a very

short high-energy pulse is intricate to achieve with practical antennas. For this reason, high energy is generated by transmitting a longer pulse where the energy is distributed over the duration of the longer pulse. To achieve the range resolution comparable to the use of short pulses, the so-called pulse compression technique (Skolnik, 1981) is used. That is, the emitted pulses are linearly modulated in frequency for duration of time T_p . The frequency of the signal sweeps a band B centered on a carrier at frequency f_0 . Such a signal is called *chirp*. The received signal is subsequently processed with a matched filter which compresses the long pulse to an effective duration equal to $1/B$ (Moreira et al., 1996). The slant range resolution is then given by

$$\delta r \approx \frac{c}{2B} \quad (2.3)$$

where c is the speed of light.

The ground range resolution δx is the change in ground range associated with a slant range of δr , with

$$\delta x \approx \frac{\delta r}{\sin \theta} \quad (2.4)$$

where θ denotes the incidence angle. Hence, the ground range resolution varies nonlinearly across the swath.

In the along-track direction, the echoes of two reflecting objects are received by the antenna at the same time when both targets are in the radar beam simultaneously. However, the reflected echo from a third object, located outside the radar beam, is not received until the radar moves on. At the time the third target is illuminated, the first two are no longer illuminated, and thus the echo of this target can be recorded separately. In case of a *real aperture radar*, two objects in the azimuth or along-track resolution can be separated only if the distance between them is larger than the radar beamwidth. Thus, the azimuth instantaneous resolution for a range R_0 is given by (Reigber, 2001)

$$\delta y = \Delta Y = R_0 \theta_Y = \frac{R_0 \lambda}{L_Y} \quad (2.5)$$

Hence, it can be seen that high resolution in azimuth requires large antennas. The solution to achieve high resolution without the use of impractical large antennas is given by the concept of *synthetic aperture* (Brown, 1967; Elachi, 1987). The basic idea behind this concept is to simulate a very long antenna by moving a small antenna along the flight direction (Curlander & McDonough, 1991). Based on the exploitation of the *Doppler Effect* (Kownacki, 1967), the coherent integration of the received signals along the flight track allows synthesizing a long (virtual) antenna. The maximum length for the synthetic aperture is the length of the flight path from which a target is illuminated and is equal to the size of the antenna footprint on the ground (ΔY). If a scattering target, at a given range R_0 , is coherently integrated along the flight track, the azimuth resolution is equal to

$$\delta y = \frac{L_Y}{2} \quad (2.6)$$

It is interesting to note that the resolution in azimuth is determined only by the physical size of the real antenna of a radar system, while being independent of range and wavelength. The corresponding azimuthal resolution expression for an orbital SAR imaging system is given by (Oliver & Quegan, 2004)

$$\delta y = \frac{R_E}{R_E + H} \frac{L_Y}{2} \quad (2.7)$$

where R_E is the Earth's radius and H is the platform altitude.

Today the constraints on the spatial resolution of a SAR system are given by practical limitations on the transmitted power, the data rate, and bandwidth leading to resolutions of several meters at lower frequencies (e.g. L-band) and in the order of one meter or better at high frequencies (e.g. X-band). In case of the follow-on mission to the Japanese ALOS (Kankaku et al., 2010), which will be launched in 2013, the large bandwidth of 80 MHz at the L-band center frequency requires a diligent coordination with space-borne navigation systems

(e.g. GPS, Galileo) operating at similar frequencies. This will allow spatial resolutions of up to 3 m, what is very high for an L-band system.

2.5 SAR Complex Images

A SAR image can be described as a 2-D array of pixels formed by columns and rows where a pixel is associated with a small area of the Earth's surface. The size of these image resolution cells depends only on the SAR system characteristics. Each of them provides a *complex number* (amplitude and phase information) which is associated to the reflectivity of all scatterers situated within the pixel. It is important to note that the surface reflectivity, usually expressed as the radar backscattering coefficient σ^0 , is a function of the radar system parameters (frequency f , polarization, incidence angle θ_i of the emitted EM waves) and of the surface parameters (topography, local incidence angle, roughness, dielectric properties of the medium, moisture content, etc.). The backscattering coefficient σ^0 will be discussed in detail in section 2.7.

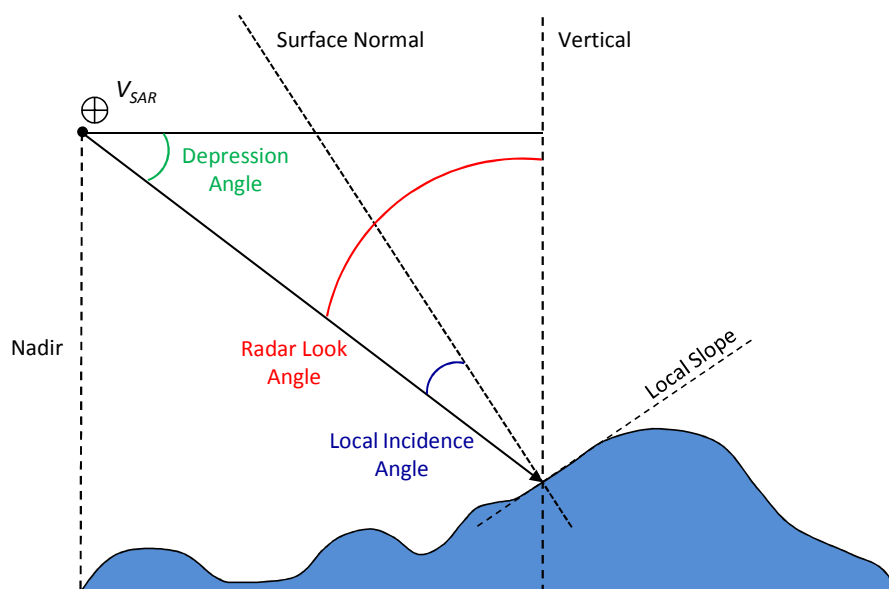


Figure 2.6: Geometric effects of terrain slope variations.

It should be emphasized that the knowledge of the imaging geometry is essential for the physical interpretation of a SAR image. Of special importance is the *radar look angle* (RLA)

which is defined as the angle between the vertical of the antenna to the ground and the range direction as shown in Fig. 2.6. On the one hand, the scattering process itself depends on the direction of the incident wave. On the other hand it directly effects the projection which defines the mapping of the scene into the SAR image. Due to this projection, information about the spatial structure of the scene is lost. Consequently, all points located at the same range distance to the sensor are mapped into the same position in the image independently of their individual height. This circumstance leads to the characteristic geometric distortion effects in SAR images. In case of a flat planar scene without any topographic variations, all points in the scene are located at the same height so that the geometric distortion is caused only by the RLA variation over range. Hence, the geometrical relationship between the scene and the corresponding image is given completely by the radar look angle. For a non-planar natural terrain, however, the topography has a considerable impact on the SAR images. Since the imaging SAR system is a side-looking radar sensor with an illumination perpendicular the flight direction, the cross-track dimension in SAR images is determined by a time measurement associated with the direct distance from the radar to the point of the surface (Meier et al., 1992). Thus, in the case of topographic variations inside the illuminated scene, SAR images present inherent geometrical distortions that are due to the difference between the slant range and the horizontal distance or ground range as illustrated in Fig. 2.7. Of the three different inherent distortions, *radar shadow*, *foreshortening*, and *layover*, the last two are considered as the main specific distortion sources in SAR imaging (Curlander & McDonough, 1991).

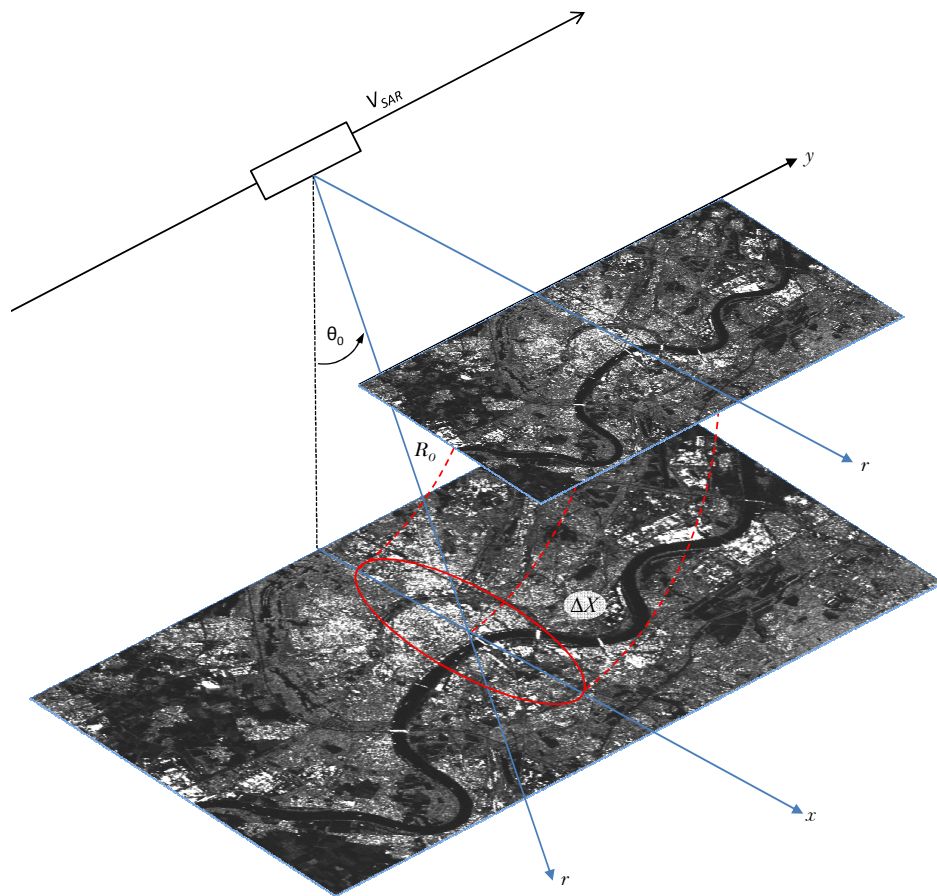


Figure 2.7: Schematic representation of the ground range to slant range projection.

Foreshortening is a dominant effect in mountainous areas and probably the most striking feature in SAR images along the range direction. Especially in the case of steep-looking space-borne sensors, the cross-track slant-range difference between two points located on fore slopes of mountains are smaller than they would be in flat areas. This effect results in a cross-track compression of the radiometric information backscattered from fore slope areas as shown in Fig. 2.8. It can be seen that the points A, B, and C are equally spaced when vertically projected on the ground. However, the distance between A' and B' is considerably shortened compared to the distance between B' and C', because the mountain top is relatively closer the SAR system and the mountains seem to “lean” towards sensor.

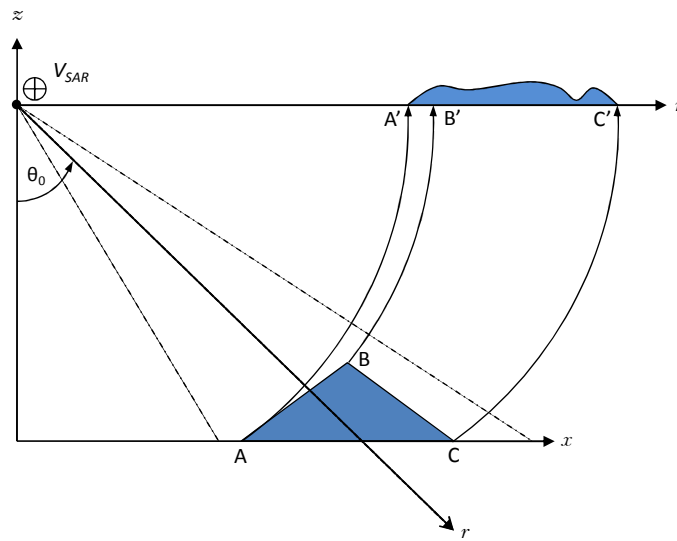


Figure 2.8: Foreshortening effect.

Due to the fact that a target on the top of the mountain is relatively closer to the SAR sensor than a target located in the valley, in the case of a very steep slope, the foreshortening is “reversed” in the slant range image. This phenomenon, where the ordering of surface elements on the radar image is the reverse of the ordering on the ground, is called layover (Fig. 2.9).

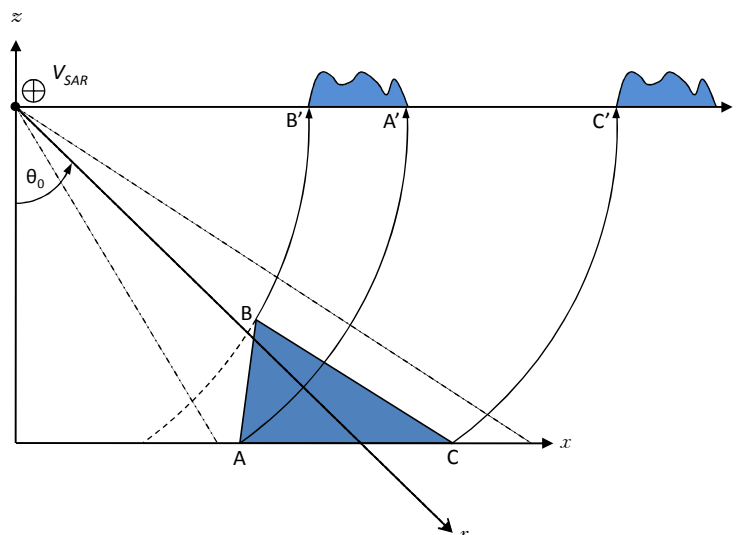


Figure 2.9: Layover effect.

Finally, slopes turned away from the radar illumination with an angle that is steeper than the sensor depression angle, provoke *radar shadow* as illustrated in Fig. 2.10. Shadow regions appear as dark areas in SAR images, corresponding to a zero signal. Note that due to the system noise level of the radar sensor, the intensity level of such a region still may not be zero. As can be seen from Fig. 2.10, the geometry of the mountain determines that the segment between the points B and C is not contributing to the slant range direction.

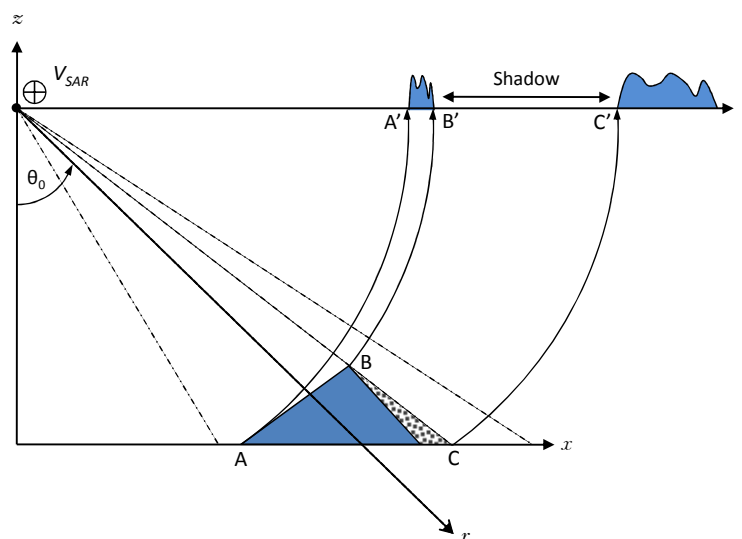


Figure 2.10: Radar shadow effect.

2.6 Radar Backscattering Coefficient

In the previous sections SAR systems were treated as imaging instruments. In this section SAR shall be considered as a measurement instrument. It is important to note that the quantitative use of SAR data, as opposed to the qualitative, requires calibrated images. In other words, the comparison of data from different sensors and/or modes, the extraction of geophysical parameters by using models, multitemporal studies, etc., can only be carried out using well calibrated SAR data. The procedure to establish the relation between the pixel values of a radar image and the physical observable is called *radiometric calibration*. It can be considered as a two-step process: i) *relative calibration* accounting for the relative relationship within the image, and ii) *absolute calibration* to establish absolute observables

comparable between different SAR images with different imaging geometries (Freeman, 1992).

For distributed targets, the intensity information of the SAR image is expressed in terms of the *radar brightness* and the *radar backscattering coefficient*. The radar brightness β^0 corresponds to the average radar cross section (RCS) per unit image area (Wang et al., 2006), i.e. the pixel or resolution cell, in dB and is the standard radiometric product for uncalibrated radar images. It is a direct result of the amplitude of the received signal expressed in terms of the digital number DN as

$$\beta^0 = 10 \times \log_{10} \left(\frac{DN^2}{K} \right) \quad (2.8)$$

where K is the so-called *absolute calibration constant*, which is derived - in the ASAR and PALSAR case - from measurements over precision transponders during the Cal/Val periods. For the ASAR sensor aboard ENVISAT K is 55 dB (Rosich & Meadows, 2004) and for the PALSAR sensor aboard the ALOS K is -83 dB (Shimada et al., 2009).

The radar backscattering coefficient σ^0 is defined as the average RCS per unit ground area in dB. Hence, σ^0 can be obtained by normalizing β^0 to the ground patch corresponding to the projection of each pixel onto the ground with

$$\sigma^0 = \beta^0 \times \sin \theta \quad (2.9)$$

The angle θ is the *local incidence angle* (LIA), also known as *angle of incidence* (AOI), defined as the angle between the incident radar beam to the surface normal (Fig. 2.6). The *radiometric resolution* describes the ability of a SAR sensor to discriminate differences in σ^0 , and thus indicates its quality as a measurement instrument. It can be seen from Eq. (2.9) that the incidence angle is important in order to obtain the normalized intensity observable. As mentioned above, the values of σ^0 are defined by the physical and electrical properties of the target, by the wavelength and polarization, as well as by the radar look angle.

In case of a flat terrain, the local incidence angle corresponds to the radar look angle and can be estimated directly from the imaging geometry as

$$\theta = \arccos\left(\frac{H - \bar{z}}{R_0}\right) \quad (2.10)$$

where H is the platform altitude above mean sea level, \bar{z} is the averaged terrain elevation, and R_0 is the slant-range distance to the target. However, it is important to understand that the local incidence angle is no longer given by the radar look angle if topographic variations are present in the scene. Then the relative orientation of the terrain – in terms of its surface normal – is required to estimate the LIA. In general, this information cannot be extracted from a single SAR image. Commonly, this is accounted for by using an ancillary *digital elevation model* (DEM) of the imaged terrain (Small et al., 2004; Small et al., 2009).

2.7 Speckle

It is a well known fact that SAR images usually display a noiselike characteristic over distributed targets. This typical granular appearance, known as *speckle*, is inherent to all kinds of coherent imaging systems operating at wavelengths smaller than the spatial resolution. It is a consequence of the interference of the individual scattering processes occurring within an image pixel.

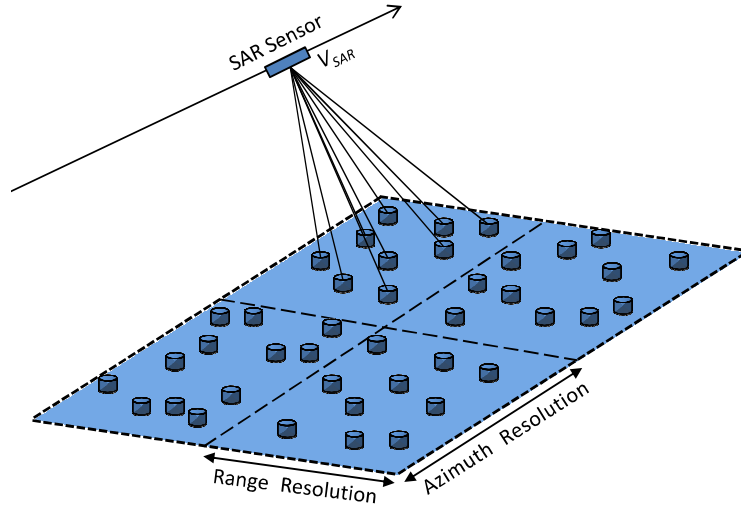


Figure 2.11: Schematic illustration of distributed targets and imaging geometry.

Distributed targets can be modeled to consist of a large number of randomly distributed discrete scatterers as illustrated in Fig. 2.11 (Goodman, 1976; Lee, 1981; Durand et al., 1987; Lopes et al., 1990; Nezry et al., 1991; Lee et al., 1994; Touzi, 2001; Lopez-Martinez et al., 2008). In this context, the total scattered field is given by the coherent superposition of the contributions of each of these discrete scatterers. The phase of each contribution depends on the location of the corresponding target inside the resolution cell. Their individual scattering contributions sum up coherently resulting in a single complex value measured by the sensor, so that the total returned modulation of the transmitted EM wave is

$$Ae^{i\phi} = \sum_{n=1}^N A_n e^{i\phi_n} \quad (2.11)$$

where A is the amplitude, ϕ is the phase, and N is the number of discrete targets within the cell. As their location varies from pixel to pixel, the resulting total scattered field varies in amplitude and phase accordingly (see Fig. 2.12).

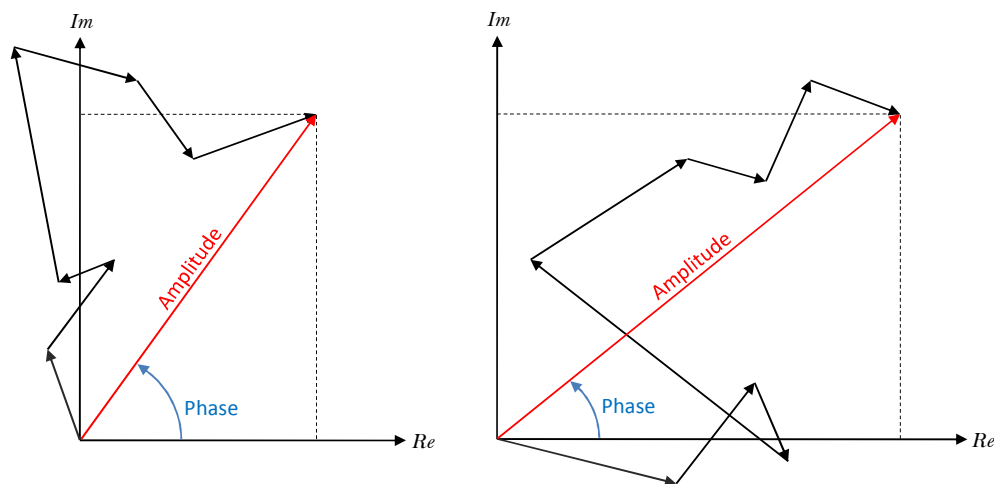


Figure 2.12: Coherent sum of discrete scatterers within one image pixel.

It is important to emphasize, that speckle is not noise but the result of constructive and destructive interferences between the complex returns from the scatterers within a resolution cell, and thus a real electromagnetic measurement. In this sense, the same imaging configuration always leads to the same speckle pattern. However, speckle limits the radiometric resolution reducing the subsequent ability to discriminate between different intensity levels. It can be reduced by averaging (multi-looking) on the cost of spatial resolution. This averaging can be carried out by different approaches, e.g.: i) by averaging adjacent pixels in the SAR image (spatial domain multi-looking), ii) by dividing the synthetic aperture into segments, which are processed separately to individual images and averaged incoherently afterwards (frequency domain approach). In the last three decades, a large variety of speckle filter algorithms have been developed in order to fulfill the requirements for different applications of SAR imaging (e.g. Frost et al., 1982; Nezry et al., 1991; Lee et al., 1991; Touzi & Lopes, 1994; Quegan & Rhodes, 1995; Lee et al., 1999b; Lee et al., 2006; Lopez-Martinez et al., 2008; Lee et al., 2009).

2.8 ENVISAT-1 ASAR

The Advanced Synthetic Aperture Radar (ASAR) was launched aboard the ENVISAT-1 satellite by the European Space Agency (ESA) in March 2002. ENVISAT-1 is an advanced polar-orbiting Earth-observation (EO) satellite providing measurements of the atmosphere, ocean, land, and ice. The mission had an ambitious and innovative payload designed to

ensure the continuity of the data measurements of the predecessors ERS-1 and ERS-2. Altogether the platform carries ten remote sensing instruments and is considered not only the most expensive European EO satellite but with a payload of more than 8.2 t also the largest. ENVISAT-1 revolves around the earth in a sun-synchronous polar orbit (SSO) with a nominal reference mean altitude of 800 km and 98.55 degree inclination. The orbital repeat cycle is thus 35 days. The ASAR instrument is a coherent, active phased-array SAR which derives from the Active Microwave Instrument (AMI) of ERS-1/2. It operates at C-band with a center frequency of 5.331 GHz and a corresponding wavelength of 5.62 cm. The antenna is 10 m x 1.33 m in size and consists of 320 T/R (Transmit/Receive) modules which are arranged in 20 tiles with 16 T/R modules each. This phased array design enables not only to adjust the incidence angle via beam steering but also allows for the first time satellite radar acquisitions with alternating polarization. The main characteristics of the instrument are summarized in Tab. 2.1. The ENVISAT-1 satellite and the space-borne ASAR sensor are shown in Fig. 2.13. Detailed instrument descriptions and technical information can be found in ESA (2007).

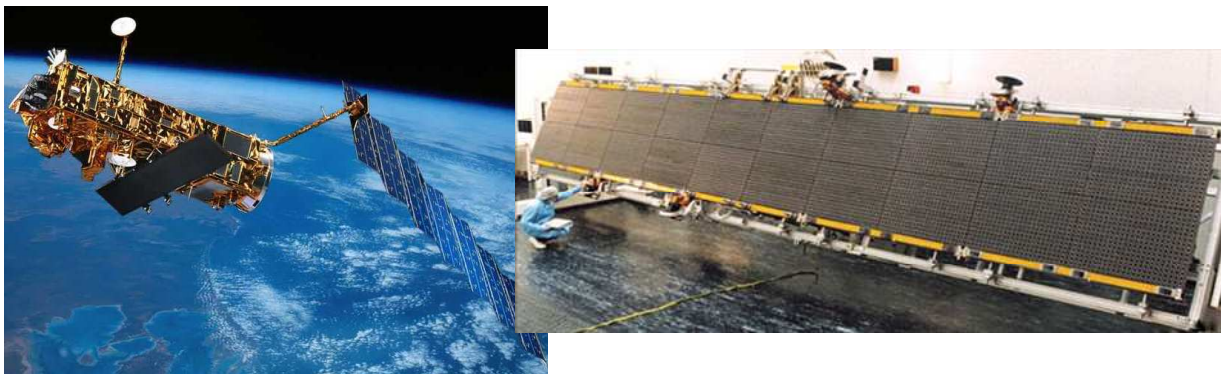


Figure 2.13: ENVISAT-1 in orbit (left) and the ASAR aperture in the laboratory (right);
(courtesy of ESA and EADS Astrium)

Table 2.1: ASAR instrument parameters

Launch Date	March 1, 2002		
Launch Vehicle	Ariane 5		
Orbit	Sun-Synchronous Polar Orbit Repeat Cycle: 35 days Altitude: 799 to 801 km (at Equator) Inclination: 98.55 deg.		
Mode	Image	Alternating Polarization	Wide Swath
Center Frequency	5331 MHz (C-band)		
Chirp Bandwidth	up to 16 MHz		
Polarization	VV or HH	VV+HH, HV+HH or VH+VV	VV or HH
Incidence Angle	15 to 45 deg.	15 to 45 deg.	
Range Resolution	25 m	30 m	150 m
Observation Swath	56 to 100 km	56 to 100 km	406 km
Radiometric Resolution	1.5 dB	2.5 dB	1.5 to 1.7 dB
Radiometric Accuracy	0.32 to 0.40 dB	0.5 to 0.55 dB	0.32 to 0.42dB

The instrument design allows for acquisitions in different images modes and with selectable swaths. The modes of interest for regional geophysical parameter inversion are namely the Image Mode (IM), the Alternating Polarization (AP) modes, and the Wide Swath (WS) mode.

- **Image Mode** of the ASAR sensor generates the highest possible spatial resolution products (Davidson et al., 1998) similar to the ERS-1/2 SAR products. This mode can image one of seven different swaths (IS1-IS7) spread over a range of incidence angles from 15 to 45 degrees in horizontal (HH) or vertical (VV) co-polarization. The standard swath is IS2 corresponding to the incidence angle of the ERS missions of 23 degrees. This mode offers the highest geometric and radiometric accuracy and thus is the first choice for quantitative geophysical investigations.
- **Alternating Polarization Mode** can also generate high resolution products in any swath but with changing polarizations of the ASAR subapertures. By employing a ScanSAR

technique (Guarnieri & Prati, 1996), albeit without changing the subswath, this mode provides dual polarized images of a scene. It should be noted that the radiometric accuracy is reduced compared to IM. Moreover, it is essential to emphasize that ASAR AP is a non-coherent polarimetric radar configuration that does not allow applying PolSAR techniques as discussed in chapter 5.

- **Wide Swath Mode** uses the ScanSAR technique to provide images covering a larger strip of the Earth's surface. The total swath width is approximately 400 km and is composed of five subswaths which are illuminated by bursts of pulses. ASAR WS acquires scenes in HH or VV polarization with a reduced resolution of 150 m. This mode is suitable for the derivation of large scale surface soil moisture patterns as described in chapter 6.

2.8.1 Basic Processing of ASAR Data

It should be noted that there is no standard processing chain for SAR images. Principally, the processing depends on how the data was acquired (radar system and acquisition mode). Additionally, the type of product that is envisaged determines how intermediate SAR products will be further processed. In this study all image processing were performed using ENVI (ITT Visual Information Solutions, Boulder, USA) and the add-on module SARscape (sarmap, Purasca, Switzerland). The processing steps are outlined in Fig. 2.14.

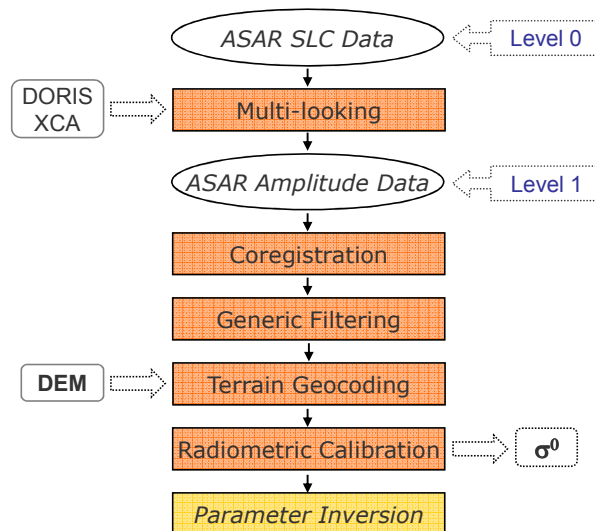


Figure 2.14: Basis processing chain for ENVISAT-1 ASAR data.

After header analysis, full resolution extraction is carried out to produce single look complex images (SLC). Wide Swath data must to be multi-looked separately for each of its 5 sub-swaths to produce the slant range intensity image with square resolution cells. The resolution of the WS SLC image is 150 m. Image Mode data is multi-looked with a factor of 5 resulting in SLC images with 25 m ground resolution. Auxiliary orbit and calibration information for each ASAR image are used to yield the most accurate multi-looked intensity images (Rosich & Meadows, 2004). The DORIS (Doppler ORbitography and Radiopositioning Integrated by Satellite) data provide precise orbital information for ENVISAT ASAR, whereby two different versions of this information are available. We used the verified orbits (VOR) since they provide the most precise location information. However, VOR data are not available until one month after the actual satellite acquisition, at the earliest. In addition, the most recent XCA (eXternal CALibration data) files were used to assure best radiometric accuracy (ESA, 2007). These ancillary ASAR data are also used in the following processing steps.

In order to render the application of a multi-temporal speckle filter possible, and to assure completely identical geometries, the multi-look images were co-registered subsequently. This step requires spatial registration to correct for relative translational shift, rotational and scale differences. Co-registration can be described as the process of superimposing, in the slant range geometry, two or more SAR images having the same acquisition geometry (Meijering & Unser, 2003).

Speckle was reduced in a two step approach. A first step to reduce the speckle is inherently performed as part of the multi-looking procedure through averaging range and/or azimuth resolution cells to produce the spatial resolution of the WS images. According to De Grandi et al. (1997), multi-temporal speckle filtering should be applied whenever two or more images of the same scene taken at different times are available. By exploiting the space-varying temporal correlation of speckle between images, this filtering process significantly reduces the noise. Hence, we used a multi-temporal De Grandi filter for despeckling of the images.

After despeckling, the images were geocoded and radiometrically calibrated to σ^0 . The ASAR images were orthorectified and terrain corrected using a high resolution (10 m) airborne laser scanner DEM (Sci Lands, 2008). As discussed in section 2.7, local terrain

slopes and aspects with respect to the incident wave result in significant radiometric as well as geometric distortions in the recorded backscatter amplitude (Meier et al., 1993). Also effects of variations in the scattering area must be accounted for (Ulander, 1996; Small et al., 2004). These terrain corrections including an incidence angle correction were performed prior to calculating the surface soil moisture using ArcGIS (Esri, Redlands, USA).

2.9 ALOS PALSAR

The Phased Array type L-Band Synthetic Aperture Radar (PALSAR) was developed by the Japanese Ministry of Economy, Trade and Industry (MITI) as a joint project with the Japan Aerospace Exploration Agency (JAXA). The sensor was launched on January 24, 2006, aboard the Advanced Land Observing Satellite (ALOS). ALOS follows the Japanese Earth Resources Satellite-1 (JERS-1) and Advanced Earth Observing Satellite (ADEOS) and utilizes sophisticated land-observing technologies. The platform carries three advanced remote sensing instrument. Apart from the PALSAR sensor, these are the Panchromatic Remote-sensing Instrument for Stereo Mapping (PRISM) and the Advanced Visible and Near Infrared Radiometer type 2 (AVNIR-2) for precise land coverage observation. After the calibration and validation (Cal/Val) period, routine operations have been conducted since October 24, 2006. ALOS revolves around the earth in the sun-synchronous orbit of 691.65 km and 98.16 degree inclination resulting in 14 revolutions per day, or once every 100 minutes. The return to the original path (repeat cycle) is every 46 days, and the inner-orbit distance is approximately 59.7 km on the equator. PALSAR operates at L-band with a center frequency of 1.27 GHz and a corresponding wavelength of 23.62 cm. The antenna is 8.9 m x 3.1 m in size and consists of 80 fully independent T/R modules. Besides the beam steering capability to adjust the off-nadir angles, the main advantage of this design is the fact that the system can operate in quad-polarized configuration. In effect, ALOS was the first satellite capable of fully polarimetric radar imaging. Tab. 2.2 gives an overview of the instrument main characteristics. Fig. 2.15 shows the PALSAR antenna mounted to the ALOS spacecraft. Detailed technical information can be found in JAXA (JAXA, 2007).

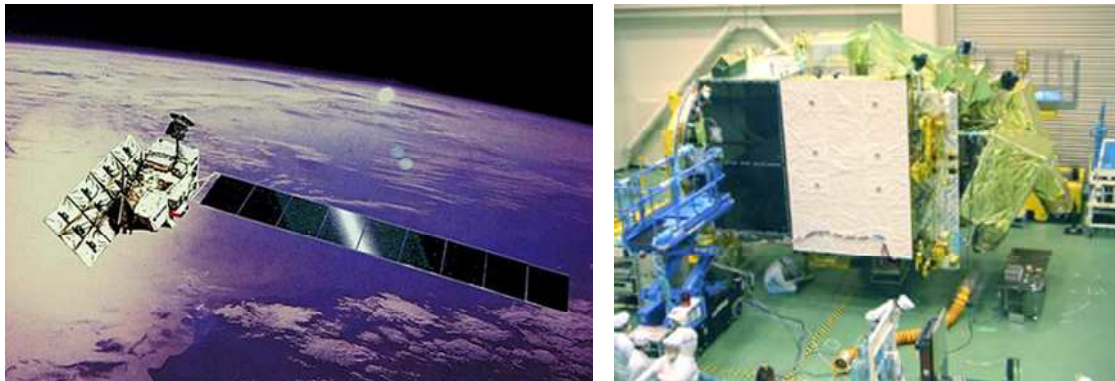


Figure 2.15: ALOS PALSAR in orbit (left) and in the laboratory (right);
(images courtesy of Dr. Shimada, JAXA)

Table 2.2: PALSAR instrument parameters

Launch Date	January 24, 2006			
Launch Vehicle	H-IIA			
Orbit	Sun-Synchronous sub-recurrent Repeat Cycle: 46 days Altitude: 691.65 km (at Equator) Inclination: 98.16 deg.			
Mode	Fine	ScanSAR	Polarimetric (experimental)	
Center Frequency	1270 MHz (L-band)			
Chirp Bandwidth	28 MHz	14 MHz	14 to 28 MHz	14 MHz
Polarization	HH or VV	HH+HV or VV+VH	HH or VV	HH+HV+VH+VV
Incidence Angle	8 to 60 deg.	8 to 60 deg.	18 to 43 deg.	8 to 30 deg.
Range Resolution	7 to 44 m	14 to 88 m	100 m	24 to 89 m
Observation Swath	40 to 70 km	40 to 70 km	250 to 350 km	20 to 65 km
Radiometric Resolution	< 1 dB	< 1 dB	< 1.5 dB	1 to 1.2 dB
Radiometric Accuracy	0.22 to 0.34 dB	0.22 to 0.54 dB	0.22 to 0.76 dB	0.22 to 0.76 dB

PALSAR can perform different acquisition modes:

- **High resolution mode** is the most commonly used under regular operation. It actually encompasses two different modes: i) *Fine Beam Single* (FBS) polarization mode measures with a horizontally co-polarized (HH) signal only. At the time of launching, its finest ground resolution of approximately 7 m was the highest as a SAR loaded on a satellite. ii) *Fine Beam Dual* (FBD) polarization mode is an innovative coherent-on-receive configuration transmitting a horizontally polarized signal and simultaneously receiving the backscattered co- (HH) and cross-polarized (HV) signals. PALSAR FBD images are acquired with a ground resolution of approximately 15 m and can be used, albeit in a limited sense compared to fully polarimetric configurations, for advanced PolSAR applications as discussed in chapter 5.
- **ScanSAR mode** enables to switch off-nadir angle from 3 to 5 times (scan by the swath of 70 km) to cover wide swaths from 250 km to 350 km. This mode operates also with an HH single-polarized signal, but the resolution is with 100 m inferior to the high resolution mode.
- **Polarimetry mode** (PLR) allows multi polarimetric acquisitions by simultaneous transmission and reception of HH, HV, VH, and VV polarizations. Since the T/R modules are split up into four groups – one for every polarization – quad-pol operation provides only a reduced spatial resolution of approximately 25 m. It should be mentioned that due to higher energy consumption the operation time is limited and frequent acquisitions are usually not available. PALSAR was the first space-borne sensor capable to measure the full scattering matrix as discussed in chapter 5. Its experimental PLR mode has been highly anticipated by the PolSAR community which considers the launch of ALOS as the beginning of the “golden age of polarimetry” (Boerner et al., 2010).

Due to the fact that the description of polarimetric ALOS PALSAR image processing requires a prior consideration of radar polarimetry theory, it will be dealt with later on in chapter 7.

In order to close this chapter it is worth showing two examples of ASAR and PALSAR image products. In Fig. 2.16 two SAR images of the Selhausen area are presented: an ASAR Image Mode acquisition on the left and a PALSAR Fine Beam Dual polarization acquisition on the right hand side. The vertically co-polarized (VV) ASAR scene was acquired in descending

orbit on June 7, 2008. The calibrated image has a spatial resolution of 25 m. The PALSAR scene is cross-polarized (HV) and was acquired in ascending orbit on June 22, 2008. The pixel size of the calibrated image is 15 m. All basic image processing performed in this study was carried out using ENVI[®] (ITT Visual Information Solutions, Boulder, USA) and the add-on module SARscape[®] (sarmap, Purasca, Switzerland). The exact processing and calibration steps for ASAR and PALSAR images are discussed in detail in sections 2.9.1 and 7.2, respectively.

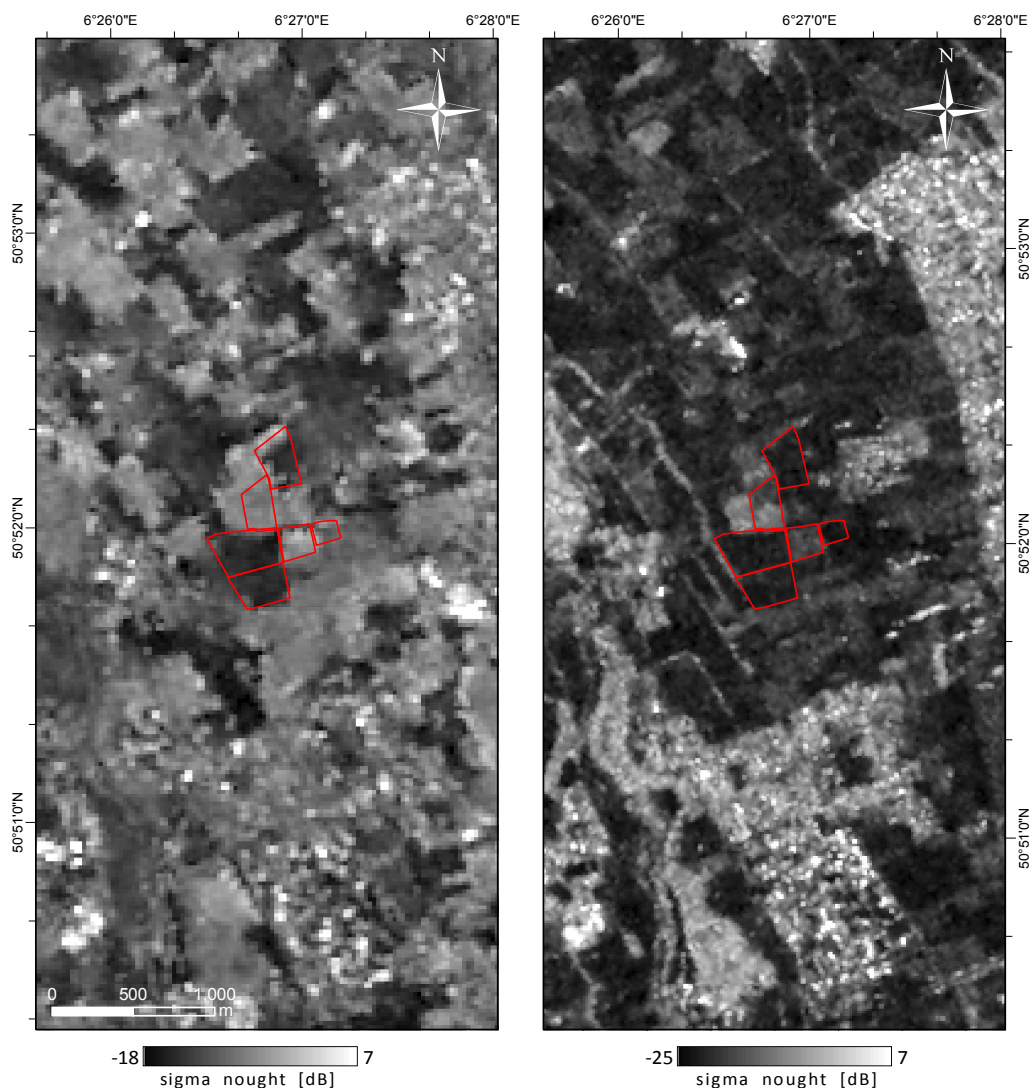


Figure 2.16: The Selhausen test site in ASAR Image Mode VV polarization (left) and PALSAR Fine Beam Mode HV polarization (right).

It can be seen that the two images differ from each other substantially. The time lag between the acquisitions is only 15 days, it is thus reasonable to assume that the great difference stems

not from significant changes in the vegetation conditions. In fact, the variations are primarily caused by different frequencies (C- and L-band), polarizations (VV and HV), and viewing geometries (ascending and descending orbit). In the ASAR case, we can just distinguish different fields while the PALSAR images with superior spatial and radiometric resolution allows identifying tree hedges, forests, arable land, and build up area easily. Another aspect worth mentioning is the fact that at C-band the reflection is substantially higher than at L-band. This is mostly due to the lower reflectance in the cross-polarized channel and the higher penetration capability of the longer waves resulting in higher attenuation of the signal. However, the return from manmade structures, where no penetration occurs, is always larger in the L-band image because of the absolute higher transmitted energy.

3. Soil Surface Physical Properties

The following chapter provides an outline of the main parameters describing the dielectric and geometric characteristics of natural soil surfaces as far as they are of importance for microwave remote sensing. The chemical and physical processes influencing these surface properties will be briefly reviewed and the corresponding variables used for their description and parameterization will be introduced. It will be discussed how these observables can be measured, and why it is important to measure them. First of all, it is important to define what soil is. In general, soil is often described as the relatively thin mantle of porous media over the land surface of the earth with properties varying widely over time and space. Its solid phase consists of the inorganic products of weathered rock or transported material together with the organic products of the inhabited flora and fauna. Thus, relevant parameters to determine the properties of a soil are time, parent material, climate, vegetation, as well as topography (Jenny, 1994). It should be mentioned that the definition of the soil surface itself is somewhat arbitrary, meaning different things to different people working in different disciplines and at different scales. In geosciences, the soil surface is often defined as being the top 2.5, 5, 10, or 15 cm of the soil column (Snell et al., 1950; Mortland, 1954; Bulfin & Gleeson, 1967; Bond & Willis, 1971; Shaver et al., 2002). In the context of radar applications, however, the soil surface is basically defined by the radar penetration depth. As will be discussed below, it hence varies as a function of the given radar band, of the soil moisture, as well as of the soil texture and density (Ulaby et al., 1982b).

3.1 Soil Moisture Content

Soils can be regarded as a three phase system of *solid particles*, *soil water*, and *soil air* within spatial and time variations of the soil matrix. According to their *grain size*, soil particles are classified into *sand*, *silt*, and *clay* in the descending order. The water within the soil matrix represents the porosity part consisting of a portion V_g / V_t (volume of gas/bulk density of a

quantity of soil) occupied by soil air and another V_l/V_t (volume of liquid/total volume of a quantity of soil) occupied by soil water. The amount of water in a soil can be expressed as

$$\text{water content, volume fraction} \quad R = V_l / V_t \quad (3.1)$$

$$\text{water content, mass basis} \quad R = m_v / m_s \quad (3.2)$$

$$\text{degree of saturation} \quad S = V_l / (V_l + V_g) \quad (3.3)$$

where m_v is the volumetric soil moisture and m_s is the dry mass of the soil. The following relationship for the conversion from the mass basis to the volume fraction, which is generally more useful in field studies, can be obtained by combining Eq. (3.1) and Eq. (3.2):

$$R_v = R_m \rho_b / \rho_w \quad (3.4)$$

Eq. (3.4) implicitly assumes that the density of water is unaffected by being adsorbed in soils, with ρ_b denoting the soil bulk density, so that m_v/V_t is equal to the density of pure free water ρ_w . The volume fraction R is equivalent to a depth fraction representing the ratio of the depth of water to the depth of the soil column. Because precipitation and evapotranspiration are also expressed as depth of water, this form is used for the examination of gains and losses of water in the field (Gardner, 1986).

The moisture content as a volume fraction ranges between zero at oven dryness and a maximum value at pore space saturation. In agronomic and hydrological applications, two intermediate stages are commonly recognized during the drying of wet soils. The wetter stage is known as the *field capacity* expressing the water content found when a thoroughly wetted soil has drained for about 2 days. The so-called *permanent wilting point*, constituting the dryer stage, expresses the moisture content found when plants wilt and do not recover. For most plants it occurs at about pF 4.2, with pF being the logarithm of the cm of water suction pressure (see Fig. 3.1). Field capacity and permanent wilting point are used as markers for the upper and lower boundaries of soil moisture at which water is usually available for plants. As found from experiments with inorganic soils, both thresholds tend to increase with increasing clay content in the soil. Moreover, at field capacity the degree of saturation of a sandy soil is far lower than the one of a clayey soil. This is due to the fact that sandy soils have a larger

amount of pore space made up of relatively large pores that drain quickly and remain air filled most of the time. As a result, the size distribution of pores influences water retention, water movement, and aeration of a soil. Hence, it is oftentimes more important than the size distribution of the soil particles (Scheffer & Schachtschabel, 2002).

The so-called *soil water retention* describes how water is held within a soil matrix by absorption at surfaces of particles and in capillaries. The surface absorption is controlled by the specific surface area of the pores and its exchangeable cations. Clay particles, on the one hand, are particularly able to absorb water actively by swelling. On the other hand, surfaces of quartz grains are not that reactive, i.e. only limited surface absorption can occur in a bed of sand. Nevertheless, water can be sucked into the pores by capillary forces. As matter of fact, it is sometimes not possible to distinguish which of the two mechanisms, surface or capillary absorption controls the water retention. The relationship between water content R and suction S is one of the basic properties of a soil and is known as the *moisture characteristics*, sometimes also denoted as *water retention curve*. Fig. 3.1 gives examples of curves $R(S)$ for three idealized soils drying from saturation. It can be seen, that sandy soils release more water at low suctions than clayey soils. Moreover, a sandy medium of fairly uniform particle sizes release most of its water over a small range of suction. Suctions of 1 and 150 m are commonly selected as useful reference points on the curve. For a wide range of soils, this corresponds, in an approximate way, to the water content at field capacity and at the permanent wilting point. The total amount of water held by a soil at a given suction is controlled by different properties of the soil including its texture, structure, organic content, and the nature of its clay minerals (Stewart & Sumner, 1992). To show the effect of these properties on the water content at different suctions, various regression equations have been established. For instance, Gupta and Larson (1979) tabulated regression coefficients for the prediction of water contents from the sand, silt, clay, and organic matter contents, as well as the bulk density for a variety of suctions. Consequently, the appropriate moisture characteristics can be estimated when these soil properties are known.

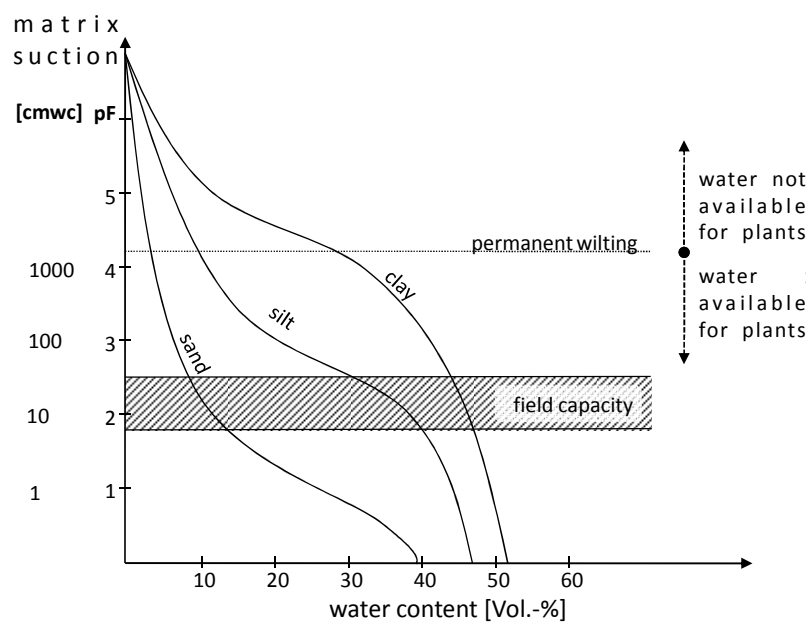


Figure 3.1: Generic relationship between water content and suction for a sand, a silt, and a clay texture (redrawn after Scheffer & Schachtschabel, 2002)

3.1.1 Unique Properties of Water

As is well known, liquid water possesses unique physical properties compared to most other liquids. This is mainly due to its strongly polarized molecular structure: The single electron of each hydrogen atom is bound to the oxygen atom causing a positive charge on both hydrogen atoms. Because the two hydrogen atoms are arranged towards one side of the oxygen atom, water acts as an *electrical dipole* with a positive pole at the hydrogen atoms and a negative pole at the oxygen atom. Further, a molecule of water can link up with another water molecule through *hydrogen bounding* allowing some degree of association between molecules of liquid water.

In a review on the structure of water, Némethy (1966) states, as one example, the effect of hydrostatic pressure on the viscosity of a liquid should increase with pressure. In water, however, it first decreases and only after applying sufficient pressure it reaches normal values. This is due to the fact that the clusters of hydrogen-bonded molecules are progressively eliminated by increasing the pressure until the water behaves like a normal liquid. Among the various unique properties of water, two are of major importance in regard to soil physics. These are namely its high *surface tension* and its *heat capacity*.

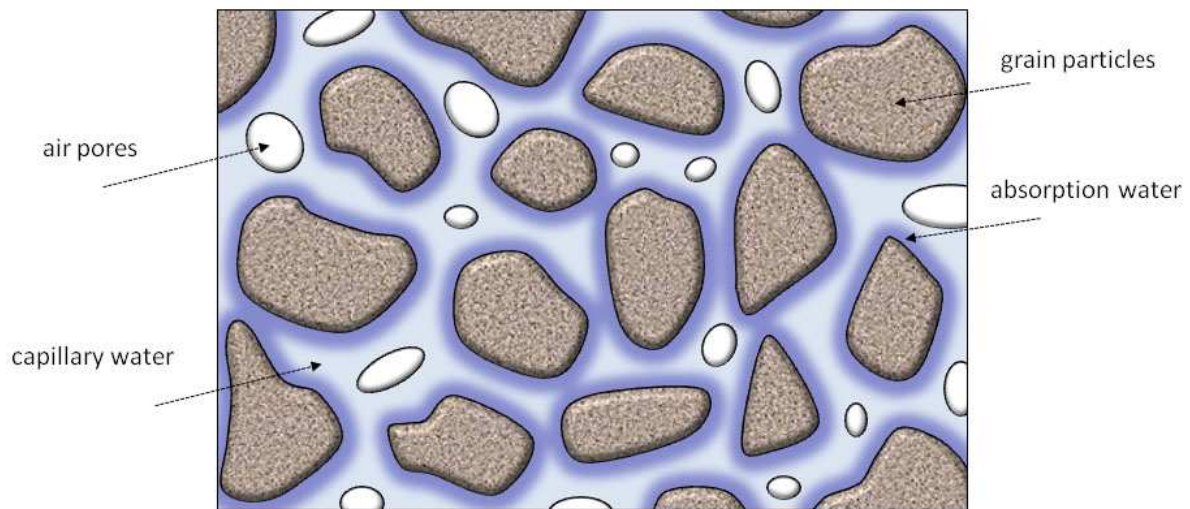


Figure 3.2: Top view of the vadose zone with predominant forces restraining water in the soil.

Since the centers of positive and negative charges are separated in the molecule, water molecules are attracted and oriented by the electrostatic field of a charged ion resulting in the *hydration* of solute ions. As evidence of the rearrangement of water molecules accompanying hydration, it can be observed that the overall volume is commonly reduced when adding salt to the water. This phenomenon is known as *electrostriction*. Hydration of ions can also occur in soils when polarized water molecules interact with exchangeable cations. It is a major mechanism in water absorption at the first stage of soil wetting. Further possible mechanisms of absorption at this first stage are intermolecular attractions between the solid surface and water over a short range due to *van der Waals forces*, as well as second hydrogen bonding of water molecules to oxygen atoms on the solid surface. Marshall et al. (1999) state that hydrogen bonding provokes a partially bounded network of water molecules originating at the oxygen atoms of the mineral surface and extending outward with decreasing effectiveness for a distance of 5 nm or more.

The next section will discuss the main physical and chemical properties of the soil matrix and the way they are influenced by the presence of water. This is important for the understanding of the relationship between soil moisture content and the dielectric properties of a soil matrix.

3.1.2 Complex Dielectric Constant

In the 1820s, Michael Faraday (1791-1867) first observed the phenomenon by which non-conducting materials can also be influenced by electrical fields. The term *dielectrica* (from “dia-electric”) was coined by William Whewell (1794-1866) in a response to a request from Faraday. The key parameter describing the behavior of a non-conductor in an electrical field is the so-called *complex dielectric constant*, which depends on numerous parameters such as frequency, temperature, salinity and ferromagnetic substances. Under the impact of an external electrical field, charged particles get out of balance, while the free electrons of a conductor move until the electrical field inside the conductor vanishes. In dielectrica, this happens only partially where the free charges move until the back force in the solid body equalizes the force provoked by the external electrical field. As positive and negative particles are polar linked, they constitute electric dipoles. In the literature, this process is also called *dielectric polarization* (Jackson, 1998; Marshall et al., 1999). A pair of main mechanisms responsible for the polarization of dielectrica can be distinguished, namely *deformation* and *orientation polarization*. The energy of a dielectrica is generated by the orientation of the electric dipole. A first part of this energy is stored as thermal energy while a second part is lost due to the internal friction. Thus, the dielectrica of a material defines the amount of electric energy which can be stored, adsorbed and lead through the medium.

The electromagnetic wave theory defines the real part of the complex dielectric constant as refraction or reflection of a wave at the interface between two different media (Snellius Law). The corresponding refraction index is a function of the incident angle and the velocity of the transmitted wave. The latter is related to the refractive angle and the velocity of propagation in the boundary layer of the wave. The refraction index is defined as the square root of the complex dielectric constant of the denser medium and constitutes a dielectric constant when related to a vacuum or the air. The complex dielectric constant can be considered as a measure of the response of a medium to an electromagnetic field. It is composed of two parts, the real and the imaginary one (Stratton, 1941; von Hippel, 1995b). The complex dielectric constant is given by

$$\varepsilon = \varepsilon' - j\varepsilon'' \quad (3.5)$$

where ε' denotes the permittivity of a material, while ε'' is referred to the dielectric loss factor of a material. The latter describes the feasibility of a medium to adsorb a wave and to transform its energy into another form. In this work ε' will always refer to the average relative dielectric constant of a material. It should be mentioned that for most natural surfaces $\varepsilon' \gg \varepsilon''$ (Stratton, 1941).

The imaginary part of the complex dielectric constant also describes the attenuation length of the electrical field in a given medium. Assuming that the propagating electromagnetic energy has exponential attenuation with depth, the penetration depth δ_p of the wave into a medium is denoted as the *skin depth* given by (Ulaby et al., 1981b)

$$\delta_p = \frac{\lambda \sqrt{\varepsilon'}}{2\pi\varepsilon''} \quad (3.6)$$

For a so-called slightly lossy medium δ_p is per definition about $1/e$ ($e = \text{Euler's Number} \approx 2.7183$) of the input value (Ulaby et al., 1982b). It follows Eq. (3.6) that δ_p increases with increasing wavelength λ , while at the same time for a fixed λ the skin depth generally increases with decreasing dielectric constant.

Generally speaking, the dielectric constant of most dielectric natural media varies between 1 and 6. It increases significantly with increasing water content, and free liquid water finally reaches ε up to 81 at low frequencies (Ulaby et al., 1986). This circumstance is the reason for the high sensitivity of the microwave spectrum towards the moisture content of the observed media. Note that the dielectric constant of water varies in dependence on the molecules rotation, e.g. freezing, tight binding to soil particles, etc.

In homogeneous media, such as pure liquid water or ice, the behavior of ε is fairly well understood (Wang & Schmugge, 1980). For pure water the frequency dependency of the dielectric constant is given by the Debye equation as

$$\varepsilon_w = \varepsilon_{w\infty} + \frac{\varepsilon_{w0} - \varepsilon_{w\infty}}{1 + j2\pi f\tau_w} \quad (3.7)$$

where ε_{w0} is a static dielectric constant of pure water and represents a high-frequency (or optical) limit of ε_w . Both formulations are dimensionless. The relaxation time of pure water τ_w is measured in seconds and the electromagnetic frequency f is given in Hz (Debye, 1929).

In dry soils the real part ε' of the complex dielectric constant ranges from two to four, while typical values for the imaginary part ε'' lie below 0.05 (Ulaby et al., 1986). As a matter of fact, the first water that is added to a dry soil will cause only a small increase of ε , because at first the molecules are tightly bound to the surface of the soil particles. Due to the behavior of the water molecules, as described in the foregoing section, adding more water will rapidly increase ε of the soil. Since the matrix forces decrease substantially with the distance from the surface of the soil particles, the water molecules located several layers away from the particles are able to move freely within the pores (Wang & Schmugge, 1980).

In the literature many empirical and theoretical models to relate the dielectric constant of a mixture to that of its constituents have been proposed. Extensive investigations in the frequency range between 0.3 and 18 GHz were, for instance, conducted by von Hippel (1995a), Hallikainen et al. (1985), or Peplinski et al. (1995). The dielectric behavior observed from experimental measurements have been summarized by polynomial expressions in dependence on the volumetric soil water content as well as the percentage of sand and clay contained in the soil. It should be mentioned that these studies classify the soil particles according to the USGS (United States Geological Survey) system. Hence, care has to be taken when they are transferred to the European or FAO (Food and Agriculture Organization) soil classification system. In order to take out the dependence on adjustable parameters, Dobson et al. (1985) introduced a physical soil model only dependent on measurable soil characteristics, thus not requiring any adjustable parameters to fit the experimental data. The model is based on two parameters: the bound water fraction and the free water fraction, both corresponding to the pore-size distribution as calculated from the particle size distribution. Studies by e.g. Hoekstra & Delaney (1974), Wobschall (1977), Topp et al. (1980), De Loor (1983), Sihvola & Kong (1988), Ren & Tateiba (1998), Kärkkäinen et al. (2001), and Mattei et al. (2008) on the permittivity of dielectric mixtures indicate that for a frequency range from 1 to 10 GHz, a two component refractive index formula considering only the volumetric

fraction of dry matter and free water is a sufficiently good approach for most soil types. In this study, the polynomial relation of the third order developed by Topp et al. (1980) is used for the conversion from volumetric water content m_v to the real part of the complex dielectric constant ϵ' , and vice versa. As for the soil types occurring in the study area the influence of the imaginary part of the complex dielectric constant is almost negligible, measurements and evaluation of ϵ'' are not considered in the following.

3.1.3 Measurement of Soil Moisture

First methods for measuring the amount of water contained in a soil were already reported in the 15th century. The most common methods for soil moisture measurements today are with regard to the mass, the volume or the saturation of soils. Gardner et al. (2001) emphasize that the measurement of soil moisture content is one of the least accurate methods in principle. Nevertheless, it can be considered as one of the relatively accurate methods in soil physics (Koorevaar et al., 1983). Still, the main problem in soil water investigations is the definition of the material state at which a soil can be characterized as dry (Gardner et al., 2001). In the literature, a large number of methods to measure directly and indirectly the soil water content has been described (e.g. Veihmeyer & Hendrickson, 1950; Schmugge et al., 1980; Topp et al., 1984; Jackson, 1988; Parchomchuk et al., 1990; Dabrowska-Zielinska et al., 2002; Huisman et al., 2003; Serbin & Or, 2004). In principle, it can be distinguished between direct and indirect methods of measuring soil moisture contents. In this sense, direct methods include all measured processes by which the soil water is evaporated, extracted, or removed by chemical reactions, while indirect methods refer to the functional relations between the physical or chemical properties of the soil matrix and the water content of the soil. In the presented study two methods were used, a direct one, namely the gravimetric method, and the indirect method of frequency domain reflectometry (Navarro et al., 2006). Both techniques will be discussed in the following.

3.1.4 Gravimetric Soil Moisture Determination

The most common direct method to obtain the water content of a soil sample is to measure the mass difference before and after drying it at 105°C until reaching a constant weight. Then,

the mass difference m_v corresponds to the water loss of the soil sample due to the drying process (Reynolds, 1970a). It should be noted that the endpoint of this drying process does not represent an entirely water free soil, but a balanced state between vapor pressure of the material and water vapor partial pressure in the drying region (Marshall, 1966). In this sense, the state for which a soil is called dry can be considered as a subjective term (Reynolds, 1970b). The water content on a mass basis is defined in Eq. (3.2) as discussed in section 3.1. The gravimetric water content is given in units of g/g expressing the weight in percent after multiplication with 100 of the soil water in weight percent (Weight-%). In case the water content is expressed in volumetric percent (Vol.-%), one has to take the bulk density into account. Therefore, the soil samples are taken with the predefined volume of so-called stick cylinders. In this study we used standard cylinders with a sample volume of 100 cm³ (Fig. 3.3). The water content as a volume fraction R , commonly expressed in Vol.-%, is obtained from R_m via Eq. (3.4), where ρ_b is the dry bulk density of the soil and ρ_w is the density of the water.

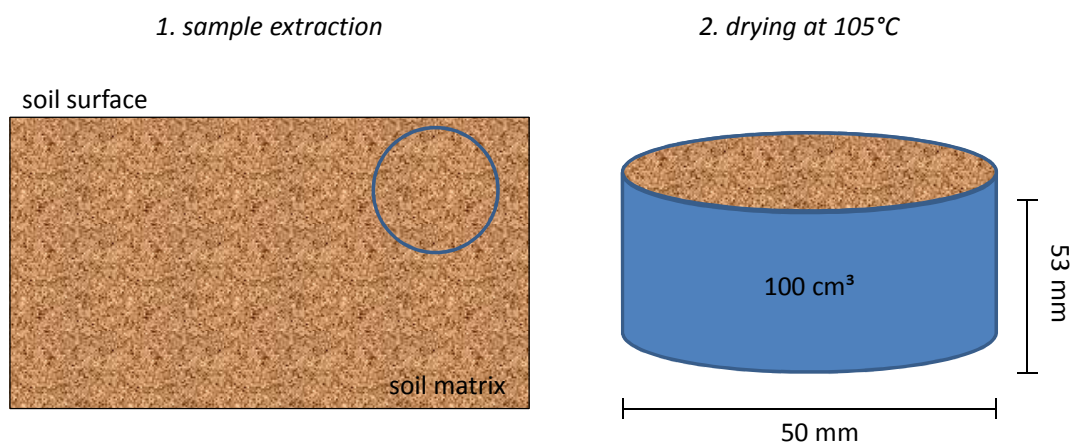


Figure 3.3: Schematic representation of the stick cylinder technique.

The technique described was introduced by Gardner (1986). In despite of its arbitrary features, the method is the established standard with which other estimations of soil moisture are compared. One downside of this approach is the fact that the nature of sampling interferes with continuous experiments. That is, every tested soil volume can only be sampled once. Moreover, when holes are dug and roots are cut, the infiltration and drainage regime is severely affected. Due to the typically strong heterogeneity of soil texture and/or structure

influencing the water retention and movement, a large number of samples may be required to map the spatial variability in the field. Finally it should be mentioned that the procedure is very time- and work-consuming. As the amount of water lost by drying increases with increasing oven temperature for any inhomogeneous soil containing clay or organic matter, the temperature has to be controlled within a range between 100 and 110°C (Reynolds, 1970b). Holmes et al. (1967) observed that a variation of about 10% or more can occur in typical field samples. Taking all this into account, the gravimetric approach is rather unattractive in terms of a time efficient and repeatable ground data collection for remote sensing studies.

3.1.5 Frequency Domain Reflectometry

In this study frequency domain reflectometry (Navarro et al., 2006) is used as standard technique for in situ soil moisture measurements. Employing hand held probes with data loggers is one of the most time efficient methods to accurately measure distributed soil moisture patterns in the field. The principle of FDR is based on the well established method of responding to changes in the relative dielectric constant. These changes are converted into a DC voltage, virtually proportional to soil moisture content over a wide working range. The hand held probes (Theta ML2x Delta-T probes, Delta-T Devices Ltd., Cambridge, UK) consist of a waterproof housing containing the electronics. According to the length of its sharpened stainless steel rods, the measured surface soil moisture provides an average value for the topmost 6 cm (Fig. 3.4). The device generates a 100 MHz sinusoidal signal which is applied to a specially designed internal transmission line extending into the soil by means of the array of the four rods. The impedance of this array varies with the impedance of the soil, which has two components: the relative dielectric constant and the ionic conductivity. The choice of the 100 MHz signal frequency minimizes the effect of ionic conductivity, so that changes in the transmission line impedance are dependent almost solely on the soil's relative dielectric constant. As mentioned earlier, the dielectric constant of water ($\epsilon' \approx 81$) is very much higher than dry soil (typically $\epsilon' \approx 3$ to 5) and air ($\epsilon' \approx 1$), and thus, the dielectric constant is determined primarily by its water content. The impedance of the rod array affects the reflection of the 100 MHz signal, and these reflections combine with the applied signal to form a voltage standing wave along the transmission line. The output of the probe is an

analogue voltage proportional to the difference in amplitude of this standing wave at two points forming a sensitive and precise measure of the soil water content (Gaskin & Miller, 1996). The output signal is 0 to 1 V DC for a range of soil dielectric constant between 1 and 32, what corresponds to a moisture content of approx. 50 Vol.-%. Studies published over many years by e.g. Topp et al. (1980), Whalley (1993), White et al. (1994), or Heimovaara et al. (1996) show almost linear correlation between the square root of the dielectric constant and the volumetric moisture content for a wide range of soil types.

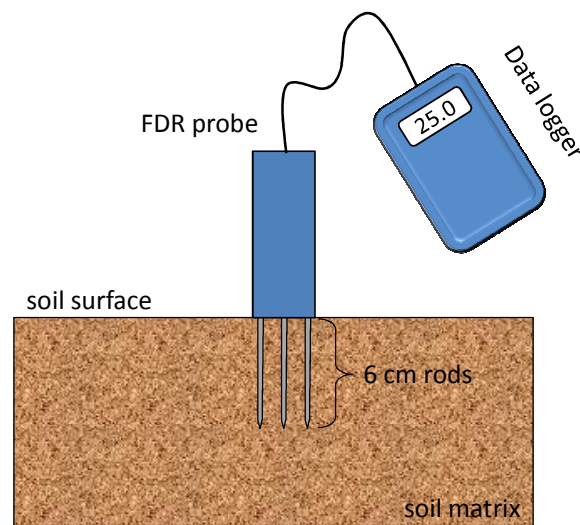


Figure 3.4: Frequency domain reflectometry scheme.

Electric transmission line theory leads to the expression for the propagation velocity of an electromagnetic wave in a slightly long transmission line (Stratton, 1941) as

$$V = c \left[\frac{1}{2} \varepsilon' \left\{ 1 + \left(1 + \tan^2 \delta \right)^{1/2} \right\} \right]^{-1/2} \quad (3.12)$$

where c is the velocity of light in vacuum and $\tan \delta = \{ \varepsilon'' + (\sigma_{dc} / \omega \varepsilon_0) \} / \varepsilon'$. The remaining symbols are the real part of the complex dielectric constant ε' , the imaginary part ε'' , the zero-frequency electrical conductivity of the medium σ_{dc} , the angular frequency ω , and the free space permittivity ε_0 . At very high frequencies, $\tan \delta$ tends to zero, so that

$$V = c/(\varepsilon')^{1/2} \quad (3.13)$$

The variation of the dielectric constant of soil with its water content R can be estimated approximately by adding the three contributions $R\varepsilon$ (water), $\phi\varepsilon$ (air), and $[1-(R+\phi)]\varepsilon$ (soil). Here, R is the volume fraction of water, ϕ is the volume fraction of air-filled pores, and $[1-(R+\phi)]$ is the volume fraction of the soil. Consequently, it is expected that R would have a functional dependence on ε as determined for the soil in question. The most recognized of such a relationship was established by Topp et al. (1980) to be

$$R = -a + b\varepsilon - c\varepsilon^2 + d\varepsilon^3 \quad (3.14)$$

the volumetric soil water content m_v

$$m_v = -5.3 \times 10^{-2} + 2.92 \times 10^{-2} \varepsilon' - 5.5 \times 10^{-4} \varepsilon'^2 + 4.3 \times 10^{-6} \varepsilon'^3 \quad (3.15)$$

and the relative dielectric constant ε'

$$\varepsilon' = 3.03 + 9.3m_v + 146m_v^2 - 76.7m_v^3 \quad (3.16)$$

The experimental values for ε were determined by pulse travel-times as shown in Eq. (3.15), and those for R by gravimetric measurements and the use of dry bulk densities. As confirmed by several studies, this empirically determined third order polynomial expression of the dielectric constant is quasi independent of the soil type and texture, the bulk density, as well as the salinity and temperature of the soil (Topp & Davis, 1985; Dalton & Van Genuchten, 1986; Whalley, 1993). Up to now this function is regarded as a universal calibration function and is used in various investigations. However it should be mentioned, that some studies indicate a limited validity for specific soil types. For example, Herkelrath et al. (1991) reported significantly divergent results for soils with high organic matter contents. Based on extensive investigations on inorganic and organic soil types, Roth et al. (1992) suggest the use of two different calibration functions – one for inorganic and one for organic soils.

The accuracy of the obtained frequency domain measurements after calibration to a specific soil type is in the range of ± 1.0 Vol.-%. However, the accuracy slightly decreases for soil temperatures $>40^{\circ}\text{C}$ (Gaskin & Miller, 1996). It should be noted that all studies report some underestimation of soil water contents for soils with high clay and/or organic matter contents. Some authors, e.g. Dobson et al. (1985) and Hallikainen et al. (1985), argue that this is due to the dielectric properties of bounded water. Minerals and swelling clay particles have a high surface tension enabling them to adsorb high amounts of water. Hydration of the exchangeable cations is largely driving this absorption as well as the accompanying increase in the interlayer spacing. The minerals and clay particles swell macroscopically due to this process. In case the solution between two parallel surfaces has a higher electrolyte concentration than that of an outer solution bathing the clay particle, water will be attracted osmotically, and consequently the distance between the surfaces will increase. Then, the exchangeable cations become unable to move freely out to the bathing solution and act as if retained with a semipermeable membrane (Koorevaar et al., 1983; Stewart & Sumner, 1992; Jury & Horton, 2004). Due to the strong binding of the water dipoles they lose their ability to rotate or polarize. Consequently, the dielectric constant of bounded water is significantly smaller than that of free water, i.e. it cannot be measured anymore by means of frequency and/or time domain reflectometry. Note that this stands in contrast to the gravimetric method where the drying process overcomes the binding forces. Hence, the use of a universal calibration function may lead to an underestimation of soil water contents. It should be emphasized that for some soil types, especially mineral and clay rich soils, the use of a soil specific calibration function is mandatory.

3.2 Surface Roughness

In order to address the geometric properties of a soil surface, it is important to understand that the solid phase of soils is composed of particles with various shapes and sizes. These particles are packed together in different ways, and this packing may be dense or open. The particles themselves may either behave as heterogeneous individuals or as clusters in so-called *soil aggregates*, where the amount of pore space and the size of the pores vary in a

complementary manner. The soil structure may then be defined as the arrangement of the solid particles and of the pore space between them (Low, 1954).

The soil structure is determined by the size distribution of the primary particles as well as by the forces affecting their arrangement. Processes like swelling and shrinking, freezing and thawing, the movement of water, the growth and decay of plant roots, as well as the action of earthworms and other borrowing animals can all cause the rearrangement of the particles. Materials aggregating these particles are mobilized and deposited by chemical and biological processes in the soil. The resulting structure and especially the size, shape, and arrangement of the aggregates is greatly influenced by weather conditions. Soil structure itself directly affects many of the soil properties. Water retention and conductance are dependent on pore space and pore size. The properties of individual particles are in a way masked in stable aggregates what may result in favorable physical conditions of soils which otherwise would not be arable. Moreover, it affects the environment for roots by influencing the water and air supply. In this sense, growth of plants can be severely hampered or completely prevented by structures which are unfavorable to water or air movement or resistant to seedling emergence or root growth.

From all these processes and descriptions of the soil structure, it becomes obvious that all natural surfaces are characterized by some kind of roughness. The scale of this roughness may range from geological dimensions like mountains down to sub-millimeter scales as found, for example, in aeolian depositions. Generally speaking, rough surfaces can be divided into two main categories: the *deterministic* and the *randomly rough surfaces*. The first are periodic surfaces with a given profile and periodic irregularities. However, natural surfaces are attributed to the latter class of random rough surfaces. This category is characterized by random irregularities on the surface. Such surfaces are best described by the statistical distribution of their deviation from a certain reference level (Davidson et al., 2000).

In terms of the application on bare agricultural fields, randomly rough surfaces are defined as the relief produced by tillage operations without taking into account the straightened soil structure (e.g. furrows and seed grooves). In the literature the term *micro-relief* is also used as synonym. According to Romkens & Wang (1986) four different types of such a relief can be distinguished in relation to the size, the genesis, and the impact of the soil: i) *relief size 0 – 2*

mm, consisting of single particles and unequally distributed micro aggregates; ii) *relief size 2 – 100 mm*, consisting of large unequally distributed soil aggregates; iii) *relief size 100 – 200 mm*, consisting of furrows and grooves caused by systematic and equally distributed tillage operations; iv) *relief size >100 m*, surface landforms resulting from geological processes. Even though these relief types are not always clearly distinguishable through their attributes, all of them have a different impact on soil processes known as *soil erosion* (Lal, 1991). Since this study mostly deals with agricultural land surfaces, the relief size of 2 to 100 mm over bare arable fields is of interest.

The influence of tillage operations as well as of chemical, physical, and biological processes on the micro-relief was investigated in numerous studies as summarized in the book of Marshall et al. (1999). It was shown by some authors that the micro-relief becomes finer with tillage (Allmaras et al., 1967; Slattery & Bryan, 1992). Others verified that roots and fungal hyphae are responsible for the stable crumbs by pressing soil particles together as they expand during growth. They separate some parts of the thoroughly ramified soil while compressing others, dry it, and incorporate organic matter to it. Moreover, some products from the decomposition of roots and other organic matter by micro-organisms may act as binding agents (Swaby, 1949; Emerson, 1954; Oades, 1993). The physical agents of cracks separating natural aggregates are mainly caused by the movement of the soil due to shrinking and swelling of the clay minerals. According to a hypothetical model proposed by Emerson (1959) the microstructure of the smallest unit of soil aggregates consists of clay domains linked to each other on the one hand, and of quartz grains held together by electrostatic bounds on the other hand. Changes in weather conditions additionally influence the micro-relief, as for instance, surface runoff, rainfall, wind, and freezing.

It should be emphasized that the characterization and categorization of roughness on arable fields depend on the given soil type, on the region, on the point of time when roughness measurements are taken, as well as on the type of crops seeded. This renders impossible a consistent classification of roughness over a large area. Finally, it is essential to understand that different tillage methods affect the roughness of cultivated fields very differently. Generally speaking, three main tillage methods widely applied in all regions of the Earth can be discriminated. In the order of decreasing roughness these are: *ploughing*, *harrowing*, and *seedbedding*. Ploughed fields are deeply gashed in the soil crumb which is oftentimes literally

turned upside down, while on harrowed fields the surface of the soil crumb is raked, and for the seedbed fields the soil crumb is flattened. In the preparation for sowing, the different methods, ploughing, harrowing, and seedbedding, are oftentimes conducted successively to enable an optimal state for the shoot of the seedlings.

In the field of microwave remote sensing, the second important state variable influencing the electromagnetic scattering behavior of natural terrains is the so called *surface roughness*. In the following section, the established approaches to define surface roughness through statistical parameters as well as the existing methods to measure these parameters will be discussed. The task to describe the roughness of natural surfaces in a suitable manner for electromagnetic scattering problems has been object of numerous studies within the last two decades (e.g. Brisco et al., 1991; Champion & Faivre, 1996; Colpitts, 1998; Davidson et al., 1998; Mattia & Le Toan, 1999; Davidson et al., 2000; Darboux & Huang, 2003; Allain et al., 2003; Zribi et al., 2006; Bryant et al., 2007; Oh & Hong, 2007). A comprehensive review on this topic has been published by Verhoest et al. (2008) and a study by Marzahn et al. (2009) summarizes the most advanced approaches to estimate surface roughness with full polarimetric SAR (PolSAR) data.

3.2.1 Statistical Description of Rough Surfaces

As already mentioned in the foregoing section, randomly rough surfaces are commonly described in terms of their height deviation from a smooth reference surface. In principle, two aspects describing the nature of a randomly rough surface can be distinguished: i) the spread of heights about the reference surface and ii) the variations of these heights along the surface. To parameterize these two surface properties, a variety of equivalent statistical distributions and parameters is available. In many theoretical investigations the parameter set of the root mean square (RMS) height s and the surface correlation length l , based on the surface correlation function, are considered best for the parametric description of natural terrain surfaces (Oh et al., 1992; Fung et al., 1992; Chen & Fung, 1995; Altese et al., 1996; Cloude, 1999; Satalino et al., 2001; Hajnsek et al., 2003b; Dash & Prusty, 2007). The RMS height s is widely used to describe the vertical surface roughness and is defined as the standard deviation of the surface height variation in cm:

$$RMS_{height} = s = \sqrt{\frac{\sum_{i=1}^n (z_i - \bar{z})^2}{n-1}} \quad (3.17)$$

The surface correlation function $p(x)$ and the associated correlation length l , on the other hand, are parameters describing the horizontal structure of the surface roughness. In the discrete case, the *normalized surface correlation function* for a spatial displacement $x' = (j-1)\Delta x$ is given by

$$p(x') = \frac{\sum_{i=1}^{n+1-j} z_i z_{j+i-1}}{\sum_{i=1}^n z_i^2} \quad (3.18)$$

where z_{j+i-1} denotes a point on the surface with a spatial displacement from the point x_i (Fung et al., 1996). The surface correlation length is defined as the displacement x' for which $p(x')$ between two points on the horizontal profile inhibits values smaller than $1/e$ (Euler's Number ≈ 2.7183)

$$p(l) = 1/e \quad (3.19)$$

Hence, the surface correlation length is a description of the statistical independence of two points on a surface and it increases with increasing correlation between two neighboring points. For a perfectly smooth surface $l = \infty$.

In regard to the characterization of a surface with two parameters, s and l describe the natural surface only as two-dimensional stationary randomly rough surface (see Fig. 3.5). In accordance to the *single scale roughness theory* (Beckmann & Spizzichino, 1987), both statistical parameters are independent from each other. That is, the surface correlation length can be either large or small for a given high or low RMS height. Experimental data acquired over natural terrain surfaces show that most bare soil surfaces are characterized by considerably large spatial variations rendering difficult the determination of consistent roughness parameters for modeling and inversion purposes. This is especially the case for the

measurement of the correlation length. It was shown in different studies that the variability of l is normally too large to define useful mean values for a natural arable land surface (Mattia & Le Toan, 1999; Zribi & Dechambre, 2003; Oh & Hong, 2007; Panciera et al., 2009). Baghdadi et al. (2007) proposed a look-up table of empirically derived correlation length values for specific land uses and soil types. Two critical aspects that are controversially discussed in the literature should be mentioned. One is the question about how long the measurements distance should be for an accurate estimation of the surface correlation length. The other question is what shape of the correlation function should be used for electromagnetic modeling.

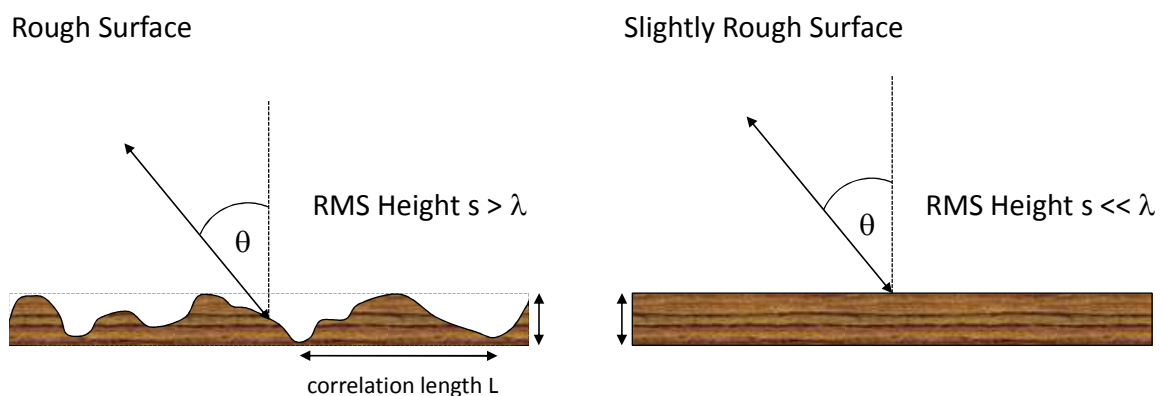


Figure 3.5: Concept of electromagnetic wave scattering on rough surfaces (Cloude, 1999).

With respect to the first question, Oh & Kay (1998) and Oh & Hong (2007) demonstrated that the variability of l estimates decreases with profile length, and that a mean estimate of l with a precision of $\pm 10\%$ requires a profile length of at least $200 l$. These and other results also illustrate that, at short profile length, the correlation length estimates are biased towards values smaller than the true underlying value of l , and that this bias increases with decreasing profile length (Alvarez-Mozos et al., 2008). In addition to that, Davidson et al. (2000) observed a correlation between s and l for a 1 m profile, what is inconsistent with the single scale roughness theory as mentioned above. The authors explain this finding with the relative size of the clods of soil which are associated with different tillage states and conclude that this result could provide a method of reducing the number of unknowns related to the surface roughness problem.

The theory of electromagnetic wave scattering from rough surfaces often follows the assumption that surface correlation functions for natural terrain surfaces have mainly two different shapes: a Gaussian or an exponential distribution function (Ishimaru, 1997). As observed by Ogilvy & Foster (1989) and Zribi (1999), measurements sometimes suggest that surface correlations close to the origin have an exponential shape that changes to a Gaussian shape for points further apart. Alternatively to the single scale roughness description, several studies propose multiscale roughness descriptions. In general, two main approaches can be distinguished: the two scale roughness models with the small and the large scale roughness (Ulaby et al., 1982a; Shin & Kong, 1984; Beaudoin et al., 1990), on the one hand, and the approaches based on random fractals (Burrough, 1981; Keller et al., 1987; Shepard et al., 1995; Arakawa & Krotkov, 1996; Mattia & Le Toan, 1999; Davidson et al., 2000; Schneeberger et al., 2004; Jester & Klik, 2005; Sun et al., 2006; Bryant et al., 2007; Garcia Moreno et al., 2008) on the other hand.

Being fully aware of the problems discussed in regard to the single scale approach, this study uses the classical single scale roughness approach to describe the randomly natural rough soil surfaces. In particular, only the RMS height for the randomly rough surface description will be used. Due to the described difficulties to accurately estimate the surface correlation length, concerning the field measurements as well as the mathematical formulation, some of the theoretical and the most empirical EM models do not consider l (Chen & Fung, 1995). Moreover, some studies showed that l has only a small influence on the radar backscatter of about 1 dB at L- and C-band, and can thus be neglected (Zribi et al., 1999; Hajnsek et al., 2003b).

Finally it should be considered that the relation of the in situ measured RMS height and the surface correlation length to the scattered EM wave are given as a function of the actual wavelength λ ($k = 2\pi/\lambda$) with ks and kl . Hence, the ks and kl are decreasing with increasing wavelength. The values for ks are ranging between 0 and 1 at L-band with a center frequency of about 1.3 GHz, and between 0 and 4 at C-band with a center frequency of about 5 GHz. This will be discussed in detail in section 4.3.2.

3.2.2 Methods of Surface Roughness Measurement

In the last century several methods of soil surface roughness measurements have been developed. In principle, these can be distinguished into two major categories: two-dimensional and the three-dimensional methods. A comprehensive summary of the most common methods can, for instance, be found in the publication by Jester & Klik (2005).

First roughness measurements for soil surfaces were taken mechanically by using long and thin steel needles attached to a normalized board. These vertical movable needles are mapping the relief of the ground profile by representing it on a scale attached on the board (Burwell et al., 1963; Allmaras et al., 1967). While first approaches date back to the early 20th century (Cole, 1939), this method was perfected in the 1960ies by Kuipers (1957). Initially, the distances between the individual rods were ranging from 50 to 100 mm. With time, the technique has been steadily improved to increase its measurement and operational efficiency. The space between the individual needles was reduced down to 5 mm to increase the estimation accuracy; while on the other hand, the digitalization of photographs of the rod positions or the automated recording of the vertical movement by means of potentiometers allowed reducing the evaluation time (Currence & Lovely, 1971). The advantage of this pin-board profilometer technique is the simple handling and the easily accessible overview of the impact of tillage on the soil surface. A major disadvantage, however, is the disturbance of the soil surface caused by the needles, rendering impossible a precise repetition of the measurements. Apart from this, the low spatial resolution with 5 mm point to point measurement distance and a vertical resolution of > 1 mm may be insufficient for detailed relief investigations. Also critical is the fact that, due to the technical limitation of the length of such needle profilometers, usually up to 1.5 m, the estimation of surface correlation length is always somewhat imprecise.

During the last decades several new methods to measure soil surface roughness were developed with the aim to satisfy the requirements of being contactless, fast, and high resolved. These methods use optical sensors and are based on photogrammetry or triangulation. The method of *photogrammetry* is based on the principle of transmitting light and measuring its reflection from the surface. Such measurements are well established, they are precise, fast and nowadays relatively low cost (Butler et al., 1998; Chandler et al., 2005).

However the processing of the recorded images and the generation of digital surface elevation models require a rather time consuming manual processing (Jeschke, 1990; Warner, 1995). Another disadvantage of this method is the disturbing influence of surrounding light as well as the influence of the color and the moisture content of the soil at time of measurement (Jester & Klik, 2005). The *laser profiler* method, where transmitted laser pulses are reflected on the soil surface and recorded with a photodiode, is much more robust to such influences. The fast sampling time and a high spatial resolution ranging from 1 to 5 mm with a vertical precision of ± 1 mm render these systems highly attractive (Darboux & Huang, 2003). Nevertheless, high costs and time effort to construct and install such profilers are disadvantages that should be considered (Davidson et al., 2000; Sun et al., 2006). Most laser profilers are only capable to measure short profiles lengths in the order of 1 to 2 m. Some advanced laser profilers allow acquiring surface profiles up to 25 m with very high location precision (Davidson et al., 1998). Profiles of this length are required for an accurate estimation of the surface correlation length and surface characterization (periodicity, stationarity, homogeneity). The latest development in this field is the use of *three-dimensional terrestrial laser scanners*. By combining areal laser scanner data with high resolution digital photography, these systems are suitable to provide high resolution models of the soil surface. It was found that such laser scanners can reproduce even small aggregates as well as voids in between them (Jester & Klik, 2005; Perez-Gutierrez et al., 2007). Even though there is yet not much literature about using terrestrial laser scanners to characterize the soil surface roughness, some studies indicate that this approach may be the best choice for such applications (Perez-Gutierrez et al., 2007; Wenjian et al., 2009). It should be mentioned, however, that these systems are still very expensive, and the processing of the data requires considerable expertise.

In this study, the measurements of the soil surface roughness were carried out using a terrestrial 3D laser scanner (LMS-Z390i, Riegl GmbH, Horn, Austria) and a prototype field laser scanner device (Technology of Crop Farming Institute, University Bonn). The different devices employed in this study are shown in Fig. 3.6, and the description of the measurements procedure is given in chapter 4.

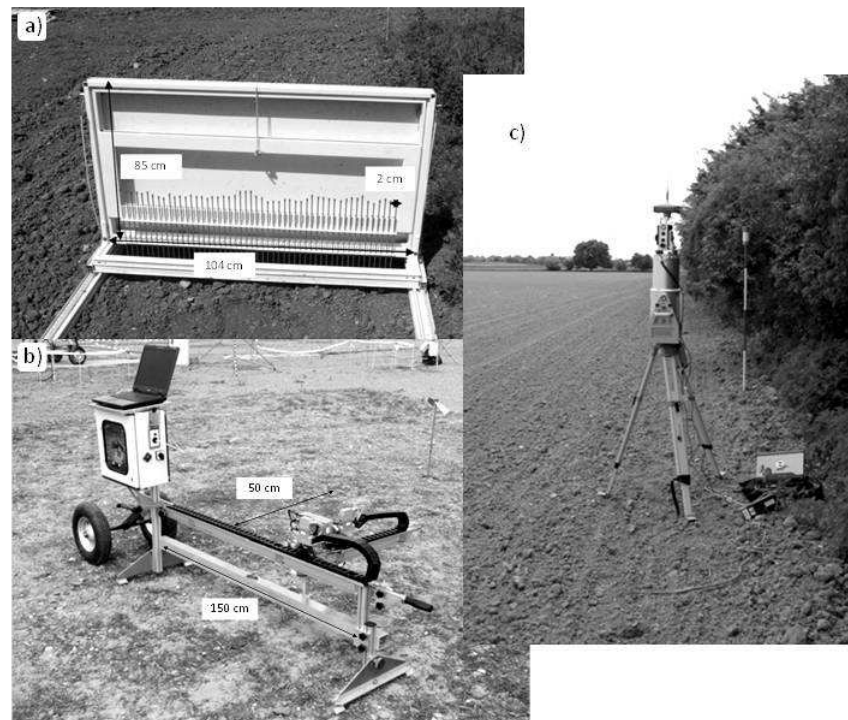


Figure 3.6: Devices for the measurement of the soil surface roughness: a) classical pin meter, b) field laser scanner, and c) terrestrial 3D laser scanner.

3.2.3 Electromagnetic Scattering from Rough Surfaces

In order to conclude this chapter it is essential to discuss the effect of the soil surface roughness on the backscattering behavior of EM waves. Generally speaking, all natural surfaces can be considered as rough, and this roughness is considered as the dominant factor for the scattering behavior of an EM wave from this surface (Stratton, 1941). It is important to note that the electromagnetic roughness of any scattering surface is not an intrinsic property of this surface but a function of the properties of the transmitted EM wave. Both the frequency and the local incidence angle (LIA) of the incoming plane wave determine how smooth or rough a surface appears to be. As discussed in the foregoing section, the roughness term in radar science depends on the given wavelength, so that its appearance changes with different frequencies. That is, at lower frequencies, the surface of an illuminated target appears smoother than at higher frequencies. To compensate this effect, the RMS height s is scaled to the actual wavelength using the wavenumber k ($2\pi/\lambda$) with the following equation:

$$ks = s \times \frac{2\pi}{\lambda} \quad (3.20)$$

where ks is the RMS height s , as defined by Eq. (3.17), normalized to the wavelength λ .

Besides the wave frequency, also the LIA plays an important role in defining electromagnetic roughness of a target. In the near field of the propagating EM wave the same surface appears rougher than in the far field, comparable to the reflection of the sunset over the sea (Beckmann & Spizzichino, 1987).

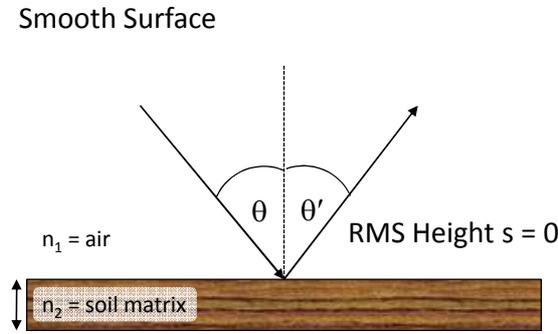


Figure 3.7: Schematic representation of Fresnel reflection.

For an ideal smooth surface, the characteristics of the reflection can be described by the so called *Fresnel reflectivity* Γ (Ulaby et al., 1981b). The Fresnel reflectivity, named after the French engineer and physicist Agustin Jean Fresnel (1788-1827), describes the reflection of a transmitted wave at the interface between two dielectric media n , e.g. the air n_1 and a homogeneous soil column n_2 . The Fresnel coefficient Γ is a function of the angle of the incoming θ and reflected wave θ' , and the complex dielectric constant ϵ of the target:

$$\Gamma_h(\theta) = \frac{\mu \cos \theta - \sqrt{\mu \epsilon - \sin^2 \theta}}{\mu \cos \theta + \sqrt{\mu \epsilon - \sin^2 \theta}} \quad \Gamma_v(\theta) = \frac{\epsilon \cos \theta - \sqrt{\mu \epsilon - \sin^2 \theta}}{\epsilon \cos \theta + \sqrt{\mu \epsilon - \sin^2 \theta}} \quad (3.21)$$

where Γ_h and Γ_v represent the horizontal and vertical polarizations of the EM wave, and for non-ferromagnetic media, like natural terrain surfaces, the variable μ is always equal to one. The response of the horizontal polarization increases with increasing LIA, while the vertical

polarization decreases to zero at a certain incidence angle. At this angle, known as *Brewster angle*, the transmitted wave is absorbed completely by the illuminated dielectric medium. With further increased LIA, however, Γ_v suddenly increases again (Fung, 1994).

Assuming a constant wavelength at a fixed LIA, the interaction of the incoming plane wave with differently rough surfaces can, generally speaking, be treated as follows: the rougher the surface, the more diffuse the scattering behavior, and the smoother the surface, the more directional the scattering behavior. As described above, the Fresnel reflectivity is valid only for a perfectly smooth surface boundary. In natural environments, however, surface conditions generally vary from medium to rough. Thus, the backscattering of an EM wave from natural terrain surfaces consists of two components, a reflected or coherent and a scattered or incoherent one. In this sense, the coherent component behaves as a specular reflection on a smooth surface. Hence, in the case of monostatic radar, there is no return of the coherent part back to the sensor as can be seen Fig. 3.8. The incoherent component is a diffuse scatterer, where the reflected power is spread in all directions. With increasing roughness the coherent component becomes negligible and the incoherent component consists only of diffuse scattering.

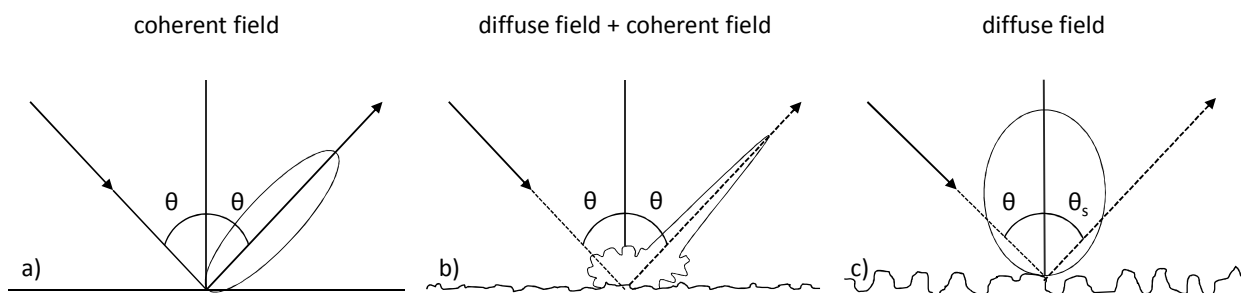


Figure 3.8: Characterization of roughness components on a) smooth, b) rough, and c) very rough surfaces.

As already mentioned, in electromagnetic terms, the definition of a surface as smooth or rough is obviously somewhat arbitrary. Nonetheless, the literature offers two main criteria to define a smooth surface: the *Rayleigh criterion* and the *Fraunhofer criterion* (Ulaby et al., 1982b). In the case of a plane monochromatic wave impinging at some angle θ upon a rough surface (Fig. 3.9), the phase difference $\Delta\phi$ between two rays scattered from separate points on the surface can be calculated in a simple manner with

$$\Delta\phi = 2h \frac{2\pi}{\lambda} \cos\theta \quad (3.22)$$

where h is the standard deviation of the roughness height from a reference height and the local incidence angle θ .

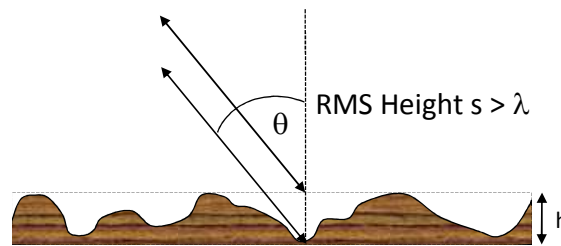


Figure 3.9: Scheme for the determination of the phase difference between two parallel EM waves scattered from different points on a rough surface.

The *Rayleigh criterion* defines that a surface can be considered as smooth if the phase difference $\Delta\phi$ between two reflected waves is smaller than $\pi/2$ radians, as given by Eq. (3.23)

$$h < \frac{\lambda}{8\cos\theta} \quad (3.23)$$

This criterion is considered as a useful first-order classifier of surface roughness or smoothness. However, due to the fact that for modeling the scattering behavior of natural terrain surfaces in the microwave region a more stringent criterion is needed, Ulaby et al. (1982b) proposed to adopt a criterion which was originally used to define the far-field distance of an antenna. According to this criterion, which they named the *Fraunhofer criterion*, a surface is defined as smooth, if the phase difference is $\Delta\phi < \pi/8$ leading to Eq. (3.24)

$$h < \frac{\lambda}{32\cos\theta} \quad (3.24)$$

Having understood the essential aspects of microwave interactions with natural soil surfaces, we can now proceed to consider the experimental settings of this study by introducing the study area and the ground based data set used in this dissertation in the next chapter.

4. Study Area and Field Measurements

In situ measurements are essential for calibration and/or validation of remotely sensed data products. Ground truth information is used to validate the quality of existing models and is a prerequisite for the adaption or development of new models. In this chapter the description of the study area, as well as of the individual test sites is provided followed by the detailed description of the ground based measurements which are used later on for the development of a new semi-empirical soil moisture retrieval model as well as for the validation of this and other models applied in this dissertation.

4.1 The River Rur Catchment

The catchment basin of the River Rur, a sub-catchment basin of the River Meuse, is located in the Belgian-Dutch-German border region (Fig. 4.1). The River Rur, with a length of 165 km, drains a total area of 2354 km² of which about 157 km² (6.7%) belong to Belgium and about 108 km² (4.6%) to Dutch territory. The largest city in the area is Aachen with a population of approximately 260,000. Arable land accounts for 36% of the catchment area followed by forests and grassland covering 34% and 22%, respectively.

The catchment basin is located in the Lower Rhine Embayment, which is a geological subsidence structure located in North Rhine-Westphalia, and is separated into two major landscape units. The southern part covers the hilly landscape of the Eifel low mountain range, with a high long-term annual precipitation of 850–1300 mm/a and a moderate annual potential evapotranspiration of 450–550 mm/a. The northern part belongs to the eastern extension of the Belgium-Germany loess belt and is characterized by virtually flat terrain with a relatively low annual precipitation of 650–850 mm and a high potential evapotranspiration of 580–600 mm/a. As the name indicates, the soils of this fertile loess plain evolved mainly from loess which accumulated on Tertiary and Quaternary depositions

of the Rivers Rhine and Meuse. Water-saturated conditions are found in 1% of the entire catchment. In accordance with this morphological and climatic division, the land use types are clearly distinguishable. Forest and grassland patches characterize the southern part, whereas in the northern part intensively used agricultural land predominates.

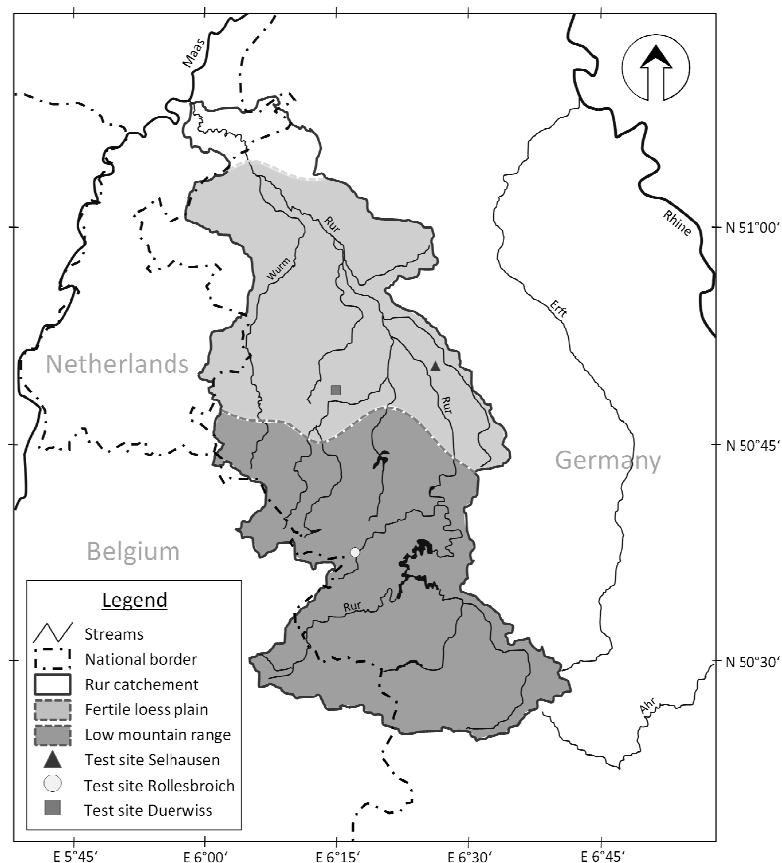


Figure 4.1: River Rur catchment with the two major landscape units (grey shaded) and locations of the three test sites for in situ soil moisture measurements.

4.1.1 Precipitation Characteristics of the Rur Catchment

Considering precipitation as the major source of water in the soil and as a dominant driver for spatial variability (Koyama et al., 2010), it is important to consider the rainfall regime in the region. In the northern part of the Rur basin the annual precipitation rates are relatively uniformly distributed in space ranging between 700 mm/a in the North and 900 mm/a near the city of Aachen. However, in the southern part of the Rur catchment a clear differentiation of the precipitation rates can be observed. Being located in the European west wind zone, the moist marine air flowing in from the Atlantic Ocean, predominantly from south-west to

north-west directions, cause a significant precipitation shadowing effect in the area. Thus, the precipitation rates in the elevated regions of the Rhenish Massif (“High Fens”) are higher than those in the eastern part (lee regions). While annual precipitation rates of 1200 mm/a and more can occur in the elevated regions, leeward precipitation rates below 700 mm/a are observed in the Selhausen area. This example demonstrates that the windward and lee effects should be taken into account in a consideration of the topography dependent spatial distribution of precipitation in the study area. In the middle part of the Rur catchment, the winter/summer precipitation ratio is fairly balanced. Whereas, in the low mountain range areas, winter precipitation is dominant. Hence, the highest amounts of precipitation fall in the period of the lowest evapotranspiration potential. Due to the low transpiration rates in winter and the associated high soil moisture contents, a large portion of this precipitation water becomes runoff. This stands in sharp contrast to the northern part of the catchment where the highest amounts of rainfall occur in summer, i.e. the period of the highest potential evapotranspiration (Schulze & Matthies, 2001; Bogena et al., 2005; Montzka et al., 2008).

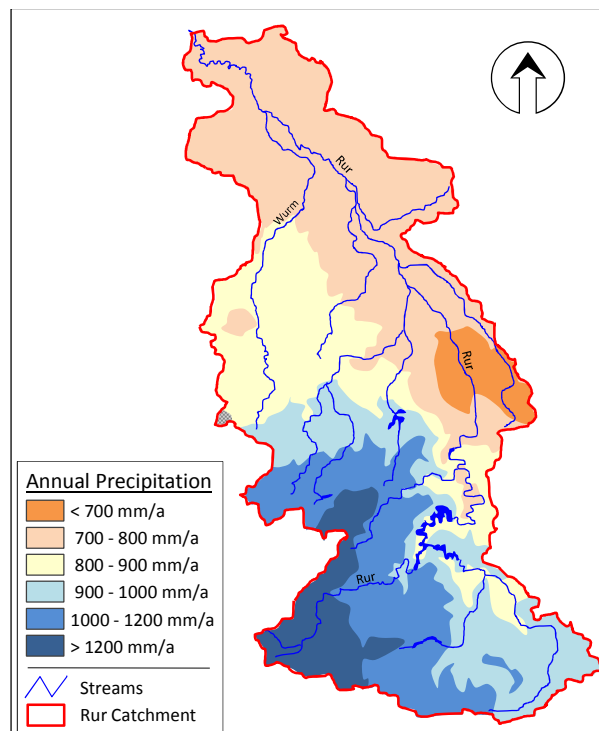


Figure 4.2: Distribution of annual precipitation in the Rur catchment; (redrawn after Bogena et al., 2005).

4.1.2 Geological Overview

The geology of the River Rur catchment is complex. Paleozoic and Mesozoic rocks crop out mainly in the southern part of the catchment occupying about 47% of the catchment area. The Paleozoic rocks of the Rhenish Massif were formed in the course of the Variscan orogenesis. With an area fraction of 33%, this is the most widespread geological formation. Predevonian rocks crop out only in few locations, making up about 7% of the catchment area. For example, they can be found as Cambrian and Ordovician clay slates and quartzites in the region of the High Fens. The Rhenish Massif itself is predominantly formed of Devonian and Carboniferous sedimentary rocks, which can reach a thickness of several thousand meters. They are composed by alternating sequences of silt- and mudstones as well as of sandstones and greywackes with small cavity and groundwater storage volumes. The Middle and Upper Devonian carbonate rocks, e.g. the Givetian reef limestone “Massenkalk” south to the city of Stolberg, on the other hand exhibit higher groundwater storage volumes.

Mesozoic rocks crop out in the east border region of the Rur catchment between the localities of the cities of Nideggen and Kall. These rocks were primarily formed during the Lower Triassic Age and consist mainly of semisolid sandstones of the Lower Triassic stage superimposed by Triassic limestone. Approximately 53% of the near-surface rocks within the Rur basin are composed by unconsolidated sediments which are mainly formed from Quaternary deposits. Thick Tertiary unconsolidated rock deposits are above all present in the northern part of the catchment, albeit mostly covered by Pleistocene terrace deposits, namely sands and gravels of the main, middle, and lower terraces of the rivers Maas and Rur, as well as by aeolian deposits, i.e. loess and dune sands.

4.2 Test Sites and Sampling Fields

Ground based measurements were conducted at two test sites representing the typical land use of the two major landscape units, namely grassland and arable fields. For a single PALSAR acquisition in fully polarimetric (PLR) mode, not covering the whole area due to steeper incidence angle and smaller swath width (cf. section 2.10), field measurements were taken at a third test site once. The three different test sites will be introduced in the following.

4.2.1 Test Site Selhausen

The test site “Selhausen” represents an intensively used agricultural area. Crops are grown on virtually flat terrain with slopes from 0-3°. The mean elevation is approximately 100 m above sea level. As situated in the lee region of the Rhenish Massif, mean annual precipitation does not exceed 700 mm. The dominant soils are Cambisols and Luvisols with a silt loam texture according to the FAO soil classification. The six sampling fields cover an area of approximately 34 ha. The corner coordinates are given in Tab. 4.1.

Table 4.1: Corner coordinates of the Selhausen test site.

Corner	Geographical		UTM (Zone N32)	
	Longitude [°]	Latitude [°]	Easting [m]	Northing [m]
Upper left	6°26'36" E	50°52'22" N	320130	5638800
Lower right	6°28'05" E	50°51'35" N	320950	5637650

Fig. 4.3 shows an aerial image of the test site with the arrangement of the individual sampling fields. Due to the homogenization of the topsoil caused by tillage, variability in soil conditions is considerably small on the different sampling fields. In the eastern parts of field A03 slightly increased clay contents were observed, while in the western parts of A10 and A02 a relatively high stoniness occurs. The stones are alluvial deposits from an eroded river terrace located west of the test site.

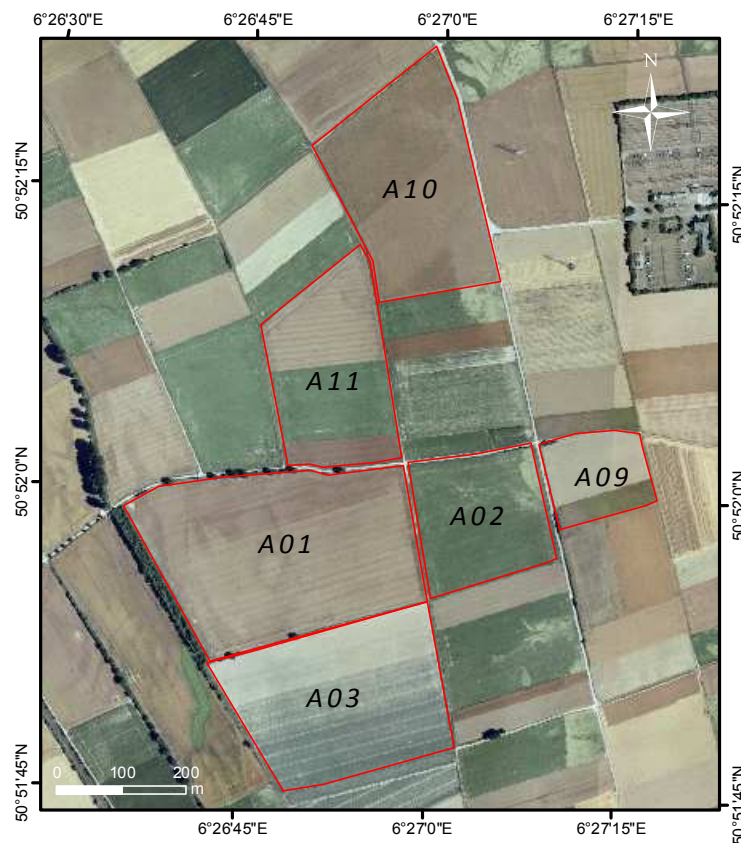


Figure 4.3: Aerial view of the Selhausen test site.

4.2.2 Test Site Rollesbroich

The test site “Rollesbroich” represents typical grassland within the rolling topography of the Eifel. This test site is characterized by a mean elevation of approx. 510 m above sea level and slopes ranging from 0-10°. The mean annual precipitation is fairly high with amounts of 1200 mm. The site covers a total area of approximately 20 ha. Tab. 4.2 show the corner coordinates of the grassland site.

Table 4.2: Corner coordinates of the test site Rollesbroich.

Corner	Geographical		UTM (Zone N32)	
	Longitude [°]	Latitude [°]	Easting [m]	Northing [m]
Upper left	6°17'55" E	50°37'40" N	308950	5611920
Lower right	6°18'17" E	50°37'10" N	309350	5610980

The dominant soils of the test site are (gleyic) Cambisols, Stagnosols and Cambisol-Stagnosols according to the FAO classification. Significant variations in the soil conditions occur on the sampling fields. Apart from gleyic conditions prevailing at most locations, especially the soil depth is highly variable ranging from < 0.5 m up to > 1 m. Consequently, it can be assumed that the routing of the interflow has a large impact on the moisture patterns found at the soil surface.

A peculiarity of any grassland is the presence of a *thatch layer* right below the grass plants. This thatch consists of dead un-decayed plant material and forms a barrier to water and air movement in the manner of a thatched roof. Such a layer can hold enormous amounts of water of up to and higher than 80 Vol.-%. Since, from a remote sensing point of view, this thatch layer constitutes the actual “soil surface”, this effect has to be taken into account in the development of a soil moisture retrieval model, as will be discussed in section 7.3. An aerial image of the test site with the arrangement of the individual sampling fields is shown in Fig. 4.4.

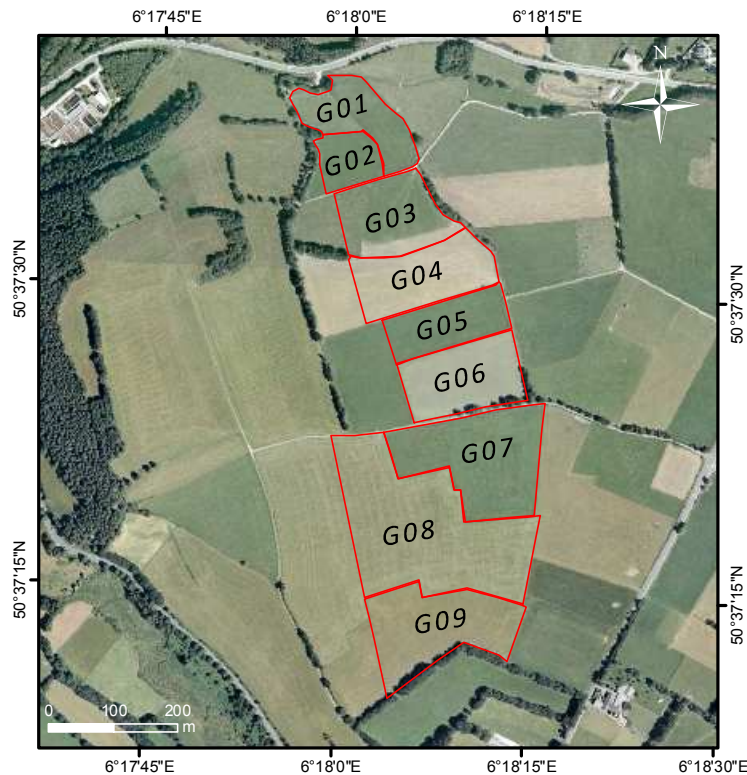


Figure 4.4: Aerial view of the Rollesbroich test site.

4.2.3 Test Site Duerwiss

The test site “Duerwiss” is located near the city of Eschweiler. The characteristics are similar to the Selhausen test site. In effect the site is completely flat. The dominant soils are also Cambisols and Luvisols with a silt loam texture. The mean annual precipitation is with 760 mm slightly higher than in the other arable land site. The four sampling fields cover an area of approximately 22 ha. Tab. 4.3 gives the corner coordinates of the site. At the measurement day May 14, 2009, fields D01 and D04 were at bare soil state, while D02 and D03 were covered with a winter wheat.

Table 4.3: Corner coordinates of the test site Duerwiss.

Corner	Geographical		UTM (Zone N32)	
	Longitude [°]	Latitude [°]	Easting [m]	Northing [m]
Upper left	6°15'02" E	50°50'30" N	306432	5635821
Lower right	6°15'58" E	50°50'10" N	307504	5635162

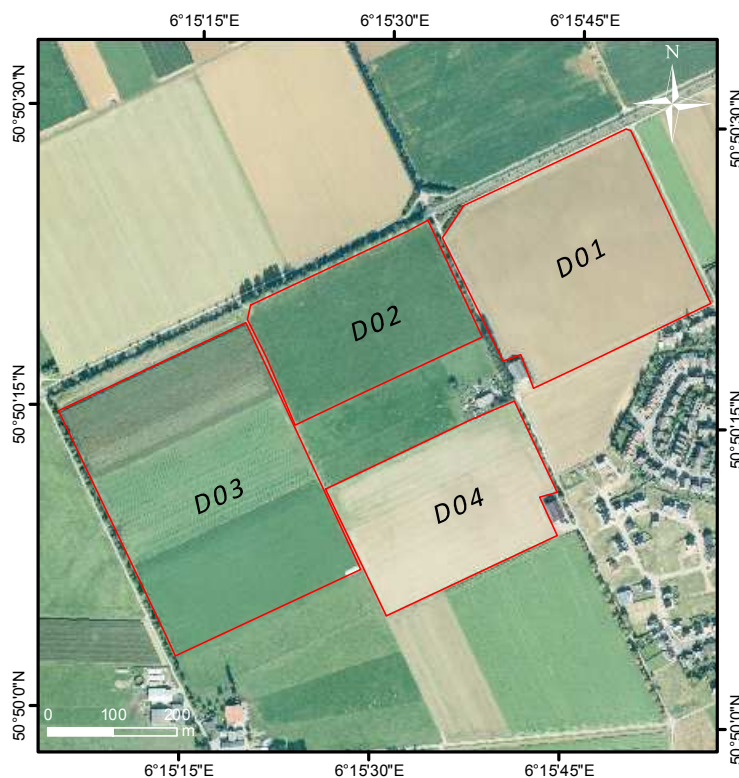


Figure 4.5: Aerial view of the Duerwiss test site.

4.3 Ground Truth Data Set

The following section provides a comprehensive overview of the ground truth data set used in this dissertation. The different in situ surface and vegetation parameters as measured at the three test sites are discussed. Special emphasize should be put on the measurement ranges for soil moisture, surface roughness, and vegetation biomass, because this observation space has direct impacts on the validity ranges of the new semi-empirical soil moisture retrieval model introduced in chapter 7.

4.3.1 In Situ Surface Soil Moisture

In situ surface soil moisture measurements were taken on 15 sampling fields at the Selhausen (A01-A11) and Rollesbroich (G01-G09) test sites between August 2007 and June 2010 (see Fig. 4.3 and 4.4). The measurements were performed on different land cover types, namely bare soil, sugar beet (*Beta vulgaris* L.), winter wheat (*Triticum aestivum* L.), and grassland vegetation dominated by a ryegrass society, particularly perennial ryegrass (*Lolium perenne* L.) and smooth meadow grass (*Poa pratensis* L.). As mentioned before the size of the individual sampling fields ranged from 2 to 10 ha. The surface soil moisture measurements were arranged in a grid with a sampling point spacing of 30 to 60 m, with 12 to 24 points per field. According to the length of the rods of the hand-held frequency domain reflectometry (FDR) probes, as described in chapter 3, the measured surface soil moisture is an average value for the topmost 6 cm of the soil column. Thus, in this study the surface soil moisture is defined as the mean water content within these topmost 6 cm below the soil surface. This depth is considered to be a suitable choice in regard to the radar penetration depth at L-band (cf. section 2.2). To minimize sampling errors and to yield a representative value for every sampling location, each sampling location is represented by the mean of six individual measurements taken within a radius of 40 cm. Obvious measurement errors, which might occur, for instance, by incomplete contact with the substrate, were excluded from further analysis.

In the ASAR case, all images were acquired on descending tracks on $\pm 10:00$ h local time. The measurement campaigns were conducted within a time frame starting 2 h before and ending 2 h after the satellite pass. In the PALSAR case, however, all images were acquired on ascending tracks on $\pm 21:45$ h local time. This is due to the ALOS systematic observation strategy (JAXA, 2007). In general, the descending daytime acquisitions are designated for the two optical remote sensing instruments AVNIR-2 and PRISM (cf. section 4.10). The ground based measurements were taken in the afternoon, typically from 14:00 to 18:00 h, prior to the ALOS overflight. This measurement strategy is considered as a suitable compromise between the requirement to cover large areas, to provide representative samples for each land cover type, the limited amount of time for sampling, and the personnel available for this study. Usually, two 2-person teams per test site were available for field measurements. Tab. 4.4 gives an overview of the different measurement dates with the land cover specific m_v averaged from all sampling locations for the given land cover type.

Table 4.4: Overview of measured average surface soil moisture for the different land cover types and dates of ASAR and PALSAR acquisitions.

Date	Sensor	land cover specific mean m_v [Vol.-%]			
		bare soil	sugar beet	winter wheat	grassland
2-Aug-2007	PALSAR	28.0	19.1	-	-
17-Sep-2007	PALSAR	-	31.5	-	50.3
29-Apr-2008	ASAR	30.1	-	31.2	52.1
4-May-2008	PALSAR	29.9	-	31.4	52.4
3-Jun-2008	PALSAR / ASAR	32.1	-	32.3	35.0
8-Jul-2008	ASAR	-	23.0	24.5	-
18-Jul-2008	PALSAR	-	22.9	21.3	-
16-Sep-2008	ASAR	24.5	23.6	-	48.9
14-May-2009	PALSAR	25.3	-	29.8	-
7-Jun-2009	ASAR	27.4	-	28.2	38.9
21-Jul-2009	PALSAR	14.7	16.5	-	35.7
10-May-2010	PALSAR	20.8	-	22.1	49.1

In total, 120 and 96 sampling locations were distributed over the arable land and grassland test site, respectively. Tab. 4.4 provides an overview of the measured average soil moisture for the different land cover types and dates of ASAR and PALSAR overflights. Each mean m_v value is composed from 36 to 96 sampling locations. It is interesting to note that for each

measuring day the variations between the different land covers are relatively small. In effect, the variability within one land cover type, with standard deviations typically ranging between 2 and 3 Vol.-%, is always larger than that between two different land covers. Another aspect worth mentioning is the fact that the average bare soil m_v is always lower than the one measured under a vegetation cover. This is most likely due to the canopy reducing the evaporation from the soil surface, while the roots extract water mostly from soil regions below 6 cm depth.

It should be mentioned that in the case of the PALSAR scene acquired on June 2, 2008, ground based soil moisture measurements were obtained on the morning of the next day about 10 hours after the satellite pass. Despite the time lag between satellite pass and field measurements, the in situ data set is fully comparable with the satellite measurements, because there was no precipitation or dew formation at night and only very little evapotranspiration. Evidence for the comparability of both data sets is provided by continuous surface soil moisture measurements in Selhausen and Rollesbroich. Fig. 4.6 provides continuous soil moisture measurements for the time frame from June 2, 6 pm, until the end of our field measurements at 12 noon, June 3. The measurements were taken in 10 cm depth. Obviously, there is no significant change in surface soil moisture conditions in both test sites. The TDR measurements in Rollesbroich show a higher noise level as compared to the FDR measurements in Selhausen. However, both measurements do not show a significant trend. The temporal variations of the soil moisture are well below the accuracy level of the hand held field probes used for spatial sampling and are an order of magnitude smaller than the spatial variations of the surface soil moisture. It should be mentioned that this kind of comparison was carried out for every PALSAR measurement campaign to assure the suitability of the m_v values measured shortly prior to the image acquisitions.

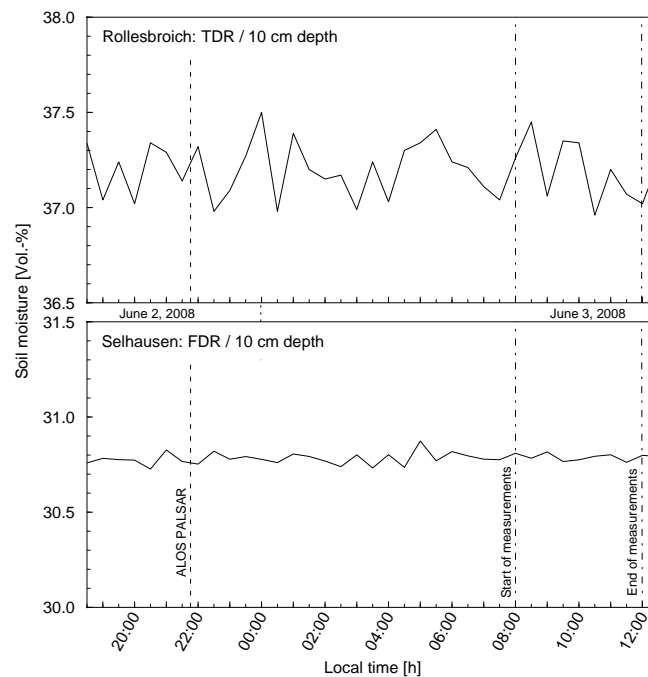


Figure 4.6: Continuous surface soil moisture measurements with TDR (Rollesbroich, G03) and FDR (Selhausen, A10) probes in 10 cm depth.

4.3.2 In Situ Surface Roughness

Measurements of surface roughness were conducted on the agricultural sampling fields of the Selhausen test site on six different days of PALSAR acquisitions. The recorded surface roughness varied significantly between the different measurement days and locations with RMS heights s ranging from 0.51 to 3.37 cm. As can be seen from Tab. 4.5, four different surface states were identified, namely very smooth, seeded, harrowed, and ploughed.

Table 4.5: Measured surface roughness for different test fields and dates.

Field ID	Date	RMS h [cm]	surface state	method	PALSAR <i>ks</i>
A01-1	4-May-2008	2.11	ploughed	3D laser scanner	0.56
A01-2	4-May-2008	1.98	ploughed	3D laser scanner	0.53
A03-1	4-May-2008	3.53	ploughed	3D laser scanner	0.94
A03-2	4-May-2008	3.37	ploughed	3D laser scanner	0.90
A01-1	2-Jun-2008	0.66	very smooth	3D laser scanner	0.18
A01-2	2-Jun-2008	0.51	very smooth	3D laser scanner	0.14
A03-1	2-Jun-2008	0.73	very smooth	3D laser scanner	0.19
A03-2	2-Jun-2008	0.59	very smooth	3D laser scanner	0.16
A01-1	5-Sep-2009	1.21	harrowed	3D laser scanner	0.32
A01-2	5-Sep-2009	1.48	harrowed	3D laser scanner	0.39
A03-1	5-Sep-2009	1.18	seedbed	3D laser scanner	0.31
A03-2	5-Sep-2009	1.09	seedbed	3D laser scanner	0.29
A10-1	14-May-2009	1.25	seedbed	3D laser scanner	0.33
A10-2	14-May-2009	1.17	seedbed	3D laser scanner	0.31
A10-3	14-May-2009	1.12	seedbed	3D laser scanner	0.30
A10-4	14-May-2009	1.3	seedbed	3D laser scanner	0.35
A11-1	10-May-2010	1.47	harrowed	laser profiler	0.39
A11-2	10-May-2010	1.53	harrowed	laser profiler	0.41
A11-3	10-May-2010	1.42	harrowed	laser profiler	0.38
A11-4	10-May-2010	1.58	harrowed	laser profiler	0.42
A11-1	22-Jun-2010	1.37	harrowed	laser profiler	0.36
A11-2	22-Jun-2010	1.25	harrowed	laser profiler	0.33
A11-3	22-Jun-2010	1.82	ploughed	laser profiler	0.48
A11-4	22-Jun-2010	1.79	ploughed	laser profiler	0.48

As discussed in section 3.3.2, the surface roughness was estimated by means of two different techniques: i) RMS heights were estimated from three-dimensional surface models as generated from the terrestrial laser scanner (LMS-Z390i, Riegl GmbH, Horn, Austria). Fig. 4.7 shows a 3D composite image of the surface model recorded on field A01 at the beginning of May, 2008. The advantage of this kind of data is the fact that one can easily calculate a sufficient amount of roughness profiles for all possible directions (e.g. perpendicular (PPR) and parallel to the ridges (PAR), or perpendicular (PPF) and parallel to the flight direction), ii) *s* values were derived from two-dimensional laser profiler data (Technology of Crop Farming Institute, University Bonn).



Figure 4.7: Terrestrial laser scanner 3D composite image of field A01 on May 4, 2008.

In this dissertation we use RMS heights averaged from 12 profiles 1.5 m in length all oriented parallel to the flight direction of ALOS. Due to the SAR viewing geometry, this orientation of the profiles is perpendicular to the incident EM waves (cf. section 2.3). The RMS height s for each profile is calculated using Eq. (3.17). The averaged s values were then normalized to the PALSAR wavelength of 23.62 cm to obtain the electromagnetic roughness ks by using Eq. (3.20), as described in section 3.2.3. The resulting ks values ranged from 0.14 to 0.93 (see Tab. 4.5). It should be noted, that the sampling fields were split up into sub fields in order to get a larger number of field mean s values for the calibration of the retrieval model. The area taken into account for each ks value equals 8 x 6 PALSAR FBD pixels (approximately 10,800 m²).

Note that the very smooth surface state measured on June 2, 2008, resulted from an intense precipitation event flattening the bare soil surfaces in the area. In effect, one of the farmers reported that there hasn't been such an extreme event in the area since the 1960ies (Peter Holzkamp, personal communication, June 2, 2008)

The 2010 measurements were conducted in cooperation with the Research Center Jülich. Field A11 was kept free from vegetation throughout the vegetation period and different tillage induced roughness states were prepared for investigation. Fig. 4.8 shows a picture of the test field with two different surface roughness states.

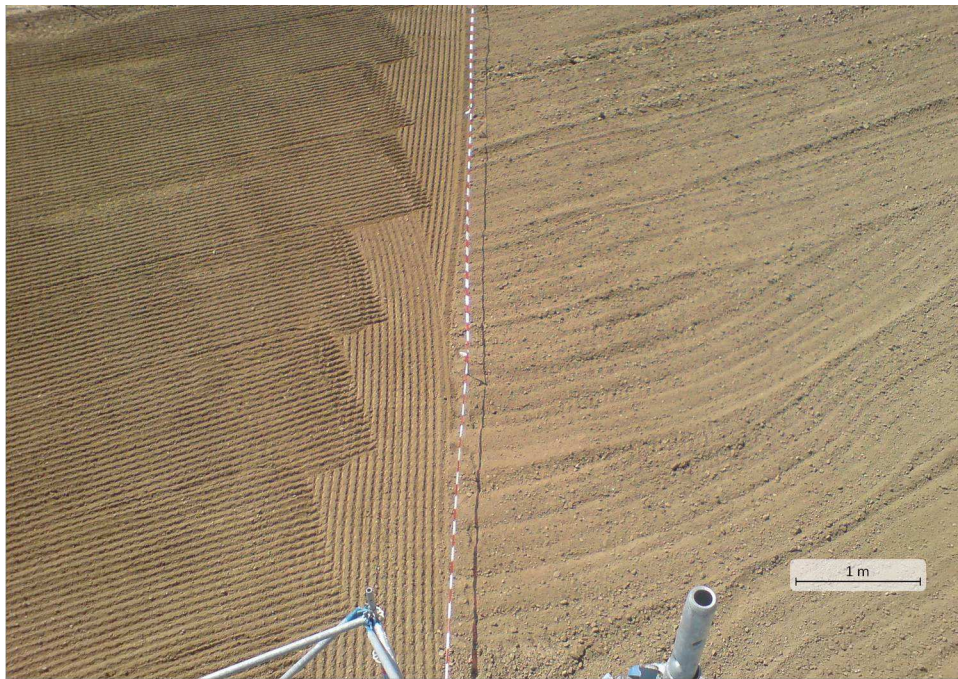


Figure 4.8: Tower view of the test field A11 with seedbed (left) and ploughed surface (right).

4.3.3 In Situ Vegetation Parameters

A variety of plant parameters for the different vegetation covers were measured at the two test sites during the growing seasons 2008, 2009, and 2010. At the arable land test site, sugar beet and winter wheat was monitored (one field per crop). Field measurements were carried out fortnightly. Biomass (wet and dry weights), leaf area index, canopy height, phenological stage and plant density were determined.

Crop measurements were carried out at three sampling locations per field. Phenological stages were documented according to the BBCH-scale (Meier, 2001). In the case of sugar beet crops, at least three representative plants per sampling point were taken. Wheat plants were harvested from a 60 cm long row. To determine fresh weight biomass, the plants were divided into their constituents of living and dead leaves (if available), stem (including leaf sheath) and storage organ (including grain, glume and rest of the ear in the case of wheat). The fresh weight of the plant organs was determined for each single sampled plant of sugar beet. For the determination of dry matter, sub-samples of each portion were dried at 105 °C until reaching a constant weight. Note that for winter wheat only above ground biomass was considered, while for sugar beet both above and below ground biomass was measured.

Leaf area index (LAI) was measured using a destructive (direct) method (LI-3000A Area Meter, *LI-COR Biosciences*, Lincoln, NE, USA). The leaf area is measured by a scanning head combined with a transparent belt conveyer. As the leaves have already been collected to be weighed for dry matter determination, this procedure requires only little extra effort.

At the grassland test site, above ground biomass was harvested at three locations per field. Also, fresh and dry weights were determined following the above procedure. It should be pointed out that we assume the grass, sugar beet, and winter wheat samples taken at one location to be representative for the whole area covered by the corresponding PALSAR FBD pixel ($\approx 225 \text{ m}^2$). Thus, the measured plant parameters can be used for a backscattering analysis on a pixel by pixel basis, as will be discussed later on in this dissertation.

The experimental data set introduced in this chapter is used for the validation of the classical soil moisture inversion models in chapter 6 and is prerequisite for the development of a new semi-empirical approach in chapter 7. But before that, it is important to discuss the concepts of polarimetric SAR remote sensing in the following chapter.

5. Polarimetric Radar Imaging and the $H/A/\alpha$ Decomposition Theorem

Polarimetric SAR (PolSAR) remote sensing offers an efficient and reliable means of collecting information required to extract geophysical and biophysical parameters from Earth's surface. This remote sensing technique has found many successful applications in crop monitoring and damage assessment, in forestry clear cut mapping, deforestation and burn mapping, in land surface structure (geology) land cover (biomass) and land use, in hydrology (soil moisture, flood delineation), in sea ice monitoring, in oceans and coastal monitoring (oil spill detection) etc. PolSAR represents today a very active area of research in radar remote sensing, and it is important for future generations of researchers to understand this very important topic to be able to handle this kind of advanced EO products. The aim of the following sections is to give an introduction to the most important polarimetric parameters used for the extraction of physical information about the scattering process properties of a distributed target. A substantial introduction to the basic theory, scattering concepts, systems and advanced concepts, and applications typical to radar polarimetric remote sensing is given in the appendix of this thesis. For further reading and fully understanding of this complex topic it is recommended to take a look at the PolSAR tutorials provided by the European Space Agency (<http://earth.eo.esa.int/polsarpro/tutorial.html>) or the Canadian Space Agency (http://ccrs.nrcan.gc.ca/resource/tutor/polarim/pdf/polarim_e.pdf) and the recently published reference books by Lee & Pottier (2009) and Cloude (2010). A good and comprehensive introduction to modern matrix algebra can be found in the book by Schmidt & Trenkler (2006).

The method for extracting average parameters from polarimetric radar data by using a smoothing algorithm based on second-order statistics was first proposed by Cloude and Pottier (1997). As will be discussed in this section, this method does not rely on the assumption of a particular underlying statistical distribution and thus is free from physical constraints imposed by such multivariate models. The authors use an eigenvector analysis of

the 3×3 coherency $[T_3]$ matrix as it provides a basis invariant description of the scattering target with a specific decomposition into types of scattering processes (i.e. the eigenvectors) and their relative magnitudes (i.e. the eigenvalues). This original approach employs a three-level Bernoulli statistical model to generate estimates of the average target matrix parameters. Generally speaking, this statistical model sets out with the assumption that there is always one dominant “average” scattering mechanism in each resolution cell and then undertakes the task of finding the parameter of this average component (Cloude & Pottier, 1996; 1997; Lee & Pottier, 2009).

5.1 Diagonalization of the Coherency $[T_3]$ Matrix

Due to the fact that the coherency $[T_3]$ matrix is hermitian positive semi-definite, it is always diagonalizable by unitary similarity transformation of the form (Cloude, 1986; Cloude, 1992; Cloude & Pottier, 1995)

$$[T_3] = [U_3][\Lambda][U_3]^{-1} \text{ where } [\Lambda] = \begin{bmatrix} \lambda_1 & 0 & 0 \\ 0 & \lambda_2 & 0 \\ 0 & 0 & \lambda_3 \end{bmatrix}, [U_3] = [\vec{e}_1, \vec{e}_2, \vec{e}_3]^T \quad (5.1)$$

where $[\Lambda]$ is the diagonal eigenvalue matrix with elements corresponding to the real non-negative eigenvalues, i.e. $0 \leq \lambda_1 \leq \lambda_2 \leq \lambda_3$, of $[T_3]$, and $[U_3]$ is the unitary eigenvector matrix with columns corresponding to the orthonormal eigenvectors \vec{e}_1 , \vec{e}_2 , and \vec{e}_3 of $[T_3]$. The basic idea of this eigenvector approach is the diagonalization of the coherency $[T_3]$ matrix of a distributed target, which is in general of rank 3, to decompose it into the non-coherent sum of three independent coherency $[T_{3i}]$ matrices

$$[T_3] = [U_3][\Lambda][U_3]^{-1} = \lambda_1(\vec{e}_1 \times \vec{e}_1^+) + \lambda_2(\vec{e}_2 \times \vec{e}_2^+) + \lambda_3(\vec{e}_3 \times \vec{e}_3^+) = [T_{31}] + [T_{32}] + [T_{33}] \quad (5.2)$$

Each $[T_{3i}]$ matrix is of rank 1 in accordance with a deterministic backscattering contribution, which is characterized by single target matrix. It follows, that Eq. (5.2) may be interpreted as

the decomposition of $[T_3]$ into three single scattering components described by $[T_{31}]$, $[T_{32}]$, and $[T_{33}]$. In terms of power, the contribution of each matrix is given by the appropriate eigenvalue. The sum of the three eigenvalues is defined as the *span* or the *total power* received from the scattering target

$$span = \lambda_1 + \lambda_2 + \lambda_3 \quad (5.3)$$

In this sense, the information about the kind of scattering targets presented by the three $[T_{3i}]$ matrices is contained in the corresponding eigenvectors. An exact interpretation of the eigenvectors in terms of the scattering mechanism will be discussed in the subsequent section. Note that the physical basis of the eigenvector decomposition is provided by the orthogonal nature of \bar{e}_i and the statistical significance of diagonal coherency matrices. The former guarantees always the existence of a set of orthonormal basis matrices in which the expansion of $[T_3]$ leads to a diagonal coherency matrix. Hence, the choice of the basis matrices is dictated by the eigenvectors. In comparison, the absence of off-diagonal terms establishes the statistical independence between the component vectors.

5.2 Polarimetric Scattering Alpha Angle

Among the mean angular parameters ($\bar{\alpha}$, $\bar{\beta}$, $\bar{\delta}$, and $\bar{\gamma}$) of the dominant scattering mechanism, which can be extracted from the 3x3 coherency $[T_3]$ matrix, the roll-invariant $\bar{\alpha}$ is the main parameter for indentifying the dominant scattering mechanism in terms of random media problems. The other three parameters ($\bar{\beta}$, $\bar{\delta}$, and $\bar{\gamma}$) can be used to define the target polarization orientation angle (Pottier, 1998; Pottier et al., 1999; Lee et al., 2000; Lee et al.; 2002). As will be shown in section 5.5, the study of the scattering mechanism is mainly performed through the interpretation of the parameter $\bar{\alpha}$ because its value can be easily related with the physics behind the scattering process. Considering the backscattering case from a cloud of identical anisotropic particles with a target matrix $[S]$

$$[S] = \begin{bmatrix} a & 0 \\ 0 & b \end{bmatrix} \quad (5.4)$$

where a and b are complex scattering coefficients in the particle characteristic coordinate system. In this case, the effect of rotation about the line of sight on the associated coherency $[T_3]$ matrix can be generated as (Cloude & Pottier, 1996)

$$\begin{aligned} [T_3(\theta)] &= [R_3(\theta)] \begin{bmatrix} \varepsilon & \mu & 0 \\ \mu^* & \nu & 0 \\ 0 & 0 & 0 \end{bmatrix} [R_3(\theta)]^{-1} \\ &= \begin{bmatrix} \varepsilon & \mu \cos 2\theta & \mu \sin 2\theta \\ \mu^* \cos 2\theta & \nu \cos^2 2\theta & \nu \cos 2\theta \sin 2\theta \\ \mu^* \sin 2\theta & \nu \cos 2\theta \sin 2\theta & \nu \sin^2 2\theta \end{bmatrix} \end{aligned} \quad (5.5)$$

where $[R_3(\theta)]$ is the unitary similarity rotation matrix and $\varepsilon = 1/2|a+b|^2$, $\nu = 1/2|a-b|^2$, and $\mu = 1/2(a+b)(a-b)^*$. Assuming a uniform distribution, the coherency $[T_3]$ matrix averaged over all angles θ is the given by

$$\langle [T_3] \rangle_\theta = \int_0^{2\pi} [T_3(\theta)] P(\theta) d\theta = \frac{1}{2} \begin{bmatrix} 2\varepsilon & 0 & 0 \\ 0 & \nu & 0 \\ 0 & 0 & \nu \end{bmatrix} \quad (5.6)$$

It can be noticed that the averaged coherency $[T_3]$ matrix is diagonal and the matrix of the eigenvectors corresponds to the identity $[I_{D_3}]$ matrix. Hence, the parameter $\bar{\alpha}$ is given by

$$\bar{\alpha} = \frac{\pi}{2}(P_2 + P_3) \text{ with } P_2 = P_3 = \frac{\nu}{\varepsilon + \nu} \quad (5.7)$$

5.3 Polarimetric Scattering Entropy

As firstly demonstrated by Cloude (1986), there are two important physical features arising directly from the eigenvalues of the coherency $[T_3]$ matrix. The first one is the *polarimetric scattering entropy* H defined by using the logarithmic sum of the eigenvalues of $[T_3]$

$$H = \sum_{i=1}^3 -P_i \log_3 P_i \quad (5.8)$$

where P_i expresses the appearance probabilities for each contribution as defined from the eigenvalues of $[T_3]$ by

$$P_i = \frac{\lambda_i}{\sum_{j=1}^3 \lambda_j} = \frac{\lambda_i}{\lambda_1 + \lambda_2 + \lambda_3} \text{ so that } P_1 + P_2 + P_3 = 1. \quad (5.9)$$

Following its definition, the entropy H ranges from 0 to 1. The parameter can be interpreted as a measure of randomness of the backscattering mechanisms within a resolution cell. In other words, H expresses the number of effective scattering processes occurring: An entropy $H = 0$ indicates a rank 1 $[T_3]$ matrix with only one non-zero eigenvalue, i.e. $\lambda_2 = \lambda_3 = 0$. This characterizes a coherent non-depolarizing backscattering process described by a single target matrix. At the other extreme, an entropy $H = 1$ indicates the presence of three equal non-zero eigenvalues, i.e. $\lambda_1 = \lambda_2 = \lambda_3$. It describes a *random noise scattering* process completely depolarizing the incident wave. As a matter of fact, most natural distributed targets lie in between these two extreme cases, i.e. they have intermediate entropy values. If the polarimetric entropy H is low ($H < 0.3$), the system may be considered weakly depolarizing and the dominant scattering mechanism in terms of a specifically identifiable “equivalent point target” may be recovered. In the course of this, the eigenvector corresponding to the largest eigenvalue is chosen and the other eigenvector components are neglected. However, if the entropy is high, the “scattering target ensemble” is depolarizing and a single equivalent point target no longer exists. Thus, a mixture of possible point targets

types has to be considered from the full eigenvalue spectrum. As H further increases, the number of distinguishable classes identifiable from polarimetric observations is reduced.

5.4 Polarimetric Scattering Anisotropy

The second important feature is the polarimetric scattering anisotropy which is defined as the normalized difference between the appearance probabilities of the second and the third target component (Cloude, 1986a; Pottier, 1998)

$$A = \frac{P_2 - P_3}{P_2 + P_3} = \frac{\lambda_2 - \lambda_3}{\lambda_2 + \lambda_3} \quad (5.10)$$

The polarimetric anisotropy A also ranges from 0 to 1 and is a complementary parameter to the polarimetric entropy H . The anisotropy measures the relative importance of the second and the third eigenvalues of the eigen decomposition. From a practical point of view, the anisotropy A can be regarded as a source of discrimination especially when $H > 0.7$. This is due to the fact that for lower entropies, the second and third eigenvalues are highly affected by noise. Hence, the anisotropy A is also significantly noisy. Inherent to the spatial averaging, however, the entropy increases, while the number of distinguishable classes reduces. For instance, an entropy $H > 0.9$ can correspond to two limit types of scattering process with associated eigenvalues spectra given by $(\lambda_1 = 1, \lambda_2 = 0.4, \lambda_3 = 0.4)$ and $(\lambda_1 = 1, \lambda_2 = 1, \lambda_3 = 0.3)$. To distinguish between these two different types of scattering processes, it is thus possible to use the anisotropy A information, where it takes e.g. the corresponding values $A = 0$ and $A = 0.54$ for the two previous examples (Cloude & Pottier, 1997; Cloude, 1999). It is important to note that the polarimetric anisotropy A plays a key role in PolSAR applications and represents a very useful parameter to improve the capability to distinguish different types of scattering processes in case the polarimetric entropy reaches high values. Generally speaking, for targets characterized by intermediate entropy values, a high anisotropy indicates the presence of only one significant secondary scattering process, while a low anisotropy indicates the appearance of two equally strong scattering processes.

In the polarimetric backscattering problem, the great advantage of these two parameters arises from the invariance of the eigenvalue problem under unitary transformations (Touzi, 2007). In this sense, the same scattering target leads to the same eigenvalues and hence to the same entropy and anisotropy values independent from the basis used to measure the corresponding target matrix.

5.5 Scattering Mechanism Interpretation

In section 5.1 it was discussed that the diagonalization of $[T_3]$, according to Eq. (5.1), produces a set of three orthogonal components, which at first have no physical significance. The aim of the following section is the physical interpretation of the resulting components and the corresponding eigenvectors of the coherency $[T_3]$ matrix. The unitary $[U_3]$ matrix in Eq. (5.1) is a general unitary matrix with $3^2 - 1 = 8$ degrees of freedom (Cloude, 1986b). The unitary $[U_3]$ matrix describing the change of polarization basis transformation possesses only two degrees of freedom. Hence, Eq. (5.1) cannot be interpreted as a simple change of polarization basis transformation, and the corresponding eigenvectors cannot be considered as conventional polarization states (Lee & Pottier, 2009).

It is important to note that the critical idea for the interpretation of the eigenvector decomposition is to associate the unitary complex vectors with polarimetric scattering mechanisms. In this sense, a scattering target with a target matrix / vector given by

$$[S] = \begin{bmatrix} S_{xx} & S_{xy} \\ S_{xy} & S_{yy} \end{bmatrix} \text{ and } \vec{k}_P = \frac{1}{\sqrt{2}} [S_{xx} + S_{yy}, S_{xx} - S_{yy}, 2S_{xy}]^T \quad (5.11)$$

where $S_{xy} = S_{yx}$ is considered. The target vector \vec{k}_P can be normalized to obtain the associated unitary vector \vec{e}

$$\vec{e} = \frac{1}{|\vec{k}_P|} \vec{k}_P \quad (5.12)$$

Such an arbitrary three-dimensional unitary vector \vec{e} has five degrees of freedom, and thus, can be written in terms of five angular variables (Cloude, 1995)

$$\vec{e} = \frac{1}{|\vec{k}_P|} \vec{k}_P = \begin{bmatrix} \cos \alpha \exp(i\phi_1) \\ \sin \alpha \cos \beta \exp(i\phi_2) \\ \sin \alpha \sin \beta \exp(i\phi_3) \end{bmatrix} = \frac{1}{\sqrt{2}|\vec{k}_P|} \begin{bmatrix} S_{xx} + S_{yy} \\ S_{xx} - S_{yy} \\ S_{xy} \end{bmatrix} \quad (5.13)$$

In accordance to the *Scattering Vector Reduction Theorem* introduced by Cloude (1997), it is always possible to generate this arbitrary scattering mechanism, described by the associated complex unitary vector \vec{e} , by starting from the identity vector $[1,0,0]^T$ and applying a set of three ordered matrix transformations

$$\vec{e} = \begin{bmatrix} \exp(i\phi_1) & 0 & 0 \\ 0 & \exp(i\phi_2) & 0 \\ 0 & 0 & \exp(i\phi_3) \end{bmatrix} \begin{bmatrix} 1 & 0 & 0 \\ 0 & \cos \beta & -\sin \beta \\ 0 & \sin \beta & \cos \beta \end{bmatrix} \begin{bmatrix} \cos \alpha & -\sin \alpha & 0 \\ \sin \alpha & \cos \alpha & 0 \\ 0 & 0 & 1 \end{bmatrix} \begin{bmatrix} 1 \\ 0 \\ 0 \end{bmatrix} \quad (5.14)$$

The scattering phase angles are contained in the first matrix. It accounts for the phase relations between the elements of the vector \vec{e} and, in the following, will be ignored for convenience. The second and third matrices represent canonical forms of plane rotations, i.e. a change about $\Delta\bar{\alpha}$ and $\Delta\bar{\beta}$ of the parameterization angles corresponds to a change from one scattering mechanism \vec{e} to an alternate \vec{e}' . For the angles $\bar{\alpha}$ and $\bar{\beta}$, the transformation matrices are simple plane rotations given by

$$\vec{e}' = \begin{bmatrix} 1 & 0 & 0 \\ 0 & \cos \Delta\beta & -\sin \Delta\beta \\ 0 & \sin \Delta\beta & \cos \Delta\beta \end{bmatrix} \vec{e} \quad \text{and} \quad \vec{e}' = \begin{bmatrix} \cos \Delta\alpha & -\sin \Delta\alpha & 0 \\ \sin \Delta\alpha & \cos \Delta\alpha & 0 \\ 0 & 0 & 1 \end{bmatrix} \vec{e} \quad (5.15)$$

The second transformation matrix in Eq. (5.14) represents physically a rotation of the scattering target about the RLOS by an angle $\beta/2$. Note that this correspondence is only valid as long as the Pauli basis is used for the vectorization of the target matrix. In effect, it follows directly from the nature of the Pauli matrices which relate physical rotations to matrix transformations (Cloude, 1986b).

However, the third matrix cannot be associated with a physical rotation. Instead, $\bar{\alpha}$ represents an internal degree of freedom of the scattering target. In this sense, the parameter, continuous within a range of $0^\circ \leq \bar{\alpha} \leq 90^\circ$, is associated with the “type” of backscattering mechanism. This feature becomes apparent by substituting different values of the $\bar{\alpha}$ angle into Eq. (5.14) and interpreting the generated vector \vec{e} in terms of the target vectors, assuming $\bar{\beta} = 0^\circ$ for the sake of simplicity.

I) For $\bar{\alpha} = 0^\circ$

$$\vec{e} = \begin{bmatrix} 1 & 0 & 0 \\ 0 & 1 & 0 \\ 0 & 0 & 1 \end{bmatrix} \begin{bmatrix} 1 \\ 0 \\ 0 \end{bmatrix} = \begin{bmatrix} 1 \\ 0 \\ 0 \end{bmatrix} = \frac{1}{\sqrt{2}|\bar{k}_P|} \begin{bmatrix} S_{xx} + S_{yy} \\ S_{xx} - S_{yy} \\ 2S_{xy} \end{bmatrix} \quad (5.16)$$

\vec{e} as obtained from Eq. (5.14) is associated with the target vector of an isotropic surface, i.e. a surface where both horizontally and vertically co-polarized waves are in phase and $|XX| = |YY|$.

II) For $\bar{\alpha} = 90^\circ$

$$\vec{e} = \begin{bmatrix} 0 & 1 & 0 \\ 1 & 0 & 0 \\ 0 & 0 & 1 \end{bmatrix} \begin{bmatrix} 1 \\ 0 \\ 0 \end{bmatrix} = \begin{bmatrix} 0 \\ 1 \\ 0 \end{bmatrix} = \frac{1}{\sqrt{2}|\bar{k}_P|} \begin{bmatrix} S_{xx} + S_{yy} \\ S_{xx} - S_{yy} \\ 2S_{xy} \end{bmatrix} \quad (5.17)$$

\vec{e} corresponds to the target vector of an isotropic dihedral with a phase difference between HH and VV of 180° , i.e. a dihedral with $|xx| = |yy|$.

III) For $\bar{\alpha} = 45^\circ$

$$\vec{e} = \begin{bmatrix} 1/\sqrt{2} & 1/\sqrt{2} & 0 \\ 1/\sqrt{2} & 1/\sqrt{2} & 0 \\ 0 & 0 & 1 \end{bmatrix} \begin{bmatrix} 1 \\ 0 \\ 0 \end{bmatrix} = \begin{bmatrix} 1/\sqrt{2} \\ -1/\sqrt{2} \\ 0 \end{bmatrix} = \frac{1}{\sqrt{2}|\bar{k}_P|} \begin{bmatrix} S_{xx} + S_{yy} \\ S_{xx} - S_{yy} \\ 2S_{xy} \end{bmatrix} \quad (5.18)$$

the obtained \vec{e} is associated with the target vector of a horizontally oriented dipole scattering target, where $S_{xx} = 1$ and $S_{yy} = S_{xy} = 0$. In order to illustrate the effect of $\bar{\beta}$, keeping $\bar{\alpha} = 45^\circ$, $\bar{\beta} = 90^\circ$ is applied as follows

$$\vec{e} = \begin{bmatrix} 1 & 0 & 0 \\ 0 & -1 & 0 \\ 0 & 0 & -1 \end{bmatrix} \begin{bmatrix} 1/\sqrt{2} & 1/\sqrt{2} & 0 \\ 1/\sqrt{2} & 1/\sqrt{2} & 0 \\ 0 & 0 & 1 \end{bmatrix} = \begin{bmatrix} 1 \\ 0 \\ 0 \end{bmatrix} = \begin{bmatrix} 1/\sqrt{2} \\ -1/\sqrt{2} \\ 0 \end{bmatrix} = \frac{1}{\sqrt{2}|\vec{k}_P|} \begin{bmatrix} S_{xx} + S_{yy} \\ S_{xx} - S_{yy} \\ 2S_{xy} \end{bmatrix} \quad (5.19)$$

Now, \vec{e} corresponds to a vertically oriented dipole scattering target, where $S_{yy} = 1$ and $S_{xx} = S_{xy} = 0$. In case that $\bar{\alpha}$ takes intermediate values, anisotropic backscattering mechanisms are represented, and $|xx|$ and $|yy|$ are no longer equal. The range of possible variations in backscattering mechanism can be depicted by the variation of $\bar{\alpha}$ along the real line as shown in Fig. 5.1. It should be emphasized that the type of scattering target is defined by its $\bar{\alpha}$ angle independently of its orientation $\beta/2$. It thus does not matter if there is a misalignment between radar and target coordinates. Tab. 5.1 gives the angular values for some canonical scattering mechanisms, which are of interest in radar polarimetry (Ferro-Famil et al., 2001).

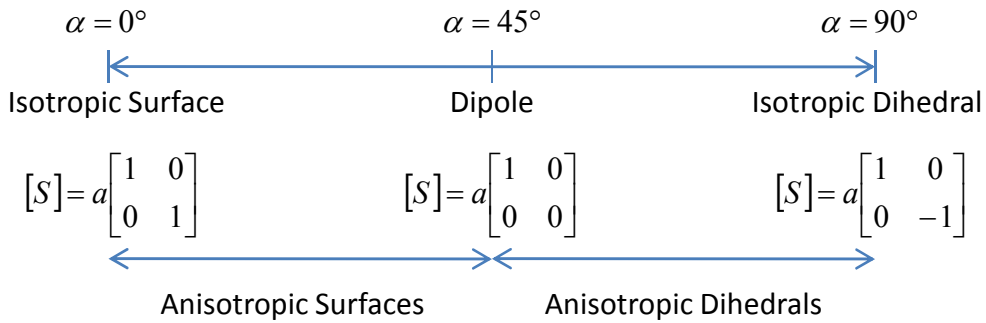


Figure 5.1: Schematic representation of the $\bar{\alpha}$ angle interpretation.

Taking these aspects into consideration, the general $[U_3]$ transformation of the target vector \vec{k} describes not only polarimetric basis transformation, but also linear combinations of three orthogonal coherent scattering mechanisms corresponding to changes in the selected

scattering mechanism (Cloude & Pottier, 1996). Consequently, the physical interpretation of the diagonalization of $[T_3]$ is the generation of a set of complex projections of the target vector onto three orthogonal backscattering mechanisms given by the three eigenvectors of $[T_3]$. The origin of the eight degrees of freedom in the general $[U_3]$ matrix should now become evident.

Table 5.1: Angular values of canonical targets (∞ represents non-fixed values); (Ferro-Famil et al., 2001).

Sphere	$\alpha = 0^\circ$	$\beta = \infty$	$\phi_1 = \tau$	$\phi_2 = \phi_3 = \infty$
Dihedral at θ°	$\alpha = 90^\circ$	$\beta = 2\theta^\circ$	$\phi_1 = \infty$	$\phi_2 - \phi_3 = 0^\circ$
Dipole at θ°	$\alpha = 45^\circ$	$\beta = 2\theta^\circ$	$\phi_1 = \tau$	$\phi_2 = \phi_3 = \tau$
Surface at θ°	$\alpha = 0^\circ$	$\beta = 2\theta^\circ$	$\phi_1 \approx 0^\circ$	$\phi_2 \approx \phi_3 = 0^\circ$
Helix	$\alpha = 90^\circ$	$\beta \pm 45^\circ$		$\phi_2 - \phi_3 = -90^\circ$

The fact that each of the three eigenvectors \vec{e}_i contains five parameters, leads to a sum of 15 parameters. The constraint that the three mechanisms must be orthogonal, however, provides six equations. Thus, the number of parameters reduces down to nine. Moreover, to establish the correct phase relationship between the components, the phase of the determinant should be zero according to the special unitary of $[U_3]$. This lastly results in eight independent parameters of the $[U_3]$ matrix.

As discussed in section 5.1, the eigen decomposition of a rank 3 $[T_3]$ matrix leads to three eigenvalues and three eigenvectors. The polarimetric scattering entropy H and anisotropy A can be estimated directly from the eigenvalues using Eq. (5.8) and Eq. (5.10), respectively. But then, for each eigenvector

$$\vec{e}_1 = \begin{bmatrix} e_{11} \\ e_{12} \\ e_{13} \end{bmatrix}, \vec{e}_2 = \begin{bmatrix} e_{21} \\ e_{22} \\ e_{23} \end{bmatrix}, \vec{e}_3 = \begin{bmatrix} e_{31} \\ e_{32} \\ e_{33} \end{bmatrix} \quad (5.20)$$

the corresponding $\bar{\alpha}_i$ angle is obtained from the absolute value of the first element according to Eq. (5.19) as

$$\bar{\alpha}_1 = \arccos(|e_{11}|), \bar{\alpha}_2 = \arccos(|e_{21}|), \bar{\alpha}_3 = \arccos(|e_{31}|) \quad (5.21)$$

whilst the corresponding parameter $\bar{\beta}_i$ is obtained by using the ratio between the absolute values of the second and third eigenvectors elements as

$$\bar{\beta}_1 = \arctan\left(\frac{|e_{13}|}{|e_{12}|}\right), \bar{\beta}_2 = \arctan\left(\frac{|e_{23}|}{|e_{22}|}\right), \bar{\beta}_3 = \arctan\left(\frac{|e_{33}|}{|e_{32}|}\right) \quad (5.22)$$

In the exact same manner three sets of target angles can be obtained as (Boerner, 1992)

$$\begin{aligned} \phi_{11} &= \arctan\left(\frac{\text{Im}(e_{11})}{\text{Re}(e_{11})}\right) & \phi_{12} &= \arctan\left(\frac{\text{Im}(e_{12})}{\text{Re}(e_{12})}\right) & \phi_{13} &= \arctan\left(\frac{\text{Im}(e_{13})}{\text{Re}(e_{13})}\right) \\ \phi_{21} &= \arctan\left(\frac{\text{Im}(e_{21})}{\text{Re}(e_{21})}\right) & \phi_{22} &= \arctan\left(\frac{\text{Im}(e_{22})}{\text{Re}(e_{22})}\right) & \phi_{23} &= \arctan\left(\frac{\text{Im}(e_{23})}{\text{Re}(e_{23})}\right) \\ \phi_{31} &= \arctan\left(\frac{\text{Im}(e_{31})}{\text{Re}(e_{31})}\right) & \phi_{32} &= \arctan\left(\frac{\text{Im}(e_{32})}{\text{Re}(e_{32})}\right) & \phi_{33} &= \arctan\left(\frac{\text{Im}(e_{33})}{\text{Re}(e_{33})}\right) \end{aligned} \quad (5.23)$$

Hence, the 15 angular variables extracted from the eigenvectors composing the general unitary $[U_3]$ matrix are obtained. Due to the fact that the $[U_3]$ matrices contain only eight independent parameters, as previously discussed, the 15 extracted angles are not independent from each other. This renders it problematic to interpret each individual $\bar{\alpha}_i$ and $\bar{\beta}_i$ parameter. To tackle this problem, the interpretation is performed in terms of a dominant scattering mechanism: Since the distributed target is modeled to be decomposed into three elementary scattering processes, occurring with a probability P_i and corresponding to an $\bar{\alpha}_i$ and $\bar{\beta}_i$ angle, the best estimate (in a maximum likelihood sense) of the parameters $\bar{\alpha}$ and $\bar{\beta}$ are given by their mean values (Cloude, 1997)

$$\begin{aligned}\bar{\alpha} &= P_1\alpha_1 + P_2\alpha_2 + P_3\alpha_3 \\ \bar{\beta} &= P_1\beta_1 + P_2\beta_2 + P_3\beta_3\end{aligned}\tag{5.24}$$

These two angular parameters for the dominant backscattering mechanism along with the entropy and anisotropy values have so far mainly been used for the classification of natural targets from fully polarimetric SAR data (e.g. Cloude & Pottier, 1997; Lee et al., 1999a; Ferro-Famil et al., 2001; Kimura et al., 2004; Lee et al., 2004; Cao et al., 2007; Ainsworth et al., 2009).

5.6 ALOS PALSAR Experimental PolSAR Data Analysis

Before closing this chapter, a first order interpretation of basic PolSAR images obtained from the experimental polarimetry mode of ALOS PALSAR shall be given. Namely Pauli-RGB (Fig. 5.2), entropy, anisotropy and alpha angle maps will be addressed (Fig. 5.3). The detailed description of the river Rur catchment study area as well as the local test sites within the fertile loess plain and the low mountain range regions can be found in Chapter 4. The description of the fully polarimetric ALOS PALSAR intensity images is given in Chapter 2. As learned before, the mesoscale catchment is basically subdivided into two parts. The fertile loess plain in the north is mainly composed of agricultural fields, small urban areas, small forest areas, some grassland, and little surface water. As a distinctive feature of the area, one should not forget to mention the open-cast mining Garzweiler, Hambach, and Inden. The low mountain range part, on the other hand, is dominated by grassland, coniferous forests, and bushes. Build up areas are usually rather small.

The virtue of using the Pauli target vectors lies in the straightforward physical interpretation in terms of the dominant scattering mechanism occurring in a PolSAR image resolution cell (cf. section A.4). Fig. 5.2 shows a Pauli vector color-coded image of the fully polarimetric ALOS PALSAR scene for the Rur catchment. The three Pauli vectors $|HH-VV|$, $|HV+VH|$, and $|HH+VV|$ are displayed as the three RGB channels, respectively. The image shows surface scattering in black to blue colors, volume scattering in green colors, and double bounce in red colors. Hence the Pauli representation of the PALSAR data allows an easy

identification of the different land cover types within the catchment. The fertile loess plain is characterized by surface scattering on the bare or sparsely vegetated agricultural fields, while the low mountain range is dominated by volume scattering in the forest areas. Moreover, the double bounce scattering in build-up areas clearly shows that the northern part of the catchment is far more densely populated than the southern part.

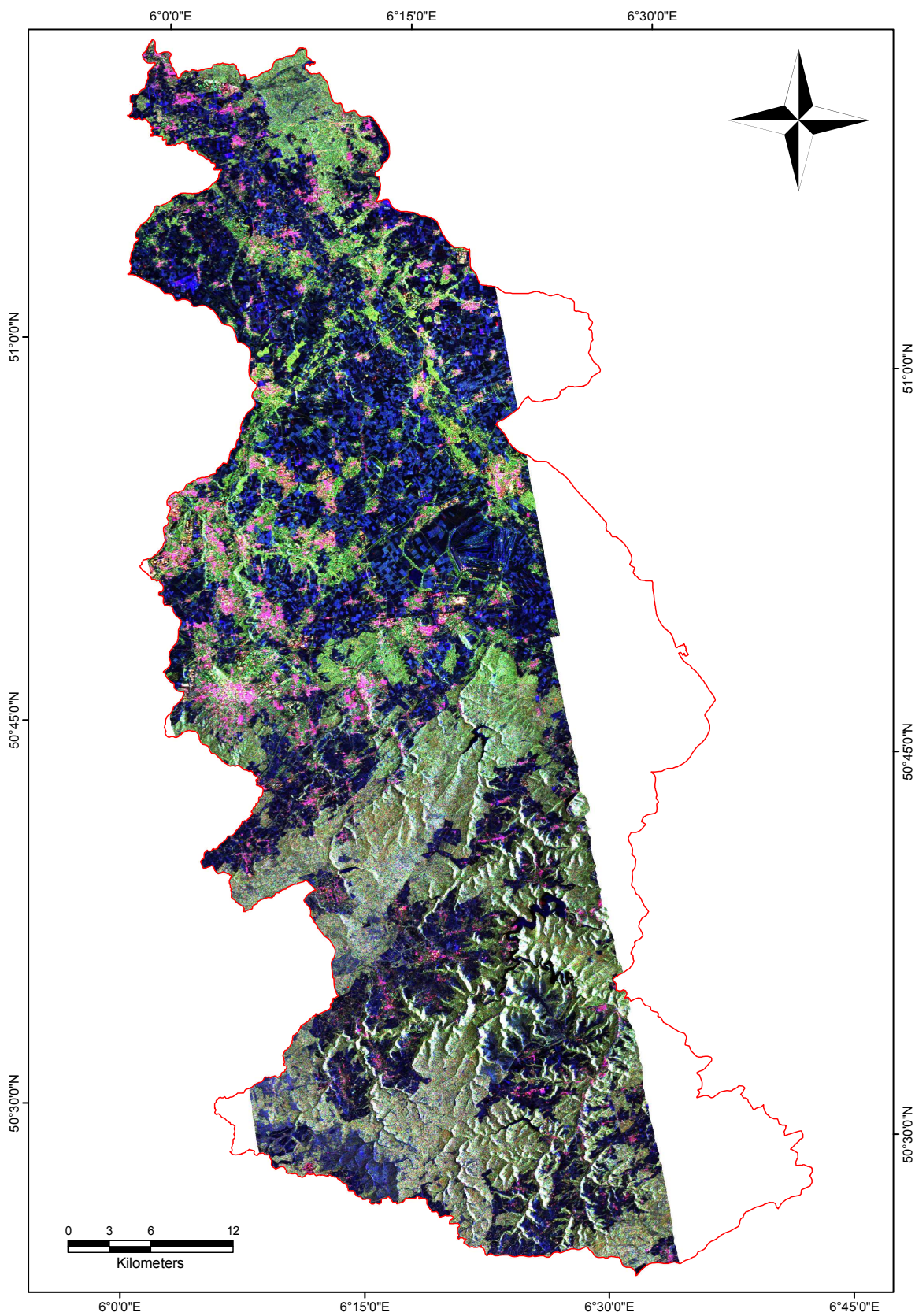


Figure 5.2: ALOS PALSAR Pauli-RGB of the River Rur catchment. The Pauli vectors are color coded as red = $|HH-VV|$, green = $|HV-VH|$, and blue = $|HH+VV|$.

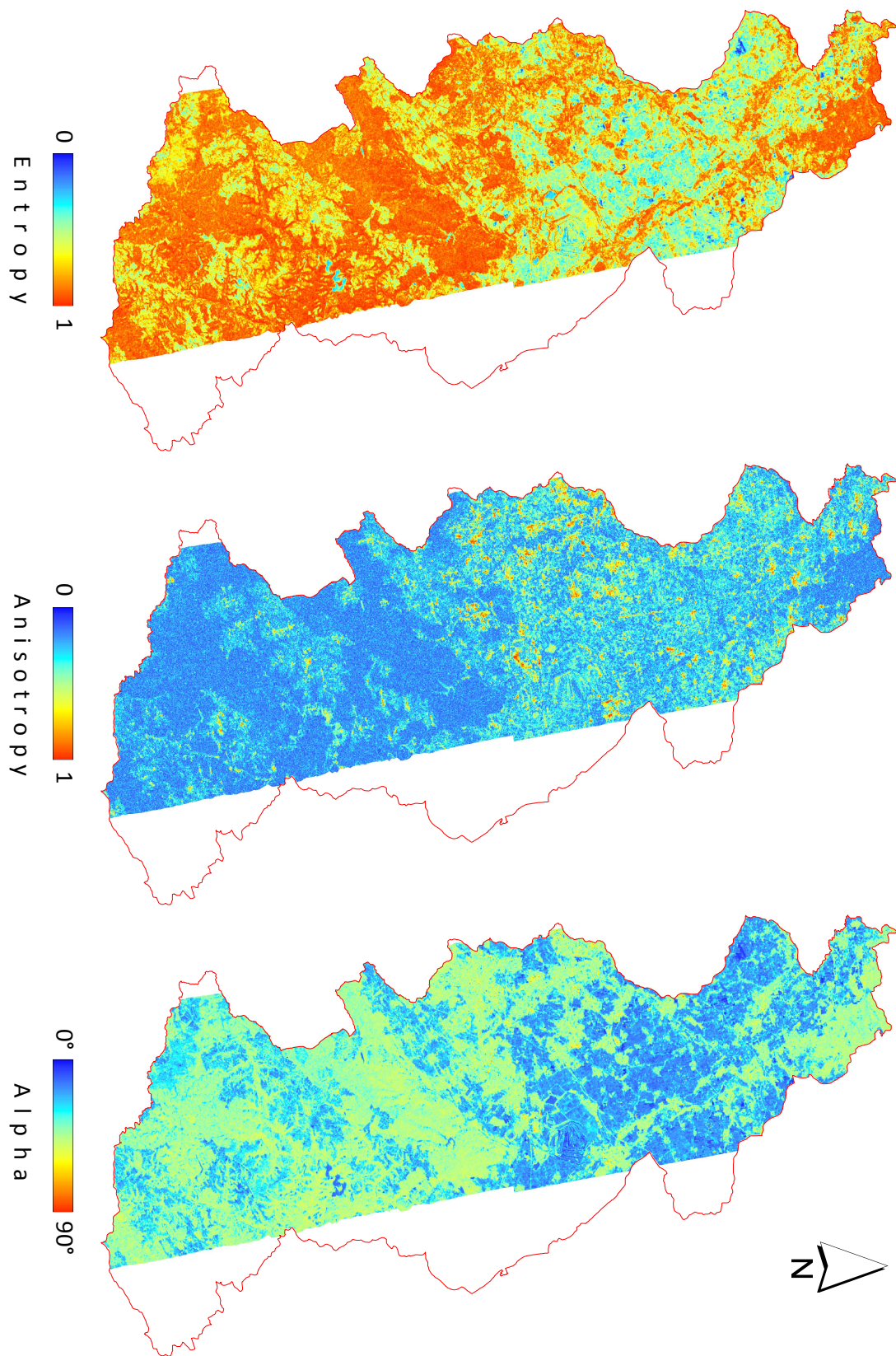


Figure 5.3: Polarimetric entropy (left), anisotropy (middle), and alpha angle maps (right) of the River Rur catchment.

The bare and sparsely vegetated agricultural fields have low entropy values ranging from 0.1 to 0.6, as can be seen in Fig. 5.3. The anisotropy ranges from 0 to 0.6 and alpha angles are low ranging from 10° to 30° . The low values of H indicate the presence of a single dominant scattering mechanism. The low α values at the same time suggest an anisotropic surface scattering. The polarimetric parameter A varies between 0 and 0.8 with low values over rougher surfaces for which the presence of a secondary scattering effect can be expected, to high values over smoother surfaces for which the scattering process is quasi deterministic.

Table 5.2: Land cover type specific ranges of values for polarimetric target parameters.

	Arable fields	Grassland	Forest	Build-up area
Entropy	0.1 - 0.6	0.4 - 0.8	0.7 - 1	0.1 - 1
Anisotropy	0 - 0.8	0.1 - 0.9	0.1 - 1	0 - 1
Alpha angle	$10^\circ - 30^\circ$	$12^\circ - 40^\circ$	$30^\circ - 80^\circ$	$40^\circ - 80^\circ$

The polarimetric scattering from grassland and agricultural fields with higher amounts of biomass at L-band include components from the vegetation as well as from the underlying soil surface. Hence, we expect the presence of secondary scattering processes. Indeed such scattering targets are characterized by a medium range of H and α , while A again covers a larger range between 0.1 and 0.9. As shown in Tab. 5.2, H ranges from 0.4 to 0.8 and α from 12° to 40° . Medium H values are characteristic for the presence of two (or more) scattering mechanisms. The corresponding α values indicate dipole-like scattering behavior.

Finally, forest and build-up urban areas are represented by both high H and α values while A varies over its whole definition range between 0 and 1. The high entropy region indicate the superposition of three scattering mechanism. The large alpha angles indicate that dihedral scattering is dominant. Here, high anisotropy represents the presence of two main scattering mechanisms, whereas low values indicate three scattering mechanisms.

5.7 ALOS PALSAR Dual Polarimetric Decomposition

In the forgoing sections it was discussed that the entropy/alpha approach was originally designed to simplify multi-parameter depolarization occurring in quad polarized backscattering. However, Cloude (2007) demonstrated that it can also be applied to the simpler case of dual polarization. In this scenario the radar transmits only a single polarization and receives, either coherently or incoherently, two orthogonal components of the scattered signal. In the coherent case, this corresponds to measurement of the full state of polarization of the scattered signal for fixed illumination (Cloude & Pottier, 1996; Touzi, 2007; Touzi et al., 2008; Lee & Pottier, 2009). The ALOS PALSAR sensor (ERSDAC, 2006) has such a fully coherent-on-receive mode. Cloude (2007) investigated development and application of a dual polarized entropy/alpha technique that can be used to take advantage of such coherent dual polarized systems. In this section we will discuss the eigen decomposition of the dual polarized ALOS PALSAR FBD data.

In radar science there are two important special cases when the dual formalism becomes important. From a cost, data rate and coverage point of view, it is often advantageous in radar design to employ a single transmitted polarization state and a coherent dual channel receiver to measure orthogonal components of the scattered signal. Note that such dual polarized systems are not capable of reconstructing the complete scattering matrix, as discussed in section A.3, but instead can be used to reconstruct a column of the $[S]$ matrix (Raney, 2006). This allows for constructing a 2×2 wave coherency matrix $[J]$ to estimate depolarization. One key decision in the design of such radars is the best single polarization to employ (the reference point X on the Poincaré sphere shown in Fig. 5.4). As mentioned before, the FBD mode of ALOS PALSAR employs horizontally polarized transmission, while the experimental dual polarization mode of TERRASAR-X, for example, transmits in vertical polarization. Both systems employ dual channel reception of horizontally and vertically polarized components.

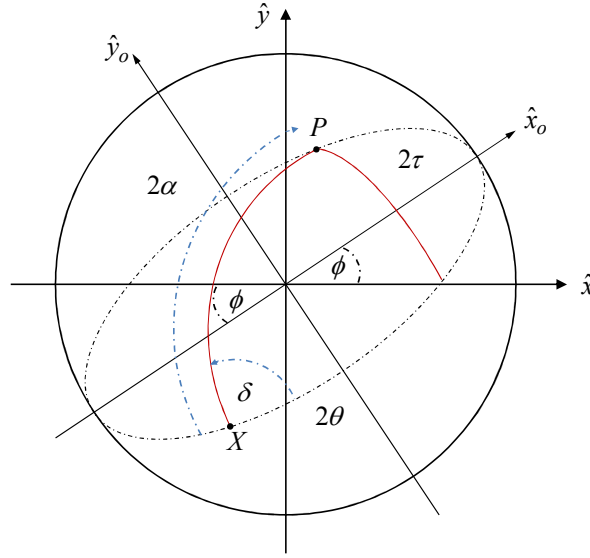


Figure 5.4: The Poincaré sphere interpretation of the dual polarized alpha angle.

These radars can then be used, via local averaging, to estimate the following forms of the 2x2 wave coherency matrix

$$\begin{aligned}
 [J_H] &= \begin{bmatrix} \langle S_{xx} S_{xx}^* \rangle & \langle S_{xx} S_{xy}^* \rangle \\ \langle S_{xy} S_{xx}^* \rangle & \langle S_{xy} S_{xy}^* \rangle \end{bmatrix} \\
 [J_V] &= \begin{bmatrix} \langle S_{yy} S_{yy}^* \rangle & \langle S_{yy} S_{yx}^* \rangle \\ \langle S_{yx} S_{yy}^* \rangle & \langle S_{yx} S_{yx}^* \rangle \end{bmatrix}
 \end{aligned} \tag{5.25}$$

It should be mentioned, that some dual polarization radars are not capable to employ the coherent-on-receive mode. For example, the European ENVISAT ASAR system in alternating polarization (AP) mode cannot measure the off-diagonal elements of $[J]$ and obtains only the two diagonal terms. It is important to realize that such non-coherent polarimetric radars do not allow applying the polarized/depolarized decompositions.

5.9.1 The Dual Polarized Entropy/Alpha Decomposition

Using the standard interpretation of normalized eigenvalues of $[J]$ as probabilities P_i , together with the fact that in 2x2 problems the second eigenvector can be derived from the principal

eigenvector using orthogonality, we obtain an entropy/alpha parameterization of the wave coherency matrix $[J]$ as shown in Eq. (5.26)

$$\begin{aligned}
 [J] = \begin{bmatrix} J_{xx} & J_{xy} \\ J_{xy}^* & J_{yy} \end{bmatrix} &\Rightarrow \begin{cases} [U_2] = \begin{bmatrix} \cos \alpha & -\sin \alpha e^{-i\delta} \\ \sin \alpha e^{i\delta} & \cos \alpha \end{bmatrix} \\ [D] = (\lambda_1 + \lambda_2) \begin{bmatrix} P_1 & 0 \\ 0 & P_2 \end{bmatrix} \end{cases} \\
 \Rightarrow \begin{cases} \bar{\alpha}_2 = P_1 \alpha + P_2 \left(\frac{\pi}{2} - \alpha \right) = \alpha (P_1 - P_2) + P_2 \frac{\pi}{2} \\ H_2 = \sum_{i=1}^2 P_i \log_2 P_i \end{cases} & \quad (5.26)
 \end{aligned}$$

$$\begin{aligned}
 \begin{bmatrix} 1 & 0 \\ 0 & m \end{bmatrix} 0 \leq m \leq 1 &\Rightarrow \bar{\alpha}_{\min} = \frac{m\pi}{2(1+m)} \\
 \begin{bmatrix} m & 0 \\ 0 & 1 \end{bmatrix} 0 \leq m \leq 1 &\Rightarrow \bar{\alpha}_{\max} = \frac{\pi}{2(1+m)}
 \end{aligned} \quad (5.27)$$

In this dual polarized case we have a simple interpretation of α on the Poincaré sphere (Fig. 5.4). The angle α is the angular separation between the received wave polarization state P and the reference state X used for construction of the wave coherency matrix. Indeed, the angles α and δ are related to the orientation and ellipticity angles θ, τ of the received wave's polarization ellipse via a spherical triangle construction on the Poincaré sphere as shown in Fig. 5.4. One reason for employing this approach as opposed to the conventional Stokes vector/degree of polarization (Raney, 2006) is the continuity it provides with the entropy/alpha decomposition for quadpol backscatter (Cloude & Pottier, 1996; 1997). In this sense the same phenomenology to describe all polarized scattering problems can be used. It should be noted that Cloude (2007) refers to the dual polarized case as $H2\alpha$ to distinguish it from the quad polarized H/α case as discussed in section 5.5. The averaging implied by the entropy/alpha approach does not pick out the state P corresponding to the maximum eigenvalue as in the polarized/depolarized decomposition but instead forms an average based on a probabilistic interpretation of making measurements on the wave and obtaining polarization X and Y with probabilities P_1 and P_2 respectively. Hence the average polarization state would have a corresponding alpha value given by $\bar{\alpha}$. In this sense, the

coherency matrix approaches the identity (noise) when $\bar{\alpha} = \pi/4$, being an equal mixture of the state X ($\bar{\alpha} = 0$) with its antipodal orthogonal state Y ($\bar{\alpha} = \pi/2$). It should be noted that in the partial polarimetric case the anisotropy A has no physical meaning since it compares two secondary scattering mechanisms while in dual polarimetry only one secondary mechanism can be identified (Breuer et al., 2003).

5.9.3 Experimental Observations

To demonstrate the use of these theoretical considerations for real life data, Koyama & Schneider (2011) calculated a series of $H2\alpha$ planes for different land cover types from the PALSAR FBD images and compared it with different in situ measured ground truth parameters. Fig. 5.5 shows the array of $H2\alpha$ planes for major land cover types bare soil, grassland, sugar beet, and winter wheat. To alleviate the interpretation of the diagrams, each $H2\alpha$ plane includes the mean m_v value of all pixels and the mean ks or fresh weight (FW) of the biomass, respectively. In addition, the mean values are supplemented with the corresponding standard deviation. Several interesting observations can be noted from the plots. The most notable are summarized in the following points.

The comparison between bare soil and winter wheat $H2\alpha$ planes indicate that both land covers have similar scattering behavior. Surprisingly, the entropy is rather lower for the winter wheat pixels. In effect, the absolute minimum entropy of $0.1 < H < 0.4$ is found on the wheat fields on June 2, 2008, while the bare soil fields show higher entropy values of $0.2 < H < 0.6$. Note that this is the date with the measured absolute minimum ks .

It is very interesting to note that the absolute maximum entropy occurs on the bare soil fields on May 4, 2008. This is the date with the highest measured surface roughness with ks values up to 0.92. This significant observation indicates that we have very high volume scattering within the ploughing layer of the freshly ploughed fields. Note that this has drastic consequences for the applicability of surface scattering models with L-band SAR data, i.e. possibly these models could, in general, not be true for such surface conditions at low radar frequencies.

From the grassland planes we receive the impression that depolarization decreases with decreasing water content of soil and thatch. For instance, the entropy reaches the minimum of $0.3 < H < 0.7$ for the date with the measured absolute minimum moisture contents in the grassland test site (June 2, 2008). This could be explained by decreased scattering from grass plants and thatch due to their lower dielectric constants. This leads to a better penetration of the signal towards the real soil surface and thus increases the surface scattering.

Finally, it should be mentioned that the entropy of the sugar beet pixels seems to increase with increasing biomass. It can be seen that H reaches very high values up to 0.85 for mature sugar beet on September 17, 2007.

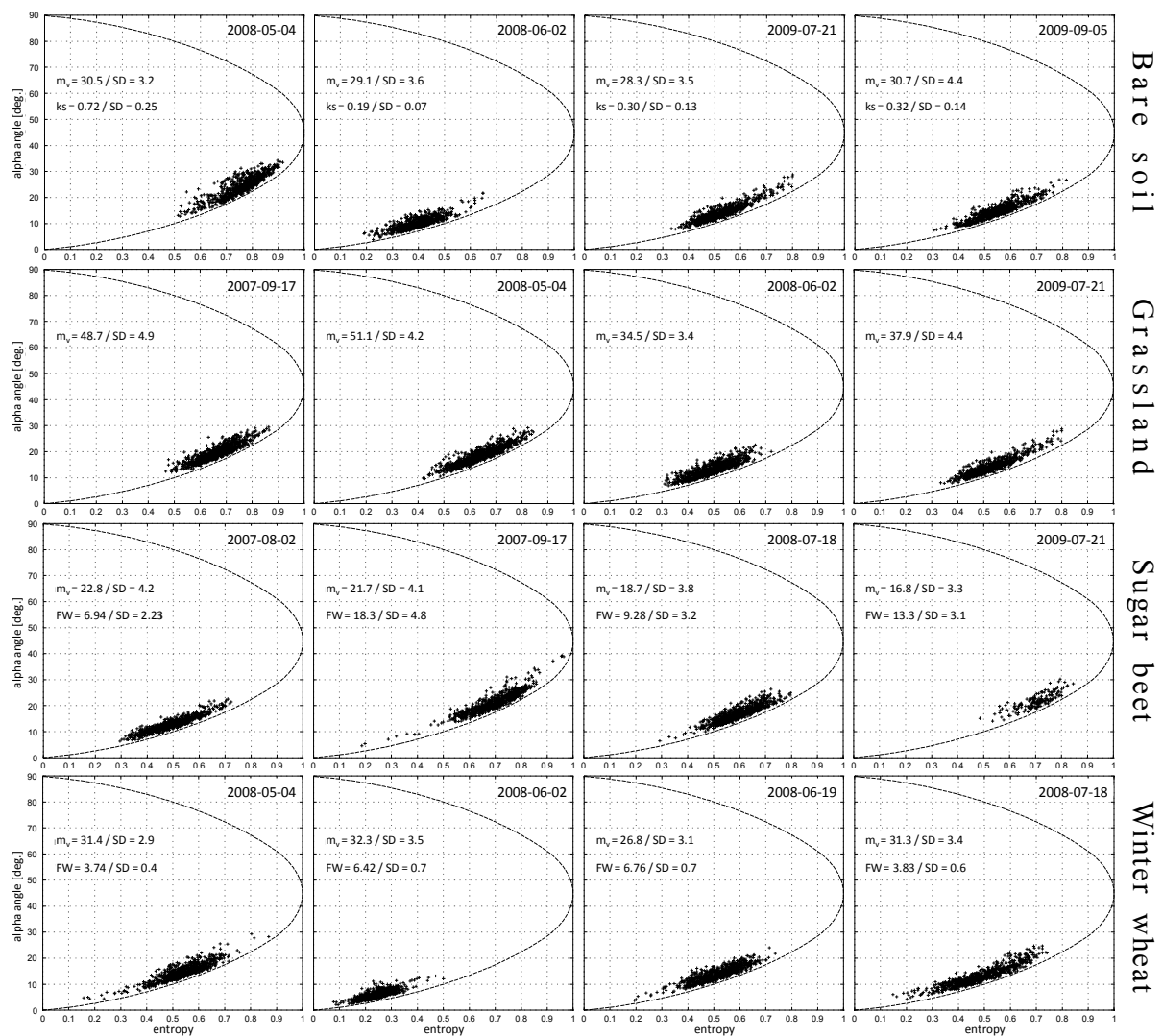


Figure 5.5: Land use specific PALSAR dual-pol $H2\alpha$ planes for different imaging dates; m_v is the mean surface soil moisture in Vol.-%, k_s is the surface roughness, and SD is the corresponding standard deviation.

In order to conclude this chapter, an additional way to demonstrate the potential of the partial polarimetric H/α decomposition by calculating composite images of the different decomposition products is considered. Koyama & Schneider (2010) proposed the application of a HSV color-coding scheme with the hue equal to the alpha angle. The entropy is used as saturation term, so the color saturation decreases with increasing entropy. The scattered total power is used to modulate the intensity through the value term. Fig. 5.6 shows the different signatures in the entropy/alpha domain for the Selhausen sampling fields on July 21, 2009. Significant variations of scattering behavior can be noted for the various land cover types indicating the potential of discrimination and classification based on the dual-pol phase information. The green color represents low or no vegetation. Sugar beet fields and tree hedges appear bluish, while the maize in the northern part of field A11 occurs reddish. The very bright areas in the eastern part represent double bounce effects from man-made structures with high reflected total power.

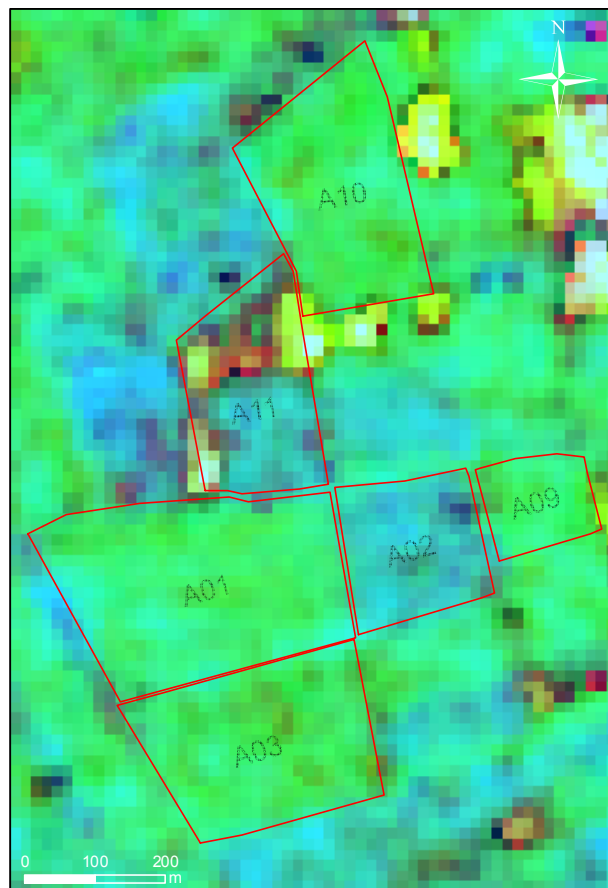


Figure 5.6: HSV image of the Selhausen test site from 21st July 2009
(Hue = Alpha, Saturation = Entropy, Value = Span)

6. Classical Models for Quantitative Soil Moisture Estimation

In the last decades a large variety of models have been developed to quantitatively invert land surface parameters, i.e. soil moisture and roughness, from radar measurements. These models range from experimental relationships to physically based theoretical approaches and vary significantly in regard to their complexity and validity ranges. In this chapter a critical review of different approaches for the estimation of soil moisture content from SAR imaging is provided. The chapter is basically divided into three parts according to three different approaches for the inversion of geophysical parameters based either on theoretical, physical based, semi-empirical or fully empirical models. In the first part, the small perturbation surface scattering model (SPM) is considered followed by the integral equation model (IEM) – which is today by far the most common and best investigated theoretical scattering model for computing electromagnetic wave scattering on rough surfaces. Part two is concerned with the two famous semi-empirical extensions of the SPM which were developed to improve the performance of the original theoretical approach. The first one is the semi-empirical model proposed by Oh et al. (1992) and the second is the empirical extension introduced by Dubois et al. (1995). In the last part, a fully empirical approach which has no physical basis but relies solely on observed linear or polynomial relationships between the backscattering coefficient and volumetric water content of a soil is addressed. The empirical retrieval model was especially designed for spaceborne single channel C-band SAR systems (i.e. ERS/SAR, Envisat/ASAR) and allows, in contrast to the former approaches, estimating soil moisture under a vegetation cover. Finally, the chapter concludes with a discussion of why it is necessary to develop a new semi-empirical model for spaceborne radar imaging at low frequencies.

6.1 Theoretical Scattering Models

Even though the scattering problem of electromagnetic waves on randomly rough surfaces has been intensively researched over decades, it still cannot be considered as satisfactorily solved. That is, up to this date, no exact closed-form solution exists for this problem (Lee & Pottier, 2009). Nonetheless, a wide range of approximate methods to model EM wave scattering on rough surfaces have been developed, and, as a matter of fact, for many practical applications such approximate solutions may be sufficient. In radar science, the most prevalent approximate methods of treating this problem have been the so called *Kirchhoff Approximation* (KA) and the *Small Perturbation Model* (SPM) (Ishimaru, 1997). However, in the last decade the Integral Equation Model (IEM) has become the most commonly used physical model in inversion procedures for the retrieval of soil moisture and/or roughness for most practical radar applications (Song et al., 2009). This is mostly due to the fact that, unlike the above models, the IEM validity domain covers the range of surface roughness values typically found on agricultural soils.

It should be pointed out that the KA is only valid if the dimensions of surface roughness are large compared to the actual radar wavelength (Ishimaru & Chen, 1991). Thus, it is more suitable for radar applications at high frequencies, e.g. at X- or C-band, and for large surface correlation lengths of $kl > 6$. Under such conditions, the scattering at a given point on the rough surface may be treated as scattering on the tangent plane of this point (Rodríguez, 1991). Nonetheless, this approximation does not allow obtaining an analytical solution, and thus, it requires additional assumptions. For that reason, two modifications of the KA have been introduced: i) the *Geometric Optics Model* (GOM) and ii) the *Physical Optics Model* (POM). The GOM represents the low frequency solution of the KA where obtained backscattering coefficients depend mainly on the surface slope. It is valid for very rough surfaces with $ks > 2$ (Macaskill, 1991). Contrary to this, the POM may be considered as the high frequency solution of the KA valid for high surface roughness conditions of $ks > 0.25$ (Papa et al., 1986). The restricted validity ranges of these three approximations make it obvious that they have only limited relevance in practical radar applications (Chen & Fung, 1988).

6.1.1 The Small Perturbation Model

The Small Perturbation Model sets on the assumption that the deviations in surface height are small compared to the given wavelength. Hence, it is more appropriate for applications at lower frequencies such as S-, L-, and P-band (Chen & Fung, 1988). Despite the fact that the SPM is also only valid within a limited range of roughness conditions, it is one of the classical and most widely used solutions for the rough surface scattering problem. In effect, this method requires the surface standard deviation to be less than 5% of the electromagnetic wavelength. Nonetheless, it is considered as one standard approach and has been extensively used in various practical applications (Engman & Wang, 1987). The analytical conditions for its validity have been subject of investigation in several studies (Beckmann & Spizzichino, 1987; Chen & Fung, 1995).

As discussed in section 3.4, a perfectly smooth surface has zero backscatter at oblique incidence. In the so called Bragg scattering region where the deviations in surface height are relatively small compared to the wavelength, however, the presence of a certain roughness can be treated as a perturbation of the smooth surface scattering problem. In this particular case, the backscattering coefficients can be obtained by means of the small perturbation or Bragg scattering model derived directly from Maxwell's equation (Borgeaud et al., 1989; Ishimaru, 1997). In this model, the random surface is decomposed into its Fourier spectral components, each of which is corresponding to an ideal sinusoidal surface. The scattering process itself is mainly driven by the spectral surface component as a function of wavelength and local incidence angle. For a Bragg surface, the polarimetric scattering matrix $[S]$ takes the form of

$$[S] = \begin{bmatrix} S_{hh} & S_{hv} \\ S_{vh} & S_{vv} \end{bmatrix} = A_s \begin{bmatrix} S_{hh}(\theta, \varepsilon') & 0 \\ 0 & S_{vv}(\theta, \varepsilon') \end{bmatrix} \quad (6.1)$$

where A_s denotes the backscattering amplitude holding the information about the surface roughness conditions, and S_{HH} and S_{VV} are the so called *Bragg scattering coefficients* perpendicular and parallel to the plane wave's direction of travel, respectively. Both of which

are functions of the complex dielectric constant ε of the medium and the local incidence angle θ given by

$$S_{hh} = \frac{\cos \theta - \sqrt{\varepsilon' - \sin^2 \theta}}{\cos \theta + \sqrt{\varepsilon' - \sin^2 \theta}} \quad S_{vv} = \frac{(\varepsilon_r - 1)(\sin^2 \theta - \varepsilon'(1 + \sin^2 \theta))}{(\varepsilon_r \cos \theta + \sqrt{\varepsilon' - \sin^2 \theta})} \quad (6.2)$$

Note that one of the most important statements of the SPM arises directly from Eq. (6.1). That is, the co-polarized ratio S_{HH}/S_{VV} depends only on the complex dielectric constant and the local incidence angle, and thus is independent of surface roughness. Several studies investigated the dependency of the co-pol ratio on the given soil moisture for incidence angles ranging from 25 to 60 degrees (Engman & Wang, 1987; Chen & Fung, 1988; Hajnsek et al., 2003b) showing that for dry surfaces, the S_{HH}/S_{VV} ratio is high and decreases with increasing water content. A strong variation at all incidence angles was observed for m_v values between 0 and 20 Vol.-%, while saturating at $m_v > 20$ Vol.-%. These findings indicate that the SPM is quasi insensitive to (very) wet surfaces, and thus its inversion yields get out of true for soil moisture values above the saturation level. Hence, it can be concluded that for most natural bare soil surfaces the validity range for both roughness and moisture conditions is too strict to be of any practical importance. It should be mentioned that not one of the test fields, as sampled in this study, actually meets the requirements of the Bragg region (cf. section 4.3.2). This demonstrates the limited applicability of the SPM under realistic conditions in radar remote sensing.

In order to increase these strict validity ranges of the SPM, Hajnsek (2001) (Hajnsek et al., 2003b) introduced an extension of the Bragg surface scattering model. The *X-Bragg model* is a two-component scattering model with one Bragg scattering term and one roughness related perturbation term. Hence, it allows dealing with roughness-induced depolarization as well as with cross-polarized backscattering contributions. The approach extends the validity range of the original SPM up to $m_v = 35$ Vol.-%, rendering it more suitable for parameter inversions over natural bare surfaces. Another advantage of this model is the fact that it allows a straightforward separation of roughness and dielectric constant estimations. However, it should be noted that the estimation of ε' was found to be highly sensitive towards variations in the incidence angle (Hajnsek et al., 2003b). The X-Bragg model was used in several

studies dealing with fully polarimetric airborne SAR data (Breuer et al., 2003; Hajnsek et al., 2009; Jagdhuber & Hajnsek, 2010).

6.1.2 The Integral Equation Model

The Integral Equation Model developed by Fung et al. (1992; 1996) offers an alternative theoretical approach for the retrieval of soil moisture and/or surface roughness from active microwave data. As already mentioned, the model is valid for a wider range of roughness conditions compared to other theoretical models like KA, POM, GOM, or SPM. However, it should be noted that, in return, the IEM requires a multitude of parameters such as surface RMS height, surface power spectrum of the surface correlation function, and correlation length; sensing configuration parameters such as frequency (or wavelength) and look angle, as well as permittivity of the soil. As demonstrated in several studies (Oh & Kay, 1998; Davidson et al., 2000; Mattia et al., 2003a; Callens et al., 2006), of all these variables in the IEM, especially the roughness-related parameters are difficult to determine. Moreover, the complexity of this model along with the implicit relationship between soil dielectric constant and radar data make it difficult to directly invert soil moisture and roughness parameters from reflectivity measurements over natural terrain surfaces.

In chapter 2 it was discussed that the radar backscattering coefficient of a bare soil surface is a function of soil texture, structure, density, roughness (RMS height), soil moisture, and soil surface conditions described by the autocorrelation function of a random surface height and correlation length. According to the electromagnetic scattering theory, in the case of natural terrains that have a small RMS slope, multiple scattering is not significant, and thus, single scattering will dominate in most situations (Beckmann & Spizzichino, 1987). Therefore, only co-polarized backscattering coefficients are considered by the IEM

$$\sigma_{pp}^0 = \frac{k^2}{2} \exp(-2k_z^2 s^2) \sum_{n=1}^{\infty} s^{2n} |I_{pp}^n|^2 \frac{W^n(-2k_x, 0)}{n!} \quad (6.3)$$

where $p = h$ (horizontal) or v (vertical) polarization and

$$I_{pp}^n = (2k_z)^n f_{pp} \exp(-k_z^2 s^2) + k_z^n \Phi_p(k_x)/2 \quad (6.4)$$

$$f_{vv} = \frac{2R_{\parallel}}{\cos\theta} \quad (6.5)$$

$$f_{hh} = -\frac{2R_{\perp}}{\cos\theta} \quad (6.6)$$

$$\begin{aligned} \Phi_v &= F_{vv}(-k_x, 0) + F_{vv}(k_x, 0) \\ &= \frac{2 \sin^2 \theta (1 + R_{\parallel})^2}{\cos \theta} \left[\left(1 - \frac{1}{\varepsilon_r} \right) + \frac{\mu_r \varepsilon' - \sin^2 \theta - \varepsilon_r \cos^2 \theta}{\varepsilon_r^2 \cos^2 \theta} \right] \end{aligned} \quad (6.7)$$

$$\begin{aligned} \Phi_h &= F_{hh}(-k_x, 0) + F_{hh}(k_x, 0) \\ &= \frac{2 \sin^2 \theta (1 + R_{\perp})^2}{\cos \theta} \left[\left(1 - \frac{1}{\mu_r} \right) + \frac{\mu_r \varepsilon' - \sin^2 \theta - \mu_r \cos^2 \theta}{\mu_r^2 \cos^2 \theta} \right] \end{aligned} \quad (6.8)$$

where s is the surface RMS height, k is the wavenumber as given by Eq. (2.20), $k_z = k \cos \theta$, $k_x = k \sin \theta$, with θ being the incidence angle, ε' the relative dielectric constant of the soil, μ_r is the relative permeability, and R_{\parallel} and R_{\perp} are the vertically and horizontally polarized Fresnel reflection coefficients, respectively. $W^n(k_x, k_y)$ is the Fourier transform of the n th power of a known surface correlation function which can be calculated by (Fung, 1994)

$$W^n(k_x, k_y) = \frac{1}{2\pi} \iint \rho^n(x, y) \exp(jk_x x + jk_y y) dx dy \quad (6.9)$$

where $\rho(x, y)$ is the surface correlation function as given by Eq. (3.18) in section 3.3.1.

Studies by Shi et al. (1997) and Zribi & Dechambre (2003) showed that the single-scattering IEM is suitable to compute both soil backscattering coefficients for bare soil and short-vegetated surfaces. However, application of the model to retrieve m_v from the radar backscattering coefficient is difficult because the dependence of the model on ε' , θ , s ,

surface power spectrum of the surface roughness correlation function, and correlation length is complicated and thus requires model inversion. Therefore, different approaches to modify the original IEM with the aim to derive a direct inversion model suitable to retrieve ϵ' directly from the backscattering coefficient have been published in the last two decades (Fung et al., 1996; Shi et al., 1997; Hsieh & Fung, 1997; Licheri et al., 2001; Baghdadi et al., 2002; Paloscia et al., 2004; Lee et al., 2007; Song et al., 2009). Baghdadi et al. (2004; 2011) developed an empirical calibration to enable a good fit between model simulations and measured radar data. Their approach consists of replacing the measured correlation length by a calibration parameter. This calibration parameter considers the true correlation length taking into account the imperfections of the IEM, and is dependent on roughness, incident angle, polarization and wavelength. Chen et al. (2000) and Wu & Chen (2004) proposed new expressions for both single and multiple scattering from rough surfaces. Comparisons with numerical simulations and laboratory measurements indicate that the original IEM was improved.

However, it should be noted that recent studies often still use the original version of the IEM for the theoretical retrieval of soil moisture and surface roughness (e.g. Bindlish & Barros, 2000; Dash & Prusty, 2007; Le Morvan et al., 2008; Paloscia et al., 2008). In this study, the original version with the empirical calibration parameters for the surface roughness correlation length as proposed by Baghdadi et al. (2004) was used.

6.1.2.1 Experimental Results

The IEM model was used to estimate m_v from the fully polarimetric PALSAR PLR image acquired over the Duerwiss test site on May 14, 2009. The model results were evaluated against in situ soil moisture values taken on the bare soil field *D01*. Altogether 108 sampling locations were distributed over the 6 ha field. Taking into account the reduced spatial resolution of the PLR image, each 25x25 m pixel is represented by three sampling locations. By this we assume that the averaged m_v value reasonably represents the according PALSAR resolution cell, rendering a pixel by pixel comparison possible. Consequently, 36 pixel values were available for the validation procedure. It should be noted that the limited observation space, with just a single roughness value of $ks = 0.6$, a single incidence angle of $\theta = 21.3^\circ$, and a small soil moisture range of $24.9 \leq m_v \leq 33.3$ Vol.-%, allows only a limited evaluation of the model performance.

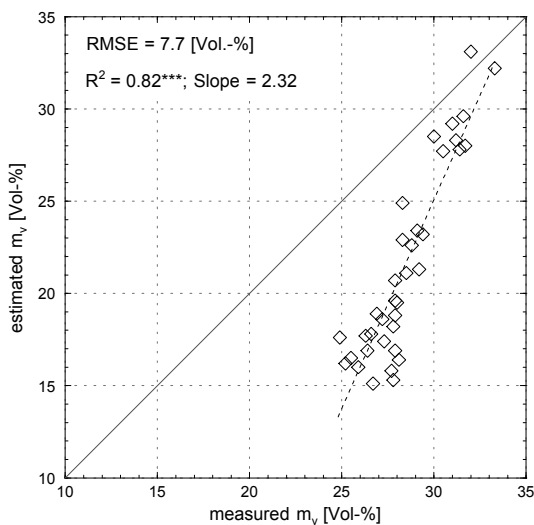


Figure 6.1: Pixel-wise comparison between estimated and measured m_v using the IEM.

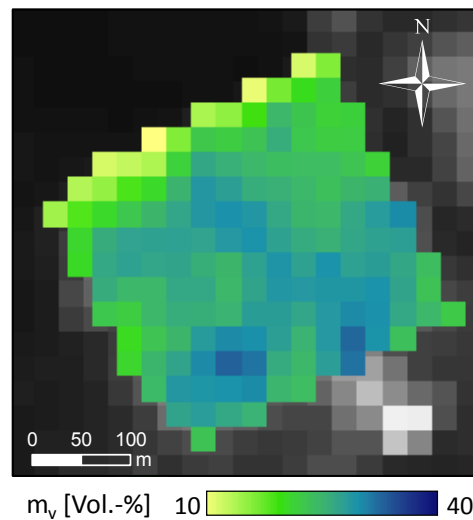


Figure 6.2: Soil moisture distribution on field D01 in the Duerwiss test site on May 14.

Fig. 6.1 shows the pixelwise comparison between modeled and measured m_v . It can be seen that the IEM significantly underestimates the water content for $m_v < 30$ Vol.-%, while the fit for $m_v > 30$ Vol.-% appears to be fairly good. As indicated by the slope of the linear fit ($a = 2.32$), this underestimation increases with decreasing m_v . It is interesting to note that the original soil moisture range is also significantly increased to $15.3 \leq m_v \leq 33.1$ Vol.-%. The RMS error taking into account all pixels is 7.7 Vol.-%. This is consistent with observations reported in the literature (Rakotoarivony et al., 1996; Boisvert et al., 1997; Bindlish & Barros, 2000; Baghdadi & Zribi, 2006). It should be mentioned that these authors also found that the error tends to increase with increasing surface roughness. This is especially the case at higher frequencies (e.g. C-band), where the surface is always considerably rougher than at lower frequencies, such as used here. Fig. 6.2 is a PALSAR image tile from the Duerwiss test site showing the surface soil moisture distribution on field *D01* as calculated with the IEM.

6.2 Semi-empirical Inversion Models

Generally speaking, semi-empirical approaches are based on theoretical scattering models and extend or modify these according to empirical observations. By this, the performance of the original model to simulate and/or interpret experimental data is increased. To establish the underlying experimental calibration relationships, a large number of experimental

measurements is required. However, such empirical relationships are often difficult to apply to sites other than those where they were developed. Moreover, they are generally valid only for specific soil conditions. This may limit their use significantly. Among the numerous semi-empirical models reported in the literature, the most popular are the two extension of the SPM, namely the ones developed by Oh et al. (1992) and Dubois et al. (1995). Both will be considered in the following.

6.2.1 The Oh Model

Oh et al. (1992; 1994; 2002) developed this semi-empirical algorithm at the University of Michigan based on theoretical models and radar measurements with a truck-mounted scatterometer operating at three frequencies, 1.5, 4.5, and 9.5 GHz. The radar data was acquired in a fully polarimetric mode with an incidence angle range from 10° to 70°. Based on the observed relationships between the scatterometer data and field measurements over a wide variety of bare soil conditions, an empirically determined function for the co- and cross-polarized backscattering ratios was proposed (Oh et al., 1992):

$$p = \frac{\sigma_{hh}^0}{\sigma_{vv}^0} = \left[1 - \left(\frac{2\theta}{\pi} \right)^{\frac{1}{3\Gamma_0}} e^{-ks} \right] \quad (6.10)$$

and

$$q = \frac{\sigma_{hv}^0}{\sigma_{vv}^0} = 0.23\sqrt{\Gamma_0}(1 - e^{-ks}) \quad (6.11)$$

where θ is the local incidence angle, ks is the electromagnetic roughness (i.e. RMS height normalized to the wavelength), Γ_0 is the Fresnel reflectance coefficient at nadir (i.e. $\theta = 0$) with

$$\Gamma_0 = \left| \frac{1 - \sqrt{\varepsilon'}}{1 + \sqrt{\varepsilon'}} \right|^2 \quad (6.12)$$

and ε' is the real part of the complex dielectric constant.

To incorporate the effect of varying incidence angles, a new expression for q was introduced (Oh et al., 1994):

$$q = 0.25\sqrt{\Gamma_0} \left(0.1 + \sin^{0.9} \theta \right) \left(1 - e^{-(1.4-1.6\Gamma_0)ks} \right) \quad (6.13)$$

Later on, the expression for p and q were further modified, and an expression for the cross-polarized backscattering coefficient was suggested (Oh et al., 2002):

$$p = 1 - \left(\frac{2\theta}{\pi} \right)^{0.35m_v - 0.65} e^{-0.4(ks)^{1.4}} \quad (6.14)$$

$$q = 0.1 \left(\frac{s}{L} + \sin 1.3\theta \right)^{1.2} \left(1 - e^{-0.9(ks)^{0.8}} \right) \quad (6.15)$$

$$\sigma_{hv}^0 = 0.11m_v^{0.7} \cos^{2.2} \theta \left(1 - e^{-0.32(ks)^{1.8}} \right) \quad (6.16)$$

Finally, taking into account the fact that the measurement of the surface roughness correlation length is not exact (cf. section 3.3) and that the ratio q is insensitive to the roughness parameter, Oh (2004) proposed a new formulation of the cross-polarized ratio which ignores the correlation length:

$$q = 0.095(0.13 + \sin 1.5\theta)^{1.4} \left(1 - e^{-1.3(ks)^{0.9}} \right) \quad (6.17)$$

In general, the Oh model allows accurate estimations of m_v within a validity range of $ks < 3$ and $9 < m_v < 31$ Vol.-% (Oh, 2006; Baghdadi & Zribi, 2006). Due to this fact the algorithm is more suitable for applications at lower frequencies like S-, L-, or P-band.

6.2.1.1 Experimental Results

The latest version of the Oh model (2004) was applied to estimate soil moisture from the fully polarimetric PALSAR image acquired over the Duerwiss test site on May 14, 2009. The modeled soil moisture values were validated against the in situ measurements taken on the bare soil field *D01*. The validation was performed following the procedure described in section 6.1.2.1. The pixel by pixel comparison yields a RMS error of 14.2 Vol.-%. This poor performance of the model is illustrated in Fig. 6.3. It can be seen that the modeled water contents are highly underestimated. This result is consistent with evaluations reported in other studies (Boisvert et al., 1997; Hajnsek, 2001; Baghdadi & Zribi, 2006), which all observed a systematical underestimation of the modeled backscattering coefficients. However, Hajnsek (2001) found that in cases with a high roughness component, the Oh model may actually strongly overestimate the soil moisture content. The soil moisture distribution map retrieved from the PALSAR PLR image for field *D01* is shown in Fig. 6.4.

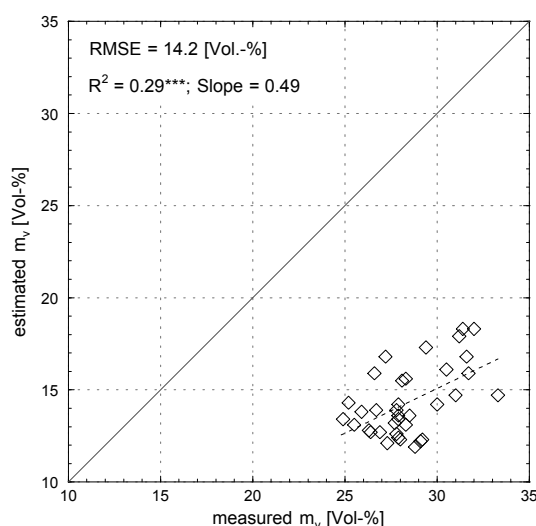


Figure 6.3: Pixel-wise comparison between estimated and measured m_v using the Oh model.

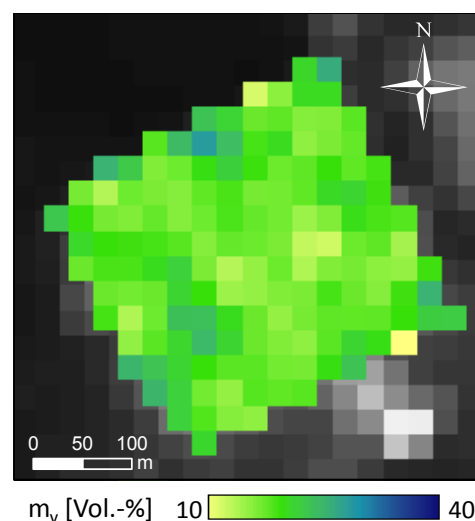


Figure 6.4: Surface soil moisture distribution on field *D01* in the Duerwiss test site on May 14, 2009.

6.2.2 The Dubois Model

The semi-empirical model developed by Dubois et al. (1995) may be considered as a simplification of the Oh model addressing only the co-polarized backscattering coefficients. The radar data used in the original study was also collected with scatterometer, while in later investigations the algorithm was widely applied to SAR data. Based on the observed relationships between scatterometer data and field measurements, the empirical co-polarized backscattering coefficients σ_{hh}^0 and σ_{vv}^0 were expressed as a function of radar parameters, i.e. the local incidence angle and frequency, and of soil parameters, such as permittivity and surface roughness. After investigating the dependency of the backscattering coefficient ratio on different moisture conditions and varying incidence angles, the roughness-induced deviations were accounted for by an empirically derived expression for the roughness term $\log(k_s \times \sin \theta)$. The following empirical expressions for the co-polarized backscattering coefficients were found:

$$\sigma_{hh}^0 = 10^{-2.75} \frac{\cos^{1.5} \theta}{\sin^5 \theta} 10^{0.028\varepsilon' \tan \theta} (k_s \times \sin \theta)^{1.4} \lambda^{0.7} \quad (6.18)$$

$$\sigma_{vv}^0 = 10^{-2.37} \frac{\cos^3 \theta}{\sin^3 \theta} 10^{0.046\varepsilon' \tan \theta} (k_s \times \sin \theta)^{1.1} \lambda^{0.7} \quad (6.19)$$

where θ is the local incidence angle, ε' is the relative dielectric constant, k_s is the normalized surface roughness, and λ is the wavelength. Hence, for known θ , Eq. (6.18) and Eq. (6.19) constitute a system of two non-linear equations with two unknowns: k_s and ε' .

Note that the backscattering coefficients of Eq. (6.18) and Eq. (6.19) decrease with increasing θ and/or with decreasing k_s . This is similar to the prediction of the SPM. On the other hand, the backscattering coefficients increase with increasing m_v . This increase is stronger in vertical than in horizontal co-polarization. The sensitivity of the model to m_v decreases with increasing LIA. Moreover, it can be seen that the empirically determined expressions condition that the $\sigma_{hh}^0 / \sigma_{vv}^0$ ratio is dependent on roughness and increases with increasing k_s . This, however, is different from the SPM, where the co-polarized term is not roughness-

dependent. The co-polarized ratio increases steadily with increasing m_v , while its sensitivity to m_v decreases with decreasing θ (Hajnsek, 2001).

Dubois et al. (1995) estimated the validity range for the surface parameters to be $m_v \leq 35$ Vol.-% and $k_s \leq 2.5$. Their accuracy is stated as 4.2 Vol.-% for the soil moisture estimates and as k_s of 0.4 for the surface roughness over bare soil. However, there are some important aspects which are not considered by the Dubois model, such as the influence of the surface correlation length on the fields, or the influence of topographic variations on the accuracy of the estimates.

Finally, it should be mentioned that the authors had several reasons to consider only the co-polarized signals in their model. First of all, the co-polarized backscattering coefficients are less sensitive to system noise and cross talk rendering the calibration of co-pol channels simpler and more accurate (Freeman, 1992). Moreover, the deployment of effective and reliable calibration algorithms for polarimetric SAR data was still under development in the early and mid 1990's (Touzi et al., 2008). And finally, the use of only two channels allows applying the model on data acquired with dual polarized radar systems, whereas the Oh model strictly requires fully polarimetric data.

6.2.2.1 Experimental Results

Following the validation procedure described in section 6.1.2.1, the soil moisture values estimated from the PALSAR image by means of the Dubois model are compared with the in situ measurements from field *D01*. It can be seen from Fig. 6.5 that, in contrast to the ones discussed above, the model significantly overestimates the soil water contents. Again this result is in agreement with other studies reported in the literature (e.g. Hajnsek, 2001; Leconte et al., 2004; Álvarez-Mozos et al., 2007; McNairn et al., 2010). Ji et al. (1996), for instance, applied the model on test fields similar to *D01* and observed a high error in the retrieved soil moisture for L- as well as C-band imagery. Wang et al. (1997) and Baghdadi & Zribi (2006) found a general overestimation of the backscattering coefficients especially in HH polarization. The soil moisture distribution for field *D01* as calculated with the Dubois model is shown in Fig. 6.6.

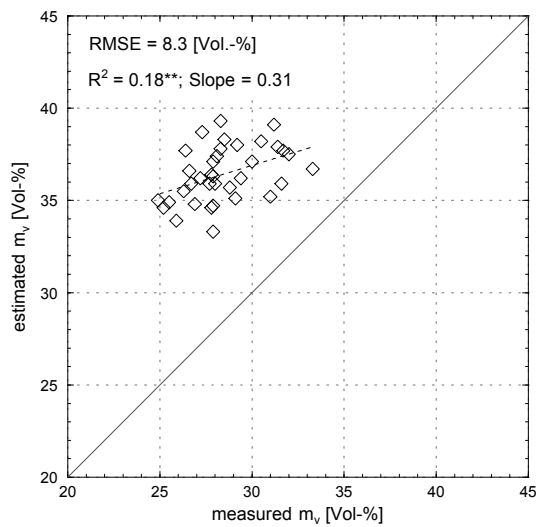


Figure 6.5: Pixel-wise comparison between estimated and measured m_v using the Dubois model.

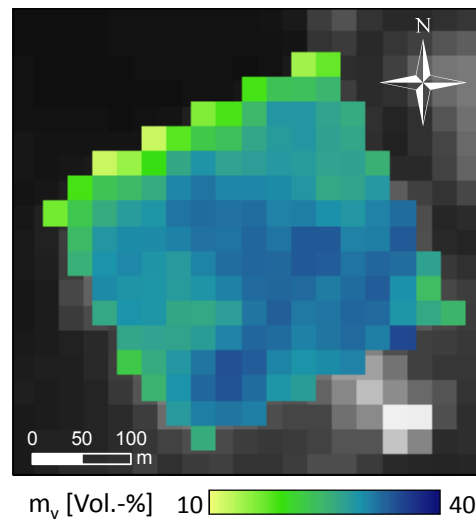


Figure 6.6: Soil moisture distribution on field D01 in the Duerwiss test site on May 14, 2009

6.3 Empirical Retrieval Models

Empirical relationships between the radar backscattering coefficient and soil moisture have been presented by numerous studies (Wang & Schmugge, 1980; Bernard et al., 1984; Cognard et al., 1995; Rakotoarivony et al., 1996; Wang et al., 1997; Deroin et al., 1997; Weimann et al., 1998; Quesney et al., 2000; Le Hégarat-Masclé et al., 2002; Zribi & Dechambre, 2003). For a bare soil surface, there exists a functional relationship between the topsoil water content and the backscattering coefficient, which, of course, also includes a roughness term (cf. section 3.4). Under these conditions, many studies have shown that either a linear or a polynomial relationship between σ^0 and m_v is a reliable approximation for a given study site, setting on the assumption that surface roughness remains constant between successive radar acquisitions. However, the coefficients of these relations may vary significantly for different studies. Hence, it is generally difficult to apply such empirical relationships in areas other than the one in which the observations were made. Apart from their simplicity, which usually allows a straightforward estimation of m_v , the greatest advantage of the fully empirical approaches is the fact that it also renders possible to establish such relations for vegetated areas. In effect, several studies reported accurate soil moisture estimations under a crop canopy by using empirical retrieval models (Taconet et al., 1996;

Rombach & Mauser, 1997; Schneider & Oppelt, 1998; Mattia et al., 2003b; Loew et al., 2006). The following section will provide a review of just such a model, as it was actually applied in this study to derive the watershed scale soil moisture distribution from single channel Envisat/ASAR data.

6.3.1 Empirical Soil Moisture Retrieval Model for Single Channel ASAR Data

The inversion approach for ENVISAT ASAR data was developed at the LMU Munich with the aim to provide soil moisture maps for mesoscale catchments in an operational manner, and was based on an antecedent empirical inversion scheme developed for C-band SAR data from the European Remote Sensing (ERS) satellite mission (Rombach & Mauser, 1997). As the given approach calculates the real part of the complex dielectric constant ε' as a function of land use, it requires a detailed land use map as well as additional soil texture information for the inversion of ε' to m_v by means of a dielectric mixture model. The ERS model has proven its applicability in different studies showing that surface soil moisture contents can be derived with an RMSE of 4-7 Vol.-%, and that it is also usable for mesoscale C-band SAR data (Schneider & Oppelt, 1998; Mauser et al., 2000; Loew et al., 2003). An advantage of this empirical retrieval approach is that it only requires very few model parameters to derive spatially distributed surface soil moisture patterns. The soil moisture retrieval model has been validated for land cover types cereals, root crops, bare soils, harvested fields, and grassland using C-band SAR data, and thus, is only valid for these land cover and frequency settings. Soil moisture is inverted in 2 steps. First, ε' is derived from the backscattering coefficient σ^0 using the empirical algorithm and ancillary land use information. The second step is the conversion of ε' to volumetric soil moisture content m_v by using a dielectric mixture model based on a soil texture map. In the present study the dielectric mixture model proposed by Hallikainen et al. (1985) is used.

The backscattering coefficient is related to the relative dielectric constant of a soil volume using empirically derived land use specific relationships as

$$\varepsilon' = a + b\sigma^0[dB] + c\sigma^0[dB]^2 \quad (6.20)$$

where a , b , and c are land use dependant model parameters as shown in Tab. 2, ε' is the real part of the complex dielectric constant, and σ^0 is the vertically co-polarized backscattering coefficient expressed in dB.

The relationship given by (6.20) is based on an extensive empirical database from two test sites in Southern Germany. Between 1992 and 1997 soil moisture was monitored with TDR-probes on 10 test fields with varying surface roughness conditions at each site. Thus, the found relationship between σ^0 and ε' can be considered to represent the mean surface roughness of a given land cover type (Davidson et al., 2000). The bare soil function of (6.20) is comparable to relationships between soil water contents and bare soil backscattering coefficients as described in other studies (Cognard et al., 1995; Quesney et al., 2000; Le Hégarat-Masclé et al., 2002).

Table 6.1: Land use dependant coefficients for the inversion of σ^0 to ε' using (6.20) and biomass correction coefficients for (6.21) at an incidence angle of 23°. (Loew et al., 2006)

Land use	Model parameters			R ²
	a	b	c	
bare soil	34.20	4.42	0.15	0.90
cereals	42.77	4.91	0.16	0.88
harvested fields	45.71	5.87	0.20	0.81
grassland	40.94	5.33	0.18	0.92
root crops	42.05	4.42	0.15	0.84
biomass correction	α	β		
meadow extensive use	0.9765	0.7278		
meadow intensive use	1.0350	0.5934		

6.3.2 Radar-Vegetation Interactions

As a first approximation, the vegetation cover causes a bias in the relationship between the dielectric constant and the backscattering coefficient (El-Rayes & Ulaby, 1987; Karam et al., 1992; Le Vine & Karam, 1996). Loew et al. (2006) point out that for vegetated areas the polynomials given by (6.20) are only valid after canopy closure. They found from the empirical field data, that the vegetation influence on the backscattering coefficient at an incidence angle of 23° saturates after this phenological stage. Since the vegetation structure (height, phenological stage, vegetation type) and water content determine the scattering mechanism of the incident electromagnetic wave, a quasi non-varying vegetation influence can only be explained by interactions of different aspects as, for instance, an increasing surface scattering compensated by increasing signal attenuation (Mattia et al., 2003b). In case of vertically structured canopies the backscattered signal is strongly influenced by the vertically oriented stems. Picard et al. (2003) as well as Brown et al. (2003) showed that the stem ground interactions become the predominant scattering term for wheat fields after canopy closure, and that it remains stable during the whole vegetation period, while the contributing part of the soil surface declines. Comparable findings were also published by Le Toan and Le Toan (1988), Ferrazzoli et al. (1992) and Cookmartin et al. (2000). It should be noted that this empirical approach substantially simplifies the physical interactions between the plane incidence waves and the vegetation canopy. Moreover, the studies mentioned above have shown that the phenological development of a plant as well as changes in incidence angle can also result in essentially different mechanisms and attenuation properties of the vegetation cover.

In contrast to the constant vegetation influence for the field crops in vertical co-polarization (VV) as described by the authors of the model, a different behavior was observed in case of grassland vegetation (Rombach & Mauser, 1997). According to Dubois et al. (1995) the significant differences in backscatter intensities observed between grassland fields with the same soil moisture content could be attributed to the varying amount of biomass. The authors propose the use of an attenuation factor Ω that is related to the dry biomass of the grassland vegetation M_{DRY} [kg/m²] as

$$\Omega = \alpha - \beta \sqrt{M_{DRY}} \quad (6.21)$$

where α and β are specific parameters, as given in Tab. 6.1, that depend on the type of grassland, since differences were also observed between intensively and extensively used grassland. However, it should be mentioned that the actual physical scattering mechanisms and attenuation properties due to interactions between above-ground biomass, thatch, and underlying mineral soil, constitutes a major problem for the estimation of soil moisture from C-band SAR under grassland vegetation (Martin et al., 1989; Saatchi et al., 1994; Wang et al., 1997).

6.3.2.1 Experimental Results

Koyama et al. (2010) evaluated the empirical soil moisture retrieval model using eight Wide Swath images acquired in 2008. As ASAR WS pixels provide an average value for a 150 x 150 m area, comparison of remote sensing and ground measurement was done on the basis of individual fields and for all available dates with ground truth data. Fig. 6.7a shows the comparison of measured and retrieved soil moisture values for all eight maps. Triangles indicate the average values measured for the different fields. According to the individual size, each field is represented by 10 - 24 measurement locations each covered by six samples. In addition, measurements taken at our continuous measuring sites are shown as circles. Since the continuous measurements represent only the given measurement location instead of an areal average, larger differences of the point measurements and the spatial mean covered by the remote sensing data may exist. Nevertheless, the measurements taken at the continuous measurement sites match the values derived from remote sensing very well. It should be mentioned that due to the small penetration capabilities of the C-band signal, a reliable ground truth is very difficult to acquire. That is, the in situ measurements using hand held probes give an average soil moisture value for the topmost 6 cm, while the skin depth of the ASAR images may actually be less than 1 cm, as discussed in section 2.2.1. Fig. 6.8 exemplarily shows the spatial surface soil moisture pattern for March 25. Areas where the land cover does not allow the calculation of m_v (e.g. built-up areas, forests, or water) remain unspecified as grey or white pixels.

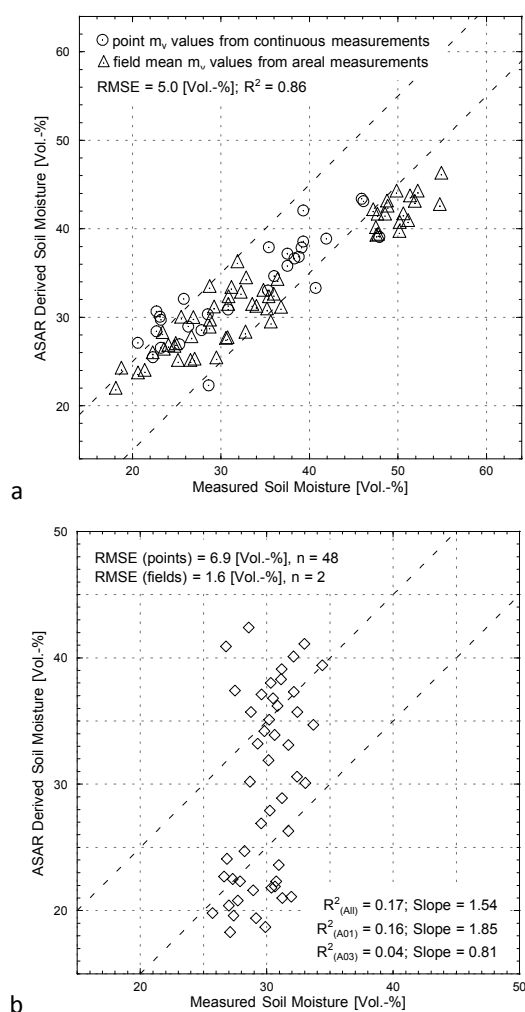


Figure 6.7: Comparison between measured and a) ASAR WS derived and b) ASAR IM derived surface soil moisture. Dashed lines indicate the ± 5 Vol.-% margins.

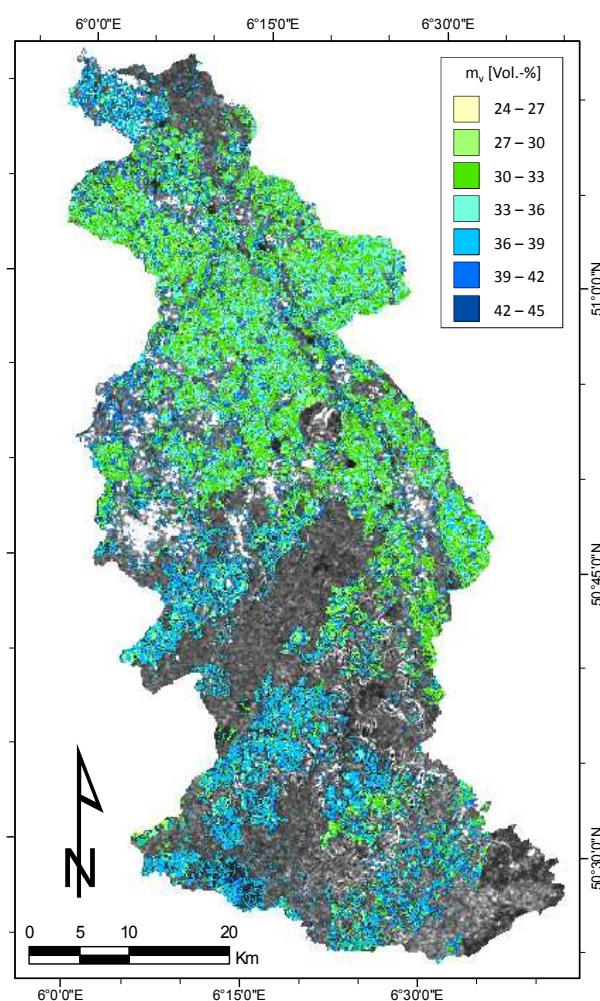


Figure 6.8: Soil moisture distribution map of the Rur catchment on 25 March 2008 as derived from ASAR WS image.

Comparison of the field average ground truth data with ASAR derived soil moisture values yields a RMSE of 5 Vol.-% (Fig. 6.7a). While field measurements and remote sensing estimates agree well in the mid and low soil moisture range, at high soil moisture states, the ASAR retrievals significantly underestimate the field measurements. Very high soil moisture values in excess of 45 Vol.-% were measured only under grassland. Here, the handheld probes integrate over the wet thatch and the mineral soil part. The thatch layer of the grass cover and the organic top soil layer provide a large storage capacity for water, which exceeds the porosity of mineral soils and thereby dominates the soil moisture measurement. The empirical inversion algorithm does not appropriately account for this effect. In addition, the

soil texture map does not reflect the large water retention characteristic of the organic top-layer of this land use - soil combination. For dry conditions, the soil moisture estimates for grassland as well as for arable land agree well with field measurements. This indicates that for dry conditions, the measured water content of the soil is mainly determined by the properties of the mineral soil, rather than the thatch layer.

Soil moisture conditions of the arable land of the loess plain are generally well represented by the ASAR estimates. Since the inversion algorithms were developed mainly for mineral soils, they perform well here. However, it should be pointed out that, even though the validation using field mean values delivers good results, a pixel by pixel comparison, as carried out for the above models, yields far less accurate results. In effect it was found, that a pixelwise evaluation for the 25x25 m ASAR Image Mode resolution cell is in the order of RMS errors of 7 Vol.-%. Fig. 6.7b shows the comparison between measured m_v and estimates derived from ASAR IM data acquired on April 29, 2008. The in situ values were taken on bare soil fields *A01* and *A03* in the Selhausen test site, each of which is represented by 24 sampling locations. It can be seen, that despite the relatively large total error, the field mean evaluation would yield a high accuracy of RMS error 1.6 Vol.-%. Thus, it can be stated that in terms of within-field variability this empirical model does not perform significantly better than the IEM, Oh, or Dubois model.

Finally, one has to be aware of different sources of uncertainty in the estimation of surface soil moistures from ASAR data which can arise from the following: (i) Image calibration errors which range between 0.5 and 1.0 dB for the ASAR products (ESA, 2007). Insufficient speckle reduction can add a stochastic component to σ^0 . Both error sources are assumed to be small, since accurate ancillary data were used and state of the art image processing was employed. (ii) Imprecise land use information and land use specific conversion, which can result in a false inversion of σ^0 to ε' . (iii) Unknown or imprecise biomass information for grassland pixels. Spatial variability in biomass results in spatial variability of the attenuation factor. We used field measurements to determine the biomass of grassland. While these measurements provide accurate data for our sample fields, they might not be accurate everywhere in the catchment. (iv) Unknown or imprecise soil texture information can result in a false conversion of ε' to volumetric soil moisture by means of dielectric mixture models.

6.4 The Need for a New L-band Model

From the foregoing sections it should have become clear that up to now no paramount model exists which allows quantitative soil moisture estimations in an operational manner anywhere at any time of the year. That is, the presence of a varying vegetation cover during the growth period and a changing surface roughness caused by land management or rainfall greatly hamper their operational application. The theoretical scattering models all have significant constraints in their validity ranges, and they commonly require a large amount of parameters which are usually very difficult to collect for larger areas. Moreover, these approaches only consider surface scattering, so that they are only suitable for bare soil surfaces or, at the best, for surfaces with a very sparse vegetation cover (Daniel et al., 2007). The semi-empirical Oh and Dubois model (Oh et al., 1992; Dubois et al., 1995) fail to cover the wide range of soil moisture and surface roughness typically found on natural surfaces. Besides, they were developed with antennas that did not have the sophisticated performance (e.g. radiometric accuracy, cross-talk, etc.) of the ones employed in current SARs and thus in general lack accuracy. For the inversion of the two major surface parameters m_v and ks , the SPM, IEM, as well as the Oh and Dubois model have to resolve two unknowns from a system of two non-linear coupled equations. The first parameter is calculated in step one and subsequently used as input to resolve the second parameter. Hence, the error of the first parameter propagates into the calculation of the other one.

The fully empirical approaches available in the literature were all developed for single channel C-band data. Hence, it is due to the limited penetration capabilities always difficult to find a meaningful relation between soil dielectric constants in depth > 1 cm, and even more difficult under a vegetation cover. Moreover, the fact that the C-band signal is always more sensitive towards surface roughness effects represents a greater source of error.

To conclude this chapter, it can be emphasized that not a single semi-empirical nor empirical L-band model exists which is capable to correct for the dynamic effects caused by surface roughness and/or vegetation. This motivates us to consider development of just such a model in the next chapter. We introduce a semi-empirical soil moisture retrieval model for dual-polarized L-band SAR data, which is not only capable of accurate quantitative soil moisture

estimations for any given surface roughness state and all possible vegetation conditions, but in addition, allows accurately deriving m_v at high spatial resolution rendering remote sensing of within-field spatial heterogeneities possible.

7. A New Semi-Empirical Soil Moisture Model for Dual Polarimetric L-band SAR Data

Despite the several promising results reported in the literature, there exists no theoretical nor (semi) empirical approach which has the potential to reliably retrieve the water content of soils over large areas with high resolution. In case of the theoretical scattering models this is partly due to the fact that they are just not true for many conditions of natural surfaces (cf. section 5.7.3 and 6.1). On the other hand the semi-empirical and empirical approaches were all developed and/or adopted using high frequency radar satellites operating at C-band which is widely recognized to be a suboptimal choice for this purpose. That is, the limited penetration capability greatly hampers a consistent investigation of relationships between soil permittivity and backscattering coefficients regardless of single, dual, or quad polarization modes (McNairn et al., 2010). However, the reason why no such model is available for L-band satellite data is simply the fact that up to the launch of ALOS PALSAR only C-band satellites were available. The only spaceborne SAR systems operating at L-band were aboard the SEASAT and JERS-1 satellites. These however, had either not the radiometric accuracy and/or not the spatial resolution to make an in-depth analysis in terms of soil moisture inversion feasible.

The development of a new semi-empirical soil moisture retrieval model in this chapter is based on correlation analysis between PALSAR observables and in situ data. First, the suitability of different empirical estimation algorithms to provide information on surface roughness and vegetation cover is assessed. The best parameter models to derive surface roughness and biomass are subsequently used to correct the co-pol backscattering coefficients in order to yield more accurate estimates of m_v . Four different land cover specific models are introduced for the land cover types bare soil, grassland, sugar beet, and winter wheat.

7.1 Dual Polarimetric ALOS PALSAR Data

An overview of all PALSAR images acquired over the study area during the investigation period is shown in Tab. 7.1. As can be seen, 13 FBD images with dual polarization (HH + HV) plus 2 PLR images with quad polarization (HH+HV+VH+VV) were available for this study. Note that not all ground based measurements were taken for each scene. This may have different reasons such as incorrect information from ESA about upcoming acquisitions, defect measurement equipment, or short-term strategy changes by JAXA. In effect, plenty more measurements campaigns were carried out on days with potential or planned PALSAR acquisitions which ultimately did not take place. These additional measurements not considered in this dissertation were used in a study on soil moisture patterns by Korres et al. (2010).

Table 7.1: PALSAR data and associated field measurements (m_v , s , and v represent measurements of soil moisture, RMS height, and vegetation parameters, respectively).

Date	Polarization	AOI	Track	m_v	s	v
2-Aug-07	HH, HV	34.3°	648	X		
17-Sep-07	HH, HV	34.3°	648	X		
4-May-08	HH, HV	34.3°	648	X	X	X
2-Jun-08	HH, HV	34.3°	647	X	X	X
19-Jun-08	HH, HV	34.3°	648			X
18-Jul-08	HH, HV	34.3°	647	X		X
12-Mar-09	HH, HV, VH, VV	21.5°	642			X
14-May-09	HH, HV, VH, VV	23.1°	643	X	X	X
22-Jun-09	HH, HV	34.3°	648			X
21-Jul-09	HH, HV	34.3°	647	X		X
5-Sep-09	HH, HV	34.3°	647		X	X
22-Sep-09	HH, HV	34.3°	648	X		X
21-Oct-09	HH, HV	34.3°	647			
10-May-10	HH, HV	34.3°	648	X		X
22-Jun-10	HH, HV	34.3°	648	X	X	X

Key for the development of a new semi-empirical soil moisture retrieval model is the Fine Beam Dual polarization mode (FBD) which employs a single transmit polarization (H) and

dual coherent reception of horizontal and vertical polarization. Note that the fully polarimetric mode (PLR) which enables full coherent scattering matrix collection by alternating H and V polarization on transmit (cf. section 4.10) was used to simulate FBD data by taking only the HH and HV scattering terms as demonstrated by Cloude et al. (2008). The preprocessing of these partial polarimetric SAR images will be addressed in the following section.

7.2 Preprocessing of Polarimetric PALSAR Data

To extract the full information contained in the partial polarimetric FBD data an advanced processing scheme was developed. As discussed earlier in this dissertation, the coherent-on-receive operation of the PALSAR sensor allows decomposing the images by means of PolSAR techniques. Hence, the processing requires not only a radiometric calibration of the horizontally and vertically polarized channels to obtain the backscattering coefficients in HH and HV polarization, but also decomposition of the scattering matrix into its eigenvectors and eigenvalues (cf. section 5.7). A simplified representation of the processing chain is shown in Fig. 7.1. The intensity images were processed using ENVI (ITT Visual Information Solutions, Boulder, USA) and the add-on module SARscape (sarmap, Purasca, Switzerland). The polarimetric processing was performed using the polarimetric SAR data processing and educational toolbox PolSARpro (Pottier et al., 2008). This software was compiled and programmed by Eric Pottier and his associates under the sponsorship of ESA and can be downloaded free of charge from the internet (<http://earth.esa.int/polsarpro>).

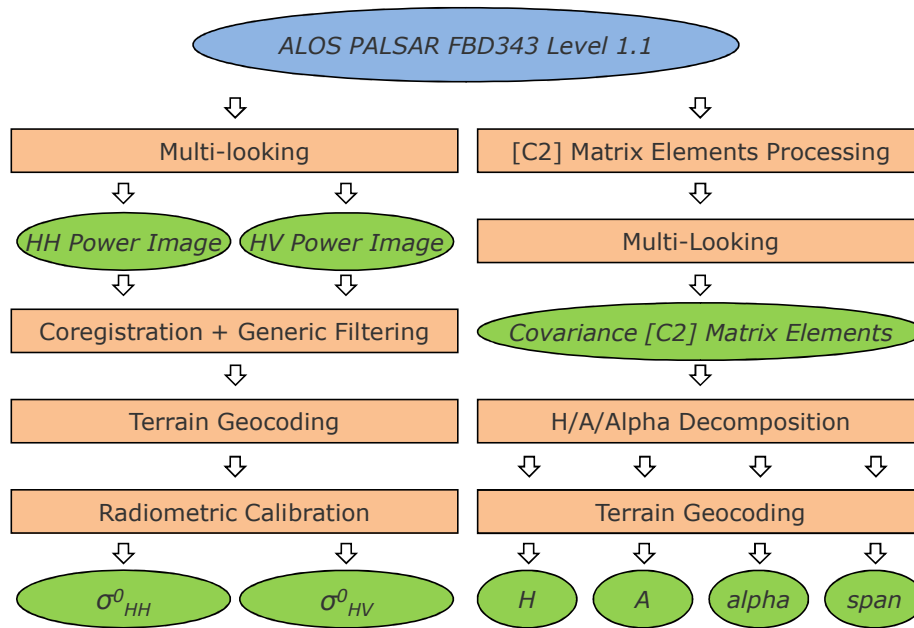


Figure 7.1: Simplified processing chain for dual polarized ALSO PALSAR data.

In principle, the radiometric calibration to sigma nought is performed according to the processing procedure for single polarized ASAR data as discussed in section 2.9.1. After header analysis of the Level 1.1 products, full resolution extraction is carried out to obtain the single look complex (SLC) images. To produce the slant range intensity image with square resolution cells, multi-looking is executed with a factor of 5:1 (Azimuth/Range). Subsequently these intermediate products are coregistered to assure fully identical geometries. Note that the images are only moderately despeckled using an adaptive Lee-filter with a box-size of 3x3 pixels. It was found that this filtering best preserves the full spatial information based on the higher geometric accuracy of ALOS PALSAR compared to Envisat -1 ASAR. Once the despeckling is conducted, the images are geocoded and radiometrically calibrated to σ^0 using the high resolution DEM of the study area (Sci Lands, 2008). For every scene this processing has to be performed individually for the co- and cross-polarized channels resulting in two separate images of σ_{hh}^0 and σ_{hv}^0 .

As discussed in detail in section 5.7, the dual polarized FBD acquisitions of ALOS PALSAR enable the exploitation of the distributed target (2x2) complex covariance matrix ([C2]) raw binary data off-diagonal elements. In order to extract the full information content of these images, the eigenvectors constructed from the [C2] matrix are used to calculate the dual-pol

target parameters entropy, anisotropy, and alpha angle by applying the $H/A/\alpha$ decomposition (Cloude & Pottier, 1996).

As the fully coherent-on-receive FBD mode of ALOS/PALSAR is not capable of reconstructing the complete (3x3) scattering matrix, the dual polarization $H/A/\alpha$ polarimetric decomposition is based on an eigenvector decomposition of the (2x2) complex Covariance [C2] matrix as shown in Eq. (7.1).

$$[C2] = \begin{bmatrix} C_{11} & C_{12} \\ C_{12}^* & C_{22} \end{bmatrix} \quad (7.1)$$

In the dual polarization case the eigenvector decomposition of a distributed target covariance matrix is performed using a simple statistical model consisting in the expansion of the (2x2) complex covariance matrix into a weighted sum of two covariance matrices as

$$\langle [C2] \rangle = \sum_{i=1}^2 \lambda_i \underline{v}_i \underline{v}_i^{T*} = \lambda_1 [C2]_1 + \lambda_2 [C2]_2 \quad (7.2)$$

where λ denotes the eigenvalues and v the eigenvectors of the covariance matrix.

After this, pseudo-probabilities of the (2x2) complex covariance [C2] matrix expansion are defined from the set of sorted eigenvalues given by

$$p_i = \frac{\lambda_i}{\sum_{j=1}^2 \lambda_j} = \frac{\lambda_i}{span} \quad \text{with } p_1 \geq p_2 \quad (7.3)$$

The distribution of the probabilities can then be fully described by two parameters. The entropy H indicates the degree of statistical disorder of the scattering phenomenon, while for high entropy values (> 0.7), a complementary parameter is necessary to fully characterize the set of probabilities. In this sense, the anisotropy A is defined as the relative importance of the secondary scattering mechanism. In the partial polarimetric case, A is equivalent and equal to the wave degree of polarization (Mott, 2007). It should be mentioned that the condition of

mutual orthogonality between the eigenvectors entails that the two polarimetric parameters sets resulting from the matrix expansion are not independent of each other.

Each unitary eigenvector \underline{v} of the (2x2) complex covariance [C2] matrix is then parameterized using the two real angular variables α and δ , as discussed in section 5.9.1 (see Fig. 5.8), with

$$\underline{v}_i = [\cos\alpha_i, \sin\alpha_i e^{j\delta_i}]^t \quad (7.4)$$

The final products of the polarimetric decomposition are four images, namely the *entropy*, *anisotropy*, *alpha angle*, and *span* image. Before they are imported into a GIS together with the calibrated backscattering products, the images are geocoded and orthorectified to obtain identical geometries. It should be pointed out that, consequently, every PALSAR resolution cell is represented by six parameters. Compare this to the single channel ASAR data with just one parameter, as discussed in section 2.9. An example of such an image set is shown in Fig. 7.2.

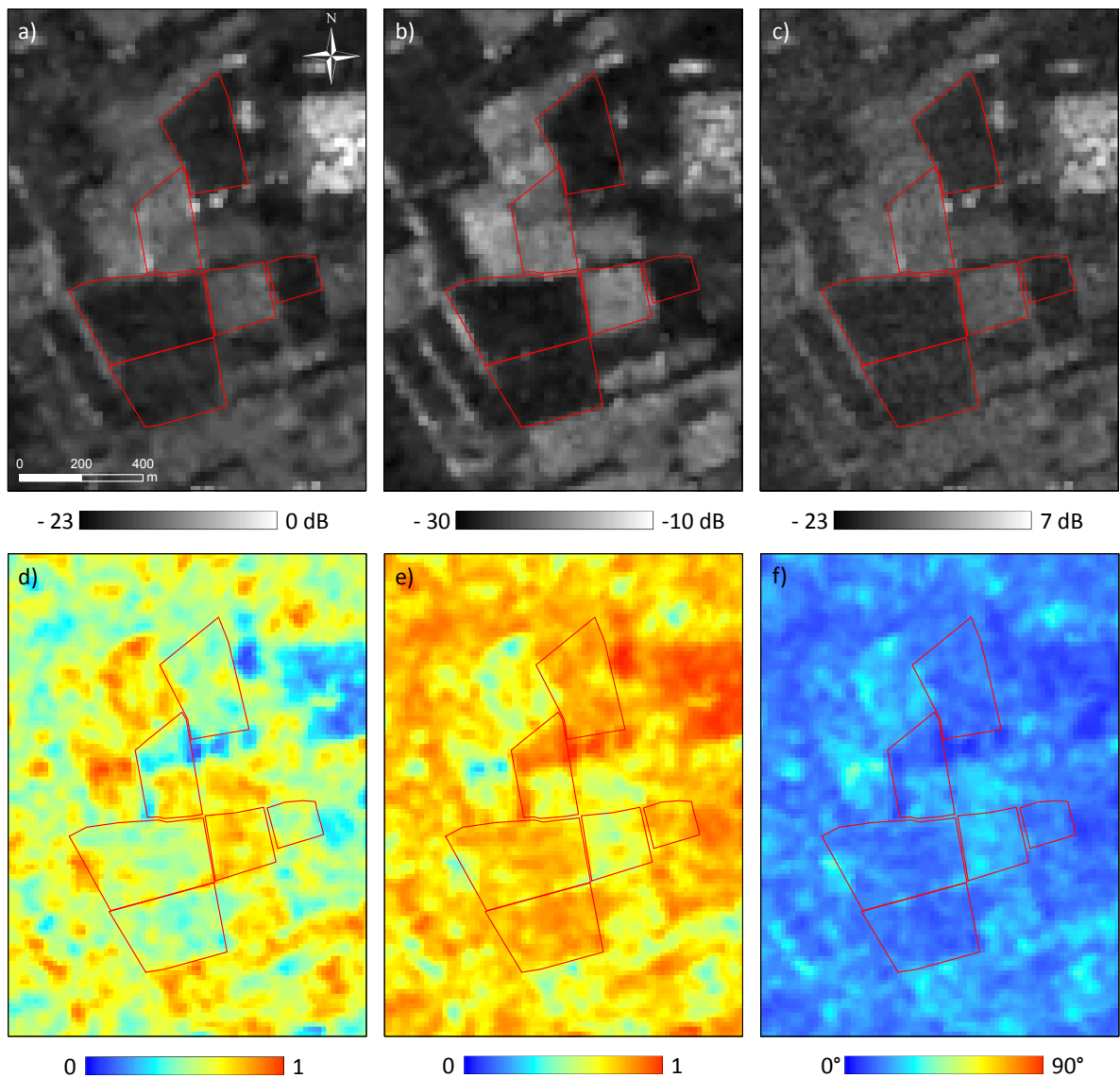


Figure 7.2: Dual polarization image set of the Selhausen area as obtained from PALSAR FBD data with a) HH, b) HV, c) span, d) entropy, e) anisotropy, and f) alpha angle.

7.2 Bare Soil Model

In chapter 6 it was discussed that the radar backscattering coefficient of bare soils is principally a function of the radar system parameters as well as of the roughness and dielectric properties of the illuminated surface. Since the system parameters are known, the inversion of m_v is a problem with two unknowns. Hence, the effect of the surface roughness needs to be accounted for to correctly estimate the permittivity of the soil. For this reason, several surface roughness measurement campaigns were conducted within the frame of this

study (cf. section 4.3.2). The measured roughness conditions at the time of satellite acquisitions allow investigating relationships between ks and the different PALSAR observables. The approach of the bare soil model is to use these relationships to estimate ks . Subsequently, these estimates are used to correct the horizontally co-polarized backscattering coefficients, to yield more accurate retrievals of m_v by taking into account the actual roughness state at the time of acquisition. We use the horizontally polarized transmit, horizontally polarized receive case (HH) because the co-polarized signal is generally more sensitive towards the dielectric properties of a surface (Ulaby et al., 1978; Ulaby et al., 1982b; Oh et al., 1992).

7.2.1 Surface Roughness Estimation

From the backscatter analysis it was found that the cross-pol ratio $\sigma_{hv}^0/\sigma_{hh}^0$ is highly sensitive towards measured ks . The comparison between the ratio [dB] and ks is shown in Fig. 7.3. It can be seen that this comparison yields a highly significant coefficient of determination of 0.94 using a polynomial regression of second order.

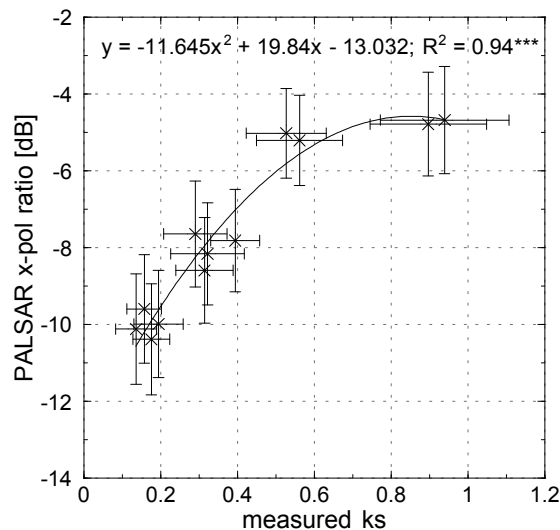


Figure 7.3: Comparison between HV/HH ratio and measured ks .

A comparable sensitivity was observed for the dual polarized anisotropy. As can be seen from Fig. 7.4, the comparison between ks and A also yields a highly significant relationship with $R^2 = 0.92$.

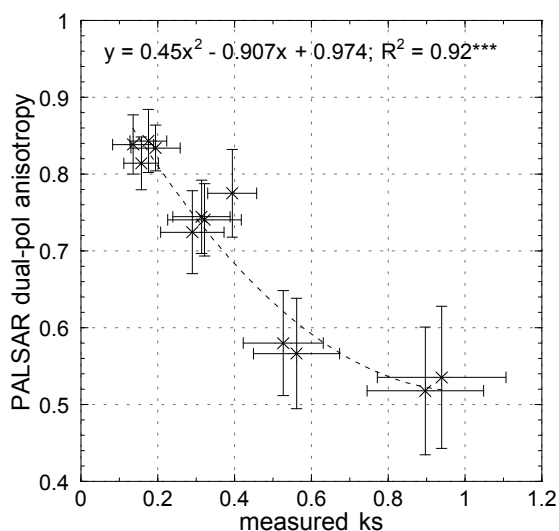


Figure 7.4: Comparison between anisotropy A and measured ks .

Based on these findings, we can invert the surface roughness directly from the FBD data using the following relationship between ks and cross-pol ratio with

$$ks = 0.0157 \times \left(\frac{\sigma_{hv}^0}{\sigma_{hh}^0} dB \right)^2 + 0.3452 \times \left(\frac{\sigma_{hv}^0}{\sigma_{hh}^0} dB \right) + 2.0634 \quad (7.5)$$

or between ks and A with

$$ks = 4.89 \times A^2 + 8.7081 \times A + 4.0563 \quad (7.6)$$

To validate the accuracy of the calculated surface roughness, the estimates are compared with measured ks values as shown in Fig 7.5. We retrieve ks from the FBD data with a RMS error of 0.11. Note that the validation data has not been used in the correlation analysis before, and thus is considered to be fully independent.

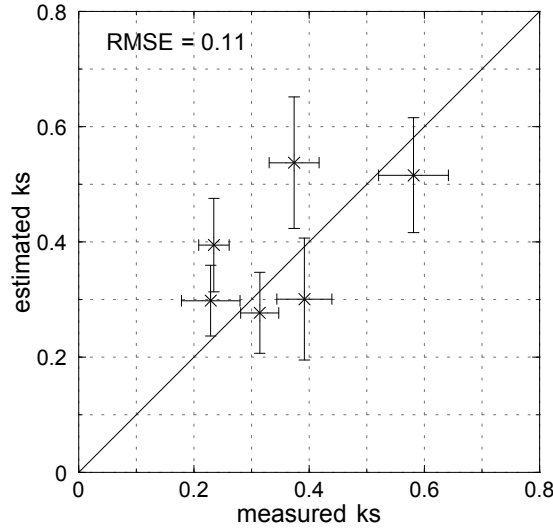


Figure 7.5: Comparison between estimated and measured ks . The bars indicate the corresponding standard deviations.

7.2.2 Soil Moisture Estimation on Bare Soil using Roughness Corrections

Having obtained information about the roughness state of the soil surface by following the above procedure, we subsequently use this roughness estimates to correct for its effect on the horizontally co-polarized backscattering coefficients. The relative dielectric constant of the soil is then derived using a simple linear relationship between σ_{hh}^0 and ε' as empirically derived from our extensive data set (Koyama & Schneider, 2010). We use the estimated surface roughness information to correct sigma nought with

$$\sigma_{hh}^0 = (\sigma_{hh}^0) \times ks^{0.3} \quad (7.7)$$

Then ε' is calculated by

$$\varepsilon' = -0.625(\sigma_{hh}^0 \text{ dB})^2 - 20.128(\sigma_{hh}^0 \text{ dB}) - 132.11 \quad (7.8)$$

Finally, ε' is inverted to soil moisture content by using the dielectric mixture model proposed by Hallikainen et al. (Hallikainen et al., 1985). The comparison between estimated and measured m_v shows that the RMS error is 4.48 Vol.-% for the backscattering coefficients

without roughness correction and 3.57 Vol.-% for the backscattering coefficients with roughness correction (Fig. 7.6). It is obvious that the estimates are distributed much closer to the zero error line after applying the roughness correction.

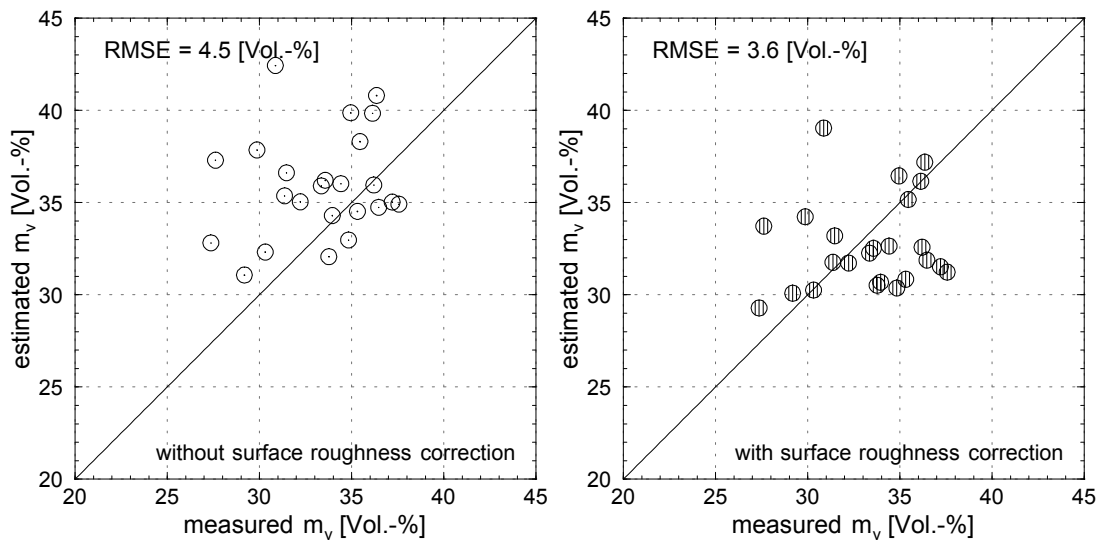


Figure 7.6: Comparison between measured and estimated m_v before (left) and after surface roughness correction (right).

7.3 Grassland Model

Grassland vegetation is one of the important land cover classes not only of the Rur catchment but of the Earth's land surface in general. However, in terms of microwave remote sensing only few studies on grassland can be found in the literature most of which concerning the retrieval of biomass (Martin et al., 1989; Saatchi et al., 1994; Hill et al., 1999; Van Der Heijden et al., 2007). The most comprehensive investigation was conducted by Stiles & Sarabandi (2000) and by Stiles et al. (2000) who tried to develop a semi-empirical scattering model using multi-frequency (L-, C-, and X-band) polarimetric scatterometer data. Even though, good estimation results were reported for above ground biomass at C-band, their highly complex approach based on the modeling of backscattering from single grass blades did not provide reliable estimates for soil moisture. It is important to note that the least significant relationship between biomass and radar backscatter was found at L-band. This is consistent with the findings from our study. In effect, the detailed investigation of the dual polarized PALSAR data interactions with ground based biomass information (amount of

fresh weight biomass, canopy height) did not show significant relationships between the L-band data and measured plant parameters. This indicates that the attenuation properties of the grassland vegetation at low radar frequencies are of minor importance compared to the interactions with the soil surface. Hence, the semi-empirical approach for quantitative soil moisture retrieval under grassland vegetation developed in this study is not based on a biomass attenuation correction. Instead, a parameter model is derived that is capable to account for the different effects of soil properties and biomass on the soil moisture estimation.

In the description of the grassland test site (section 4.2.2), the special characteristics of the thatch layer were discussed and the implications of this organic top layer in terms of radar remote sensing were treated in section 6.3.2. For wet conditions, the large storage capacity of the thatch layer dominates the dielectric properties of the surface. It can be considered, that the penetration depth of the incoming EM waves decreases with increasing ϵ' of the thatch (Saatchi et al., 1994). This effect is larger at higher frequency rendering the retrieval of soil moisture under grassland problematic. Also at L-band the backscattering contribution from the underlying soil matrix will decrease if the thatch is very wet. Moreover, it is important to understand that this feature can cause very high water contents of up to 75 Vol.-% for the skin depth at L-band. However, it should be mentioned that most studies dealing with microwave grassland interactions do not account for this very important aspect (Martin et al., 1989; Dubois et al., 1995; Chiu & Sarabandi, 1997; Hill et al., 1999; Stiles et al., 2000; Loew et al., 2006). A schematic representation of the different scattering contributions within a grassland pixel is shown in Fig. 7.7.

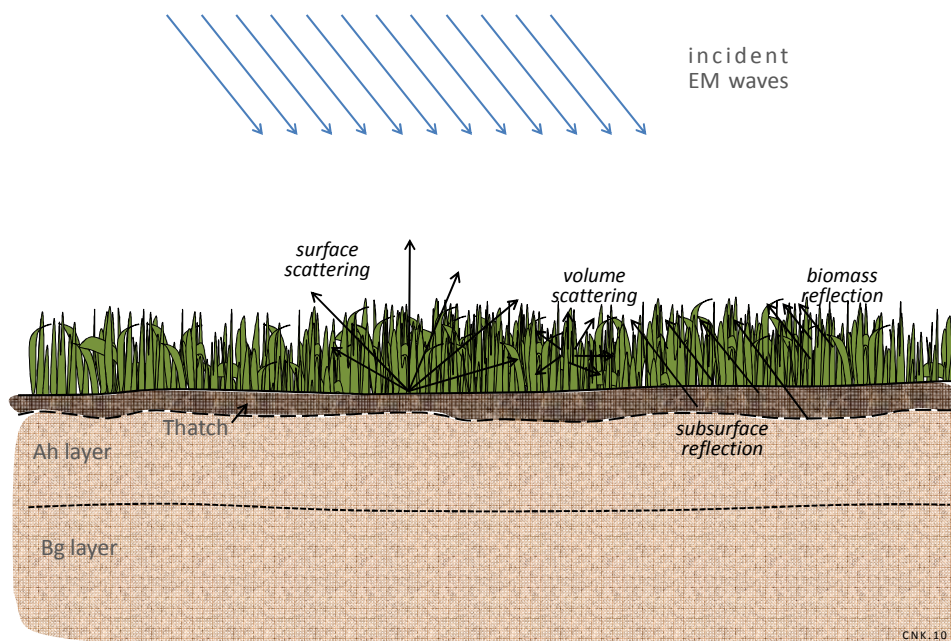


Figure 7.7: Schematic representation of the different scattering contributions occurring in a grassland pixel.

7.3.1 Soil Moisture Estimation under Grassland Vegetation

As discussed above, a biomass correction is not feasible for the retrieval of m_v under grassland vegetation. Taking into account all measured variations in the amount of biomass and water content at the soil surface (including the thatch layer), it was found that the most accurate estimates of m_v are obtained by using a dedicated grassland parameter directly in a linear regression model. The effective parameter P_{HERBA} was empirically derived from our extensive data set as

$$P_{HERBA} = \left(\frac{\sigma_{hh}^0}{H} \right)^A \times (HA)^{span} + \left(\frac{\sigma_{hv}^0}{(1-H) \times (1-A)} \right) \times \left(\frac{\sigma_{hv}^0}{\sigma_{hh}^0} \right) \quad (7.9)$$

where σ_{hh}^0 and σ_{hv}^0 are the co- and cross-polarized backscattering coefficient in DN, respectively, H is the entropy, A is the anisotropy, and $span$ is the total reflected power. Note that the parameter model also accounts for the surface roughness effect via the cross-pol ratio $\sigma_{hv}^0 / \sigma_{hh}^0$.

The comparison between P_{HERBA} and in situ ε' is shown in Fig. 7.8. The highly significant correlation with $R^2 = 0.61$ demonstrates that this parameter model is well suited to explain the soil permittivity under grassland vegetation.

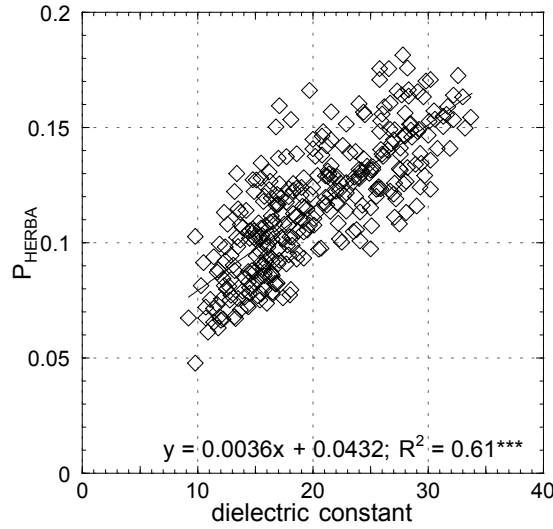


Figure 7.8: Grassland parameter model vs. measured dielectric constant.

The relationship found from the linear regression can then be used to derive ε' as

$$\varepsilon' = 169.32 \times P_{HERBA} + 0.4748 \quad (7.10)$$

After this, m_v can be calculated using the dielectric mixture model for intermediate organic soils as proposed by Topp et al. (1980). The estimated soil moisture values are validated against independent in situ measurements in Fig. 7.9. The number of validation pixels taken from different dates to cover all possible moisture and vegetation conditions is as large as 80. The proposed soil moisture retrieval model allows estimating m_v with a RMS error of 4.1 Vol.-%. It should be pointed out that the validation data represents a (above ground) biomass range from 0.6 – 2.2 kg/m². This demonstrates the large validity range of the model in regard to surface soil moisture as well as to vegetation conditions.

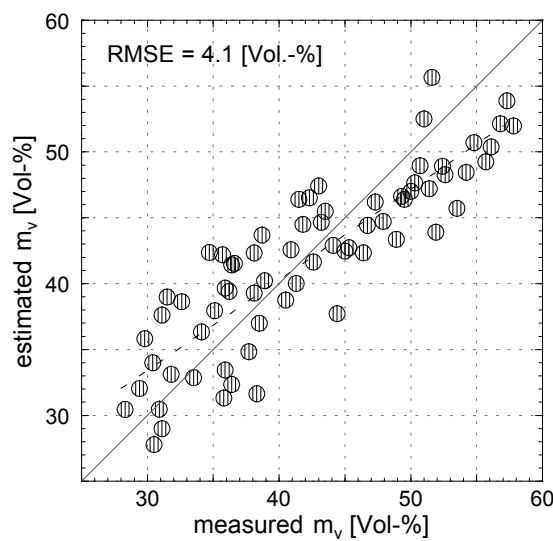


Figure 7.9: Comparison between measured and estimated m_v for grassland pixels on various dates.

7.4 Sugar Beet Model

Sugar beet constitutes one of the most important cash crops in the study area. In 2009, it was cultivated on 364 000 ha in Germany, representing 3% of the entire arable land (Wirtschaftliche Vereinigung Zucker, 2010). Due to the favorable soil conditions of the fertile loess plain the percentage of area under sugar beet is with 6.8% somewhat larger within the Rur catchment.

As mentioned before, sugar beet parameters were monitored on the sampling fields by harvesting 3 to 5 plants at different locations. We assume that the means of the harvested plants at any location represent the mean for the area of the corresponding PALSAR pixel. In regard to interactions with incident EM waves, sugar beet as root crop constitutes a special case compared to other crops (e.g. maize, winter wheat, rape seed, soy beans). Since most of the biomass (and water) is below ground, the above ground vegetation is of minor importance when it comes to the attenuation properties at L-band (Ulaby & Jedlicka, 1984). Indeed, as observed from the field measurements, on sugar beet fields the crops within the soil can easily hold up to 20 kg/m² of water modulating not only the waves while passing through the canopy, but changing the dielectric constant of the illuminated soil column itself. The dielectric constant of the crops is typically about 60 (Konstantinovic et al., 2008), while the surrounding soil matrix reaches a maximum of about $\epsilon' \approx 25$ at saturation. The different scattering contributions occurring on such a sugar beet pixel are illustrated in Fig. 7.10. As

can be seen, the backscattering is still influenced by surface roughness through the surface scattering term. However, it can be assumed that surface scattering is of minor importance compared to the contributions from volume scattering, sub-surface and fruits. Moreover, a measurement of ks is generally not feasible on vegetated fields. On the other hand, the overall roughness of a sugar beet field is mainly induced by the crops sticking out of the soil matrix. Hence, the surface roughness effect is neglected in the retrieval process.

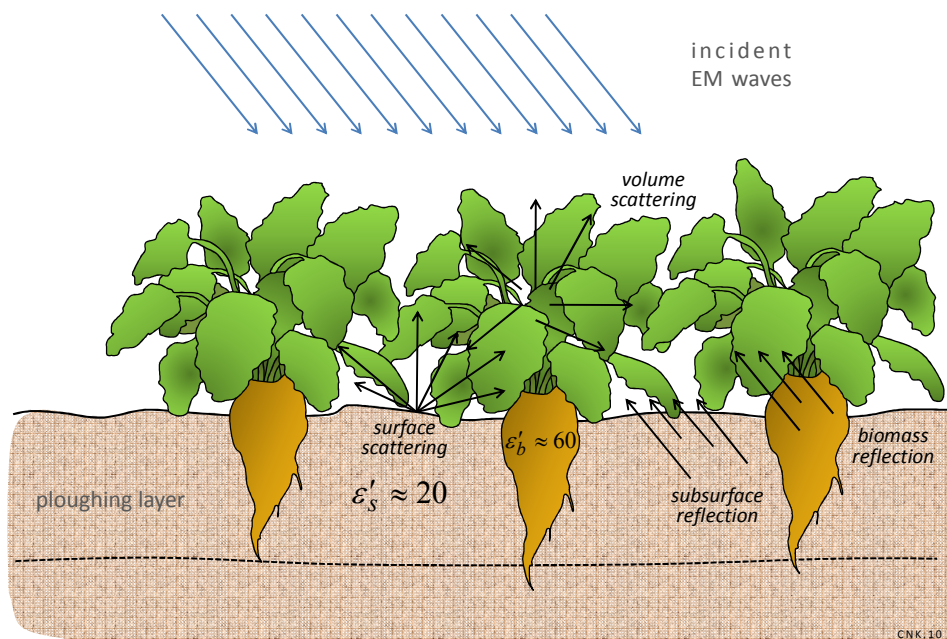


Figure 7.10: Schematic representation of the different scattering contributions occurring in a sugar beet pixel.

7.4.1 Sugar Beet Biomass Estimation

To estimate the amount of biomass within a PALSAR pixel needed to correct the corresponding attenuation of the backscattering coefficients, we developed a dedicated sugar beet biomass parameter capable to account for the different scattering effects discussed above. Based on comprehensive sensitivity analysis for all available observables, it was found that the PALSAR signal is most sensitive towards the total fresh weight biomass, while other plant parameters like LAI, phenology stage, or canopy height did not yield significant correlations. The effective parameter M_{Beta} was empirically derived from our dataset with:

$$M_{BETA} = \sqrt{\frac{|\sigma_{hv}^0|^2}{span}} \times \bar{\alpha} \quad (7.11)$$

where σ_{hv}^0 is the cross-polarized backscattering coefficient in DN, $span$ is the total reflected power, and $\bar{\alpha}$ is the dual polarimetric alpha angel.

As shown in Fig. 7.11, the correlation analysis between M_{Beta} and the sum of in situ fresh weight above and below ground biomass ($FW_{a.g.}+FW_{b.g.}$) yields a highly significant coefficient of determination of 0.64.

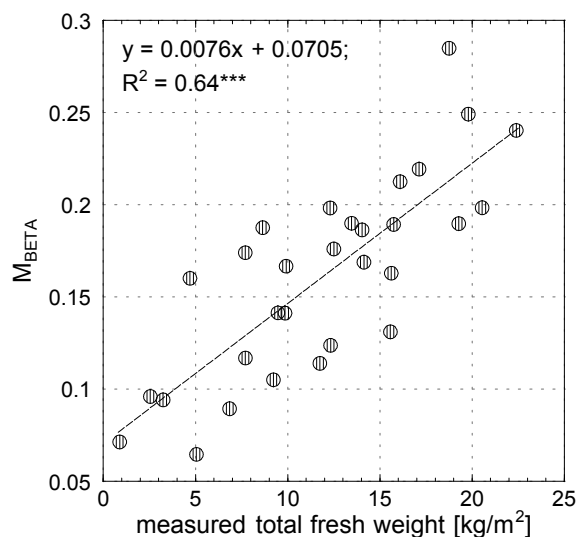


Figure 7.11: Comparison between effective biomass parameter M_{BETA} and measured total fresh weight of sugar beet biomass.

This highly significant correlation between in situ total fresh weight and M_{BETA} demonstrates the potential of the introduced parameter. Using the relationship found from the correlation analysis between polarimetric PALSAR parameter M_{BETA} and in situ sugar beet biomass, we can estimate above and below ground fresh weight of the crops with

$$FW_{a.g.+b.g.} = 83.747M_{BETA} - 1.599 \quad (7.12)$$

A comparison between measured and estimated total fresh weight yields an RMS error of 2.7 kg/m² as can be seen in Fig. 7.12. It can be noted that the biomass estimates are well aligned along the zero error line.

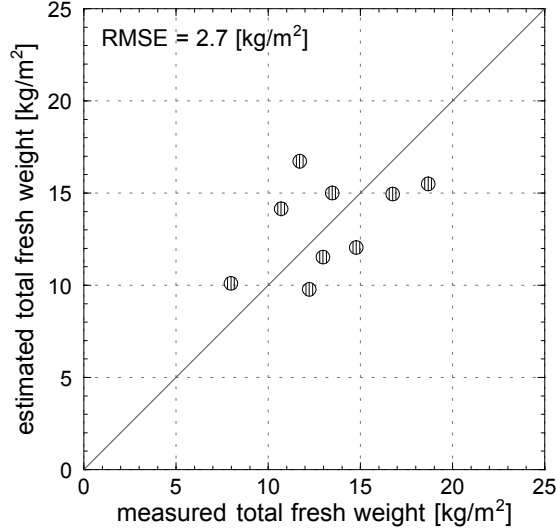


Figure 7.12: Estimated vs. measured total fresh weight of sugar beet biomass.

7.4.2 Soil Moisture Estimation using Sugar Beet Biomass Corrections

Finally, we use the estimates of sugar beet biomass to correct for their disturbing effects on the PALSAR backscattering coefficient. The dielectric constant estimation is carried out using an empirically derived second order polynomial relationship between ε' and the horizontally co-polarized signal. The retrieved biomass information is used to correct σ_{hh}^0 with

$$\sigma_{hh}^{0'} = (\sigma_{hh}^0) \times \sqrt{\frac{\sigma_{hh}^0}{0.5 \times FW_{total}}} \quad (7.13)$$

where σ_{hh}^0 is the co-polarized backscattering coefficient in DN and FW_{total} is the sum of above and below ground fresh weight biomass.

Then ε' is calculated with:

$$\varepsilon' = -0.064(\sigma_{hh}^0 [dB])^2 + 0.375(\sigma_{hh}^0 [dB]) + 23.528 \quad (7.14)$$

After applying this biomass correction, the comparison between estimated and measured m_v yields a RMS error of only 4.2 Vol.-% for the sugar beet pixels (Fig. 7.10). Without the correction procedure the estimation error applying Eq. (7.14) varied between 7.8 and 16.6 Vol.-%, depending on the amount of biomass at the time of image acquisition. It can be seen that the estimates are aligned fairly well along the zero error line ($b = 0.82$). Although the amount of pixels available for the validation is limited to 46, the comparison shows a highly significant coefficient of determination ($R^2 = 0.61^{***}$) indicating that the algorithm has potential to cover the within-field spatial heterogeneity of sugar beet biomass.

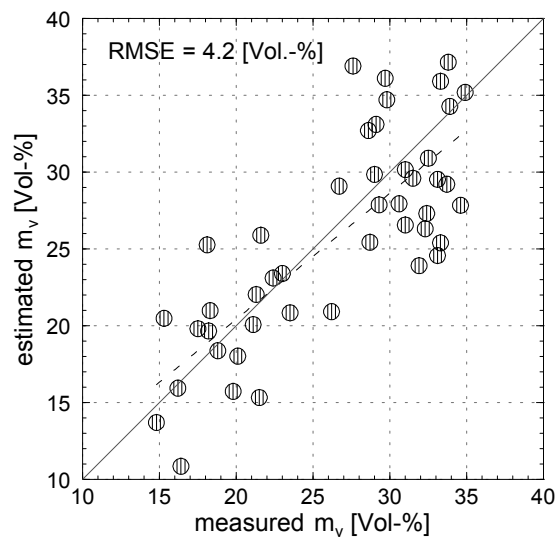


Figure 7.13: Estimated versus measured soil moisture for sugar beet pixels on various dates.

7.5 Winter Wheat Model

In terms of cultivated area and production, winter wheat constitutes by far the most important land cover type within the study area. Usually > 60% of the entire arable land is used for its production. With respect to microwave remote sensing, winter wheat may be considered as the best studied vegetation type. A variety of studies dealing with winter wheat microwave interaction at high radar frequencies (C- and X-band) can be found in the literature (Attema & Ulaby, 1978; Lin-Kun et al., 1985; Cognard et al., 1995; Taconet et al., 1996; Cookmartin et al., 2000; Marliani et al., 2002; Picard et al., 2003; Brown et al., 2003; Mattia et al., 2003b). The effect of a wheat canopy on the backscattering behavior of arable fields at C-band was discussed in detail section 7.x. However, the attenuation properties of wheat canopies at L-band have been addressed by only few studies (Ulaby & Jedlicka, 1984; Dabrowska-Zielinska et al., 2007; Hajnsek et al., 2009; Lievens & Verhoest, 2011).

Despite the fact that some author's consider LAI as the primary parameter to be correlated with attenuation and scattering behavior (Prevot et al., 1993; Brown et al., 2003) we could not find a significant relationship from our data set. Dabrowska-Zielinska et al. (Dabrowska-Zielinska et al., 2007) related the leaf water area index (LWAI) with canopy backscatter. The LWAI is the product of the LAI with the vegetation water expressed as the ratio of the difference between the fresh and dry biomass. However, this parameter also did not show meaningful relations in this study. The only vegetation parameter that allowed a significant correlation with the PALSAR observables is the fresh weight of above ground biomass. It should be mentioned that this is consistent with studies attributing the magnitude of attenuation mainly to the dielectric properties of a canopy at frequencies below 1.5 GHz (Ulaby et al., 1981a; Ulaby & Jedlicka, 1984; Senior et al., 1987; El-Rayes & Ulaby, 1987).

7.5.1 Winter Wheat Biomass Estimation

As discussed above, we relate the amount of above ground fresh weight biomass ($FW_{a.g.}$) to the dual polarimetric SAR observables. Various parameter models were tested to find the one with highest explanatory content. Based on this investigation we empirically derived the effective parameter M_{TRITI} as

$$M_{TRITI} = \sqrt{\frac{\sigma_{hh}^0 \times \sigma_{hv}^0}{H}} \quad (7.15)$$

where σ_{hh}^0 and σ_{hv}^0 are the co- and cross-polarized backscattering coefficient in DN, respectively, and H is the entropy.

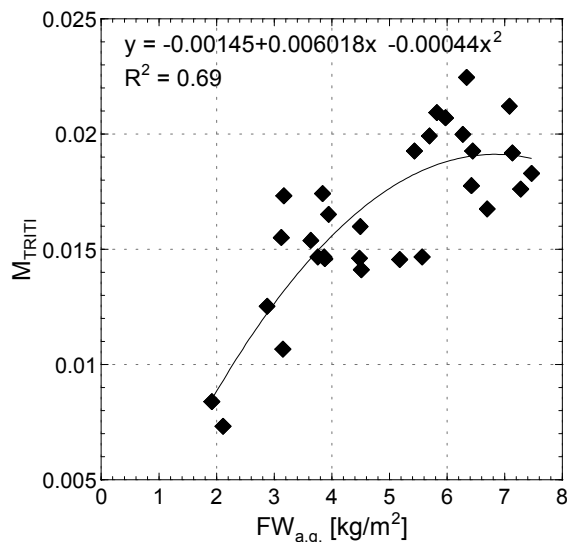


Figure 7.14: Winter wheat biomass parameter model vs. above ground fresh weight.

The comparison between above ground fresh weight of winter wheat biomass [kg/m^2] and M_{TRITI} ($R^2=0.62$) is shown in Fig. 7.11. The second order polynomial regression model found from this relationship may then be used to invert $FW_{a.g.}$ with

$$FW_{a.g.} = 6746.4 \times (M_{TRITI})^2 + 153.81 \times M_{TRITI} + 0.329 \quad (7.16)$$

The estimates of above ground biomass [kg/m^2] as derived from the dual polarized SAR data yield an accuracy of $0.8 kg/m^2$ (RMSE) using the relationship (7.16) The comparison between $FW_{a.g.}$ estimates and independent in situ values is shown in Fig. 7.12.

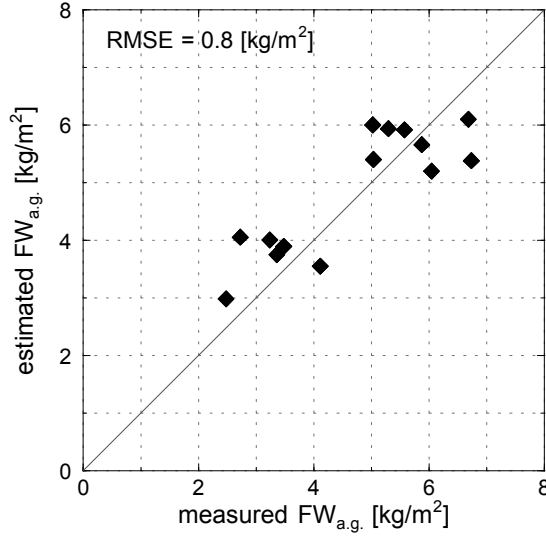


Figure 7.15: Estimated vs. measured above ground fresh weight winter wheat biomass.

7.5.2 Soil Moisture Estimation using Winter Wheat Biomass Corrections

The good quality of the biomass estimates allows correcting for the attenuation properties of the winter wheat canopy according to the procedure used in the sugar beet model. After this, the dielectric constant estimation can be performed using an empirically derived second order polynomial regression model for ε' as a function of the horizontally co-polarized backscattering coefficient. The retrieved biomass information is used to correct σ_{hh}^0 with

$$\sigma_{hh}^0{}' = (\sigma_{hh}^0) \times \sqrt{\frac{\sigma_{hh}^0}{0.7 \times FW_{a.g.}}} \quad (7.17)$$

where σ_{hh}^0 is the co-polarized backscattering coefficient in DN and $FW_{a.g.}$ is the above ground fresh weight biomass.

Then ε' is derived with:

$$\varepsilon' = -0.416(\sigma_{hh}^0{}' dB)^2 - 10.137(\sigma_{hh}^0{}' dB) - 45.829 \quad (7.18)$$

After applying this biomass correction, the comparison between estimated and measured m_v yields a RMS error of only 3.9 Vol.-% for the winter wheat pixels (Fig. 7.16). Before the backscattering correction, the estimation error ranged from 4.3 to 8.9 Vol.-%, depending on the amount of biomass at the time of image acquisition. As can be seen in Fig. 7.16 the estimates are aligned fairly well along the zero error line ($b = 0.78$). Despite the limited amount of pixels ($n = 44$) available for the validation, the comparison yields a highly significant coefficient of determination ($R^2 = 0.53^{***}$). Again, this indicates that the proposed retrieval algorithm has potential to cover the within-field spatial heterogeneity of winter wheat biomass. It should be noted that the amount of biomass for the validation pixels ranged from 2.6 to 7.1 [kg/m²]. Hence, the proposed algorithm might not be valid for biomass conditions below this range.

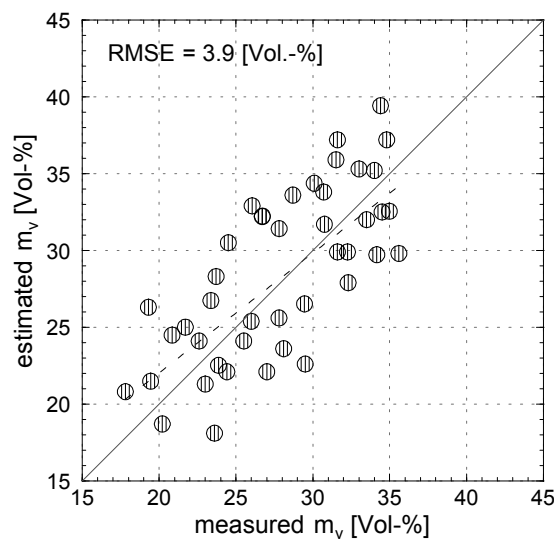


Figure 7.16: Comparison between estimated and measured m_v for winter wheat pixels.

7.6 PALSAR Soil Moisture Maps

The four different models introduced in the foregoing sections can then be used to calculate surface soil moisture distribution maps from the dual polarization ALOS PALSAR data. Fig. 7.17 shows two derived soil moisture patterns in the arable land test site Selhausen. The first map shows the spatial surface soil moisture distribution for the sampling fields on June 22, 2009. Two different retrieval algorithms were used: for the sugar beet fields (A04 and A11) m_v was calculated using the sugar beet model with Eq. (7.11) – (7.14), while for the winter wheat fields (A01, A03, A09, and A10) the winter wheat model with Eq. (7.15) – (7.18) was used to derive m_v . It can be seen that the fields are all fairly wet. However, the surface of the southern winter wheat fields is somewhat wetter than the neighboring one. The second map shows the soil moisture pattern for September 5, 2009. As can be seen, the soil surfaces on most fields are significantly dryer on that day. Especially the bare soil fields (A01, A03, A09, and A10), as calculated using the bare soil model with Eq. (7.5), (7.7), and (7.8), show a rather dry surface state, while the values of m_v for the surfaces of the sugar beet fields (A04 and A11) are still somewhat higher. Note that this observation is consistent with the in situ measurements, as discussed in section 4.3.

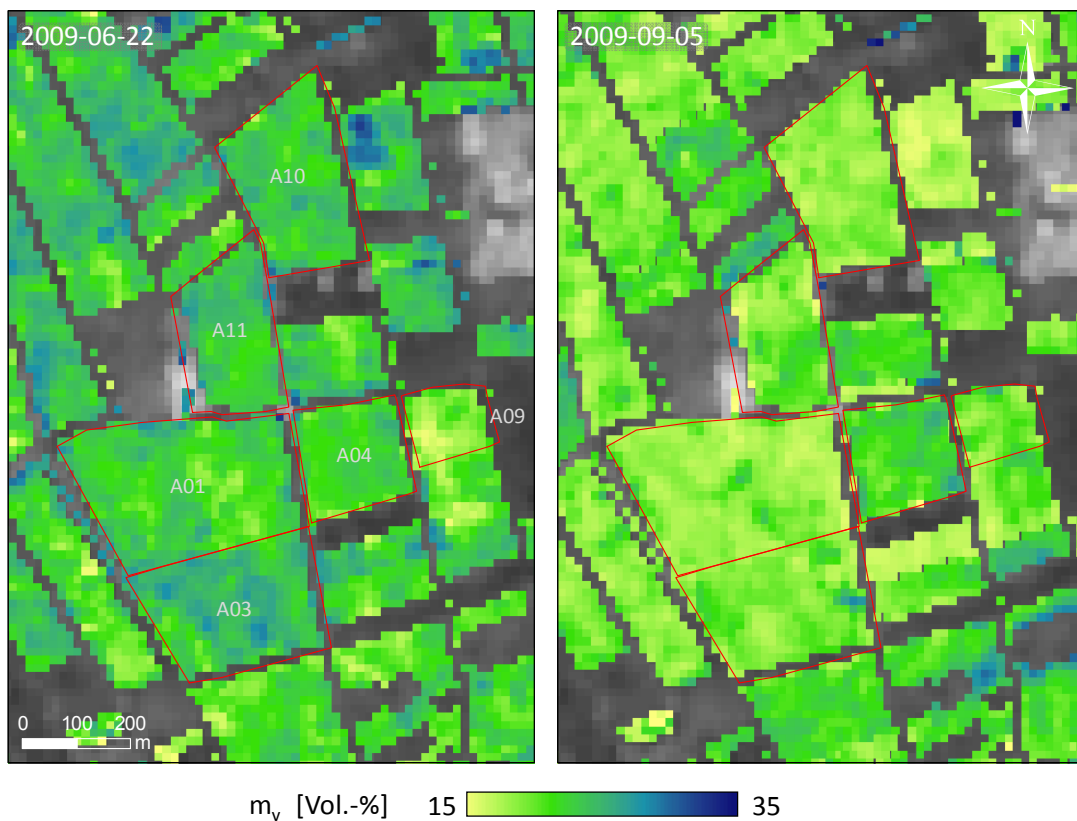


Figure 7.17: PALSAR derived surface soil moisture patterns for the Selhausen sampling fields on June 22 (left) and September 5, 2009 (right).

Application of the grassland model is demonstrated in Fig. 7.18. The two maps show the spatial distribution of surface soil moisture for the grassland test site Rollesbroich on July 18, 2008 and July 21, 2009. The moisture patterns were derived using Eq. (7.9) and (7.10) as discussed in section 7.3. It can be seen that, although the site-average moisture states are fairly comparable, both patterns differ from each other substantially. It should be noted that pixels with trees do not allow calculating m_v by means of the grassland model, and thus were masked out from the maps.

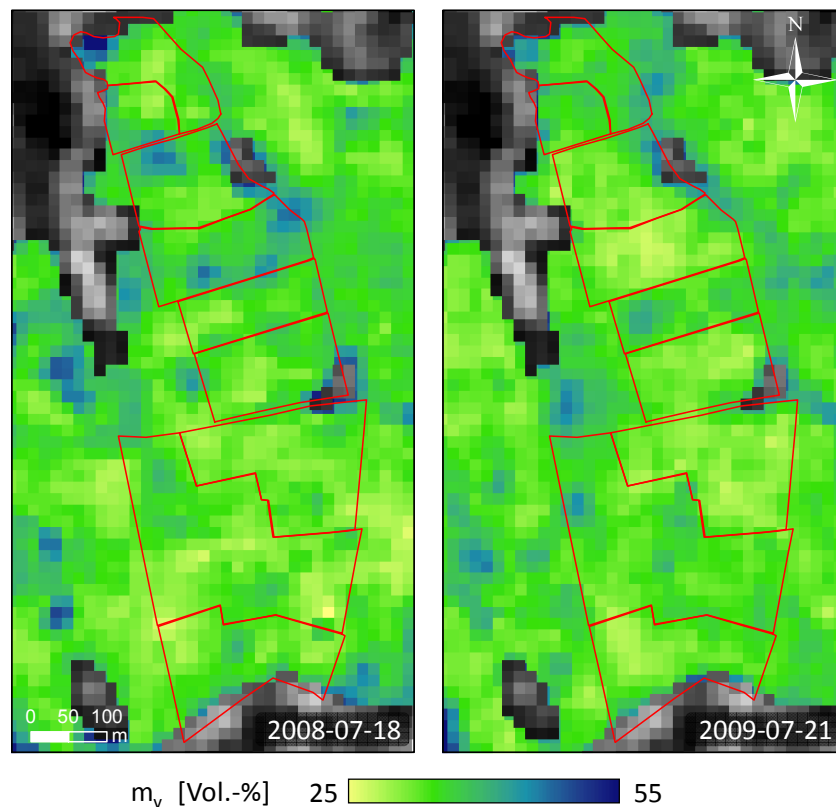


Figure 7.18: PALSAR derived surface soil moisture patterns for the grassland test site Rollesbroich on July 18, 2008 (left) and July 21, 2009 (right).

Fig. 7.19 finally shows a PALSAR derived soil moisture map of the entire Rur catchment. The map represents the spatial distribution of surface soil moisture for the land cover types bare soil, grassland, sugar beet, and winter wheat on June 22, 2009. It can be seen that the large scale spatial moisture pattern follows the major landscape units in the catchment. Hence, we can clearly distinguish the wet grassland in the low mountain range area from the relatively dryer agricultural area of the fertile loess plain (cf. section 4.1). While most parts of the “Eifel” area show a soil moisture range from 35 – 50 Vol.-%, the northern part exhibits basically a range between 20 and 35 Vol.-%. However, some dryer and/or wetter areas can be found in both parts. Worth mentioning is the feature of the wet floodplains along the courses of the rivers (cf. Fig. 4.1). These areas predominantly characterized by grassland cover are significantly wetter than the surrounding arable fields. Finally, it is important to note that the classification of the PALSAR pixels into the different land cover types is performed on the basis of a classical land use classification derived from optical satellite imagery. Thus care has to be taken in areas where the land surface is not classified correctly resulting in a false estimation of m_v .

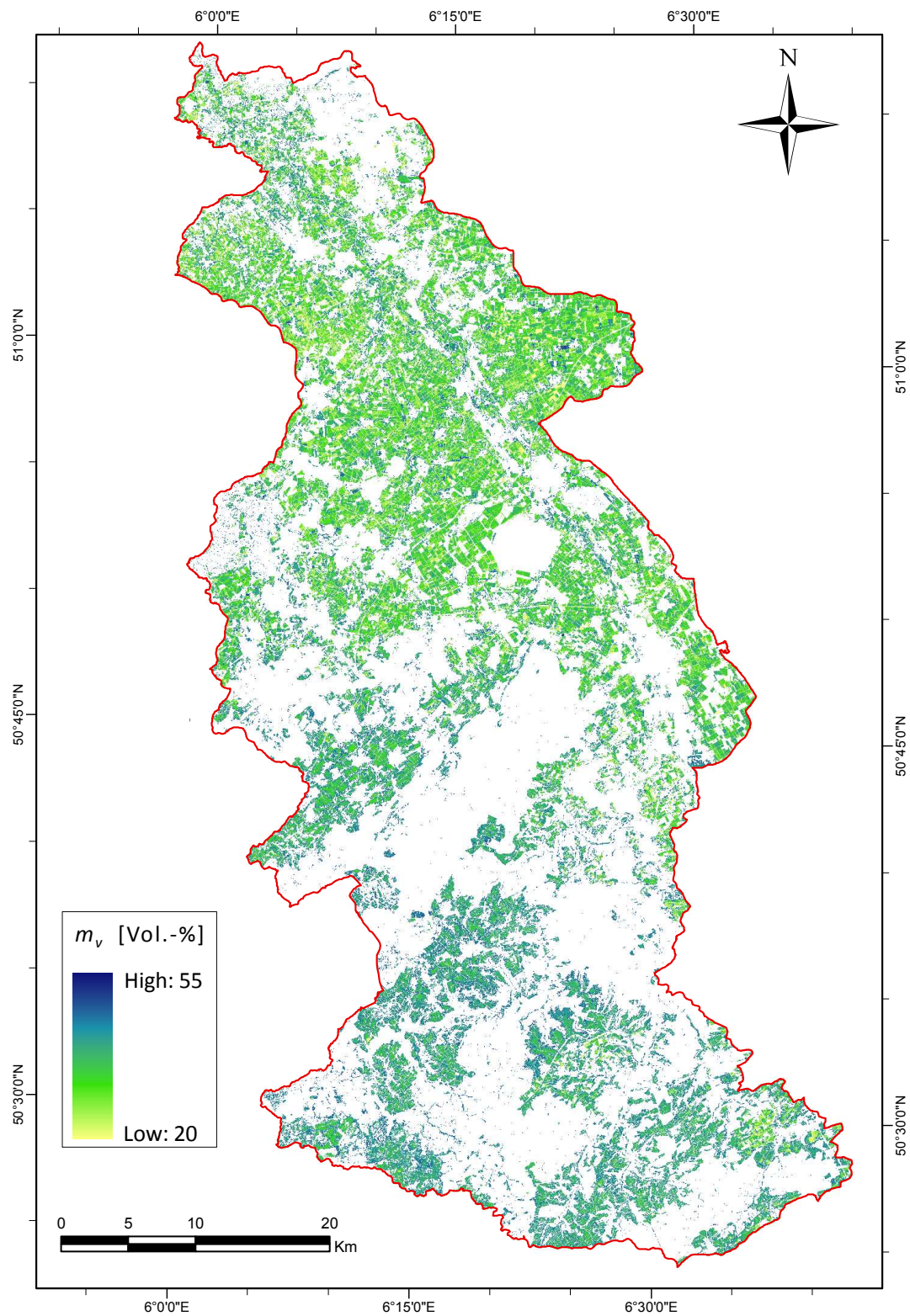


Figure 7.19: PALSAR derived surface soil moisture distribution in the Rur catchment on June 22, 2009.

8. Variability of Surface Soil Moisture

In this chapter we analyze the spatial variability of the surface soil moisture at different spatial scales based upon field measurements and remote sensing estimates. Surface soil moisture patterns derived from multitemporal ENVISAT ASAR data by means of an empirical C-band retrieval algorithm, as discussed in section 6.3.1, are used. Eight Wide Swath (WS) images with a spatial resolution of 150 m acquired between February and October 2008 are used to determine surface soil moisture contents. The accuracy of the surface soil moisture retrievals was evaluated by comparison with in situ measurements. This comparison yielded a root mean square error of 5 Vol.-%.

Based upon in situ measurements as well as remote sensing results, the relationship of the coefficient of variation of the spatial soil moisture patterns and mean soil moisture is analyzed on different spatial scales ranging from catchment scale to the field scale. The results show that the coefficient of variation decreases at all scales with increasing soil moisture. However, the gain of this relationship decreases with scale, indicating that at a given soil moisture state, the spatial variations at the large scale of whole catchments is larger than on the field scale. Knowledge of the spatial variability of the surface soil moisture is important to better understand energy exchange processes and water fluxes at the land surface as well as their scaling properties.

8.1 Soil Moisture Patterns

A key issue with regards to soil moisture is to understand the spatial patterns at different scales, the scaling behavior, as well as the processes which lead to spatial patterns. Several studies have investigated the spatial variability of soil moisture based upon remotely sensed as well as ground based measurements. Reynolds (1970c) classified the controls into static (e.g. topography, soil texture) or dynamic (e.g. rainfall and varying vegetation cover) parameters. Based upon theoretical considerations for any given soil texture, a relationship between the spatial variance of soil moisture and the average moisture value can be assumed

that should result in a reduction of variance at low, as well as at high soil moisture values, since the lower boundary of the wilting point and the upper boundary of soil saturation provides physical limits to soil moisture variations. The lower boundary of the wilting point and the upper boundary of the soil saturation provides the physical limits for variations in water contents for a given soil texture. Thus, one can assume that the relationship between the spatial variance of soil moisture and the average moisture content shows a decrease in variance at low, as well as at high soil moisture values. Measurements provided by Famiglietti et al. (1998), for instance, support this assumption. They monitored time series of soil moisture along a 200 m hill slope transect and found that the magnitude of the spatial variability across the transect decreases with decreasing mean moisture values. Owe et al. (1982), as well as Albertson and Montaldo (2003) found the trend of variability to depend on the mean soil moisture state. Comparable findings were also published by other groups (e.g. Bell et al., 1980; Western & Grayson, 1998; Choi & Jacobs, 2007). Nevertheless, studies with contradictory observations can be found. Hawley et al. (1983) as well as Charpentier and Groffman (1992) did not find a relationship between mean soil moisture and soil moisture variability. Other authors found an increasing moisture variability with decreasing mean soil moisture (e.g. Famiglietti et al., 1999; Hupet & Vanclooster, 2002; Oldak et al., 2002). These observations indicate that in a complex landscape, the spatial variability is a result of the interactions of many different parameters and processes. Moreover, observations have been made, showing that the dependency of the soil moisture variability upon the mean soil moisture varies with spatial scale (Rodriguez-Iturbe et al., 1995; Crow & Wood, 1999). Teuling and Troch (2005) showed that both soil and vegetation controls can cause either the creation or destruction of spatial variance. Vereecken et al. (2007) conducted a re-examination of recent experimental work (e.g. Choi & Jacobs, 2007; Choi et al., 2007) showing that the spatial variance increases when drying occurs from a very wet state. Spatial variability peaks at a moisture value in the mid range between maximum and minimum values, and decreases accordingly with further drying.

The primary aim of this chapter is to analyze the spatial variability of surface soil moisture based upon remote sensing and field measurements at different spatial scales. To this end, we derive a time series of surface soil moisture patterns from Advanced Synthetic Aperture Radar (ASAR) data of the European Earth Observation satellite ENVISAT using an empirical soil moisture retrieval algorithm published by Loew et al. (2006) as discussed in section 6.3.1. Based upon these data, the dependence of spatial soil moisture variability upon the soil

moisture state is analyzed for different spatial scales ranging from the field to the catchment scale.

8.2 Statistical Description of Soil Moisture Variability

In order to analyze soil moisture variability on different spatial scales, field and remote sensing data with different aggregation levels were used in a three step approach: (i) In a first step the ASAR soil moisture retrievals were analyzed on the scale of the entire Rur catchment and on the scales of the two major landscape units. On these scales, differences in soil moisture variability should result from variations in soils, topography (especially in the low mountain range area), land cover types, and potential variations in the spatial distribution of antecedent rainfall. (ii) In a next step we analyzed 1.5 x 1.5 km boxes (10 x 10 pixels) of the ASAR derived soil moisture (number of boxes per image was 293). This analysis was restricted to the fertile loess plain as effects of topography on rainfall, soil type and soil moisture, as well as small scale patterns in land cover type, should be reduced as far as possible. The 1.5 x 1.5 km boxes were created using a moving window shifted box-wise over the ASAR images. To calculate mean and soil moisture variability for each box, only those boxes were included in the analysis, where at least 30% of the pixels represent a soil moisture value. Mean soil moisture and variance for the 1.5 x 1.5 km boxes were calculated by shifting a non-overlapping moving 10 x 10 pixels window over the ASAR images. Since not all of the pixels in the image (e.g. built up areas, forests, water) represent a soil moisture value, only those boxes that have at least 30% (30/100) of the pixels classified were included in the analysis. On this spatial scale, soil moisture differences should be dominated by differences in land cover type, while differences due to varying soil texture should be small and homogenous antecedent rainfall is still a reasonable assumption. (iii) For a field-scale evaluation, the field measurements at Selhausen were analyzed on the basis of individual fields (0.02-0.10 km²) to address the within-field soil moisture variability, as differences in soil texture is small and homogenous antecedent rainfall per field can be assumed. On all spatial scales, soil moisture variability was compared with mean soil moisture content. To avoid interdependency between both statistical moments, coefficients of variation instead of standard deviations were used to represent variability.

8.3 ASAR Derived Soil Moisture Patterns

Eight Wide Swath images were processed for 2008. Fig. 8.1 exemplarily shows the spatial patterns and frequency distribution of the soil moisture map for March 25. Areas where the land cover does not allow calculating surface soil moisture (e.g. built up areas, forests, water) remain unspecified in the soil moisture maps. The soil moisture frequency distribution of the derived pattern is shown in the histogram. The histogram shows a bimodal soil moisture distribution averaging at 34.5 Vol.-% with a range of 25 to 47.5 Vol.-%, the first and second peaks are centered at 31.5 Vol.-%, and 38 Vol.-%, respectively. While the soil moisture map shows quite similar soil moisture values within the major landscapes units, it can be seen that the low mountain range part is wetter than most areas of the fertile loess plain. Within a period of two days prior to the satellite overpass, the catchment received precipitation amounts ranging from 2.2 to 8.5 mm. The image covers 97% of the Rur catchment area. The south-eastern part of the catchment (approximately 70 km²) is not covered due to missing land use information.

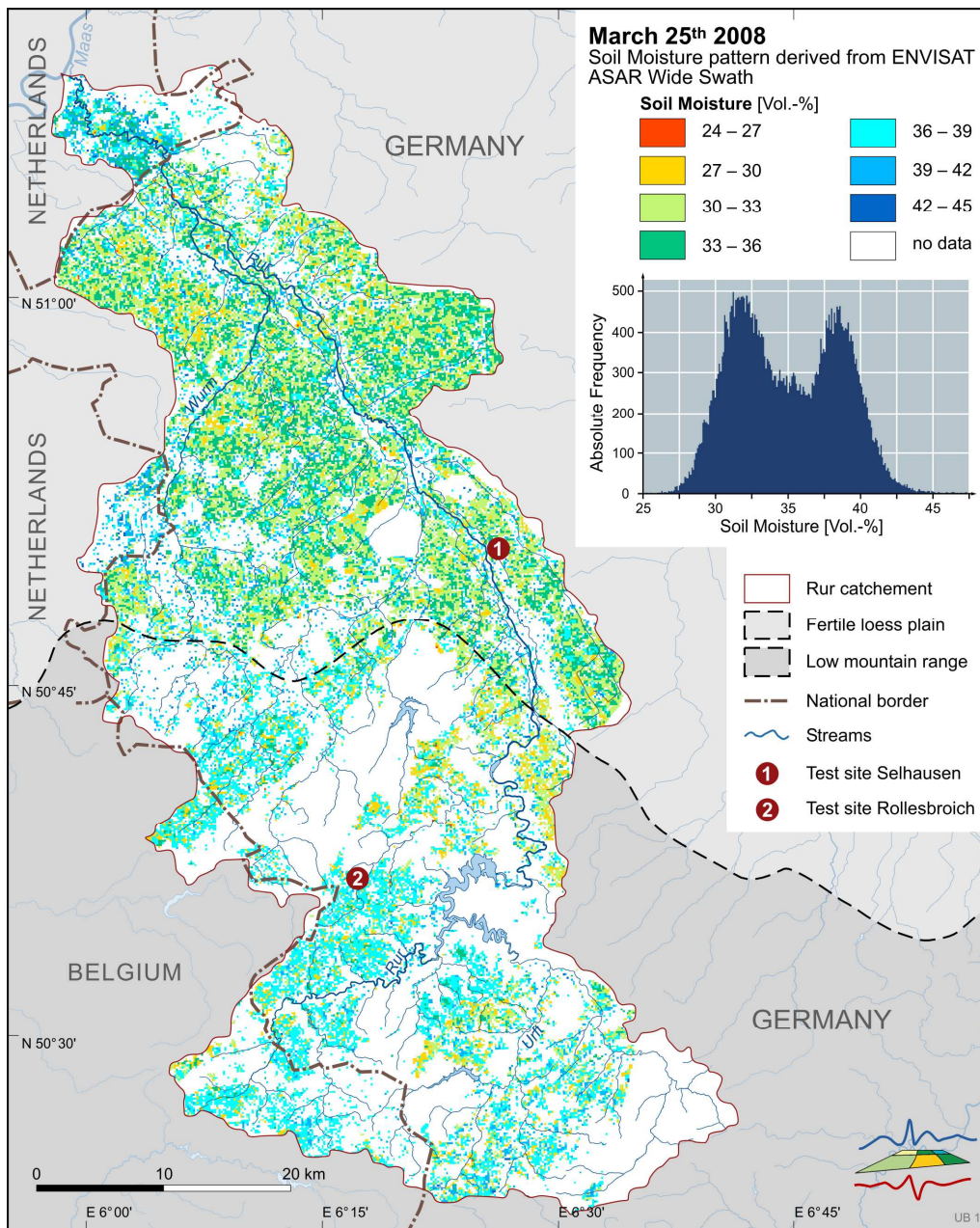


Figure 8.1: Envisat ASAR derived soil moisture pattern of the River Rur catchment from March 25, 2008.

8.4 Analysis of Soil Moisture Variability

The relationship between the mean soil moisture and the coefficient of variation calculated for the whole Rur watershed using all ASAR soil moisture images is shown in Fig. 8.2. The coefficient of variation decreases linearly with increasing mean soil moisture. A decreasing soil moisture variability with increasing soil moisture has been described in the literature (e.g.

Famiglietti et al., 1999; Hupet & Vanclooster, 2002; Choi et al., 2007) and should be expected particularly when areas with homogeneous soil textures approach saturation.

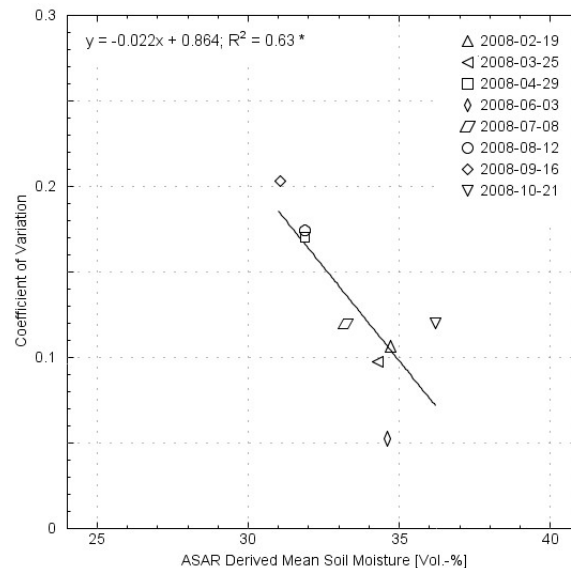


Figure 8.2: Relationship between ASAR derived mean soil moisture and the CV for the entire River Rur catchment.

As described previously, the watershed consists of two distinctively different regions: The flat loess plain and the mountainous Eifel region. Land use and soil textures as well as their spatial variability are significantly different in both regions. While in the Eifel region, the topography results in large spatial heterogeneity particularly with respect to soil texture, the loess plain exhibits more or less uniform soil textures but differs strongly with respect to different types of arable land use. These differences in landscape properties may result in a different relationship between average soil moisture and soil moisture variability. Consequently, we analyzed this relationship separately for both regions (Fig. 8.3).

The correlation for the loess plain (Fig. 8.3) yields a very strong negative relationship ($R^2 = 0.83$) between mean soil moisture and spatial moisture variability expressed by the coefficient of variation. The slope of the relationship is very close to the slope for the whole catchment. In contrast, the relationship for the Eifel area does not show a clear trend (Fig. 8.3). Even at high soil moisture levels the spatial variability is high. While the soil texture in the loess plain is rather uniform, the soil textures in the Eifel vary considerably from mineral soils saturating at moisture values between 45 to 50 Vol.-% to organic soil or soils with an

organic top soil layer with surface soil moisture values in excess of 60 Vol.-%. Thus, even at or close to saturation, the Eifel soils show large spatial variability. Moreover, the hilly topography of the Eifel also causes larger spatial variations of precipitation.

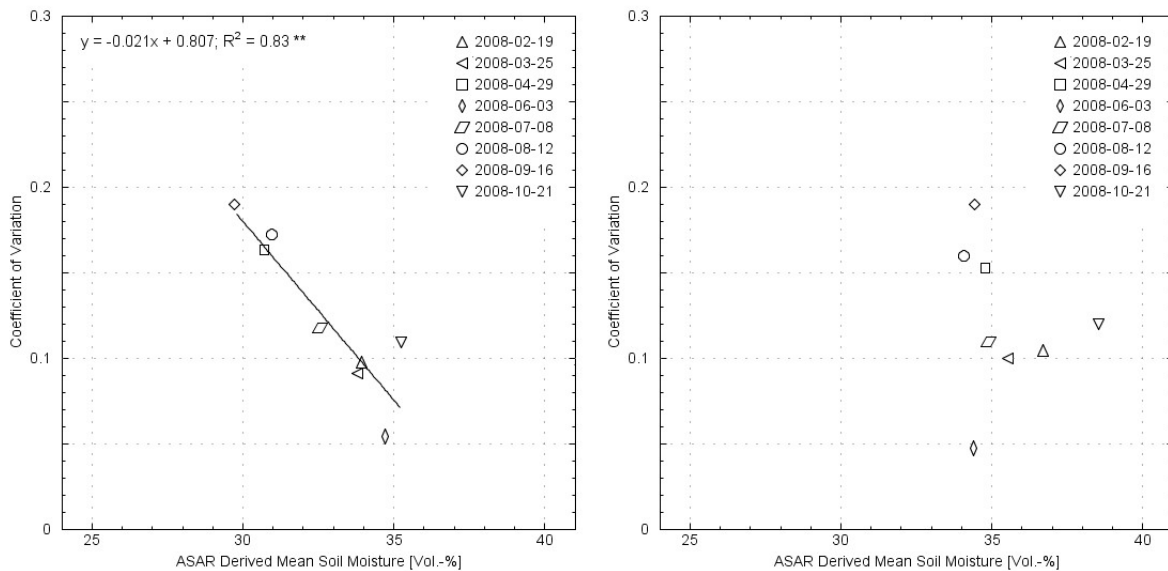


Figure 8.3: Relationship between ASAR derived soil moisture and coefficient of variation for the fertile loess plain (left), and the low mountain range region (right).

Fig. 8.4 shows the relationship of the coefficient of variation and the mean surface soil moisture based upon 10 x 10 pixel boxes for the fertile loess plain. The different acquisition dates of the images are color coded to allow assessment of the variability with a given scene. The slope of the regression line in Fig. 8.4 is significantly smaller than the respective slope for the whole area (Fig. 8.3). While the soil moisture varies considerably within the 10 x 10 boxes for all soil moisture values, the previously described decrease of the coefficient of variation with increasing soil moisture is still obvious. In addition, the upper limit of the soil moisture variability decreases significantly with increasing soil moisture and the lower limit of the soil moisture variability within the 10 x 10 boxes is considerably larger at lower soil moistures than at soil moistures in excess of 32 Vol.-%.

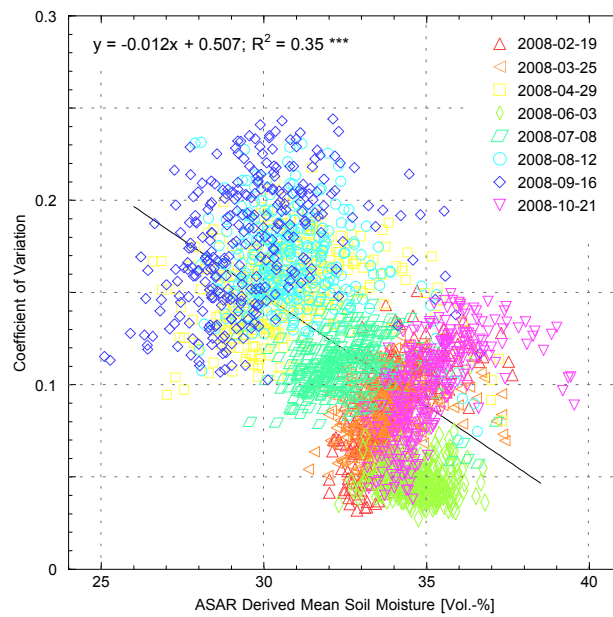


Figure 8.4: Relationship between ASAR derived soil moisture and coefficient of variation for (a) the fertile loess plain pixels taking into account all dates and land cover classes.

Fig. 8.5 shows the relationship between the mean field surface soil moisture measured during our field campaigns and the coefficient of variation within the individual fields. It can be seen that the coefficient of variation decreases again with increasing mean soil moisture. For the soil moisture range from 15 to 34 Vol.-%, the linear regression results in a coefficient of determination of 0.59 and a slope of -0.0063 on the winter wheat fields, and in a coefficient of determination of 0.76 and a slope of -0.0065 on the sugar beet fields, respectively. At the field scale, the slope of the regression line is significantly smaller than the slope for the mesoscale (10x10 pixel boxes) or the regional scale. Thus, while the level of spatial variation shows a comparable range of values at all spatial scales, the decrease of the soil moisture variability with increasing soil moisture is smaller at the local scale than at the large scale.

Choi and Jacobs (2007) also used an exponential fit as an efficient way to explain soil moisture variability patterns as function of mean soil moisture. An exponential fit $CV = Ae^{B\theta}$ between mean soil moisture and coefficient of variation yields a tighter coefficient of determination of 0.60, with $A = 0.521$ and $B = -0.059$, and of 0.81, with $A = 0.591$ and $B = -0.073$ for the winter wheat and sugar beet fields, respectively. The parameter A describes the relative variability range and B indicates the variability change as related to mean soil moisture. Hence, parameter A is related to the maximum relative variability, while parameter B is related to the slope of the relative variability. The parameters, A and B , as

observed from our in situ field measurements are consistent with the observations of surface soil moisture variability from SMEX as reported by Choi et al. (2007).

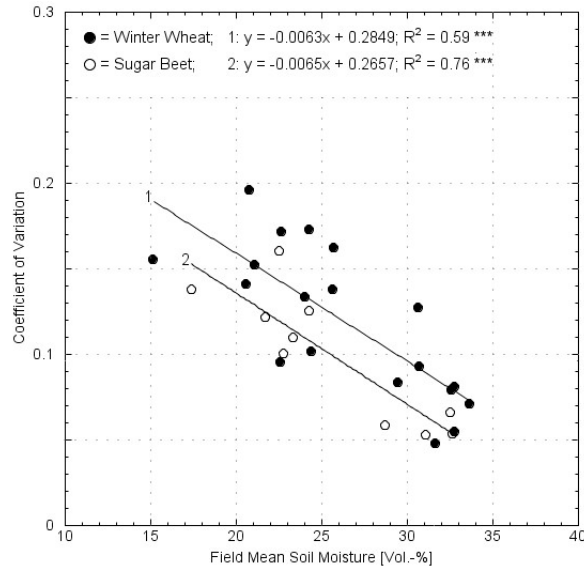


Figure 8.5: Relationship between field mean soil moisture and coefficient of variation from in situ measurements at the Selhausen test site.

The negative correlations between soil moisture variability and mean soil moisture content found in our study are consistent with previous studies of Famiglietti et al. (1999), Hupet and Vanclooster (2002), and Choi and Jacobs (2007). Nonetheless, it should be noted that some studies also found positive relationships between the mean surface soil moisture content and the soil moisture variability (Famiglietti et al., 1998; Western & Grayson, 1998). These studies postulated that variability peaked under wet conditions, as soil heterogeneity would be maximized after precipitation events. While we concur that spatially heterogeneous precipitation, particularly when investigating large areas, results in increased heterogeneity if soil saturation is not reached, our findings indicate, that for areas with homogeneous soil textures, the soil moisture variability decreases with increasing soil moisture. However, in regions with large differences in soil texture and thus soil porosity / maximum soil moisture values at saturation, this relationship might not hold and may result in a large soil moisture variability even at high soil moistures as evidenced by the data for the Eifel. According to Famiglietti et al. (1998) the combined effects of soil texture, hysteresis effects, vegetation, topography, and sampling scale may lead to different relationships between spatial variability and soil moisture.

Fig. 8.6 provides a comprehensive overview about the relationship of spatial soil moisture variability and soil moisture value for different spatial scales. As can be seen in the graph, the gain of the relationship between soil moisture value and coefficient of variation decreases with scale. Hence, at a given soil moisture level, we observed the highest variability on the scale of the entire Rur catchment and the smallest variability on the very field-scale. We postulate that this is due to the fact that the drivers of variations in surface soil moisture contents (e.g. precipitation, soil characteristics, vegetation, etc.) are also much more variable on the large scale. If we consider precipitation as the dominant driving process for spatial variance on days with high mean soil moisture values, the variability of surface soil water contents increases with increasing scale, as the amounts of rainfall, with annual means of approx. 600 mm in the fertile loess plain and over 1200 mm in the low mountain range, vary significantly over the whole Rur catchment. At smaller scales, on the other hand, these fluctuations in precipitation decrease and contribute only small amounts of variance. On days with dry conditions, i.e. low mean soil moisture values, variance is more likely driven by processes associated with evapotranspiration. Thus, soil moisture variability also increases with increasing scale due to the fact that spatial heterogeneities of factors like soil clay content, vegetation (including agricultural management aspects), and topographic conditions become larger the larger the scale.

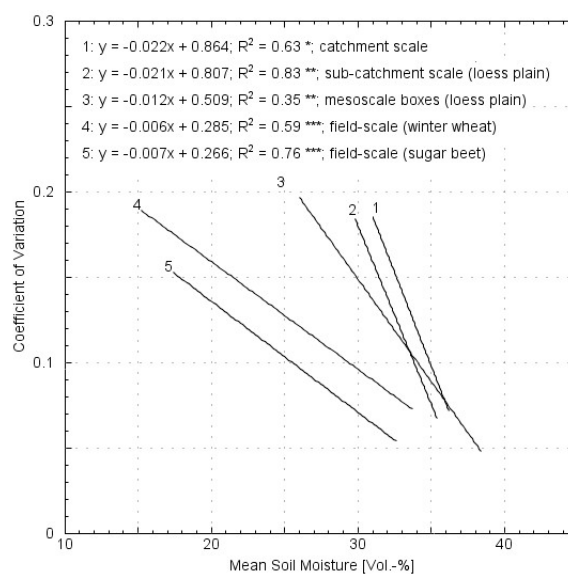


Figure 8.6: Overview of the scale dependent relationships between coefficient of variation and surface mean soil moisture.

As microwave remote sensing at C-band only provides information about the top surface layer of a soil volume, it is unclear if these relationships also hold for deeper soil layers. Thus, care should be taken in extrapolating statistics from surface measurements (e.g. SAR) to the entire root zone. Choi and Jacobs (2007) found that surface soil moisture had the least negative relationship (slope closest to zero) between coefficient of variation and mean soil moisture in comparison to deeper soil layers. According to the authors, these small variability patterns for the surface layer are affected by the high variation of mean soil moisture at the surface. Several other studies found less variability at deeper depths as compared to surface soil moisture observations (Famiglietti et al., 1999; Hupet & Vanclooster, 2002; Albertson & Montaldo, 2003).

In this chapter, an empirical retrieval algorithm of surface soil moisture from ENVISAT ASAR data at C-band was applied successfully within the Rur catchment. The validation of the model to derive soil moistures for a catchment in central Europe yielded an RMSE of 5.0 Vol.-%, as discussed in section 6.3.2.1. The main advantage of the inversion scheme is that it only requires very few parameters in comparison to other retrieval approaches. In regard to an operational use of any parameter inversion model for either optical or microwave remote sensing data, the availability of input parameters is of great importance. Highest deviations of the derived soil moisture from in situ values were recorded on wet meadows and mature sugar beet field. The model parameters could be further improved using empirical data measured under these conditions. However, any improvement of the algorithm will rely on a better assessment of the vegetation influence on the C-band backscattering mechanisms taking into account dynamic vegetation effects.

The variability of mean surface soil moisture was investigated on different scales using in situ measurements and eight ASAR derived soil moisture patterns. By analyzing the relationships between spatial variance and mean soil moisture state on the scales of the entire catchment (~2400 km²), the two major landscape units (~1000 km²), boxes (2.25 km²), and individual fields (~0.1 km²), it was found that the coefficients of variation decreases with decreasing sampling scale for all datasets. The different slopes of the linear correlations, ranging from -0.0063 on the field-scale to -0.022 on the catchment-scale, indicate that small-scale and large-scale variances depend differently on mean soil moisture content.

9. Conclusions and Perspectives

The sensitivity of radar backscattering to the dielectric properties, i.e. the water content of soil and vegetation biomass, and to the geometric structure of bare and vegetated land surfaces, i.e. surface roughness and plant geometry, render microwave remote sensing a valuable tool for a wide range of Earth Observation issues related to the physical conditions of natural surfaces. Notably, its potential for the quantitative estimation of soil moisture at high spatial and/or temporal resolution constitutes an important contribution to hydrological and meteorological modeling, as well as to ecological and economic optimization of agricultural procedures and water management from local scales to global scales.

Since a careful preprocessing, i.e. calibration, of the satellite images is prerequisite for any quantitative analysis of SAR data, different sophisticated processing chains were developed for different ENVISAT ASAR and ALOS PALSAR products using state-of-the-art image processing techniques. The use of high resolution auxiliary terrain information in the form of a LiDAR-derived Digital Elevation Model (Sci Lands, 2008) allowed for most accurate corrections of the geometric and radiometric distortions induced by topography effects. To extract the full information content of multi-channel PALSAR data sophisticated PolSAR preprocessing techniques were employed.

Taking into account all sampling fields from the three individual test sites Duerwiss, Rollesbroich, and Selhausen, the in situ measurements cover a wide soil moisture range with field mean values between 14 and 52 Vol.-% (i.e. $7 < \epsilon' < 34$), and a wide surface roughness range with RMS height values between 0.5 and 3.5 cm (i.e. $0.14 < k_s < 0.94$, at L-band). With respect to plant measurements, the observations also cover a fairly large range of vegetation conditions for grassland, sugar beet, and winter wheat crops. Uncertainties of field measurements which can occur during sample collection should be minded. Inaccurate ground truth not only may be the reason for low correlations between measurements and estimates, but also for deficient parameterization of new models. In this context, special emphasis should be put on the aspect of the small scale spatial heterogeneity of surface soil

moisture distribution. Particularly, the question of how well are local observations suited to represent the area of a given remote sensing pixel is very important to consider.

In this study, a sampling strategy was established which enables a pixel by pixel comparison between calibrated SAR images and ground based measurements. As described in section 4.3, each image resolution cell is represented by multiple measurements in order to account for this sub-pixel heterogeneity. However, it should be pointed out that comparisons between SAR observables and in situ values on a pixel-by-pixel basis were only feasible for the high resolution products of ALOS PALSAR. This is, the sampling strategy used is still suitable to cover the spatial variability of surface soil moisture for the 15 m (225 m²) resolution cells, while the magnitude of variability within the larger 25 m (625 m²) cells of ENVISAT ASAR render a pixelwise approach problematic.

The major impediment for the quantitative retrieval of surface soil moisture from SAR data lies in the separation of different scattering contributions to the backscattering coefficients. Polarimetry is the key to overcome these problems because it allows a direct or indirect separation of attenuation effects induced by surface roughness and vegetation. In effect, most of the popular inversion approaches use polarimetric SAR imaging. The fundamental principles of radar polarimetry have been introduced in *Chapter 5*.

A large variety of models for the inversion of soil moisture from spaceborne SAR data have been addressed within the last decades. In *Chapter 6*, five representative retrieval approaches were addressed and their estimation performances were tested against in situ measurements. Two theoretical scattering models, the SPM and the IEM, two semi-empirical extensions of the SPM, the Oh model and the Dubois model, as well as one empirical retrieval model were discussed.

In *Chapter 7*, new semi-empirical retrieval algorithms were introduced for land cover types grassland, bare soil, sugar beet, and winter wheat. Key for the development of the novel soil moisture model for dual channel L-band SAR data was the coherent-on-receive dual polarimetry mode (FBD) of ALOS PALSAR. By applying a PolSAR decomposition technique, namely the H/A/Alpha decomposition, the phase information was exploited to increase the amount of observables. The potential to derive information on biomass and

surface roughness from the dual-pol data was investigated based on correlation analyses between PALSAR observables and in situ measurements. High sensitivities towards surface roughness and crop biomass could be ascertained. Using these findings, surface roughness ks was estimated with RMS errors of 0.11. Sugar beet total fresh weight and winter wheat above ground fresh weight were estimated with RMS errors of 2.7 kg/m² and 0.8 kg/m², respectively. The good quality of the estimates allowed correcting the horizontally co-polarized backscattering coefficients for the surface roughness and vegetation effects. The accuracy of soil moisture retrievals could be increased from 4.5 to 3.6 Vol.-% using the roughness correction for bare soil and from >10.0 to 4.2 and 3.9 Vol.-% using the biomass correction for sugar beet and winter wheat, respectively. In the grassland case, no such corrections were performed. Instead it was found that the most accurate estimates of m_v are obtained when a dedicated grassland parameter model incorporating the co- and cross-polarized backscattering coefficients, the $\sigma_{hv}^0/\sigma_{hh}^0$ ratio, as well as the PolSAR observables, is used directly in a linear regression model. This grassland model yielded an estimation error of 4.2 Vol.-%.

These observations demonstrate the suitability of dual polarized H/alpha parameters to improve the capabilities to estimate surface parameters. Along with the land cover classification capabilities of dual-pol L-band SAR systems (Lee et al., 2001; Ohki & Shimada, 2010; Yamaguchi et al., 2011), the findings give a promising outlook in terms of the possibility to develop an operational soil moisture retrieval model where information on the land cover and the disturbing effects from vegetation and surface roughness can be derived directly from the SAR image without the need for a priori knowledge or ancillary EO data.

The results obtained in this thesis lead to the conclusion that state-of-the-art dual polarimetric L-band SAR data is not only suitable to retrieve surface soil moisture contents of bare as well as of vegetated agricultural fields and grassland with an absolute accuracy of better than 5 Vol.-%, but for the first time also allows investigating within-field spatial heterogeneities from space.

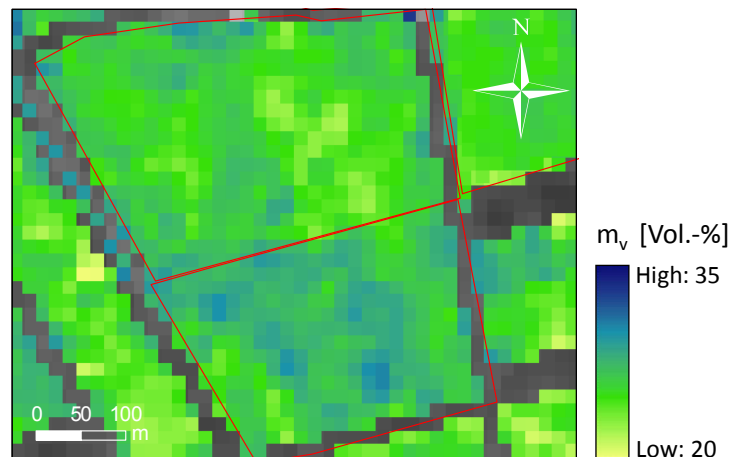


Figure 9.1: Within-field variability of surface soil moisture distribution as seen by ALOS PALSAR.

Furthermore, several other interesting observations were made through the course of this extensive SAR study. The most important key findings of this dissertation research are summarized in the following.

Fresh weight biomass is the vegetation variable to which L-band SAR data is most sensitive. At L-band the attenuation effects caused by above ground vegetation can be neglected if the amount of fresh weight biomass is below 2 kg/m^2 . The sophisticated dual polarization modes of current SAR satellites, i.e. ALOS, RADARSAT-2, and TanDEM-X, can be used, albeit in a limited sense compared to quad polarization modes, for advanced PolSAR applications. For such coherent-on-receive dual polarization configurations, both the cross-pol ratio $\sigma_{hv}^0 / \sigma_{hh}^0$ and the dual-pol anisotropy A are suitable to describe the surface roughness over bare agricultural fields. Terrestrial 3D laser scanner measurements allow for improved analysis and monitoring of surface roughness on agricultural fields. In grassland ecosystems, the most important feature limiting the estimation accuracy of soil moisture is the thatch layer rather than the above ground biomass. Remotely sensed soil moisture patterns can help to improve the understanding of scaling problems in hydrology. The variability of surface soil moisture decreases with increasing wetness states at all scales ranging from the field scale ($\sim 0.1 \text{ km}^2$) to the catchment scale ($> 1000 \text{ km}^2$).

The ALOS follow on mission, ALOS-2, will be launched in 2013 with the next generation L-band SAR aboard. With even more advanced performance in terms of resolution and operation modes, along with a much better repetition cycle of only 14 days (Okada et al., 2011), PALSAR-2 will again constitute a big step forward in hydrological remote sensing and Earth Observation in general. With a remarkably large bandwidth of 84 MHz, this sensor will be able to image the Earth's surface with resolutions of about 3 m. Moreover, it will be the first system capable of both left and right looking acquisitions. This will offer all new possibilities for surface scattering studies, and it can be expected that it will bring improvements in many application like land classification, biomass monitoring, soil moisture and surface roughness estimation, etc. The planned Tandem-L mission (Moreira et al., 2011), a joint project of DLR and NASA, is now scheduled to be launched in 2019. Both systems will be highly suitable for single and repeat pass PolInSAR applications (Cloude & Papathanassiou, 1998; Papathanassiou & Cloude, 2001) and thus will greatly improve the capabilities to estimate soil moisture under all kinds of vegetation with high accuracy and with high temporal and spatial resolutions. The sensitivity of the interferometric phase towards the coherent location of effective scattering centers within a resolution cell provide a powerful approach to estimate even weak ground scattering under vegetation. In addition, the variation of the interferometric coherence as a function of baseline allows retrieving more detailed information about the vegetation cover over the soil surface. The combination of polarimetry and interferometry is probably the most promising approach for a better estimation of geophysical parameters from SAR data acquired over natural terrain (Hajnsek et al., 2003a; Papathanassiou et al., 2007; Lopez-Martinez et al., 2008).

Improvements in the monitoring techniques for soil surface and vegetation parameters will also improve the capabilities to develop and validate inversion models. For instance, the newly installed sensor networks within the TERENO framework will greatly increase the availability of in situ soil moisture information for remote sensing studies. Terrestrial 3D laser scanners will not only improve the monitoring of surface roughness but also can provide accurate ground based biomass measurements in a fast and efficient manner. The use of such 3D data will greatly improve the possibility to develop better biomass retrieval algorithms.

The results reported in this thesis along with the future perspectives in the field of radar remote sensing and environmental monitoring give a promising outlook in terms of the

possibility to develop a fully operational soil moisture retrieval model for spaceborne L-band SAR in the near future. The author hopes that this work, including the various publications and presentations made during the course of his PhD studies, will have a meaningful contribution to this challenging topic.

References

- Ainsworth, T. L., J. P. Kelly, and J. S. Lee, (2009). "Classification comparisons between dual-pol, compact polarimetric and quad-pol SAR imagery," *ISPRS Journal of Photogrammetry and Remote Sensing*, vol. 64, no. 5, pp. 464-471.
- Albertson, J. D. and N. Montaldo, (2003). "Temporal dynamics of soil moisture variability: 1. Theoretical basis," *Water Resources Research*, vol. 39, no. 10.
- Allain, S., L. Ferro-Famil, and E. Pottier, (2003). "Surface parameters retrieval from polarimetric and multi-frequency SAR data," in *Proceedings of IGARSS '03: Learning from Earth's Shapes and Sizes*, pp. 1417-1419.
- Allmaras, R. R., R. E. Burwell, and R. F. Holt, (1967). "Plow-Layer Porosity and Surface Roughness from Tillage as Affected by Initial Porosity and Soil Moisture at Tillage Time," *Soil Sci Soc Am J*, vol. 31, no. 4, pp. 550-556.
- Altse, E., O. Bolognani, M. Mancini, and P. A. Troch, (1996). "Retrieving soil moisture over bare soil from ERS 1 synthetic aperture radar data: Sensitivity analysis based on a theoretical surface scattering model and field data," *Water Resources Research*, vol. 32, no. 3, pp. 653-661.
- Álvarez-Mozos, J., M. González-Audicana, and J. Casali, (2007). "Evaluation of empirical and semi-empirical backscattering models for surface soil moisture estimation," *Canadian Journal of Remote Sensing*, vol. 33, no. 3, pp. 176-188.
- Alvarez-Mozos, J., M. Gonzalez-Audicana, J. Casali, and A. Larranaga, (2008). "Effective versus measured correlation length for radar-based surface soil moisture retrieval," *International Journal of Remote Sensing*, vol. 29, no. 17-18, pp. 5397-5408.
- Arakawa, K. and E. Krotkov, (1996). "Fractal modeling of natural terrain: Analysis and surface reconstruction with range data," *Graphical Models and Image Processing*, vol. 58, no. 5, pp. 413-436.
- Attema, E. P. W. and F. T. Ulaby, (1978). "Vegetation Modeled As A Water Cloud," *Radio Science*, vol. 13, no. 2, pp. 357-364.
- Autret, M., R. Bernard, and D. Vidal-Madjar, (1989). "Theoretical study of the sensitivity of the microwave backscattering coefficient to the soil surface parameters," *International Journal of Remote Sensing*, vol. 10, no. 1, pp. 171-179.
- Baghdadi, N., M. Aubert, O. Cerdan, L. Franchisteguy, C. Viel, E. Martin, M. Zribi, and J. F. Desprats, (2007). "Operational mapping of soil moisture using synthetic aperture radar data: Application to the touch basin (France)," *Sensors*, vol. 7, no. 10, pp. 2458-2483.
- Baghdadi, N., J. A. Chaaya, and M. Zribi, (2011). "Semiempirical Calibration of the Integral Equation Model for SAR Data in C-Band and Cross Polarization Using Radar Images and Field Measurements," *IEEE Geoscience and Remote Sensing Letters*, vol. 8, no. 1, pp. 14-18.
- Baghdadi, N., I. Gherboudj, M. Zribi, M. Sahebi, C. King, and F. Bonn, (2004). "Semi-empirical calibration of the IEM backscattering model using radar images and moisture and roughness field measurements," *International Journal of Remote Sensing*, vol. 25, no. 18, pp. 3593-3623.

- Baghdadi, N., C. King, and L. Bonnifait, (2002). "An empirical calibration of the Integral Equation Model based on SAR data and soil parameters measurements," *Proceedings of IGARSS '02: Remote Sensing - Integrating Our View of the Planet*, pp. 2646-2650.
- Baghdadi, N. and M. Zribi, (2006). "Evaluation of radar backscatter models IEM, OH and Dubois using experimental observations," *International Journal of Remote Sensing*, vol. 27, no. 18, pp. 3831-3852.
- Beaudoin, A., T. Le Toan, and Q. H. J. Gwyn, (1990). "SAR observations and modeling of the C-band backscatter variability due to multiscale geometry and soil moisture," *IEEE Transactions on Geoscience and Remote Sensing*, vol. 28, no. 5, pp. 886-895.
- Beckmann, P. and A. Spizzichino, (1987). *The scattering of electromagnetic waves from rough surfaces*, Artech House Inc., Norwood, p. 511.
- Bell, K. R., B. J. Blanchard, T. J. Schmutge, and M. W. Witzak, (1980). "Analysis of Surface Moisture Variations Within Large-Field Sites," *Water Resources Research*, vol. 16, no. 4, pp. 796-810.
- Bernard, R., O. Taconet, D. Vidal-Madjar, J. L. Thony, M. Vauclin, A. Chapoton, F. Wattrelot, and A. Lebrun, (1984). "Comparison of Three in Situ Surface Soil Moisture Measurements And Application to C-Band Scatterometer Calibration," *IEEE Transactions on Geoscience and Remote Sensing*, vol. GE-22, no. 4, pp. 388-394.
- Beven, K., (1995). "Linking Parameters Across Scales - Subgrid Parameterizations and Scale-Dependent Hydrological Models," *Hydrol. Process.*, vol. 9, no. 5-6, pp. 507-525.
- Bindlish, R. and A. P. Barros, (2000). "Multifrequency Soil Moisture Inversion from SAR Measurements with the Use of IEM," *Remote Sensing of Environment*, vol. 71, no. 1, pp. 67-88.
- Birrer, I. J., E. M. Bracalente, G. J. Dome, J. Sweet, and G. Berthold, (1982). "Sigma Nought Signature of the Amazon Rain Forest Obtained from the Seasat Scatterometer," *IEEE Transactions on Geoscience and Remote Sensing*, vol. 20, no. 1, pp. 11-17.
- Boerner, W., (1992). "Evaluation of optimization procedures for the 2 x 2 sinclair and the 4 x 4 mueller matrices in coherent radar polarization and its application to radar target versus background clutter discrimination in pol-sar sensing and imaging," in *Geoscience and Remote Sensing Symposium, 1992.IGARSS '92.International*, pp. 281-284.
- Boerner, W. M., M. El-Arini, C. Chung-Yee, and P. Mastoris, (1981). "Polarization dependence in electromagnetic inverse problems," *IEEE Transactions on Antennas and Propagation*, vol. 29, no. 2, pp. 262-271.
- Boerner, W. M., H. Mott, and E. Luneburg, (1997). "Polarimetry in remote sensing: basic and applied concepts," in *Proceedings of IGARSS '97: Remote Sensing - A Scientific Vision for Sustainable Development*, pp. 1401-1403.
- Boerner, W. M., H. Mott, E. Lüneburg, C. Livingstone, B. Brisco, R. Brown, and J. S. Paterson, (1998). "Polarimetry in Remote Sensing - Basic and Applied Concepts," in *Manual of Remote Sensing, Volume 2: Principles and Applications of Imaging Radar*, 3rd ed. F. M. Henderson and A. J. Lewis, Eds., John Wiley & Sons, New York, pp. 271-356.
- Boerner, W. M., Y. Yamaguchi, A. Sato, R. Sato, and H. Yamada, (2010). "Scattering power decomposition implementing rotation of coherency matrix," in *Proceedings of EUSAR 2010*, 7-10 June 2010, -, Aachen, Germany

- Bogena, H., M. Herbst, J.-F. Hake, R. Kunkel, C. Montzka, Th. Pütz, H. Vereecken, and F. Wendland, "MOSYRUR - Water balance analysis in the Rur basin," Forschungszentrum Jülich, 2005.
- Boisvert, J. B., Q. H. J. Gwyn, A. Chanzy, D. J. Major, B. Brisco, and R. J. Brown, (1997). "Effect of surface soil moisture gradients on modelling radar backscattering from bare fields," *International Journal of Remote Sensing*, vol. 18, no. 1, pp. 153-170.
- Bond, J. J. and W. O. Willis, (1971). "Soil-Water Evaporation - Long-Term Drying As Influenced by Surface Residue and Evaporation Potential," *Soil Science Society of America Proceedings*, vol. 35, no. 6, p. 984-&.
- Borgeaud, M., S. V. Nghiem, R. T. Shin, and J. A. Kong, (1989). "Theoretical Models for Polarimetric Microwave Remote Sensing of Earth Terrain," *Journal of Electromagnetic Waves and Applications*, vol. 3, pp. 61-81.
- Born, M. and E. Wolf, (1999). *Principles of optics: Electromagnetic Theory of Propagation, Interference and Diffraction of Light*, 7th exp. ed., Cambridge University Press.
- Breuer, A., I. Hajnsek, L. Ferro-Famil, and E. Pottier, (2003). "Full polarimetry versus partial polarimetry for quantitative surface parameter estimation," in *Proceedings of IGARSS '03: Learning from Earth's Shapes and Sizes*, pp. 437-439.
- Brisco, B., R. J. Brown, B. Snider, G. J. Sofko, J. A. Koehler, and A. G. Wacker, (1991). "Tillage Effects on the Radar Backscattering Coefficient of Grain Stubble Fields," *International Journal of Remote Sensing*, vol. 12, no. 11, pp. 2283-2298.
- Brown, S. C. M., S. Quegan, K. Morrison, J. C. Bennett, and G. Cookmartin, (2003). "High-resolution measurements of scattering in wheat canopies-implications for crop parameter retrieval," *IEEE Transactions on Geoscience and Remote Sensing*, vol. 41, no. 7, pp. 1602-1610.
- Brown, W. M., (1967). "Synthetic Aperture Radar," *IEEE Transactions on Aerospace and Electronic Systems*, vol. AES-3, no. 2, pp. 217-229.
- Brown, W. M. and L. J. Porcello, (1969). "An introduction to synthetic-aperture radar," *IEEE Spectrum*, vol. 6, no. 9, pp. 52-62.
- Bryant, R., M. S. Moran, D. P. Thoma, C. D. H. Collins, S. Skirvin, M. Rahman, K. Slocum, P. Starks, D. Bosch, and M. P. G. Dugo, (2007). "Measuring surface roughness height to parameterize radar backscatter models for retrieval of surface soil moisture," *IEEE Geoscience and Remote Sensing Letters*, vol. 4, no. 1, pp. 137-141.
- Bulfin, M. and T. Gleeson, (1967). "A Study of Surface Soil Conditions Under A Non-Cultivation Management System .I. Physical and Chemical Properties," *Irish Journal of Agricultural Research*, vol. 6, no. 2, p. 177-&.
- Burrough, P. A., (1981). "Fractal Dimensions of Landscapes and Other Environmental Data," *Nature*, vol. 294, no. 5838, pp. 240-242.
- Burwell, R. E., R. R. Allmaras, and M. Amemiya, (1963). "A Field Measurement of Total Porosity and Surface Microrelief of Soils," *Soil Sci Soc Am J*, vol. 27, no. 6, pp. 697-700.
- Butler, J. B., S. N. Lane, and J. H. Chandler, (1998). "Assessment of DEM quality for characterizing surface roughness using close range digital photogrammetry," *Photogrammetric Record*, vol. 16, no. 92, pp. 271-291.

- Callens, M., N. E. C. Verhoest, and M. W. J. Davidson, (2006). "Parameterization of tillage-induced single-scale soil roughness from 4-m profiles," *IEEE Transactions on Geoscience and Remote Sensing*, vol. 44, no. 4, pp. 878-888.
- Campbell, J. B., (2007). *Introduction to Remote Sensing*, 4th ed., The Guilford Press, New York, USA, p. 625.
- Cao, F., W. Hong, Y. R. Wu, and E. Pottier, (2007). "An unsupervised segmentation with an adaptive number of clusters using the SPAN/H/alpha/A space and the complex Wishart clustering for fully polarimetric SAR data analysis," *IEEE Transactions on Geoscience and Remote Sensing*, vol. 45, no. 11, pp. 3454-3467.
- Champion, I. and R. Faivre, (1996). "The field row direction relative to the radar azimuth considered as an apparent surface roughness for smooth bare soils," *International Journal of Remote Sensing*, vol. 17, no. 16, pp. 3305-3311.
- Chandler, J. H., J. G. Fryer, and A. Jack, (2005). "Metric capabilities of low-cost digital cameras for close range surface measurement," *Photogrammetric Record*, vol. 20, no. 109, pp. 12-26.
- Charpentier, M. A. and P. M. Groffman, (1992). "Soil-Moisture Variability Within Remote-Sensing Pixels," *Journal of Geophysical Research-Atmospheres*, vol. 97, no. D17, pp. 18987-18995.
- Chaudhuri, S., F. Bing-Yuen, and W. M. Boerner, (1986). "A validation analysis of Huynen's target-descriptor interpretations of the Mueller matrix elements in polarimetric radar returns using Kennaugh's physical optics impulse response formulation," *Antennas and Propagation, IEEE Transactions on*, vol. 34, no. 1, pp. 11-20.
- Chaudhuri, S. and W. Boerner, (1975). "Application of polarizational aspects of space-time integral solution to electromagnetic inverse scattering," in *Antennas and Propagation Society International Symposium, 1975*, pp. 138-141.
- Chen, K. S. and A. K. Fung, (1995). "A Comparison of Backscattering Models for Rough Surfaces," *IEEE Transactions on Geoscience and Remote Sensing*, vol. 33, no. 1, pp. 195-200.
- Chen, K. S., W. Tzong-Dar, T. Mu-King, and A. K. Fung, (2000). "Note on the multiple scattering in an IEM model," *IEEE Transactions on Geoscience and Remote Sensing*, vol. 38, no. 1, pp. 249-256.
- Chen, M. F. and A. K. Fung, (1988). "A numerical study of the regions of validity of the Kirchhoff and small-perturbation rough surface scattering models," *Radio Science*, vol. 23, no. 2, pp. 163-170.
- Chiu, T. and K. Sarabandi, (1997). "Electromagnetic scattering interaction between a dielectric cylinder and a slightly rough surface," in *Proceedings of IGARSS '97: Remote Sensing - A Scientific Vision for Sustainable Development*, pp. 901-903.
- Choi, M. and J. M. Jacobs, (2007). "Soil moisture variability of root zone profiles within SMEX02 remote sensing footprints," *Advances in Water Resources*, vol. 30, no. 4, pp. 883-896.
- Choi, M., J. M. Jacobs, and M. H. Cosh, (2007). "Scaled spatial variability of soil moisture fields," *Geophysical Research Letters*, vol. 34, no. 1.
- Cloude, S. R., (1997). "Wideband radar inversion studies using the entropy-alpha decomposition," in *Wideband Interferometric Sensing and Imaging Polarimetry*, H. Mott and W. M. Boerner, Eds., 27 July-1 Aug., San Diego, USA, pp. 118-129.

- Cloude, S. R., (2010). *Polarisation: Applications in Remote Sensing*, Oxford University Press, Oxford, UK, p. 493.
- Cloude, S. R., (1986a). "Group theory and polarisation algebra," *OPTIK*, vol. 75, no. 1, pp. 26-36.
- Cloude, S. R., (1986b). "Polarimetry: The Characterisation of Polarimetric Effects in EM Scattering," PhD Thesis, University of Birmingham, Faculty of Engineering, UK.
- Cloude, S. R., (1995). "An entropy based classification scheme for polarimetric SAR data," *Proceedings of IGARSS '95: Quantitative Remote Sensing for Science and Applications*, pp. 2000-2002.
- Cloude, S. R., (1999). "Eigenvalue parameters for surface roughness studies," in *Polarization: Measurement, Analysis, and Remote Sensing II*, D. H. Goldstein and D. B. Chenault, Eds., pp. 2-13.
- Cloude, S. R., (2007). "The Dual Polarisation Entropy/Alpha Decomposition: A PALSAR Case Study," in *Proceedings of PolInSAR 2007*, 22-26 Jan. 2007, -, Frascati, Italy
- Cloude, S. R., E. Chen, Z. Li, X. Tian, Y. Pang, S. Li, E. Pottier, L. Ferro-Famil, F. Cao, Y. P. Wang, and K. P. Papathanassiou, (2008). "Forest Structure Estimation Using Space Borne Polarimetric Radar: An ALOS-PALSAR Case Study," in *Proceedings of Dragon 1 Programme Final Results 2004-2007*, 21- 25 April 2008, Beijing, P.R. China
- Cloude, S. R. and K. P. Papathanassiou, (1997a). "Coherence optimisation in polarimetric SAR interferometry," in *Geoscience and Remote Sensing, 1997.IGARSS '97.Remote Sensing - A Scientific Vision for Sustainable Development., 1997 IEEE International*, pp. 1932-1934.
- Cloude, S. R. and K. P. Papathanassiou, (1997b). "Polarimetric optimisation in radar interferometry," *Electronics Letters*, vol. 33, no. 13, pp. 1176-1178.
- Cloude, S. R. and K. P. Papathanassiou, (1998). "Polarimetric SAR interferometry," *Geoscience and Remote Sensing, IEEE Transactions on*, vol. 36, no. 5, pp. 1551-1565.
- Cloude, S. R. and E. Pottier, (1996). "A review of target decomposition theorems in radar polarimetry," *IEEE Transactions on Geoscience and Remote Sensing*, vol. 34, no. 2, pp. 498-518.
- Cloude, S. R. and E. Pottier, (1997). "An entropy based classification scheme for land applications of polarimetric SAR," *IEEE Transactions on Geoscience and Remote Sensing*, vol. 35, no. 1, pp. 68-78.
- Cognard, A. L., C. Loumagne, M. Normand, P. Olivier, C. Otte, D. VidalMadjar, S. Louahala, and A. Vidal, (1995). "Evaluation of the Ers-1 Synthetic Aperture Radar Capacity to Estimate Surface Soil-Moisture - 2-Year Results Over the Naizin Watershed," *Water Resources Research*, vol. 31, no. 4, pp. 975-982.
- Cole, R. C., (1939). "Soil macrostructure as affected by cultural treatments," *Hilgardia*, vol. 12, no. 6, pp. 427-472.
- Colpitts, B. G., (1998). "The integral equation model and surface roughness signatures in soil moisture and tillage type determination," *IEEE Transactions on Geoscience and Remote Sensing*, vol. 36, no. 3, pp. 833-837.
- Cookmartin, G., P. Saich, S. Quegan, R. Cordey, P. Burgess-Allen, and A. Sowter, (2000). "Modeling microwave interactions with crops and comparison with ERS-2 SAR observations," *IEEE Transactions on Geoscience and Remote Sensing*, vol. 38, no. 2, pp. 658-670.

- Crow, W. T. and E. F. Wood, (1999). "Multi-scale dynamics of soil moisture variability observed during SGP'97," *Geophysical Research Letters*, vol. 26, no. 23, pp. 3485-3488.
- Cumming, I. G. and F. H. Wong, (2005). *Digital Processing of Synthetic Aperture Radar Data: Algorithms and Implementation*, Artech House, Norwood, p. 633.
- Curlander, J. C. and R. N. McDonough, (1991). *Synthetic Aperture Radar: Systems and Signal Processing*, J. A. Kong, Ed., John Wiley & Sons, New York, p. 648.
- Currence, H. D. and W. G. Lovely, (1971). "Automatic Soil Surface Profilometer," *Transactions of the Asae*, vol. 14, no. 1, p. 69-&.
- Dabrowska-Zielinska, K., M. Gruszczynska, W. Kowalik, and K. Stankiewicz, (2002). "Application of multisensor data for evaluation of soil moisture," *Advances in Space Research*, vol. 29, no. 1, pp. 45-50.
- Dabrowska-Zielinska, K., Y. Inoue, W. Kowalik, and M. Gruszczynska, (2007). "Inferring the effect of plant and soil variables on C- and L-band SAR backscatter over agricultural fields, based on model analysis," *Advances in Space Research*, vol. 39, no. 1, pp. 139-148.
- Dalton, F. N. and M. Th. Van Genuchten, (1986). "The time-domain reflectometry method for measuring soil water content and salinity," *Geoderma*, vol. 38, no. 1-4, pp. 237-250.
- Daniel, S., S. Allain, and E. Pottier, (2007). "Short vegetation influence on surface parameter estimations," *Proceedings of IGARSS '07: Sensing and Understanding Our Planet*, pp. 1838-1841.
- Darboux, F. and C. Huang, (2003). "An instantaneous-profile laser scanner to measure soil surface microtopography," *Soil Sci Soc Am J*, vol. 67, no. 1, pp. 92-99.
- Dash, S. and G. Prusty, (2007). "Simulation of radar backscattering coefficients using IEM - A tool for surface soil moisture retrieval," *3rd Int. Conference on Recent Advances in Space Technologies 2007*, pp. 383-388.
- Davidson, M., T. Le Toan, M. Borgeaud, and T. Manninen, (1998). "Measuring the roughness characteristics of natural surfaces at pixel scales: moving from 1 metre to 25 metre profiles," in *Proceedings of IGARSS '98: Remote Sensing and Managing the Environment*, pp. 1200-1202.
- Davidson, M. W. J., T. Le Toan, F. Mattia, G. Satalino, T. Manninen, and M. Borgeaud, (2000). "On the characterization of agricultural soil roughness for radar remote sensing studies," *IEEE Transactions on Geoscience and Remote Sensing*, vol. 38, no. 2, pp. 630-640.
- De Grandi, G. F., M. Leysen, J. S. Lee, and D. Schuler, (1997). "Radar reflectivity estimation using multiple SAR scenes of the same target: technique and applications," in *Proceedings of IGARSS '97: Remote Sensing - A Scientific Vision for Sustainable Development*, pp. 1047-1050.
- De Loor, G. P., (1983). "The Dielectric Properties of Wet Materials," *IEEE Transactions on Geoscience and Remote Sensing*, vol. GE-21, no. 3, pp. 364-369.
- Debye, P. J. W., (1929). *Polar Molecules*, Dover Publications Inc., New York, p. 172.
- Deroin, J. P., A. Company, and A. Simonin, (1997). "An empirical model for interpreting the relationship between backscattering and arid land surface roughness as seen with the SAR," *IEEE Transactions on Geoscience and Remote Sensing*, vol. 35, no. 1, pp. 86-92.
- Deschamps, G. A., (1951). "Techniques for Handling Elliptically Polarized Waves with Special Reference to Antennas: Part II-Geometrical Representation of the Polarization of a Plane Electromagnetic Wave," *Proceedings of the IRE*, vol. 39, no. 5, pp. 540-544.

- Dobson, M. C. and F. T. Ulaby, (1986). "Active Microwave Soil-Moisture Research," *IEEE Transactions on Geoscience and Remote Sensing*, vol. 24, no. 1, pp. 23-36.
- Dobson, M. C., F. T. Ulaby, M. T. Hallikainen, and M. A. El-Rayes, (1985). "Microwave Dielectric Behavior of Wet Soil-Part II: Dielectric Mixing Models," *IEEE Transactions on Geoscience and Remote Sensing*, vol. GE-23, no. 1, pp. 35-46.
- Dooge, J. C. I., (1986). "Looking for hydrologic laws," *Water Resour. Res.*, vol. 22, no. 9, pp. 46-58.
- Dooge, J. C. I., (1988). "Hydrology in Perspective," *Hydrological Sciences Journal-Journal des Sciences Hydrologiques*, vol. 33, no. 1, pp. 61-85.
- Dubois, P. C., J. vanZyl, and T. Engman, (1995). "Measuring Soil-Moisture with Imaging Radars," *IEEE Transactions on Geoscience and Remote Sensing*, vol. 33, no. 4, pp. 915-926.
- Durand, J. M., B. J. Gimonet, and J. R. Perbos, (1987). "Speckle in SAR images: An evaluation of filtering techniques," *Advances in Space Research*, vol. 7, no. 11, pp. 301-304.
- El-Rayes, M. A. and F. T. Ulaby, (1987). "Microwave Dielectric Spectrum of Vegetation-Part I: Experimental Observations," *IEEE Transactions on Geoscience and Remote Sensing*, vol. GE-25, no. 5, pp. 541-549.
- Elachi, C., (1987). *Spaceborne Radar Remote Sensing: Applications and Techniques*, IEEE Press, New York, p. 252.
- Elachi, C., L. E. Roth, and G. G. Schaber, (1984). "Spaceborne Radar Subsurface Imaging in Hyperarid Regions," *IEEE Transactions on Geoscience and Remote Sensing*, vol. GE-22, no. 4, pp. 383-388.
- Emerson, W. W., (1954). "The Determination of the Stability of Soil Crumbs," *Journal of Soil Science*, vol. 5, no. 2, pp. 233-250.
- Emerson, W. W., (1959). "Stability of Soil Crumbs," *Nature*, vol. 183, no. 4660, p. 538.
- Ender, J. H. G., (2003). "Signal theoretical aspects of bistatic SAR," in *Proceedings of IGARSS '03: Learning from Earth's Shapes and Sizes*, pp. 1438-1441.
- Engman, E. T. and J. R. Wang, (1987). "Evaluating Roughness Models of Radar Backscatter," *IEEE Transactions on Geoscience and Remote Sensing*, vol. GE-25, no. 6, pp. 709-713.
- ERSDAC, (2006). *PALSAR Reference Guide*, 3rd Edition, Earth Remote Sensing Data Analysis Center (ERSDAC), Chuo-ku, Tokyo 104-0054, Japan.
- ERSDAC, (2008). *ERSDAC PALSAR Product Characteristics*, Version 1.6, Earth Remote Sensing Data Analysis Center (ERSDAC), Chuo-ku, Tokyo 104-0054, Japan.
- ESA, (2007). *EnviSat ASAR Product Handbook 2.2*, European Space Agency, Frascati, p. 564.
- Famiglietti, J. S., J. A. Devereaux, C. A. Laymon, T. Tsegaye, P. R. Houser, T. J. Jackson, S. T. Graham, M. Rodell, and P. J. van Oevelen, (1999). "Ground-based investigation of soil moisture variability within remote sensing footprints during the Southern Great Plains 1997 (SGP97) Hydrology Experiment," *Water Resources Research*, vol. 35, no. 6, pp. 1839-1851.
- Famiglietti, J. S., J. W. Rudnicki, and M. Rodell, (1998). "Variability in surface moisture content along a hillslope transect: Rattlesnake Hill, Texas," *Journal of Hydrology*, vol. 210, no. 1-4, pp. 259-281.

- Farr, T. G., C. Elachi, P. Hartl, and K. Chowdhury, (1986). "Microwave Penetration and Attenuation in Desert Soil: A Field Experiment with the Shuttle Imaging Radar," *IEEE Transactions on Geoscience and Remote Sensing*, vol. GE-24, no. 4, pp. 590-594.
- Ferrazzoli, P., S. Paloscia, P. Pampaloni, G. Schiavon, D. Solimini, and P. Coppo, (1992). "Sensitivity to microwave measurements to vegetation biomass and soil moisture content: a case study," *IEEE Transactions on Geoscience and Remote Sensing*, vol. 30, no. 4, pp. 750-756.
- Ferro-Famil, L., E. Pottier, and J. S. Lee, (2001). "Unsupervised classification of multifrequency and fully polarimetric SAR images based on the H/A/alpha-Wishart classifier," *IEEE Transactions on Geoscience and Remote Sensing*, vol. 39, no. 11, pp. 2332-2342.
- Franceschetti, G. and R. Lanari, (1999). *Synthetic Aperture Radar Processing*, F. Shapiro, Ed., CRC Press, Boca Raton, p. 319.
- Freeman, A., (1992). "SAR calibration: an overview," *IEEE Transactions on Geoscience and Remote Sensing*, vol. 30, no. 6, pp. 1107-1121.
- Frost, V. S., J. A. Stiles, K. S. Shanmugan, and J. C. Holtzman, (1982). "A Model for Radar Images and Its Application to Adaptive Digital Filtering of Multiplicative Noise," *IEEE Transactions on Pattern Analysis and Machine Intelligence*, vol. 4, no. 2, pp. 157-166.
- Fung, A. K., (1994). *Microwave Scattering and Emission Models and Their Applications*, F. T. Ulaby, Ed., Artech House, Norwood, MA, USA, p. 573.
- Fung, A. K., M. S. Dawson, K. S. Chen, A. Y. Hsu, E. T. Engman, P. O. Oneill, and J. Wang, (1996). "A modified IEM model for scattering from soil surfaces with application to soil moisture sensing," in *Proceedings of IGARSS '96: Remote Sensing for a Sustainable Future*, 27-31 May, Lincoln, USA, pp. 1297-1299.
- Fung, A. K., Z. Q. Li, and K. S. Chen, (1992). "Backscattering from A Randomly Rough Dielectric Surface," *IEEE Transactions on Geoscience and Remote Sensing*, vol. 30, no. 2, pp. 356-369.
- Garcia Moreno, R., M. C. Díaz Álvarez, A. Saa Requejo, and A. M. Tarquis, (2008). "Multifractal Analysis of Soil Surface Roughness," *Vadose Zone Journal*, vol. 7, no. 2, pp. 512-520.
- Gardner, C. M. K., D. Robinson, K. Blyth, and J. D. Cooper, (2001). "Soil Water Content," in *Soil and Environmental Analysis - Physical Methods*, 2nd ed., rev. and expanded. K. A. Smith and C. E. Mullins, Eds., Marcel Dekker Inc., New York, pp. 1-64.
- Gardner, W. H., (1986). "Water Content," in *Methods of Soil Analysis Part I: Physical and Mineralogical Methods*, 2nd ed. A. Klute, Ed., American Society of Agronomy, Soil Science Society of America, Madison, pp. 493-544.
- Gaskin, G. J. and J. D. Miller, (1996). "Measurement of soil water content using a simplified impedance measuring technique," *Journal of Agricultural Engineering Research*, vol. 63, no. 2, pp. 153-159.
- Goodman, J. W., (1976). "Some Fundamental Properties of Speckle," *J. Opt. Soc. Am.*, vol. 66, no. 11, pp. 1145-1150.
- Graves, C. D., (1956). "Radar Polarization Power Scattering Matrix," *Proceedings of the IRE*, vol. 44, no. 2, pp. 248-252.
- Guarnieri, A. M. and C. Prati, (1996). "ScanSAR focusing and interferometry," *IEEE Transactions on Geoscience and Remote Sensing*, vol. 34, no. 4, pp. 1029-1038.

- Guissard, A., (1994). "Mueller and Kennaugh matrices in radar polarimetry," *IEEE Transactions on Geoscience and Remote Sensing*, vol. 32, no. 3, pp. 590-597.
- Gupta, S. C. and W. E. Larson, (1979). "Estimating Soil-Water Retention Characteristics from Particle-Size Distribution, Organic-Matter Percent, and Bulk-Density," *Water Resources Research*, vol. 15, no. 6, pp. 1633-1635.
- Hajnsek, I., (2001). "Inversion of Surface Parameters using Polarimetric SAR," PhD Thesis, Friedrich-Schiller-Universität Jena, Germany.
- Hajnsek, I., T. Jagdhuber, H. Schon, and K. P. Papathanassiou, (2009). "Potential of Estimating Soil Moisture Under Vegetation Cover by Means of PolSAR," *IEEE Transactions on Geoscience and Remote Sensing*, vol. 47, no. 2, pp. 442-454.
- Hajnsek, I., K. P. Papathanassiou, and S. R. Cloude, (2003a). "A hybrid scattering model for surface parameter estimation using polarimetric SAR interferometry," in *Geoscience and Remote Sensing Symposium, 2003.IGARSS '03.Proceedings.2003 IEEE International*, pp. 693-695.
- Hajnsek, I., E. Pottier, and S. R. Cloude, (2003b). "Inversion of surface parameters from polarimetric SAR," *IEEE Transactions on Geoscience and Remote Sensing*, vol. 41, no. 4, pp. 727-744.
- Hallikainen, M. T., F. T. Ulaby, M. C. Dobson, M. A. Elrayes, and L. K. Wu, (1985). "Microwave Dielectric Behavior of Wet Soil, Part I: Empirical-Models and Experimental-Observations," *IEEE Transactions on Geoscience and Remote Sensing*, vol. 23, no. 1, pp. 25-34.
- Hawley, M. E., T. J. Jackson, and R. H. Mccuen, (1983). "Surface Soil-Moisture Variation on Small Agricultural Watersheds," *Journal of Hydrology*, vol. 62, no. 1-4, pp. 179-200.
- Heimovaara, T. J., E. J. G. deWinter, W. K. P. vanLoon, and D. C. Esveld, (1996). "Frequency-dependent dielectric permittivity from 0 to 1 GHz: Time domain reflectometry measurements compared with frequency domain network analyzer measurements," *Water Resources Research*, vol. 32, no. 12, pp. 3603-3610.
- Henderson, F. M. and A. J. Lewis, (1998). *Manual of Remote Sensing Vol. 2: Principles and Applications of Imaging Radar*, 3rd ed., R. A. Ryerson, Ed., John Wiley & Sons, New York.
- Herkelrath, W. N., S. P. Hamburg, and F. Murphy, (1991). "Automatic, Real-Time Monitoring of Soil-Moisture in A Remote Field Area with Time Domain Reflectometry," *Water Resources Research*, vol. 27, no. 5, pp. 857-864.
- Hill, M. J., G. E. Donald, and P. J. Vickery, (1999). "Relating Radar Backscatter to Biophysical Properties of Temperate Perennial Grassland," *Remote Sensing of Environment*, vol. 67, no. 1, pp. 15-31.
- Hoekstra, P. and A. Delaney, (1974). "Dielectric Properties of Soils at UHF and Microwave Frequencies," *Journal of Geophysical Research*, vol. 79, no. 11, pp. 1699-1708.
- Holmes, J. W., S. A. Taylor, and S. J. Richards, (1967). "Measurement of soil water," in *Irrigation of agricultural lands*. R. M. Hagan, H. R. Haise, and T. W. Edminster, Eds., American Society of Agronomy, Madison, pp. 275-303.
- Hsieh, C. Y. and A. K. Fung, (1997). "Application of an extended IEM to multiple surface scattering and backscatter enhancement," *Proceedings of IGARSS '97: Remote Sensing - A Scientific Vision for Sustainable Development*, pp. 702-704.

- Huisman, J. A., S. S. Hubbard, J. D. Redman, and A. P. Annan, (2003). "Measuring Soil Water Content with Ground Penetrating Radar: A Review," *Vadose Zone Journal*, vol. 2, no. 4, pp. 476-491.
- Hupet, F. and M. Vanclooster, (2002). "Intraseasonal dynamics of soil moisture variability within a small agricultural maize cropped field," *Journal of Hydrology*, vol. 261, no. 1-4, pp. 86-101.
- Hurwitz, J. R. and R. C. Jones, (1941). "A New Calculus for the Treatment of Optical Systems II," *J. Opt. Soc. Am.*, vol. 31, no. 7, pp. 493-495.
- Ishimaru, A., (1997). *Wave Propagation and Scattering in Random Media*, First published by Academic Press 1978, Reissued by IEEE Press and Oxford University Press, IEEE Press, New York.
- Ishimaru, A. and J. S. Chen, (1991). "Scattering from very rough metallic and dielectric surfaces: a theory based on the modified Kirchhoff approximation," *Waves in Random Media*, vol. 1, no. 1, pp. 21-34.
- Jackson, J. D., (1998). *Classical electrodynamics*, 3rd ed., John Wiley & Sons, New York, p. 791.
- Jackson, T. J., (1988). "Laboratory Evaluation Of A Field Portable Dielectric/soil Moisture Probe," in *Proceedings of the IEEE Geoscience and Remote Sensing Symposium, IGARSS'88*, pp. 281-282.
- Jackson, T. J., H. McNairn, M. A. Wetz, B. Brisco, and R. Brown, (1997). "First order surface roughness correction of active microwave observations for estimating soil moisture," *IEEE Transactions on Geoscience and Remote Sensing*, vol. 35, no. 4, pp. 1065-1069.
- Jagdhuber, T. and I. Hajnsek, (2010). "Model-based Inversion of Soil Parameters under Vegetation using Ground-to-Volume Ratios," in *Proceedings of EUSAR 2010, 7-10 June 2010, Aachen, Germany*
- JAXA, (2007). *ALOS User Handbook*, Japan Aerospace Exploration Agency (JAXA), Earth Observation Research Center (EORC), Tsukuba-city, Ibaraki 305-8505, Japan, p. 143.
- Jenny, H., (1994). *Factors Of Soil Formation*, Originally published: 1941, McGraw-Hill, New York. With new foreword by R. Amundson., Dover Publications, New York, p. 271.
- Jeschke, W., (1990). "Digital Close-Range Photogrammetry for Surface Measurement," *Close-Range Photogrammetry Meets Machine Vision*, vol. 1395, pp. 1058-1065.
- Jester, W. and A. Klik, (2005). "Soil surface roughness measurement - methods, applicability, and surface representation," *Catena*, vol. 64, no. 2-3, pp. 174-192.
- Ji, J., P. van der Keur, A. Thomsen, and H. Skriver, (1996). "Soil moisture retrieval using the Danish L- and C-band polarimetric SAR," in *Geoscience and Remote Sensing Symposium, 1996.IGARSS '96. Remote Sensing for a Sustainable Future.*, International, pp. 1300-1302.
- Jones, R. C., (1941). "A New Calculus for the Treatment of Optical Systems I," *J. Opt. Soc. Am.*, vol. 31, no. 7, pp. 488-493.
- Jordan, R. L., (1980). "The Seasat - A synthetic aperture radar system," *IEEE Journal of Oceanic Engineering*, vol. 5, no. 2, pp. 154-164.
- Jury, W. A. and R. Horton, (2004). *Soil Physics*, 6th ed., John Wiley & Sons, Hoboken, NJ, p. 309.

- Kankaku, Y., Y. Osawa, Y. Hatooka, and S. Suzuki, (2010). "Overview of Advanced Land Observing Satellite-2 (ALOS-2) Mission," in *Proceedings of ISPRS TC VIII Symposium 2010 - Networking the World with Remote Sensing*, 9-12 Aug., Kyoto, Japan
- Karam, M. A., A. K. Fung, R. H. Lang, and N. S. Chauhan, (1992). "A microwave scattering model for layered vegetation," *IEEE Transactions on Geoscience and Remote Sensing*, vol. 30, no. 4, pp. 767-784.
- Karkkainen, K., A. Sihvola, and K. Nikoskinen, (2001). "Analysis of a three-dimensional dielectric mixture with finite difference method," *IEEE Transactions on Geoscience and Remote Sensing*, vol. 39, no. 5, pp. 1013-1018.
- Keller, J. M., R. M. Crownover, and R. Y. Chen, (1987). "Characteristics of Natural Scenes Related to the Fractal Dimension," *IEEE Transactions on Pattern Analysis and Machine Intelligence*, vol. PAMI-9, no. 5, pp. 621-627.
- Kennaugh, E. M., (1954). "Effects of Type of Polarization On Echo Characteristics," Antenna Laboratory, The Ohio State University Research Foundation, Columbus, OH, Reports 381-1 to 394-24, publ. 1949-1954.
- Kimura, K., Y. Yamaguchi, and H. Yamada, (2004). "Unsupervised land cover classification using H/alpha(-)/TP space applied to POLSAR image analysis," *IEICE Transactions on Communications*, vol. E87B, no. 6, pp. 1639-1647.
- Können, G. P., (1985). *Polarized Light in Nature*, Cambridge University Press, Cambridge, UK, p. 177.
- Konstantinovic, M., S. Woeckel, P. S. Lammers, and J. Sachs, (2008). "UWB radar system for yield monitoring of sugar beet," *Transactions of the Asabe*, vol. 51, no. 2, pp. 753-761.
- Koorevaar, P., G. Menelik, and C. Dirksen, (1983). *Elements of Soil Physics*, Elsevier Science Publ. B.V., Amsterdam, p. 228.
- Korres, W., C. N. Koyama, P. Fiener, and K. Schneider, (2010). "Analysis of surface soil moisture patterns in agricultural landscapes using Empirical Orthogonal Functions," *Hydrology and Earth System Sciences*, vol. 14, no. 5, pp. 751-764.
- Kostinski, A. and W. Boerner, (1986). "On foundations of radar polarimetry," *IEEE Transactions on Antennas and Propagation*, vol. 34, no. 12, pp. 1395-1404.
- Kownacki, S., (1967). "Simulation of Radar Range and of Doppler Effect by Means of A Stationary Target," *IEEE Transactions on Aerospace and Electronic Systems*, vol. AES3, no. 1, p. 148-&.
- Koyama, C. N., W. Korres, P. Fiener, and K. Schneider, (2010). "Variability of Surface Soil Moisture Observed from Multitemporal C-Band Synthetic Aperture Radar and Field Data," *Vadose Zone Journal*, vol. 9, no. 4, pp. 1014-1024.
- Koyama, C. N. and K. Schneider, (2010). "A Novel Approach To Estimate Soil Moisture Under Vegetation Using Partial Polarimetric ALOS PALSAR Data," in *Proceedings of ISPRS TC VIII Symposium 2010 - Networking the World with Remote Sensing*, 9-12 Aug., Kyoto, Japan
- Koyama, C. N. and K. Schneider, (2011). "Soil Moisture Retrieval Under Vegetation Using Dual Polarized PALSAR Data," in *Proceedings of IGARSS '11: Beyond the Frontiers - Expanding our Knowledge of the World*, pp. 1062-1065.

- Krieger, G., M. Zink, H. Fiedler, I. Hajnsek, M. Younis, S. Huber, M. Bachmann, J. H. Gonzalez, D. Schulze, J. Boer, M. Werner, and A. Moreira, (2009). "The TanDEM-X Mission: Overview and status," in *Radar Conference, 2009 IEEE*, pp. 1-5.
- Kuipers, H., (1957). "A relief meter for soil cultivation studies," *Netherlands Journal of Agricultural Science*, vol. 5, pp. 255-262.
- Lal, R., (1991). "Soil Structure and Sustainability," *Journal of Sustainable Agriculture*, vol. 1, no. 4, pp. 67-92.
- Le Hégarat-Masclé, S., M. Zribi, F. Alem, A. Weisse, and C. Loumagne, (2002). "Soil moisture estimation from ERS/SAR data: Toward an operational methodology," *IEEE Transactions on Geoscience and Remote Sensing*, vol. 40, no. 12, pp. 2647-2658.
- Le Morvan, A., M. Zribi, N. Baghdadi, and A. Chanzy, (2008). "Soil moisture profile effect on radar signal measurement," *Sensors*, vol. 8, no. 1, pp. 256-270.
- Le Toan, A. and T. Le Toan, (1988). "Retrieving Vegetation and Soil Parameters from Radar Measurements," in *Proceedings of Spectral Signatures of Objects in Remote Sensing*, T. D. Guyenne and J. J. Hunt, Eds., -, pp. 105-111.
- Le Toan, T., J. M. Davidson, F. Mattia, P. Borderies, I. Chenerie, and T. Manninen, (1999). "Improved observation and modeling of bare soil surface for soil moisture retrieval," in *Papers from the 2nd International Symposium on Retrieval of bio- and geo-physical parameters from SAR data for land applications*, -, Nordwijk, The Netherlands, pp. 20-24.
- Le Vine, D. M. and M. A. Karam, (1996). "Dependence of attenuation in a vegetation canopy on frequency and plant water content," *IEEE Transactions on Geoscience and Remote Sensing*, vol. 34, no. 5, pp. 1090-1096.
- Leconte, R., F. Brissette, M. Galarneau, and J. Rousselle, (2004). "Mapping near-surface soil moisture with RADARSAT-1 synthetic aperture radar data," *Water Resources Research*, vol. 40, no. 1.
- Lee, H. W., K. S. Chen, J. C. Wang, J. S. Lee, T. D. Wu, and J. C. Shi, (2007). "Extension of advanced integral equation model for calculations of fully polarimetric scattering coefficient from rough surface," in *Proceedings of the IEEE Geoscience and Remote Sensing Symposium, IGARSS'07*, pp. 365-368.
- Lee, J. S., (1981). "Speckle analysis and smoothing of synthetic aperture radar images," *Computer Graphics and Image Processing*, vol. 17, no. 1, pp. 24-32.
- Lee, J. S., T. L. Ainsworth, and A. J. Chen, (2009). "Improved Sigma Filter for Speckle Filtering of SAR Imagery," *IEEE Transactions on Geoscience and Remote Sensing*, vol. 47, no. 1, pp. 202-213.
- Lee, J. S., M. R. Grunes, T. L. Ainsworth, D. Li-Jen, D. L. Schuler, and S. R. Cloude, (1999a). "Unsupervised classification using polarimetric decomposition and the complex Wishart classifier," *IEEE Transactions on Geoscience and Remote Sensing*, vol. 37, no. 5, pp. 2249-2258.
- Lee, J. S., M. R. Grunes, and G. de Grandi, (1999b). "Polarimetric SAR speckle filtering and its implication for classification," *IEEE Transactions on Geoscience and Remote Sensing*, vol. 37, no. 5, pp. 2363-2373.
- Lee, J. S., M. R. Grunes, and S. A. Mango, (1991). "Speckle reduction in multipolarization, multifrequency SAR imagery," *IEEE Transactions on Geoscience and Remote Sensing*, vol. 29, no. 4, pp. 535-544.

- Lee, J. S., M. R. Grunes, and E. Pottier, (2001). "Quantitative comparison of classification capability: Fully polarimetric versus dual and single-polarization SAR," *IEEE Transactions on Geoscience and Remote Sensing*, vol. 39, no. 11, pp. 2343-2351.
- Lee, J. S., M. R. Grunes, E. Pottier, and L. Ferro-Famil, (2004). "Unsupervised terrain classification preserving polarimetric scattering characteristics," *IEEE Transactions on Geoscience and Remote Sensing*, vol. 42, no. 4, pp. 722-731.
- Lee, J. S., M. R. Grunes, D. L. Schuler, E. Pottier, and L. Ferro-Famil, (2006). "Scattering-model-based speckle filtering of polarimetric SAR data," *IEEE Transactions on Geoscience and Remote Sensing*, vol. 44, no. 1, pp. 176-187.
- Lee, J. S., L. Jurkevich, P. Dewaele, P. Wambacq, and A. Oosterlinck, (1994). "Speckle filtering of synthetic aperture radar images: A review," *Remote Sensing Reviews*, vol. 8, no. 4, pp. 313-340.
- Lee, J. S. and E. Pottier, (2009). *Polarimetric Radar Imaging - From Basics to Applications*, 1st Edition, CRC Press, Taylor & Francis Group, LLC, Boca Raton, FL 33487-2742, USA.
- Licheri, M., N. Floury, M. Borgeaud, and M. Migliaccio, (2001). "On the scattering from natural surfaces: the IEM and the improved IEM," *Proceedings of IGARSS '01: Scanning the Present, Resolving the Future*, pp. 2911-2913.
- Lievens, H. and N. E. C. Verhoest, (2011). "On the Retrieval of Soil Moisture in Wheat Fields From L-Band SAR Based on Water Cloud Modeling, the IEM, and Effective Roughness Parameters," *Geoscience and Remote Sensing Letters, IEEE*, vol. 8, no. 4, pp. 740-744.
- Lin-Kun, W., R. K. Moore, and R. Zoughi, (1985). "Sources of Scattering from Vegetation Canopies at 10 GHz," *IEEE Transactions on Geoscience and Remote Sensing*, vol. GE-23, no. 5, pp. 737-745.
- Loew, A., (2004). "Coupled Modelling of Land Surface Microwave Interactions Using ENVISAT ASAR Data," PhD Thesis, Fakultät der Geowissenschaften, Ludwig Maximilian Universität München, Germany.
- Loew, A., R. Ludwig, and W. Mauser, (2003). "Mesoscale soil moisture estimation from SAR data using subscale landuse information," in *Proceedings of IGARSS '03: Learning from Earth's Shapes and Sizes*, pp. 1396-1398.
- Loew, A., R. Ludwig, and W. Mauser, (2006). "Derivation of surface soil moisture from ENVISAT ASAR wide swath and image mode data in agricultural areas," *IEEE Transactions on Geoscience and Remote Sensing*, vol. 44, no. 4, pp. 889-899.
- Lopes, A., R. Touzi, and E. Nezry, (1990). "Adaptive Speckle Filters and Scene Heterogeneity," *IEEE Transactions on Geoscience and Remote Sensing*, vol. 28, no. 6, pp. 992-1000.
- Lopez-Martinez, C., L. Pipia, and K. P. Papathanassiou, (2008). "Analysis and Correction of Speckle Noise Effects on Polinsar Data Based on Coherent Modeling," in *Proceedings of the IEEE Geoscience and Remote Sensing Symposium, IGARSS'08*, p. II-629.
- Low, A. J., (1954). "The Study of Soil Structure in the Field and the Laboratory," *Journal of Soil Science*, vol. 5, no. 1, pp. 57-79.
- Luneburg, E., S. R. Cloude, and W. M. Boerner, (1997). "On the proper polarimetric scattering matrix formulation of the forward propagation versus backscattering radar systems description," in *Geoscience and Remote Sensing, 1997.IGARSS '97.Remote Sensing - A Scientific Vision for Sustainable Development., 1997 IEEE International*, pp. 1591-1593.

- Macaskill, C., (1991). "Geometric optics and enhanced backscatter from very rough surfaces," *J. Opt. Soc. Am.*, vol. 8, no. 1, pp. 88-96.
- Marliani, F., S. Paloscia, P. Pampaloni, and J. A. Kong, (2002). "Simulating coherent backscattering from crops during the growing cycle," *IEEE Transactions on Geoscience and Remote Sensing*, vol. 40, no. 1, pp. 162-177.
- Marshall, T. J., (1966). "Measurement and Control of Water in Soil," *Australian Journal of Instrument Technology*, vol. 22, no. 3, p. 81-&.
- Marshall, T. J., J. W. Holmes, and C. W. Rose, (1999). *Soil Physics*, 3rd Ed., Cambridge University Press, Cambridge, p. 457.
- Martin, R. D. Jr., G. Asrar, and E. T. Kanemasu, (1989). "C-band scatterometer measurements of a tallgrass prairie," *Remote Sensing of Environment*, vol. 29, no. 3, pp. 281-292.
- Marzahn, P. and R. Ludwig, (2009). "On the derivation of soil surface roughness from multi parametric PolSAR data and its potential for hydrological modeling," *Hydrology and Earth System Sciences*, vol. 13, no. 3, pp. 381-394.
- Mattei, E., A. De Santis, A. Di Matteo, E. Pettinelli, and G. Vannaroni, (2008). "Electromagnetic Parameters of Dielectric and Magnetic Mixtures Evaluated by Time-Domain Reflectometry," *IEEE Geoscience and Remote Sensing Letters*, vol. 5, no. 4, pp. 730-734.
- Mattia, F., M. W. J. Davidson, T. Le Toan, C. M. F. D'Haese, N. E. C. Verhoest, A. M. Gatti, and M. Borgeaud, (2003a). "A comparison between soil roughness statistics used in surface scattering models derived from mechanical and laser profilers," *IEEE Transactions on Geoscience and Remote Sensing*, vol. 41, no. 7, pp. 1659-1671.
- Mattia, F. and T. Le Toan, (1999). "Backscattering properties of multi-scale rough surfaces," *Journal of Electromagnetic Waves and Applications*, vol. 13, no. 4, pp. 493-527.
- Mattia, F., T. Le Toan, G. Picard, F. I. Posa, A. D'Alessio, C. Notarnicola, A. M. Gatti, M. Rinaldi, G. Satalino, and G. Pasquariello, (2003b). "Multitemporal C-band radar measurements on wheat fields," *IEEE Transactions on Geoscience and Remote Sensing*, vol. 41, no. 7, pp. 1551-1560.
- Mattia, F., G. Satalino, L. Dente, and G. Pasquariello, (2006). "Using a priori information to improve soil moisture retrieval from ENVISAT ASAR AP data in semiarid regions," *IEEE Transactions on Geoscience and Remote Sensing*, vol. 44, no. 4, pp. 900-912.
- Mausser, W., R. Stolz, K. Schneider, and H. Bach, (2000). "Comparison of ERS SAR data derived soil moisture distributions with SVAT model results," in *Proceedings of ERS-ENVISAT-Symposium - Looking Down to Earth in the Nwe Millenium*, -, Gothenburg, Sweden
- McNairn, H., A. Merzouki, and A. Pacheco, (2010). "Estimating Surface Soil Moisture Using RADARSAT-2," in *Proceedings of ISPRS TC VIII Symposium 2010 - Networking the World with Remote Sensing*, 9-12 Aug., Kyoto, Japan
- Meier, E., U. Frei, and D. Nuesch, (1993). "Precise Terrain Corrected Geocoded Images,". G. Schreier, Ed., Wichmann, Karlsruhe, Germany, pp. 173-186.
- Meier, E., F. Holecz, and D. Ntiesch, (1992). "Radiometric Corrections In Slant Range And Geocoded Sar Images Considering Topographic Effects," in *Proceedings of IGARSS '92: Space Remote Sensing*, pp. 620-622.

- Meier, U. ed., (2001). *Growth stages of mono- and dicotyledonous plants*, BBCH Monograph, German Federal Biological Research Center for Agriculture and Forestry, 2nd ed. Braunschweig, Germany, p. 158.
- Meijering, E. and M. Unser, (2003). "A note on cubic convolution interpolation," *IEEE Transactions on Image Processing*, vol. 12, no. 4, pp. 477-479.
- Montzka, C., M. Canty, R. Kunkel, G. Menz, H. Vereecken, and F. Wendland, (2008). "Modelling the water balance of a mesoscale catchment basin using remotely sensed land cover data," *Journal of Hydrology*, vol. 353, no. 3-4, pp. 322-334.
- Moreira, A., G. Krieger, M. Younis, I. Hajnsek, K. Papathanassiou, M. Eineder, and F. DeZan, (2011). "Tandem-L: A Mission Proposal for Monitoring Dynamic Earth Processes," in *Proceedings of IGARSS '11: Beyond the Frontiers - Expanding our Knowledge of the World*, pp. 1385-1388.
- Moreira, A., J. Mittermayer, and R. Scheiber, (1996). "Extended chirp scaling algorithm for air- and spaceborne SAR data processing in stripmap and ScanSAR imaging modes," *IEEE Transactions on Geoscience and Remote Sensing*, vol. 34, no. 5, pp. 1123-1136.
- Mortland, M. M., (1954). "Specific Surface and Its Relationships to Some Physical and Chemical Properties of Soil," *Soil Science*, vol. 78, no. 5, pp. 343-347.
- Mott, H., (2007). *Remote Sensing with Polarimetric Radar*, 1st Edition, John Wiley & Sons, Inc., Hoboken, New Jersey 07030, USA.
- Navarro, V., M. Candej, A. Yustres, O. Merlo, and M. Mena, (2006). "Analysis of installation of FDR sensors in a hard soil," *Geotechnical Testing Journal*, vol. 29, no. 6, pp. 462-466.
- Némethy, G., (1966). "Structure of water and of aqueous solutions," *Cryobiology*, vol. 3, no. 1, pp. 19-26.
- Nezry, E., A. Lopes, and R. Touzi, (1991). "Detection Of Structural And Textural Features For Sar Images Filtering," in *Proceedings of IGARSS '91: Remote Sensing - Global Monitoring for Earth Management*, pp. 2169-2172.
- Nolan, M. and D. R. Fatland, (2003). "Penetration depth as a DInSAR observable and proxy for soil moisture," *IEEE Transactions on Geoscience and Remote Sensing*, vol. 41, no. 3, pp. 532-537.
- Oades, J. M., (1993). "The Role of Biology in the Formation, Stabilization and Degradation of Soil Structure," *Geoderma*, vol. 56, no. 1-4, pp. 377-400.
- Ogilvy, J. A. and J. R. Foster, (1989). "Rough Surfaces - Gaussian Or Exponential Statistics," *Journal of Physics D-Applied Physics*, vol. 22, no. 9, pp. 1243-1251.
- Oh, Y., (2004). "Quantitative retrieval of soil moisture content and surface roughness from multipolarized radar observations of bare soil surfaces," *IEEE Transactions on Geoscience and Remote Sensing*, vol. 42, no. 3, pp. 596-601.
- Oh, Y., (2006). "Robust inversion technique for retrieving soil moisture from multi-polarised backscatter of bare surface," *Electronics Letters*, vol. 42, no. 7, pp. 414-415.
- Oh, Y. and J. Y. Hong, (2007). "Effect of surface profile length on the backscattering coefficients of bare surfaces," *IEEE Transactions on Geoscience and Remote Sensing*, vol. 45, no. 3, pp. 632-638.
- Oh, Y. and Y. C. Kay, (1998). "Condition for precise measurement of soil surface roughness," *IEEE Transactions on Geoscience and Remote Sensing*, vol. 36, no. 2, pp. 691-695.

- Oh, Y., K. Sarabandi, and F. T. Ulaby, (1992). "An Empirical-Model and An Inversion Technique for Radar Scattering from Bare Soil Surfaces," *IEEE Transactions on Geoscience and Remote Sensing*, vol. 30, no. 2, pp. 370-381.
- Oh, Y., K. Sarabandi, and F. T. Ulaby, (1994). "An inversion algorithm for retrieving soil moisture and surface roughness from polarimetric radar observation," in *Proceedings of IGARSS '94: Surface and Atmospheric Remote Sensing - Technologies, Data Analysis and Interpretation*, 8-12 Aug., Pasadena, USA, pp. 1582-1584.
- Oh, Y., K. Sarabandi, and F. T. Ulaby, (2002). "Semi-empirical model of the ensemble-averaged differential Mueller matrix for microwave backscattering from bare soil surfaces," *IEEE Transactions on Geoscience and Remote Sensing*, vol. 40, no. 6, pp. 1348-1355.
- Ohki, M. and M. Shimada, (2010). "A Study of Supervised Land-cover Classification by ALOS/PALSAR Polarimetric Interferometry," in *Proceedings of EUSAR 2010*, -, Aachen, Germany
- Okada, Y., T. Hamasaki, M. Tsuji, M. Iwamoto, K. Hariu, Y. Kankaku, S. Suzuki, and Y. Osawa, (2011). "Hardware Performance of L-band SAR System Onboard ALOS-2," in *Proceedings of IGARSS '11: Beyond the Frontiers - Expanding our Knowledge of the World*, pp. 894-897.
- Oldak, A., T. J. Jackson, and Y. Pachepsky, (2002). "Using GIS in passive microwave soil moisture mapping and geostatistical analysis," *International Journal of Geographical Information Science*, vol. 16, no. 7, pp. 681-698.
- Oliver, C. and S. Quegan, (2004). *Understanding Synthetic Aperture Radar Images*, corrected reprinting of the 1988 edition originally published by Artech House, SciTech Publishing, Raleigh, p. 479.
- Owe, M., E. B. Jones, and T. J. Schmugge, (1982). "Soil-Moisture Variation Patterns Observed in Hand County, South-Dakota," *Water Resources Bulletin*, vol. 18, no. 6, pp. 949-954.
- Paloscia, S., P. Pampaloni, S. Pettinato, and E. Santi, (2008). "A Comparison of Algorithms for Retrieving Soil Moisture from ENVISAT/ASAR Images," *IEEE Transactions on Geoscience and Remote Sensing*, vol. 46, no. 10, pp. 3274-3284.
- Paloscia, S., E. Santi, S. Pettinato, and M. Angiulli, (2004). "Soil properties estimates from SAR data by using a Bayesian approach combined with IEM," in *Proceedings of IGARSS '04: Science for Society - Exploring and Managing a Changing Planet*, pp. 819-822.
- Panciera, R., J. P. Walker, and O. Merlin, (2009). "Improved Understanding of Soil Surface Roughness Parameterization for L-Band Passive Microwave Soil Moisture Retrieval," *IEEE Geoscience and Remote Sensing Letters*, vol. 6, no. 4, pp. 625-629.
- Papa, R., J. Lennon, and R. Taylor, (1986). "The variation of bistatic rough surface scattering cross section for a physical optics model," *IEEE Transactions on Antennas and Propagation*, vol. 34, no. 10, pp. 1229-1237.
- Papathanassiou, K. P. and S. R. Cloude, (1997). "Polarimetric effects in repeat-pass SAR interferometry," in *Proceedings of IGARSS '97: Remote Sensing - A Scientific Vision for Sustainable Development*, pp. 1926-1928.
- Papathanassiou, K. P. and S. R. Cloude, (2001). "Single-baseline polarimetric SAR interferometry," *Geoscience and Remote Sensing, IEEE Transactions on*, vol. 39, no. 11, pp. 2352-2363.

- Papathanassiou, K. P., L. Marotti, R. Z. Schneider, and I. Hajnsek, (2007). "Pol-InSAR Results from ALOS-PalSAR," in *Geoscience and Remote Sensing Symposium, 2007.IGARSS 2007.IEEE International*, p. 3597.
- Parchomchuk, P., W. W. Wallender, and R. J. King, (1990). "Calibration of a waveguide sensor for measuring soil moisture," *IEEE Transactions on Geoscience and Remote Sensing*, vol. 28, no. 5, pp. 873-878.
- Peplinski, N. R., F. T. Ulaby, and M. C. Dobson, (1995). "Corrections to "Dielectric Properties of Soils in the 0.3-1.3-GHz Range"," *IEEE Transactions on Geoscience and Remote Sensing*, vol. 33, no. 6, p. 1340.
- Perez-Gutierrez, C., J. Martinez-Fernandez, N. Sanchez, and J. varez-Mozos, (2007). "Modeling of soil roughness using terrestrial laser scanner for soil moisture retrieval," in *Proceedings of IGARSS '07: Sensing and Understanding Our Planet*, pp. 1877-1880.
- Picard, G., T. Le Toan, and F. Mattia, (2003). "Understanding C-band radar backscatter from wheat canopy using a multiple-scattering coherent model," *IEEE Transactions on Geoscience and Remote Sensing*, vol. 41, no. 7, pp. 1583-1591.
- Pottier, E., (1998). "Unsupervised Classification Scheme of PolSAR Images based on the Complex Wishard Distribution and the H/A/alpha Polarimetric Decomposition Theorem," in *Proceedings of 4th Int. Workshop on Radar Polarimetry, PIERS*, pp. 535-547.
- Pottier, E., L. Ferro-Famil, S. Allain, S. Cloude, I. Hajnsek, K. Papathanassiou, A. Moreira, M. Williams, A. Minchella, and Y. L. Desnos, (2008). "PolSARpro v3.3: The Educational Toolbox for Polarimetric and Interferometric Polarimetric SAR Data Processing," in *Proceedings of the IEEE Geoscience and Remote Sensing Symposium, IGARSS'08*, p. III-471.
- Prevot, L., I. Champion, and G. Guyot, (1993). "Estimating Surface Soil-Moisture and Leaf-Area Index of A Wheat Canopy Using A Dual-Frequency (C and X-Bands) Scatterometer," *Remote Sensing of Environment*, vol. 46, no. 3, pp. 331-339.
- Quegan, S. and I. Rhodes, (1995). "Statistical models for polarimetric data: consequences, testing and validity," *International Journal of Remote Sensing*, vol. 16, no. 7, pp. 1183-1210.
- Quesney, A., S. Le Høgarat-Masclé, O. Taconet, D. Vidal-Madjar, J. P. Wigneron, C. Loumagne, and M. Normand, (2000). "Estimation of Watershed Soil Moisture Index from ERS/SAR Data," *Remote Sensing of Environment*, vol. 72, no. 3, pp. 290-303.
- Rakotoarivony, L., O. Taconet, D. VidalMadjar, P. Bellemain, and M. Benallegue, (1996). "Radar backscattering over agricultural bare soils," *Journal of Electromagnetic Waves and Applications*, vol. 10, no. 2, pp. 187-209.
- Raney, R. K., (2006). "Dual-polarized SAR and Stokes parameters," *IEEE Geoscience and Remote Sensing Letters*, vol. 3, no. 3, pp. 317-319.
- Reigber, A., (2001). "Airborne Polarimetric SAR Tomography," University of Stuttgart, Germany.
- Ren, W. and M. Tateiba, (1998). "Dielectric mixing formula for multiphase mixtures," in *Proceedings of IGARSS '98: Remote Sensing and Managing the Environment*, pp. 2089-2091.
- Reynolds, S. G., (1970a). "The gravimetric method of soil moisture determination Part II Typical required sample sizes and methods of reducing variability," *Journal of Hydrology*, vol. 11, no. 3, pp. 274-287.

- Reynolds, S. G., (1970b). "The gravimetric method of soil moisture determination Part I A study of equipment, and methodological problems," *Journal of Hydrology*, vol. 11, no. 3, pp. 258-273.
- Reynolds, S. G., (1970c). "The gravimetric method of soil moisture determination Part III An examination of factors influencing soil moisture variability," *Journal of Hydrology*, vol. 11, no. 3, pp. 288-300.
- Rodríguez, E., (1991). "Beyond the Kirchhoff approximation II electromagnetic scattering," *Radio Science*, vol. 26, no. 1, pp. 121-132.
- Rodriguez-Iturbe, I., G. K. Vogel, R. Rigon, D. Entekhabi, F. Castelli, and A. Rinaldo, (1995). "On the Spatial-Organization of Soil-Moisture Fields," *Geophysical Research Letters*, vol. 22, no. 20, pp. 2757-2760.
- Rombach, M. and W. Mauser, (1997). "Multi-annual analysis of ERS surface soil moisture measurements of different land uses," in *Proceedings of 3rd ERS Symposium - Space at the Service of the Environment*, -, Florence, Italy
- Romkens, M. J. M. and J. Y. Wang, (1986). "Effect of Tillage on Surface-Roughness," *Transactions of the Asae*, vol. 29, no. 2, pp. 429-433.
- Romshoo, S. A., T. Nakaegawa, T. Oki, and K. Musiake, (2000). "Estimation of Soil Moisture Using Spaceborne SAR Data and Scattering Models," in *Proceedings of 28th Remote Sensing Society of Japan Conference*, -, Tsukuba, Japan
- Rosich, B. and P. Meadows, (2004). "Absolute Calibration of ASAR Level 1 Products," *ENVI-CLVL-EOPG-TN-03-0010*, no. Issue 1 Revision 5, pp. 1-26.
- Roth, C. H., M. A. Malicki, and R. Plagge, (1992). "Empirical evaluation of the relationship between soil dielectric constant and volumetric water content as the basis for calibrating soil moisture measurements by TDR," *Journal of Soil Science*, vol. 43, no. 1, pp. 1-13.
- Saatchi, S. S., D. M. Levine, and R. H. Lang, (1994). "Microwave Backscattering and Emission Model for Grass Canopies," *IEEE Transactions on Geoscience and Remote Sensing*, vol. 32, no. 1, pp. 177-186.
- Sander, K. F. and G. A. L. Reed, (1978). *Transmission and propagation of electromagnetic waves*, Cambridge University Press, Bristol, p. 410.
- Satalino, G., F. Mattia, M. W. J. Davidson, T. Le Toan, G. Pasquariello, and M. Borgeaud, (2002). "On current limits of soil moisture retrieval from ERS-SAR data," *IEEE Transactions on Geoscience and Remote Sensing*, vol. 40, no. 11, pp. 2438-2447.
- Satalino, G., G. Pasquariello, F. Mattia, M. Davidson, T. Le Toan, and M. Borgeaud, (2001). "Soil moisture retrieval using SAR data and a priori roughness information," *Proceedings of IGARSS '01: Scanning the Present, Resolving the Future*, pp. 3111-3113.
- Schaber, G. G., J. F. Mccauley, C. S. Breed, and G. R. Olhoeft, (1986). "Shuttle Imaging Radar: Physical Controls on Signal Penetration and Subsurface Scattering in the Eastern Sahara," *IEEE Transactions on Geoscience and Remote Sensing*, vol. GE-24, no. 4, pp. 603-623.
- Scheffer, F. and P. Schachtschabel, (2002). *Lehrbuch der Bodenkunde*, 15. Aufl. / neubearb. und erw. von H.-P. Blume, Spektrum Akad. Verlag, Heidelberg, p. 593.
- Schmidt, K. and G. Trenkler, (2006). *Einführung in die Moderne Matrix-Algebra*, 2. Auflage, Springer-Verlag, Berlin, Germany, p. 275.

- Schmugge, T. J., T. J. Jackson, and H. L. McKim, (1980). "Survey of methods for soil moisture determination," *Water Resources Research*, vol. 16, no. 6, pp. 961-979.
- Schneeberger, K., M. Schwank, C. Stamm, P. de Rosnay, C. Matzler, and H. Fluhler, (2004). "Topsoil structure influencing soil water retrieval by microwave radiometry," *Vadose Zone Journal*, vol. 3, no. 4, pp. 1169-1179.
- Schneider, K. and N. Oppelt, (1998). "The determination of mesoscale soil moisture patterns with ERS data," in *Proceedings of IGARSS '98: Remote Sensing and Managing the Environment*, pp. 1831-1833.
- Schulze, C. and M. Matthies, (2001). "Georeferenced aquatic fate simulation of cleaning agent and detergent ingredients in the river Rur catchment (Germany)," *The Science of The Total Environment*, vol. 280, no. 1-3, pp. 55-77.
- Sci Lands, (2008). "Dokumentation zur Aufbereitung eines DGM10 für das Rur-Gebiet," Scilands GmbH, Göttingen, Germany.
- Senior, T. B. A., K. Sarabandi, and F. T. Ulaby, (1987). "Measuring and Modeling the Backscattering Cross-Section of A Leaf," *Radio Science*, vol. 22, no. 6, pp. 1109-1116.
- Serbin, G. and D. Or, (2004). "Ground-penetrating radar measurement of soil water content dynamics using a suspended horn antenna," *IEEE Transactions on Geoscience and Remote Sensing*, vol. 42, no. 8, pp. 1695-1705.
- Shaver, T. M., G. A. Peterson, L. R. Ahuja, D. G. Westfall, L. A. Sherrod, and G. Dunn, (2002). "Surface soil physical properties after twelve years of dryland no-till management," *Soil Sci Soc Am J*, vol. 66, no. 4, pp. 1296-1303.
- Shepard, M. K., R. A. Brackett, and R. E. Arvidson, (1995). "Self-Affine (Fractal) Topography - Surface Parameterization and Radar Scattering," *Journal of Geophysical Research-Planets*, vol. 100, no. E6, pp. 11709-11718.
- Sherwin, C. W., J. P. Ruina, and R. D. Rawcliffe, (1962). "Some Early Developments in Synthetic Aperture Radar Systems," *Military Electronics, IRE Transactions on*, vol. MIL-6, no. 2, pp. 111-115.
- Shi, J. and J. van Zyl, (1998). "On improvement of bare surface soil moisture estimation from L-band SAR measurements," in *Geoscience and Remote Sensing Symposium Proceedings, 1998.IGARSS '98.1998 IEEE International*, pp. 1834-1836.
- Shi, J. C., J. Wang, A. Y. Hsu, P. E. O'Neill, and E. T. Engman, (1997). "Estimation of bare surface soil moisture and surface roughness parameter using L-band SAR image data," *IEEE Transactions on Geoscience and Remote Sensing*, vol. 35, no. 5, pp. 1254-1266.
- Shimada, M., O. Isoguchi, T. Tadono, and K. Isono, (2009). "PALSAR Radiometric and Geometric Calibration," *IEEE Transactions on Geoscience and Remote Sensing*, vol. 47, no. 12, pp. 3915-3932.
- Shin, R. T. and J. A. Kong, (1984). "Scattering of electromagnetic waves from a randomly perturbed quasiperiodic surface," *Journal of Applied Physics*, vol. 56, no. 1, pp. 10-21.
- Sihvola, A. H. and J. A. Kong, (1988). "Effective permittivity of dielectric mixtures," *IEEE Transactions on Geoscience and Remote Sensing*, vol. 26, no. 4, pp. 420-429.

- Sinclair, G., (1950). "The Transmission and Reception of Elliptically Polarized Waves," *Proceedings of the IRE*, vol. 38, no. 2, pp. 148-151.
- Skolnik, M. I., (1981). *Introduction to Radar Systems*, 3rd ed., McGraw-Hill Book Company, Singapore, p. 581.
- Skolnik, M. J., (1990). *Radar Handbook*, 2nd ed, D. A. Gonneau and B. E. Eckes, Eds., McGraw-Hill, Boston.
- Slattery, M. C. and R. B. Bryan, (1992). "Laboratory Experiments on Surface Seal Development and Its Effect on Interrill Erosion Processes," *Journal of Soil Science*, vol. 43, no. 3, pp. 517-529.
- Small, D., M. Jehle, A. Schubert, and E. Meier, (2009). "Accurate Geometric Correction for Normalization of PALSAR Radiometry," in *Proceedings of ALOS PI Symposium 2008*, H. Lacoste and L. Ouwehand, Eds.
- Small, D., E. Meier, and D. Nuesch, (2004). "Robust radiometric terrain correction for SAR image comparisons," in *Proceedings of the IEEE Geoscience and Remote Sensing Symposium, IGARSS'04*, pp. 1730-1733.
- Snell, F. D., C. T. Snell, and I. Reich, (1950). "The Nature of Soil to be Deterged and Its Bonding to the Surface," *Journal of the American Oil Chemists Society*, vol. 27, no. 2, pp. 62-68.
- Song, K. J., X. B. Zhou, and Y. Fan, (2009). "Empirically Adopted IEM for Retrieval of Soil Moisture From Radar Backscattering Coefficients," *IEEE Transactions on Geoscience and Remote Sensing*, vol. 47, no. 6, pp. 1662-1672.
- Stewart, B. A. and M. E. Sumner, (1992). *Soil crusting : chemical and physical processes*, B. A. Stewart and M. E. Sumner, Eds., Lewis Publishers, Boca Raton : p. 384.
- Stiles, J. M. and K. Sarabandi, (2000). "Electromagnetic scattering from grassland Part I: A fully phase-coherent scattering model," *IEEE Transactions on Geoscience and Remote Sensing*, vol. 38, no. 1, pp. 339-348.
- Stiles, J. M., K. Sarabandi, and F. T. Ulaby, (2000). "Electromagnetic scattering from grassland Part II: Measurement and modeling results," *IEEE Transactions on Geoscience and Remote Sensing*, vol. 38, no. 1, pp. 349-356.
- Stratton, J. A., (1941). *Electromagnetic Theory*, McGraw-Hill Book Company, New York, p. 615.
- Sun, Y. R., J. H. Lin, P. S. Lammers, and L. Damerow, (2006). "Estimating surface porosity by roughness measurement in a silt-loam field," *Journal of Plant Nutrition and Soil Science-Zeitschrift fur Pflanzenernahrung und Bodenkunde*, vol. 169, no. 5, pp. 630-632.
- Swaby, R. J., (1949). "The Relationship Between Micro-Organisms and Soil Aggregation," *Journal of General Microbiology*, vol. 3, no. 2, p. 236-&.
- Taconet, O., D. VidalMadjar, C. Emblanch, and M. Normand, (1996). "Taking into account vegetation effects to estimate soil moisture from C-band radar measurements," *Remote Sensing of Environment*, vol. 56, no. 1, pp. 52-56.
- Teuling, A. J. and P. A. Troch, (2005). "Improved understanding of soil moisture variability dynamics," *Geophysical Research Letters*, vol. 32, no. 5.
- Tomiyasu, K., (1978). "Tutorial review of synthetic-aperture radar (SAR) with applications to imaging of the ocean surface," *Proceedings of the IEEE*, vol. 66, no. 5, pp. 563-583.

- Topp, G. C. and J. L. Davis, (1985). "Measurement of Soil-Water Content Using Time-Domain Reflectometry (Tdr) - A Field-Evaluation," *Soil Sci Soc Am J*, vol. 49, no. 1, pp. 19-24.
- Topp, G. C., J. L. Davis, and A. P. Annan, (1980). "Electromagnetic Determination of Soil Water Content: Measurements in Coaxial Transmission Lines," *Water Resources Research*, vol. 16, no. 3, pp. 574-582.
- Topp, G. C., J. L. Davis, W. G. Bailey, and W. D. Zebchuk, (1984). "The Measurement of Soil-Water Content Using A Portable Tdr Hand Probe," *Canadian Journal of Soil Science*, vol. 64, no. 3, pp. 313-321.
- Touzi, R., (2001). "Multiplicative and product model constraints upon speckle filtering of SAR images," in *Proceedings of IGARSS '01: Scanning the Present, Resolving the Future*, pp. 1161-1163.
- Touzi, R., (2007). "Target Scattering Decomposition in Terms of Roll-Invariant Target Parameters," *IEEE Transactions on Geoscience and Remote Sensing*, vol. 45, no. 1, pp. 73-84.
- Touzi, R. and A. Lopes, (1994). "The Principle of Speckle Filtering in Polarimetric SAR Imagery," *IEEE Transactions on Geoscience and Remote Sensing*, vol. 32, no. 5, pp. 1110-1114.
- Touzi, R., S. Nedelcu, and M. Shimada, (2008). "Polarimetric PALSAR System Model Assessment and Calibration," in *Proceedings of the IEEE Geoscience and Remote Sensing Symposium, IGARSS'08*, p. I-21.
- Ulaby, F. T., P. P. Batlivala, and M. C. Dobson, (1978). "Microwave Backscatter Dependence on Surface Roughness, Soil Moisture, and Soil Texture: Part I-Bare Soil," *IEEE Transactions on Geoscience Electronics*, vol. 16, no. 4, pp. 286-295.
- Ulaby, F. T., M. C. Dobson, and G. A. Bradley, (1981a). "Radar reflectivity of bare and vegetation-covered soil," *Advances in Space Research*, vol. 1, no. 10, pp. 91-104.
- Ulaby, F. T. and R. P. Jedlicka, (1984). "Microwave Dielectric Properties of Plant Materials," *IEEE Transactions on Geoscience and Remote Sensing*, vol. GE-22, no. 4, pp. 406-415.
- Ulaby, F. T., F. Kouyate, A. K. Fung, and A. J. Sieber, (1982a). "A Backscatter Model for a Randomly Perturbed Periodic Surface," *IEEE Transactions on Geoscience and Remote Sensing*, vol. GE-20, no. 4, pp. 518-528.
- Ulaby, F. T., R. K. Moore, and A. K. Fung, (1981b). *Microwave Remote Sensing Active and Passive Volume I - Fundamentals and Radiometry*, 1st Edition, D. S. Simonett, Ed., Addison-Wesley Publishing Company, Inc., Reading, Massachusetts 01867, USA, p. 456.
- Ulaby, F. T., R. K. Moore, and A. K. Fung, (1982b). *Microwave Remote Sensing Active and Passive Volume II - Surface Scattering and Emission Theory*, 1st Edition, D. S. Simonett, Ed., Addison-Wesley Publishing Company, Inc., Reading, Massachusetts 01867, USA, p. 1064.
- Ulaby, F. T., R. K. Moore, and A. K. Fung, (1986). *Microwave Remote Sensing Active and Passive Volume III - From Theory to Applications*, D. S. Simonett, Ed., Artech House, Inc., Norwood, Massachusetts 02062, USA, p. 2136.
- Ulander, L. M. H., (1996). "Radiometric slope correction of synthetic-aperture radar images," *IEEE Transactions on Geoscience and Remote Sensing*, vol. 34, no. 5, pp. 1115-1122.

- Van Der Heijden, G. W. A. M., J. G. P. W. Clevers, and A. G. T. Schut, (2007). "Combining close-range and remote sensing for local assessment of biophysical characteristics of arable land," *International Journal of Remote Sensing*, vol. 28, no. 24, pp. 5485-5502.
- van Zyl, J. J. and Y. J. Kim, (2001). "A quantitative comparison of soil moisture inversion algorithms," *Proceedings of IGARSS '01: Scanning the Present, Resolving the Future*, pp. 37-39.
- Veihmeyer, F. J. and A. H. Hendrickson, (1950). "Soil Moisture in Relation to Plant Growth," *Annual Review of Plant Physiology and Plant Molecular Biology*, vol. 1, pp. 285-304.
- Vereecken, H., T. Kamai, T. Harter, R. Kasteel, J. Hopmans, and J. Vanderborght, (2007). "Explaining soil moisture variability as a function of mean soil moisture: A stochastic unsaturated flow perspective," *Geophysical Research Letters*, vol. 34, no. 22.
- Verhoest, N. E. C., R. Hoeben, F. P. De Troch, and P. A. Troch, (2000). "Soil moisture inversion from ERS and SIR-C imagery at the Zwalm catchment, Belgium," in *Proceedings of IGARSS '00: Taking the Pulse of the Planet*, pp. 2041-2043.
- Verhoest, N. E. C., H. Lievens, W. Wagner, J. varez-Mozos, M. S. Moran, and F. Mattia, (2008). "On the soil roughness parameterization problem in soil moisture retrieval of bare surfaces from synthetic aperture radar," *Sensors*, vol. 8, no. 7, pp. 4213-4248.
- von Hippel, A., (1995). *Dielectrics and Waves*, New ed., A. S. Labounsky, Ed., Artech House, Boston, p. 284.
- Wang, H. P., K. Ouchi, M. Watanabe, M. Shimada, T. Tadono, A. Rosenqvist, S. A. Romshoo, M. Matsuoka, T. Moriyama, and S. Uratsuka, (2006). "In search of the statistical properties of high-resolution polarimetric SAR data for the measurements of forest biomass beyond the RCS saturation limits," *IEEE Geoscience and Remote Sensing Letters*, vol. 3, no. 4, pp. 495-499.
- Wang, J. R., A. Hsu, J. C. Shi, P. E. O'Neill, and E. T. Engman, (1997). "A comparison of soil moisture retrieval models using SIR-C measurements over the Little Washita River watershed," *Remote Sensing of Environment*, vol. 59, no. 2, pp. 308-320.
- Wang, J. R. and T. J. Schmugge, (1980). "An Empirical Model for the Complex Dielectric Permittivity of Soils as a Function of Water Content," *IEEE Transactions on Geoscience and Remote Sensing*, vol. GE-18, no. 4, pp. 288-295.
- Warner, W. S., (1995). "Mapping A 3-Dimensional Soil Surface with Hand-Held 35 Mm Photography," *Soil & Tillage Research*, vol. 34, no. 3, pp. 187-197.
- Weimann, A., M. von Schonermark, A. Schumann, P. Jorn, and R. Gunther, (1998). "Soil moisture estimation with ERS-1 SAR data in the East-German loess soil area," *International Journal of Remote Sensing*, vol. 19, no. 2, pp. 237-243.
- Wenjian, N., S. Guoqing, G. Zhifeng, and P. Yong, (2009). "Characterization of soil surface roughness from terrestrial laser scanner data," in *Proceedings of IGARSS '09: Earth Observation - Origins to Applications*, p. II-428.
- Western, A. W. and R. B. Grayson, (1998). "The Tarrawarra data set: Soil moisture patterns, soil characteristics, and hydrological flux measurements," *Water Resources Research*, vol. 34, no. 10, pp. 2765-2768.
- Whalley, W. R., (1993). "Considerations on the use of time-domain reflectometry (TDR) for measuring soil water content," *Journal of Soil Science*, vol. 44, no. 1, pp. 1-9.

- White, I., J. H. Knight, S. J. Zegelin, and G. C. Topp, (1994). "Comments on "Considerations on the use of time-domain reflectometry (TDR) for measuring soil water content" by W.R. Whalley," *European Journal of Soil Science*, vol. 45, no. 4, pp. 503-508.
- Wirtschaftliche Vereinigung Zucker, ed., (2010). *Zucker in Zahlen* Bonn, Germany, p. 22.
- Wobschall, D., (1977). "A Theory of the Complex Dielectric Permittivity of Soil Containing Water: The Semidisperse Model," *IEEE Transactions on Geoscience and Remote Sensing*, vol. 15, no. 1, pp. 49-58.
- Wu, T. D. and K. S. Chen, (2004). "A reappraisal of the validity of the IEM model for backscattering from rough surfaces," *IEEE Transactions on Geoscience and Remote Sensing*, vol. 42, no. 4, pp. 743-753.
- Yamaguchi, Y., A. Sato, W. M. Boerner, R. Sato, and H. Yamada, (2011). "Four-Component Scattering Power Decomposition With Rotation of Coherency Matrix," *Geoscience and Remote Sensing, IEEE Transactions on*, vol. 49, no. 6, pp. 2251-2258.
- Zacharias, S., H. Bogen, L. Samaniego, M. Mauder, R. Fuss, T. Putz, M. Frenzel, M. Schwank, C. Baessler, K. Butterbach-Bahl, O. Bens, E. Borg, A. Brauer, P. Dietrich, I. Hajsek, G. Helle, R. Kiese, H. Kunstmann, S. Klotz, J. C. Munch, H. Papen, E. Priesack, H. P. Schmid, R. Steinbrecher, U. Rosenbaum, G. Teutsch, and H. Vereecken, (2011). "A Network of Terrestrial Environmental Observatories in Germany," *Vadose Zone Journal*, vol. 10, no. 3, pp. 955-973.
- Zribi, M., N. Baghdadi, and C. Guerin, (2006). "Analysis of surface roughness heterogeneity and scattering behavior for radar measurements," *IEEE Transactions on Geoscience and Remote Sensing*, vol. 44, no. 9, pp. 2438-2444.
- Zribi, M., V. Ciarletti, and D. Vidal-Madjar, (1999). "An inversion model of soil roughness based on two radar frequency measurements," in *Proceedings of IGARSS '99: Remote Sensing of the System Earth - A Challenge for the 21st Century*, pp. 2528-2530.
- Zribi, M. and M. Dechambre, (2003). "A new empirical model to retrieve soil moisture and roughness from C-band radar data," *Remote Sensing of Environment*, vol. 84, no. 1, pp. 42-52.

Appendix

A: Radar Polarimetry in Remote Sensing: Basic Concepts.....	193
A.1 Polarization of a Plane EM Wave.....	194
A.2 Partially Polarized Waves.....	199
A.3 Polarimetric Backscattering.....	201
A.4 The Target Vector.....	204
A.5 Distributed Targets.....	207

A: Polarimetry in Microwave Remote Sensing: Basic Concepts

The aim of this chapter is to provide a substantial introduction to the basic theory, scattering concepts, systems and advanced concepts, and applications typical to radar polarimetric remote sensing. For further reading and fully understanding of this complex topic it is recommended to take a look at the PolSAR tutorials provided by the European Space Agency (<http://earth.eo.esa.int/polsarpro/tutorial.html>) or the Canadian Space Agency (http://www.ccrs.nrcan.gc.ca/resource/tutor/polarim/pdf/polarim_e.pdf) and the recently published reference books by Lee & Pottier (2009) and Cloude (2010). A good and comprehensive introduction to modern matrix algebra can be found in the book by Schmidt & Treinkler (2006).

The reviewed definitions and mathematical formulations addressed in this section are necessary to describe the polarimetric scattering problem for point and distributed targets. They are essential for the inversion of surface parameters from polarimetric ALOS/PALSAR data in this thesis. In principle, there are two main conceptual formalisms in polarimetry. The first one is a real space formalism based on the Stokes Vector for the description of the polarimetric properties of waves and on the Mueller matrix for the polarimetric description of the scatterer (Boerner et al., 1981; Können, 1985; Chaudhuri et al., 1986; Guissard, 1994; Boerner et al., 1998; Born & Wolf, 1999; Mott, 2007). The second one is a complex space formalism based on the Jones vector for the analysis of wave polarization and on the Covariance or Coherency matrix for the description of the scattering process (Jones, 1941; Kennaugh, 1954; Chaudhuri & Boerner, 1975; Cloude, 1986b; Luneburg et al., 1997). Both formalisms are equivalent. The real space formulations and concepts can be transformed unambiguously into the corresponding complex space formulations and concepts, and vice versa. Due the fact that SAR data is measured and processed in the complex domain, however, the complex space formalism is used here.

A.1 Polarization of a Plane EM Wave

The wave equation for linear source-free homogeneous media is derived from Maxwell's equations. Its solution leads to the simplest form of electromagnetic waves with constant amplitude on a plane perpendicular to the direction of propagation. Such waves are known as *plane EM waves* (Stratton, 1941; Sander & Reed, 1978; Jackson, 1998). The instantaneous real electric field vector of such a wave $\underline{\underline{\vec{E}}}(\vec{r}, t)$ propagating into the direction \vec{k} at a given location, defined by the position vector \vec{r} and a given time t , can be written as

$$\underline{\underline{\vec{E}}}(\vec{r}, t) = \underline{\underline{\vec{E}}}(\vec{r}) \cos(\omega t) \quad (\text{A.1})$$

where $\underline{\underline{\vec{E}}}(\vec{r})$ is the real amplitude of the electric field and ω is the angular frequency of the wave.

In the case that the electric field vector varies in time with a single angular frequency, the wave is characterized as monochromatic. According to the IPU (International Physical Union) convention the corresponding complex representation of the time independent electric field is given by

$$\vec{E}(\vec{r}) = \vec{E} \times e^{(i\vec{k}\vec{r})} \quad (\text{A.2})$$

where \vec{E} is the constant complex amplitude vector of the electric field.

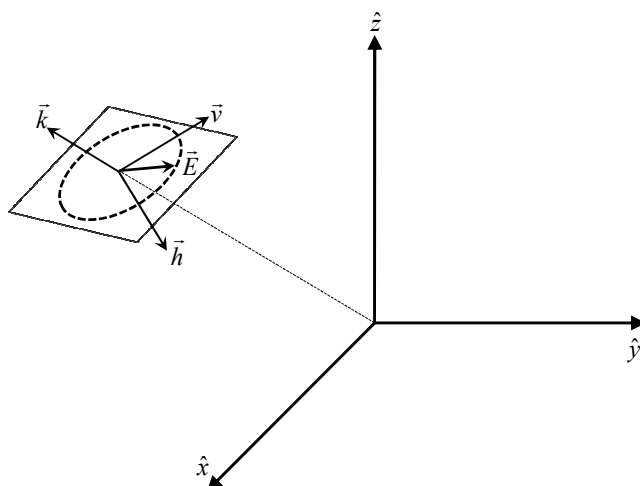


Figure A.0.1: Propagation of a plane EM wave in direction \vec{k} .

Introducing a right handed orthogonal coordinate system $(\vec{h}, \vec{v}, \vec{k})$ (Fig. A.1), the complex amplitude vector \vec{E} can be decomposed into two orthogonal coordinate complex components E_h and E_v as

$$\vec{E} = E_h \vec{h} + E_v \vec{v} \quad (\text{A.3})$$

Generally speaking, polarization is related to the vectorial nature of waves. More precisely, it describes the behavior of the field vector in time. Since polarization is a physical property of the EM wave, it is independent of the coordinate system used to describe it. Nonetheless, the definition of polarization requires a reference coordinate system and a given direction of propagation. In regard to a monochromatic plane EM wave, the polarization gives a description of the orientation of the electric field vector as a function of time in the plane perpendicular to the direction of travel. In this way, the tip of the electric field vector moves on this plane in time along an ellipse. This ellipse is known as the polarization ellipse (Deschamps, 1951; Boerner et al., 1997; Mott, 2007; Lee & Pottier, 2009).

The shape of the polarization ellipse depicts the polarization state of the plane wave and it can be fully described in terms of two angular variables, the orientation angle ϕ and the ellipticity angle τ .

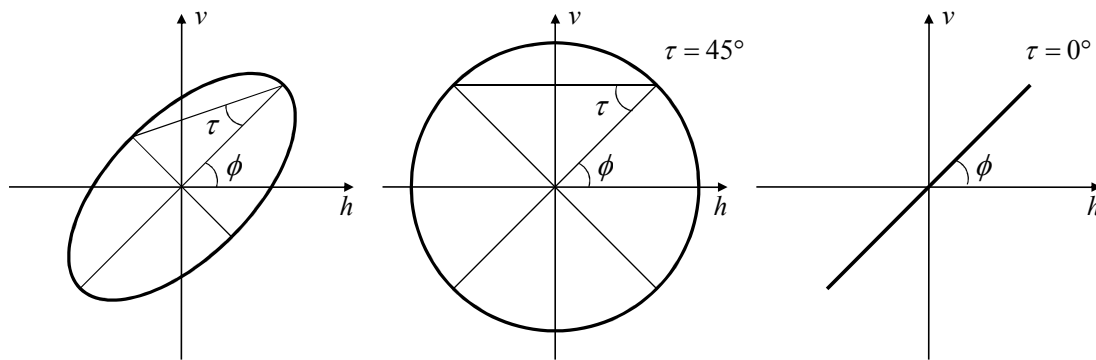


Figure A.0.2: Different shapes of the polarization ellipse expressing the polarization states of a plane wave.

As can be seen from Fig. A.2, τ describes the shape of the ellipse and varies by definition between -45° and 45° . At $\tau = 0^\circ$ the ellipse degenerates to a straight line with inclination given by the orientation angle ϕ , corresponding to linear states. In this case, $\phi = 0^\circ$ defines horizontally polarized waves, while $\phi = 90^\circ$ depicts vertically polarized waves. For $\tau = \pi/4$, the ellipse, becoming a circle, expresses circular polarization states. Ellipticity angles between 0° and 45° characterize elliptical polarized waves. Besides, the ellipticity angle τ also defines the sense of rotation of the \vec{E} vector. In case $\tau < 0$, the rotation is right-handed, otherwise, the rotation is left-handed (in the IPU System of Conventions). It should be noted that the sense of rotation is related to the direction of wave propagation and thus depends on its definition (Mott, 2007) as compiled in Tab. 5.1.

Table A.0.1: Characteristic polarization states with corresponding polarization descriptors.

	Horizontal	Vertical	Linear $+45^\circ$	Left Circular	Right Circular
Orientation angle ϕ	90°	0°	45°	$0^\circ - 180^\circ$	$0^\circ - 180^\circ$
Ellipticity angle τ	0°	0°	0°	45°	-45°
Complex ratio ρ	∞	0	1	-1	-i

In the main, a plane monochromatic EM wave has potentially four degrees of freedom, of which two are required for the description of the polarization state of the wave. As mentioned before, the two polarization angles constitute such a real pair of parameters for the description of the polarimetric state of the wave in terms of the shape of the polarization ellipse. In addition to the polarization state, two further parameters are needed for a complete

wave description: the *wave amplitude* A_0 , corresponding to the wave intensity and the size of the polarization ellipse and an initial *absolute phase* reference α , as can be seen in the full Poincaré sphere (Fig. A.3). However, since both variables are wave characteristics and not polarization parameters, they are not essential for the definition of the polarimetric state of the wave.

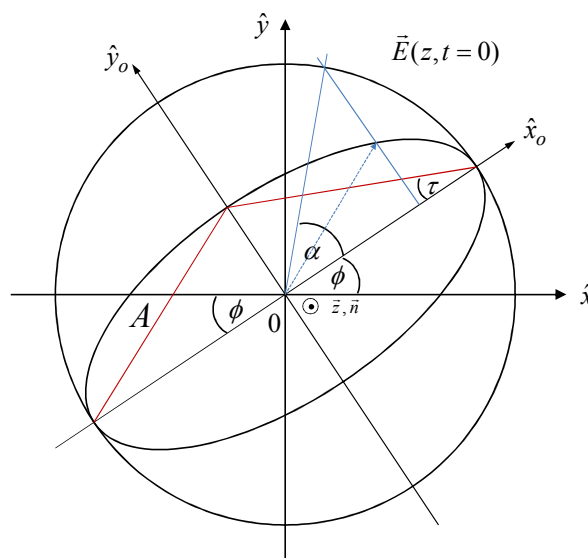


Figure A.0.3: Full Poincaré sphere with wave amplitude A , absolute phase α , orientation angle ϕ , and ellipticity angle τ .

Eq. A.3 gives the complex amplitude of the electric field represented as a linear combination of two orthogonal linear polarizations \vec{h} and \vec{v} weighted by their corresponding complex amplitudes E_h and E_v . This characterization of the electric field vector can be considered as a component representation of the electric field vector in a two-dimensional complex space with respect to the $\{\vec{h}, \vec{v}\}$ basis. In this context, a monochromatic plane wave in the two-dimensional complex space can alternatively be represented as a linear combination of two arbitrary orthonormal polarization states. Consequently, by defining two orthonormal polarization states, denoted by $\vec{\varepsilon}_m$ and $\vec{\varepsilon}_n$, which establish a polarization reference basis $\{\vec{\varepsilon}_m, \vec{\varepsilon}_n\}$, a given plane wave \vec{E} can be decomposed into its projections onto the basis polarization as

$$\vec{E} = E_m \vec{\epsilon}_m + E_n \vec{\epsilon}_n \text{ where } \vec{\epsilon}_m \vec{\epsilon}_m = \vec{\epsilon}_n \vec{\epsilon}_n = 1 \text{ and } \vec{\epsilon}_m \vec{\epsilon}_n = 0 \quad (\text{A.4})$$

Using the complex amplitudes E_m and E_n , an alternative representation of the plane wave in terms of a two-dimensional complex vector \vec{E}_{mn}

$$\vec{E}_{mn} = \begin{bmatrix} E_m \\ E_n \end{bmatrix} \quad (\text{A.5})$$

called the *Jones vector* was introduced by Jones (Jones, 1941; Hurwitz & Jones, 1941; Graves, 1956), which fully describes a coherent plane wave (also known as the *Sinclair vector* in radar polarimetry according to the IEEE standard notation). To demonstrate the equivalence between the real and complex space representation of a plane, the Jones vector can be addressed in terms of the orientation angle θ , the ellipticity angle τ , the wave amplitude A_0 and the initial phase ϕ_0 as

$$\vec{E}_{mn} = A_0 e^{-i\phi_0} \begin{bmatrix} \cos\theta & -\sin\theta \\ \sin\theta & \cos\theta \end{bmatrix} \begin{bmatrix} \cos\tau \\ -i\sin\tau \end{bmatrix} \quad (\text{A.6})$$

After the introduction of the Jones vector, a complex polarization descriptor, namely the complex polarization ration ρ , which is defined as the ratio of the orthogonal complex electric field components, can be deduced (Boerner et al., 1981; Kostinski & Boerner, 1986; Boerner et al., 1998)

$$\rho = \frac{E_n}{E_m} = \frac{a_n}{a_m} e^{i(\delta_n - \delta_m)} = \tan \alpha \times e^{i\delta} \quad (\text{A.7})$$

where $\tan \alpha = a_n / a_m$ with $0 < \alpha < \pi/2$ and $\delta = \delta_n - \delta_m$ with $0 < \delta < 2\pi$. The two angular variables α and δ , known as the *Deschamps parameters* (Deschamps, 1951), constitute an alternative two parameter real set for the description of the polarization state of an EM wave in terms of an amplitude ratio and a phase difference.

The complex polarization ration ρ has two degrees of freedom, expressed by the two Deschamps parameters, and allows the mapping of polarization states onto the two-dimensional complex plane. It should be emphasized that the absolute magnitude and phase of the polarization ellipse gets lost with the information of the polarization ratio. In accordance with Eq. (A.7) linear polarization is represented by a real ρ ($\delta = 0$ or $\tau = 0$), while elliptic polarization is represented by a complex ρ ($\delta \neq 0$ or $\tau \neq 0$). The complex polarization ρ can be depicted as a function of the polarization angles θ and τ as (Born & Wolf, 1999)

$$\rho = \frac{\cos 2\tau \sin 2\theta + i \sin 2\tau}{1 + \cos 2\tau \cos 2\theta} \quad (\text{A.8})$$

The descriptions in terms of θ and τ as well as ρ referred to a Cartesian basis for some characteristic polarization states are summarized in Tab. 5.1.

A.2 Partially Polarized Waves

In the foregoing section, completely polarized single-frequency or monochromatic plane waves were considered. As discussed, the polarization state of such waves can be fully described in terms of a single polarization ellipse or a single Jones vector. However, many waves encountered in electromagnetic science are not monochromatic. Another important class of waves is the so-called *quasi monochromatic* or *partially polarized wave*. In radar science, partially polarized waves arise primarily from scattering. These waves can be regarded as wave packets of multiple frequencies of a bandwidth centered on the mean wave frequency. Compared to completely polarized waves for which both the amplitude and the phase of the electric field are independent of time and space, partially polarized waves are characterized by temporal and/or spatial variations of the electric field amplitude, the phase, and the polarization. As a consequence, the ellipse describing the electric field vector is no longer well defined but varying in time. In that case, the wave polarization can only be defined in the sense of statistical averaging over time (Cloude & Pottier, 1996).

Born and Wolf (1999) introduced the concept of a *wave coherency matrix* in order to advance the analysis of partially polarized waves. Based on the outer product of the corresponding Jones vector averaged over a coherency time, the coherency matrix is defined as (Boerner et al., 1998; Born & Wolf, 1999; Mott, 2007)

$$[J] = \langle \bar{E}_{nm} \times \bar{E}_{nm}^+ \rangle = \begin{bmatrix} \langle E_m E_m^* \rangle & \langle E_m E_n^* \rangle \\ \langle E_n E_m^* \rangle & \langle E_n E_n^* \rangle \end{bmatrix} = \begin{bmatrix} J_{mm} & J_{mn} \\ J_{nm} & J_{nn} \end{bmatrix} \quad (\text{A.9})$$

Formally, the coherency matrix is a 2x2 hermitian positive semi definite matrix. Its elements are proportional to the second order moments of the elements of the complex Jones vector. The diagonal elements of the matrix correspond to the intensities of each element, i.e. the trace of $[J]$ equals the total intensity of the wave. The cross-correlation between the elements are contained in the off-diagonal elements of the Jones vector which expressing the amount of correlated structure in the field. In case of no correlation between E_m and E_n , $J_{mn} = J_{nm} = 0$ and $[J]$ becomes diagonal with equal diagonal elements. If so, the wave does not contain any polarized structure and thus is called completely unpolarized. Such a wave has only one degree of freedom, namely the amplitude. On the contrary, if $J_{mn}J_{nm} = J_{mm}J_{nn}$ (i.e., $\det([J]) = 0$) the correlation between E_m and E_n is maximum, i.e. the wave is completely polarized. In this case, the wave has four degrees of freedom. In between these two extreme cases falls the more general case of partial polarization ($\det([J]) > 0$) with a certain amount of correlation between E_m and E_n (Lee & Pottier, 2009).

From the discussion of the partially polarized case it becomes evident that, in addition to the two parameters required to describe the polarization state of monochromatic waves, the degree of polarization is needed as well (Boerner et al., 1998; Born & Wolf, 1999; Mott, 2007; Lee & Pottier, 2009). Hence, they cannot be described by a single Jones vector, because it holds only one degree of freedom. In fact, they require the entire wave coherency matrix for their complete description.

A.3 Polarimetric Backscattering

The foregoing section provided the description of the polarimetric properties of plane EM waves. In the following, the polarimetric properties of the interaction of waves with scattering targets will be considered. Generally speaking, the scattering process can be addressed as follows (Kennaugh, 1954): the fully polarized monochromatic plane EM wave \vec{E}^i with a defined polarization state is emitted by a transmitting antenna and travels in direction of propagation \vec{k}^i towards the target. Using a right-handed orthogonal coordinate system $(\vec{h}_i, \vec{v}_i, \vec{k}_i)$ located at the transmitter, the transmitted wave can be written as

$$\vec{E}^i = E_h^i \vec{h}_i + E_v^i \vec{v}_i \quad (\text{A.10})$$

The wave interacts with the scattering target, potentially changing its polarization and/or degree of polarization, and is backscattered with a directional characteristic, which is dependent on the scatterer. A receiving antenna, located in direction \vec{k}_s in the so-called far field region of the target, where the scattered wave is considered to be a plane wave, receives the backscattered wave \vec{E}^s . Using a right-handed orthogonal coordinate system $(\vec{h}_s, \vec{v}_s, \vec{k}_s)$ located at the receiving antenna, the received wave can be written as

$$\vec{E}^s = E_h^s \vec{h}_s + E_v^s \vec{v}_s \quad (\text{A.11})$$

At this point it should be mentioned that there are two different conventions to define the scattered wave coordinate system $(\vec{h}_s, \vec{v}_s, \vec{k}_s)$ with respect to the incident wave coordinate system $(\vec{h}_i, \vec{v}_i, \vec{k}_i)$ proposed in the literature (Ulaby et al., 1981b; Skolnik, 1990). The first one is known as the *Forward Scattering Alignment* (FSA) convention and is mainly used in bistatic scattering problems. The second one is known as the *Back-Scattering Alignment* (BSA) convention (Fig. A.4). The latter is used preferably in radar backscattering problems and thus is the one explicitly valid for this study (Boerner et al., 1998).

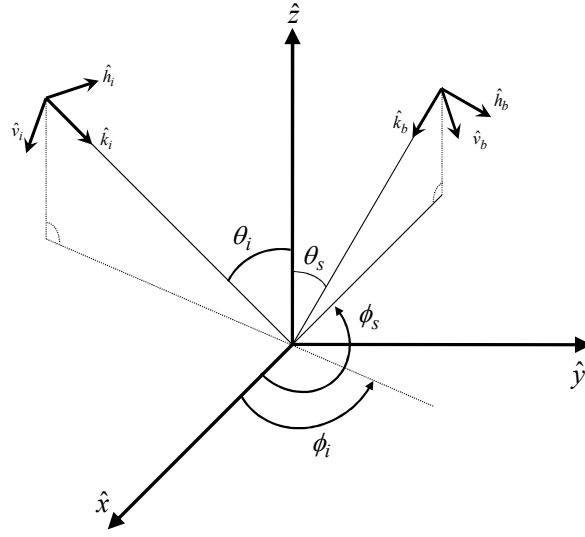


Figure A.0.4: Back-Scattering Alignment (BSA) geometry.

The scattering process itself can be described as a transformation of the incident wave into a backscattered wave caused by the scattering target. The polarization state of the wave as well as its degree of polarization may change due to this transformation. By using the Jones vector representation for the incident monochromatic wave and the backscattered wave as discussed above

$$\vec{E}^i = \begin{bmatrix} E_x^i \\ E_y^i \end{bmatrix} \text{ and } \vec{E}^s = \begin{bmatrix} E_x^s \\ E_y^s \end{bmatrix} \quad (\text{A.12})$$

this transformation can be expressed by a 2x2 complex Sinclair matrix [S] as

$$\vec{E}^s = [S]\vec{E}^i \rightarrow \begin{bmatrix} E_x^s \\ E_y^s \end{bmatrix} = \frac{e^{ikr}}{r} \begin{bmatrix} S_{xx} & S_{xy} \\ S_{yx} & S_{yy} \end{bmatrix} \begin{bmatrix} E_x^i \\ E_y^i \end{bmatrix} \quad (\text{A.13})$$

This complex 2x2 matrix is known as the *radar scattering* or *target matrix* [S] and may be considered as the very basic concept of radar polarimetry (Sinclair, 1950; Kennaugh, 1954; Kostinski & Boerner, 1986; Boerner et al., 1998; Mott, 2007; Lee & Pottier, 2009).

$$[S] = \frac{e^{ikr}}{r} \begin{bmatrix} S_{xx} & S_{xy} \\ S_{yx} & S_{yy} \end{bmatrix} \quad (\text{A.14})$$

The factor e^{ikr}/r represents both the wave attenuation which occurs during the travel time from the transmitter to the target and the corresponding phase shift (with the wavenumber k , cf. section 2.4). However, this factor is not of interest in radar polarimetry. As it allows the estimation of three-dimensional location of the scattering target, this phase shift is crucial in SAR interferometry and polarimetric interferometry (Cloude & Papathanassiou, 1997a; Cloude & Papathanassiou, 1997b).

The four elements of the scattering matrix $[S_{ij}]$ ($i, j = x$ or y , i.e. horizontal or vertical) are denoted as the complex scattering amplitudes. They are related to the corresponding radar cross section values σ_{ij}^0 in the $\{H, V\}$ polarization basis (Kennaugh, 1954):

$$\begin{aligned} S_{xx} &= c \times e^{-i\phi_{xx}} \sqrt{\sigma_{xx}^0} . \\ S_{xy} &= c \times e^{-i\phi_{xy}} \sqrt{\sigma_{xy}^0} . \\ S_{yx} &= c \times e^{-i\phi_{yx}} \sqrt{\sigma_{yx}^0} \\ S_{yy} &= c \times e^{-i\phi_{yy}} \sqrt{\sigma_{yy}^0} \end{aligned} \quad (\text{A.15})$$

where c is the scalar calibration factor. The span of $[S]$, defined by the sum of the squares of the absolute values of the complex scattering amplitudes (A.16), corresponds to the total power scattered by the target. The total power TP is an invariant with (Skolnik, 1990)

$$TP = |S_{xx}|^2 + |S_{xy}|^2 + |S_{yx}|^2 + |S_{yy}|^2 \quad (\text{A.16})$$

Disregarding an absolute phase factor, the $[S]$ matrix contains in the general bistatic case seven independent parameters: four amplitudes and three relative phases. However, it is important to note that in the monostatic backscattering case, where transmitter and receiver are located at the same position, the scattering matrix becomes symmetric in a reciprocal

scattering medium (i.e. $S_{xy} = S_{yx}$). In this case [S] is known as symmetric Sinclair matrix (Born & Wolf, 1999; Mott, 2007). This symmetry holds for all reciprocal propagation and scattering media. Hence, the number of independent parameters in [S] is reduced down to five: three amplitudes and two relative phases.

The virtue of the scattering matrix concept is accentuated by Eq. (A.15): For a given scattering geometry and at a given frequency, the scattering matrix is only dependent on the scattering target and not on the polarization of the wave used for its measurement. If the incident wave polarization is changed, the scattered wave changes accordingly, while [S] remains unchanged. It should be noted that the form of the scattering matrix certainly depends on the basis chosen to describe the incident and scattered waves.

The [S] matrix can be measured by transmitting two orthogonal polarizations on a pulse to pulse basis and receiving the scattered waves in two orthogonal polarizations (commonly the same as used for transmission). As mentioned before, most polarimetric systems (e.g. ALOS PALSAR) operate in the H, V basis, where in a first cycle a horizontally polarized wave and receiving in the horizontal H and vertical V polarizations the S_{HH} and S_{VH} scattering coefficients are measured, while the remaining coefficients S_{HV} and S_{VV} are measured in a second cycle, where a V polarized wave is transmitted and H and V polarizations are received.

A.4 The Target Vector

In this section, the concept of the target (or scattering) vector, which is needed to extend the scattering matrix in order to allow the description of distributed targets, is discussed. As an alternative to the matrix formulation in Eq. (A.14), the polarimetric backscattering problem can be addressed in a vectorial formulation based on the concept of system vectors (Kostinski & Boerner, 1986; Cloude & Pottier, 1996). Using this approach the scattering matrix is replaced by an equivalent four-dimension complex scattering vector k_4 defined as

$$[S] = \begin{bmatrix} S_{xx} & S_{xy} \\ S_{yx} & S_{yy} \end{bmatrix} \rightarrow \vec{k}_4 = V([S]) = \frac{1}{2} \text{Trace}([S] \boldsymbol{\mu}) = [k_0, k_1, k_2, k_3]^T \quad (\text{A.17})$$

where $V([S])$ is the matrix vectorization operator, $Trace([S])$ is the sum of the diagonal elements of $[S]$ and ψ is a complete set of 2x2 complex basis matrices under a hermitian inner product (Cloude, 1986a). There are several basis sets that can be used for the vectorization of $[S]$, of which two are commonly used in the literature: the first one ψ_L is denoted as the lexicographic basis corresponding to a straightforward ordering of the elements of $[S]$

$$\psi_L = \left\{ 2 \begin{bmatrix} 1 & 0 \\ 0 & 0 \end{bmatrix}, 2 \begin{bmatrix} 0 & 1 \\ 0 & 0 \end{bmatrix}, 2 \begin{bmatrix} 0 & 0 \\ 1 & 0 \end{bmatrix}, 2 \begin{bmatrix} 0 & 0 \\ 0 & 1 \end{bmatrix} \right\} \quad (\text{A.18})$$

By vectorizing the elements of $[S]$ using the lexicographic basis matrices, the corresponding scattering vector is obtained as

$$\vec{k}_{4L} = [S_{xx}, S_{xy}, S_{yx}, S_{yy}]^T \quad (\text{A.19})$$

The virtue of the resulting scattering vector is that its elements are given by the amplitudes of the scattering matrix, and thus, are directly related to the system observables.

The set of the four so-called Pauli spin matrices ψ_P constitutes the second important basis used for the vectorization of the scattering matrix as

$$\psi_P = \left\{ \sqrt{2} \begin{bmatrix} 1 & 0 \\ 0 & 1 \end{bmatrix}, \sqrt{2} \begin{bmatrix} 1 & 0 \\ 0 & -1 \end{bmatrix}, \sqrt{2} \begin{bmatrix} 0 & 1 \\ 1 & 0 \end{bmatrix}, \sqrt{2} \begin{bmatrix} 0 & -i \\ i & 1 \end{bmatrix} \right\} \quad (\text{A.20})$$

Performing the vectorization of $[S]$ by using the Pauli matrices set leads to the *Pauli scattering vector* for the general bistatic case with the explicit form

$$\vec{k}_{4P} = \frac{1}{\sqrt{2}} [S_{xx} + S_{yy}, S_{xx} - S_{yy}, S_{xy} + S_{yx}, i(S_{xy} - S_{yx})]^T \quad (\text{A.21})$$

It should be pointed out that the advantage of using the Pauli matrix lies in the straightforward physical interpretation of the Pauli matrices in terms of elementary scattering

mechanisms as well as relative polarization plane preservation (Cloude & Pottier, 1996). This physical interpretation is as follows:

- The first Pauli matrix can be interpreted as the scattering matrix of an isotropic “odd”-bounce scattering target. Such scatterers are characterized by $S_{xx} = S_{yy}$ and $S_{xy} = S_{yx} = 0$. Typical scatterers of this type are spheres, flat surfaces or trihedral corner reflectors.
- The second Pauli matrix is also diagonal but generates a π phase difference between the diagonal elements indicating isotropic “even”-bounce scattering. This mechanism is characterized by $S_{xx} = -S_{yy}$ and $S_{xy} = S_{yx} = 0$ as e.g. from dihedral corner reflectors.
- The third Pauli matrix can be interpreted as the scattering matrix of an isotropic “even”-bounce scattering target with a relative orientation of $\pi/4$ with respect to the horizontal. This is because the third can be obtained from the second Pauli matrix via a rotation of the $\{\vec{\varepsilon}_x, \vec{\varepsilon}_y\}$ reference basis by $\pi/4$.
- The fourth Pauli matrix represents a target that transforms all incident polarization states into orthogonal states. Because it is asymmetric, i.e. $S_{xy} \neq S_{yx}$, it does not appear in backscattering, unless the medium is not reciprocal (as it occurs with the Faraday rotation effect).

As demonstrated by Cloude (1986), the Pauli scattering vector is hence closely related to the physics of wave scattering. Another important advantage of the Pauli scattering vector compared to the lexicographic scattering vector relies on the close relationship between the Pauli matrices and its manipulations leading to a simplified formation of line of sight (LOS) rotation in terms of scattering targets, antennas and the Pauli scattering vector.

In the reciprocal backscattering case, one of the elements of the target vector is redundant and the reduced three-component scattering vector is commonly introduced for a simplified formulation. As follows in the case of the lexicographic scattering vector

$$\vec{k}_{3L} = [S_{xx}, \sqrt{2}S_{xy}, S_{yy}]^T \quad (\text{A.22})$$

and the corresponding three dimensional Pauli scattering vector

$$\vec{k}_{3P} = \frac{1}{\sqrt{2}} [S_{xx} + S_{yy}, S_{xx} - S_{yy}, 2S_{xy}]^T \quad (\text{A.23})$$

The factor $\sqrt{2}$ in Eq. (A.23) is required to keep the norm (total power) of the three-dimensional vector consistent with its four-dimensional representation (Boerner et al., 1981).

The transformation of the three-dimensional scattering vector from its Pauli basis into its lexicographic basis representation, and vice versa, is given by

$$\vec{k}_{3P} = [D_3] \vec{k}_{3L} \text{ and } \vec{k}_{3L} = [D_3]^{-1} \vec{k}_{3P} \quad (\text{A.24})$$

where $[D_3]$ is a 3x3 special unitary matrix (Boerner et al., 1998)

$$[D_3] = \frac{1}{\sqrt{2}} \begin{bmatrix} 1 & 0 & 1 \\ 1 & 0 & -1 \\ 0 & \sqrt{2} & 0 \end{bmatrix} \text{ and } [D_3]^{-1} = [D_3]^T = \frac{1}{\sqrt{2}} \begin{bmatrix} 1 & 1 & 0 \\ 1 & 0 & \sqrt{2} \\ 1 & -1 & 0 \end{bmatrix} \quad (\text{A.25})$$

Thus, the scattering vector contains exactly the same information as the scattering matrix, i.e. it is also characterized by five degrees of freedom. The major virtue of using the scattering vector instead of the scattering matrix is the fact that it enables the introduction of a scattering covariance matrix (similar to the concept of the wave covariance matrix, cf. section A.2). This covariance matrix can then be used to describe backscattering effects which cannot be described by a single scattering matrix (Papathanassiou & Cloude, 1997). However, the relevant case for conventional SAR remote sensing applications is the scattering problem in backscattering, and thus, will be the only one considered in the remaining of this work.

A.5 Distributed Targets

In the foregoing sections only coherently scattering targets were considered. As discussed, such deterministic scatterers can be fully described by a single scattering matrix or by a single scattering vector, respectively. Anyhow, in most geoscience radar applications the

scattering targets are embedded in a dynamic environment. Hence, they are affected by spatial and/or time variations (Ulaby et al., 1982b). These targets, called *incoherent* or *depolarizing scatterers*, can no longer be fully described by a single scattering matrix. One important class of depolarizing scatterers are *spatially distributed targets*. In effect, most of the natural terrain surfaces belong to this class. Statistically, such targets may be considered to be homogeneously composed of randomly distributed coherent scattering centers. And that means, the scattering behavior of each of these individual scattering centers can be completely described by a single scattering matrix $[S_i]$. Due to the finite resolution of imaging radar systems, the measured scattering matrix consists of the coherent superposition of the individual scattering matrices $[S_i]$ of all individual scattering centers located within the resolution cell. The measured scattering matrix $[S_i]$ can be different for another resolution element of the same scatterer because of a different spatial disposition of the individual targets. It should be noted that this is the same physical effect as the generation of speckle discussed in section 4.8 (Lee et al., 1999b).

In order to advance the analysis of distributed scattering targets, Boerner et al. (1981) introduced the concept of a *target covariance* or *coherency matrix*. The 3×3 *polarimetric covariance matrix* $[C_3]$ is defined by using the outer product of the three-dimensional lexicographic scattering vector (Boerner et al., 1981; Tragl, 1990; Boerner et al., 1998; Mott, 2007; Lee & Pottier, 2009).

$$[C_3] = \langle \vec{k}_L \times \vec{k}_L^+ \rangle = \begin{bmatrix} \langle |S_{xx}|^2 \rangle & \sqrt{2} \langle S_{xx} S_{xy}^* \rangle & \langle S_{xx} S_{yy}^* \rangle \\ \sqrt{2} \langle S_{xy} S_{xx}^* \rangle & 2 \langle |S_{xy}|^2 \rangle & \sqrt{2} \langle S_{xy} S_{yy}^* \rangle \\ \langle S_{yy} S_{xx}^* \rangle & \sqrt{2} \langle S_{yy} S_{xy}^* \rangle & \langle |S_{yy}|^2 \rangle \end{bmatrix} \quad (\text{A.26})$$

with $\langle \dots \rangle$ indicating spatial averaging, while homogeneity of the random scattering medium is assumed. According to this, the 3×3 polarimetric coherency matrix $[T3]$ is defined by using the outer product of the three-dimensional Pauli target vector (Cloude, 1992)

$$\begin{aligned}
[T_3] &= \langle \vec{k}_P \times \vec{k}_P^+ \rangle \\
&= \begin{bmatrix} \langle |S_{xx} + S_{yy}|^2 \rangle & \langle (S_{xx} + S_{yy})(S_{xx} - S_{yy})^* \rangle & 2\langle (S_{xx} + S_{yy})S_{xy}^* \rangle \\ \langle (S_{xx} - S_{yy})(S_{xx} + S_{yy})^* \rangle & \langle |S_{xx} - S_{yy}|^2 \rangle & 2\langle (S_{xx} - S_{yy})S_{xy}^* \rangle \\ 2\langle S_{xy}(S_{xx} + S_{yy})^* \rangle & 2\langle S_{xy}(S_{xx} - S_{yy})^* \rangle & 4\langle |S_{xy}|^2 \rangle \end{bmatrix} \quad (\text{A.27})
\end{aligned}$$

[C3] and [T3] are equivalent methods to describe the distributed targets and hold the same information content. By definition, both matrices are hermitian positive semi definite, i.e. that they have real non-negative and orthogonal eigenvalues. They are in general of full rank three, whereby the rank of a matrix is defined as the maximum number of linearly independent columns (or rows) of the matrix (Schmidt & Trenkler, 2006). Concerning the physical information content of the coherency (or covariance) matrix, the rank of [T3] (or [C3]) can be considered as the amount of linear independent contributions in which the target matrix can be decomposed. That is, a rank three coherency matrix implies the existence of three linearly non-zero eigenvectors (Mott, 2007; Lee & Pottier, 2009). The physical meaning of the eigenvalues and eigenvectors will be discussed in the following sections.

As elucidated, the two matrices completely describe a reciprocal distributed scattering target. They contain nine independent parameters: three real power values in the main diagonal and three off-diagonal complex cross-correlations. The latter contain the information of correlation between the complex elements of [S] over spatial averaging. Cloude (1986a) showed that the relation between [C3] and [T3] can be established by using the transformation of the corresponding scattering vectors in Eq. (A.28)

$$\begin{aligned}
[T_3] &= \langle \vec{k}_{3P} \times \vec{k}_{3P}^+ \rangle = \langle [D_3] \vec{k}_{3L} \times \vec{k}_{3L}^+ [D_3]^+ \rangle \\
&= [D_3] \langle \vec{k}_{3L} \times \vec{k}_{3L}^+ \rangle [D_3]^+ = [D_3] [C_3] [D_3]^+
\end{aligned} \quad (\text{A.28})$$

The elements of [T3] can be expressed in terms of the elements of [C3] by carrying out the matrix multiplication

$$\begin{aligned}
[T_3] &= \frac{1}{2} \begin{bmatrix} c_1 + c_6 + c_3^* + c_3 & c_1 - c_2 + c_3^* - c_6 & \sqrt{2}(c_2 + c_5^*) \\ c_1 + c_2 - c_3^* - c_6 & c_1 + c_6 - c_3^* - c_3 & \sqrt{2}(c_2 - c_5^*) \\ \sqrt{2}(c_5 + c_2^*) & \sqrt{2}(c_2^* - c_5) & 2c_4 \end{bmatrix} \\
[C_3] &= \frac{1}{2} \begin{bmatrix} c_1 & c_2 & c_3 \\ c_2^* & c_4 & c_5 \\ c_3^* & c_5^* & c_6 \end{bmatrix}
\end{aligned} \tag{A.29}$$

Accordingly, the transformation of [T3] into [C3] again is obtained by using Eq. (A.28)

$$\begin{aligned}
[C_3] &= \langle \vec{k}_{3L} \times \vec{k}_{3L}^+ \rangle = \langle [D_3] \vec{k}_{3P} \times \vec{k}_{3P}^+ [D_3]^+ \rangle \\
&= [D_3] \langle \vec{k}_{3P} \times \vec{k}_{3P}^+ \rangle [D_3]^+ = [D_3] [T_3] [D_3]^+
\end{aligned} \tag{A.30}$$

Then the [C3] elements can be expressed in terms of the elements of [T3] as

$$\begin{aligned}
[C_3] &= \frac{1}{2} \begin{bmatrix} t_1 + t_4 + t_2^* + t_2 & \sqrt{2}(t_3 + t_5) & t_1 - t_4 + t_2^* - t_2 \\ \sqrt{2}(t_3^* + t_5^*) & 2t_6 & \sqrt{2}(t_3^* - t_5^*) \\ t_1^* - t_4^* - t_2 - t_2^* & \sqrt{2}(t_3 - t_5) & t_1 + t_4 - t_2^* - t_2 \end{bmatrix} \\
[T_3] &= \frac{1}{2} \begin{bmatrix} t_1 & t_2 & t_3 \\ t_2^* & t_4 & t_5 \\ t_3^* & t_5^* & t_6 \end{bmatrix}
\end{aligned} \tag{A.31}$$

Because the transformation in Eq. (A.29) and Eq. (A.31) are unitary similarity transformations (Schmidt & Trenkler, 2006), both matrices have the same eigenvalues but different eigenvectors. The two matrices are in general of full rank three, i.e. they have three non-zero eigenvalues.

As a final note on the formation of the coherency and covariance matrix, it should be pointed out that the [T3] (or [C3]) matrix data has a reduced resolution due to the spatial averaging needed for the formation of the coherency (or covariance) matrix. This loss of resolution elements is especially critical in terms of point targets because for distributed targets the loss

is compensated by a reduced speckle noise due to the multi-looking effect. This trade-off between high resolution required for deterministic targets and reduced speckle noise over distributed targets can be resolved by applying an adaptive polarimetric speckle filter as first introduced by Lee et al. (1999b). Such filters perform a multi-looking filtering process on distributed scattering targets, while point scattering targets or edges remain unfiltered (Lee & Pottier, 2009).

Note that in this work, the scattering problem is only addressed in terms of the Pauli target vector and the coherency target matrix.

Erklärung

Ich versichere, dass ich die von mir vorgelegte Dissertation selbständig angefertigt, die benutzten Quellen und Hilfsmittel vollständig angegeben und die Stellen der Arbeit – einschließlich Tabellen, Karten und Abbildungen –, die anderen Werken im Wortlaut oder dem Sinn nach entnommen sind, in jedem Einzelfall als Entlehnung kenntlich gemacht habe; dass diese Dissertation noch keiner anderen Fakultät oder Universität zur Prüfung vorgelegen hat; dass sie noch nicht veröffentlicht worden ist sowie, dass ich eine solche Veröffentlichung vor Abschluss des Promotionsverfahrens nicht vornehmen werde. Die Bestimmungen der Promotionsordnung sind mir bekannt. Die von mir vorgelegte Dissertation ist von Prof. Dr. Karl Schneider betreut worden.

Nachfolgend genannte Teilpublikationen liegen vor:

- Koyama, C.N. and K. Schneider, (2010). “A novel approach to estimate soil moisture under vegetation using partial polarimetric ALOS PALSAR data,” In *Proc. of ISPRS Commission VIII Symposium 2010*, Aug. 8-12, Kyoto, Japan, pp. 422-426.
- Koyama, C.N., W. Korres, P. Fiener, K. Schneider, (2010). “Variability of surface soil moisture observed from multitemporal C-band synthetic aperture radar and field data,” *Vadose Zone Journal*, vol. 9, no. 4, pp. 1014-1024.
- Koyama, C.N., P. Fiener, K. Schneider, (2010). “Soil moisture estimation under vegetation from PALSAR FBD data by means of polarimetric decomposition techniques,” In *Proc. Workshop on Remote Sensing Methods for Change Detection and Process Modelling*, Nov. 18-19, Cologne, Germany, pp. 63-72.
- Koyama, C.N. and K. Schneider, (2011). “Soil moisture retrieval under vegetation using dual polarized PALSAR data,” In *Proc. of IGARSS '11*, July 24-29, Vancouver, Canada, pp. 1062-1065.

Köln, den 25. November 2011

Christian N. Koyama